The University of Nottingham School of Mechanical, Materials, Manufacturing Engineering and Management

Investigation into the operation of a cement works precalciner vessel

by

Donald Giddings

Thesis submitted to The University of Nottingham for the Degree of Doctor of Philosophy

September 2000

Abstract

This Ph.D thesis describes an investigation into the operation of the Blue Circle Cauldon Works precalciner vessel. The vessel is part of the cement making plant and it serves the purpose of providing a furnace that is maintained at approximately 900°C to calcine the limestone in the raw meal prior to cementation in the kiln. At Cauldon, tyre chips are used as a support fuel. It was the aim of this work to predict the likely behaviour of the gases and particles in the precalciner by using Computational Fluid Dynamics modelling. The commercial code Fluent was used. Investigation of the likely trajectories and combustion behaviour of tyre chips was particularly important. In this way it was hoped that a method of assessing the suitability of alternative waste fuels for incineration in the precalciner might be established.

CFD models were constructed that simulated the precalciner with all main reactions and energy exchanges occurring. The first model predicted the behaviour of the precalciner burning coal and the full load of raw meal. Subsequent models assessed the sensitivity of the first model to changes in the boundary conditions. Further models were developed together with experimental work to assess the combustion and aerodynamic behaviour of the tyre chips. Alternative injection points for the tyre chips were investigated.

This type of precalciner had not previously been modelled elsewhere. Similar models were found for the operation of the precalciner without tyre chips but the geometrical accuracy of the models was improved in this work due to improvements in commercial CFD code. No similar study of tyre chip combustion has been made elsewhere.

CFD was used successfully to model a precalciner vessel with tyre chip and coal combustion and the full raw meal loading simulated. Adjustments can be made quickly to the model to assess minor geometrical alterations. Alternative fuel injection points can be quickly assessed using the model.

Acknowledgements

During the course of this Ph.D, the guidance and support of several people has greatly assisted in carrying the work forward.

Dr. Stephen Pickering has provided guidance and clear sighted, objective thinking throughout the project. Dr. Carol Eastwick and Dr. Kathy Simmons also provided significant input. Supervision has provided a "compass" for navigating through the project work.

The Engineering and Physical Sciences Research Council provided a large proportion of the funds for the project.

Blue Circle Cement Industries Cauldon Works in Staffordshire sponsored the project. The precalciner that was the subject of this thesis is part of the plant. Martin Stocks in particular lent a pragmatic approach to the analysis of the results obtained during the work and Julie Desseix provided information and assistance to the work.

Particular thanks to Julie and Kathy for persisting in helping the author to overcome a fear of heights that developed at the cement works.

Technical staff at The University of Nottingham provided practical assistance. Andy Matthews constructed the rigs used in the project, and helped to develop the concepts into reality.

Thank you to my wife Sarah for her support.

I thank God.

Acronyms used in this thesis

BET	Brunauer-Emmett-Teller method
CFD	Computational Fluid Dynamics
DAF	Dry, Ash-Free
DO	Discrete Ordinate Model
DTRM	Discrete Transfer Radiation Model
ESP	Electro Static Precipitator
KGI	Kiln Gas Inlet
LES	Large Eddy Simulation
LOI	Loss On Ignition
NO_x	Nitrogen Oxides
PAH	Poly-Aromatic Hydrocarbon
RDF	Refuse Derived Fuel
RMI	Raw Meal Inlet
RSM	Reynold's Stress Model
SLF	Secondary Liquid Fuel
SO_x	Sulphur Oxides
tph	tonnes per hour
TAD	Tertiary Air Duct

Contents

1 Introduction to the project

This thesis describes the application of CFD to a complex internal flow in a cement manufacturing plant. The work was based on the Blue Circle Cement Industries Cauldon works in Staffordshire, UK. F.L.Schmidt (now incorporated into Fuller Company) installed the plant in 1983. Since then modifications have been made to adapt to burning tyre chip material in the precalciner vessel. A schematic of the process is shown in Fig. 1-1. The layout of the preheater tower is illustrated in Fig. 1-2. The operation of the plant is described in detail in Chapter 2. All dimensions in the following brief description are approximate.

Raw meal is injected at the top of the 80m high tower, and descends through cyclonic separation vessels in the opposite direction to hot gases rising from the kiln. The precalciner vessel, illustrated in the schematic Fig. 1-3, is located just before the kiln in the process. The cylindrical section is 15 m high and has a diameter of 6.9 m. The total height is 26 m. Raw meal drops from the stage 3 cyclone into a splash box at the raw meal inlet at the rate of 200 tonnes per hour (t.p.h.), where it bounces into the rising gas stream from the kiln. Kiln gas enters at 1100°C and 18 m/s and has oxygen content of 5%. Air from the tertiary air duct enters at 900°C and 30 m/s at an angle of 60° to the horizontal. It drives the raw meal into the main section of the precalciner and provides oxygen for fuel combustion. 4" diameter pneumatic conveying pipes deliver 2 t.p.h. of coal at 25 m/s. The coal/air stream enters the precalciner at 30° below the horizontal and in the vertical plane through the vessel centre-line. A bucket elevator and screw feeder to the tyre chip inlet convey tyre chips to the precalciner from ground level. They are dropped into a splash box and enter the precalciner on the side opposite the tertiary air and raw meal inlets and 1.5 m from the centre-line toward the kiln side. Fuel combustion supports the calcination reaction, which converts limestone to quicklime. The calcined raw meal then exits the precalciner into the stage 4 cyclone before it enters the kiln where the cement clinker is formed. From the kiln, clinker drops into the clinker cooler before being conveyed as inch-sized nodules to the cement mill where it is pulverised into the familiar cement powder.

The precalciner was the subject of this research project, which was sponsored by Blue Circle Cement Industries and the Engineering and Physical Sciences Research Council.

1.1 The problem of tyre chips

Tyre chip disposal presents a problem since landfill is a poor option. The calorific value of tyre material makes it an ideal candidate for combustion processes and the cement industry provides the ideal conditions of high temperature and long residence times.

Tyre chips have been used as a support fuel at the Cauldon works since 1993. The application is in the precalciner where approximately 2/3 of the fuel is required. The proportion of energy supplied by the tyre chips has increased with increasing allowance from the Environment Agency.

Tyres are delivered whole to the site and chipped in a tyre shredder. The shredding plant is shown in Fig. 1-4. The size of the tyre chips may have a significant effect on precalciner operation. There are reasonable arguments to support use of smaller and larger nominal chip sizes. Smaller tyre chips may have desirable combustion and aerodynamic behaviour. The cost of shredding increases as the required size of the tyre chips is reduced. The relation between size and cost is exponential so that reduction of nominal chip size must be thoroughly justified. Larger tyre chips may not be supported by the rising gases in the precalciner and so may tend to fall into the kiln. The wire content of larger tyre chips may be may be responsible for build-up in the relatively low temperature precalciner resulting in premature need to shutdown the plant for maintenance. In chapter 7 of this thesis, the mechanism of tyre chip disintegration was investigated and the observations have important consequences for the nominal chip size.

Tyre chip combustion in the cement industry is very efficient; it makes use of the whole tyre since the steel strengthening wire and other combustible material becomes part of the mineral content of the cement. The oxidation of the tyre material is complete, and it will become clear in the course of this thesis that it has a beneficial impact on the gas exhaust emission from the stack. Wire build-up in the cooler parts of the precalciner and its surrounding connections to the rest of the plant has required regular shutdown of the plant

to remove the blockages since they reduce the efficiency of the plant. Figure 1-5 illustrates the blockage inside the tertiary air duct that was typical at the commencement of the project. About a third of the area is blocked by tyre material build-up. One of the key aims of this research work was to investigate the causes of tyre material build-up on the precalciner walls and to suggest ways of reducing it.

1.2 Application of Computational Fluid Dynamics

Fluid flow and thermodynamics within the precalciner are not well understood in detail. In chapter 2 the results of the limited research done into the behaviour is summarised. Measurements on the plant are very difficult due to the high temperature and the high mass of raw meal carried by the gases passing through the vessel. The mass ratio of raw meal particles to gas is approximately 1.1:1. The use of modelling to predict the behaviour has produced a few papers using one-dimensional models and some using CFD. The CFD applied in previous work was done using early grid generation techniques so that the wall of the vessel had steps and did not conform to the true geometry of the precalciner. In this work, one of the novel features is the use of body fitted gridding technique. This feature is discussed further in the section on the application of CFD, chapter 3. Commercial codes are now highly developed and have useful features included for the numerical solution of a wide range of realistic models. During the course of this work, Fluent software was applied. The well-established k-ε model for turbulence was used. Combustion was modelled using the Magnussen-Hjerteger scheme. Particles were modelled in the Lagrangian frame of reference. These features of the model are also described in detail in chapter 3. The geometry of the precalciner from this work has not previously been modelled.

1.3 Summary of the work done during the research project

During the course of the work, the cement plant heat and mass balance was thoroughly analysed to establish realistic boundary conditions for the precalciner. This included the gas flows entering from the vessels connected to the precalciner and the injection of the raw meal, coal and tyre chips. Details of the development of the boundary conditions are discussed in detail in

chapter 4 for the model without tyre chips and then in chapter 7 for the model with tyre chips.

The CFD models generated from the work progressed quickly from the initial development of gas only models to models with reacting particles. Raw meal was simulated as a combusting particle, for which the volatile content was carbon dioxide with energy release equivalent to the enthalpy of the calcination reaction. Coal with composition similar to the plant fuel was simulated with a volatile component, char and ash content. The injection of particles led to stability problems with the solution for high mass loading with reacting particles. The techniques used to overcome these difficulties are outlined in Chapter 5 in which the results of the initial fully representative model of the precalciner are presented. Some measurements were made on site through ports in the precalciner wall. An indication of the velocity and temperature at the access points was given by using an S-type Pitot probe with thermocouple attached. The results of the model were compared at the points of measurement. Several interesting features of the flow were observed.

The initial model gave rise to questions about the sensitivity of the model to various parameters assumed for the model. In chapter 6 the sensitivity of the model to various changes was checked. The results of these further investigations showed that the initial model provided a good simulation of the precalciner. As part of the sensitivity analysis, the throat section of the model was reduced in size according to a modification made to the installation.

Tyre chip modelling was performed on the initial model and on the model with the accelerator fitted. Data for the tyre chip aerodynamic and combustion characteristics were determined by laboratory experiments. Aerodynamic characteristics in the model were determined from previous work done at the University of Nottingham and from new work involving supporting the tyre chips in a column of air against gravity. The observations of the experiment showed that the tyre chips presented the maximum area to the flow. Tyre chips' decomposition at 900°C in free air showed that the structure broke down to char granules of approximately 3mm diameter, as the volatile material was released, within 2 minutes. From this observation, the behaviour of tyre chips was simulated by starting with a large tyre chip with equivalent

aerodynamic characteristics to the face on chip which converted to the aerodynamic properties of the char granule as the volatile material was released. The details of the experiments and the results of the CFD simulations based on the data in the previous models are presented in chapter 7.

1.4 Aims

The purpose of the work done during the project is summarised by the following list of actions.

- collect relevant data from the plant for development of a model of the precalciner vessel process
- model the precalciner using Fluent computational fluid dynamics software
- develop sensitivity models based on the initial model that will confirm the reliability of the boundary conditions of the model
- conduct experiments to determine tyre chip aerodynamic and combustion characteristics
- model the behaviour of tyre chips in the precalciner
- accommodate changes made to the precalciner process in the models as the work develops
- measure features of the precalciner process
- compare the measured data to the model predictions
- determine best alternative injection points for additional tyre chip material
- provide methodology for analysis of the behaviour of other waste derived fuels in the precalciner vessel

1.5 Objectives

The intended achievements of the project are summarised in the following list.

- a model fully representative of the precalciner burning coal with simulated limestone reaction
- validation data for the initial model
- sensitivity test models based on the initial model
- data from tyre chip experiments that will enable realistic modelling of the trajectory and combustion rate of the tyre chips in the precalciner process
- a model fully representative of the precalciner including tyre chip as a support fuel

- an analysis of the behaviour of tyre chips injected at different points in the precalciner

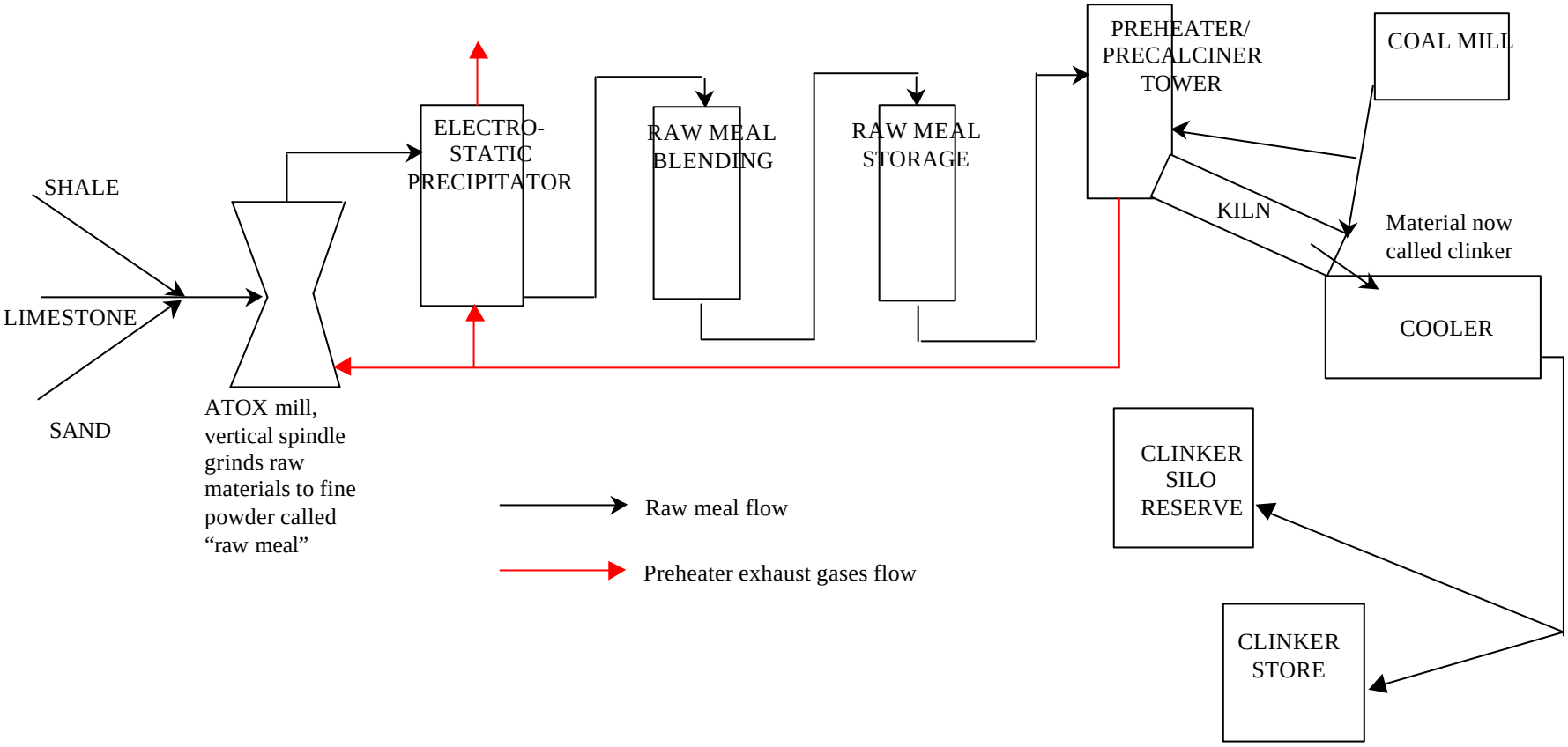

Fig. 1-1 Schematic of the overall process of cement at Blue Circle Cauldon works up to production of the clinker. Exhaust gases from the preheater tower are used to dry the raw meal at the ATOX mill, or are bypassed to the electro-static precipitator.

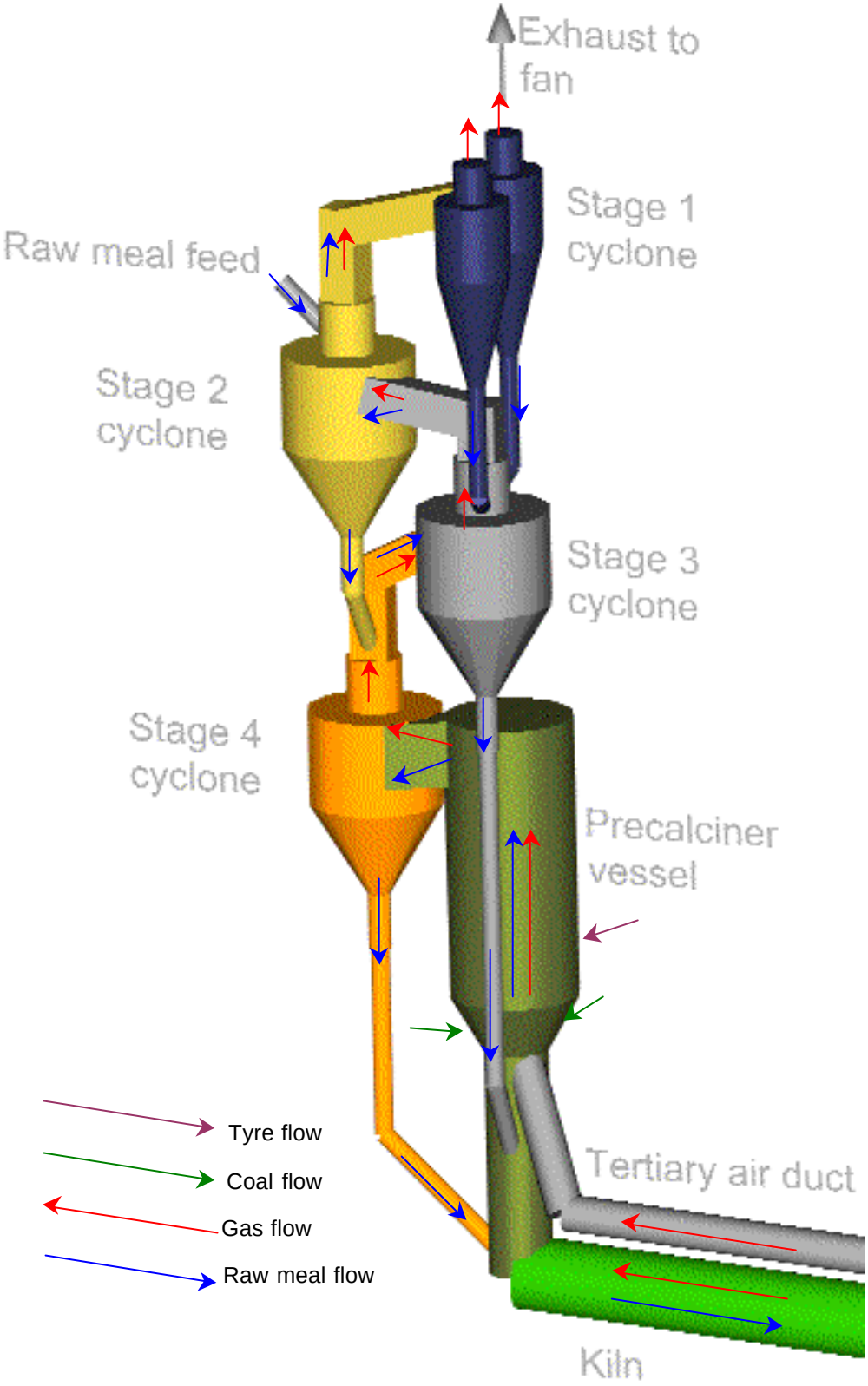

Fig. 1-2 Schematic drawing of the preheater tower at Cauldon. Gas and raw meal flow directions together with tyre and coal injection positions, are indicated with coloured arrows. Hot gases rise, exchanging heat with the descending raw meal. Most raw meal calcination occurs in the precalciner vessel. Kiln and tertiary air are drawn through the clinker cooler.

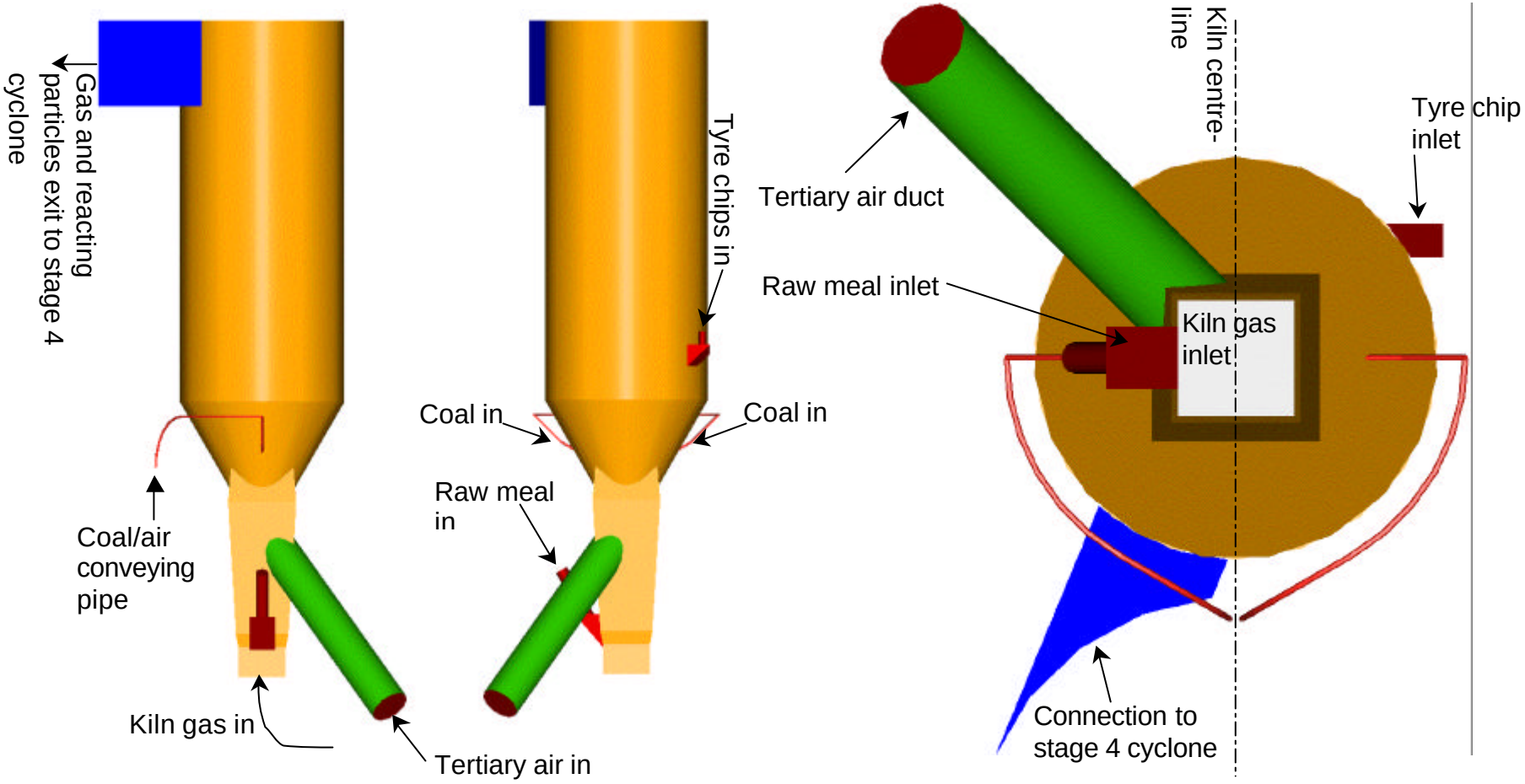

Fig. 1-2 Schematic of the precalciner vessel. Gas, raw meal, coal and tyre chip injection points and feed directions indicated with arrows.

Fig. 1-4 Tyre shredding plant at the Blue Circle Cauldon works; (a) whole tyre conveyor side and (b) chipped tyre pile side.

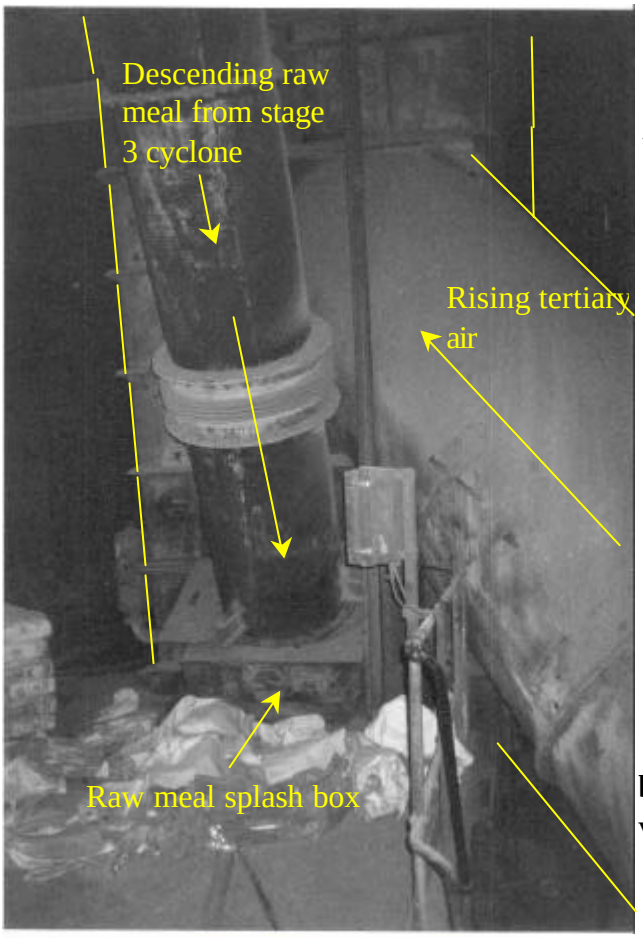

a. External view of the tertiary air duct and the stage 3 cyclone drop chute.

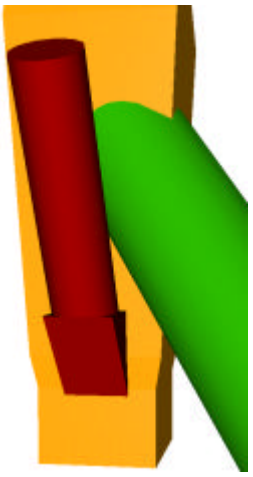

b. Schematic diagram of view shown in (a).

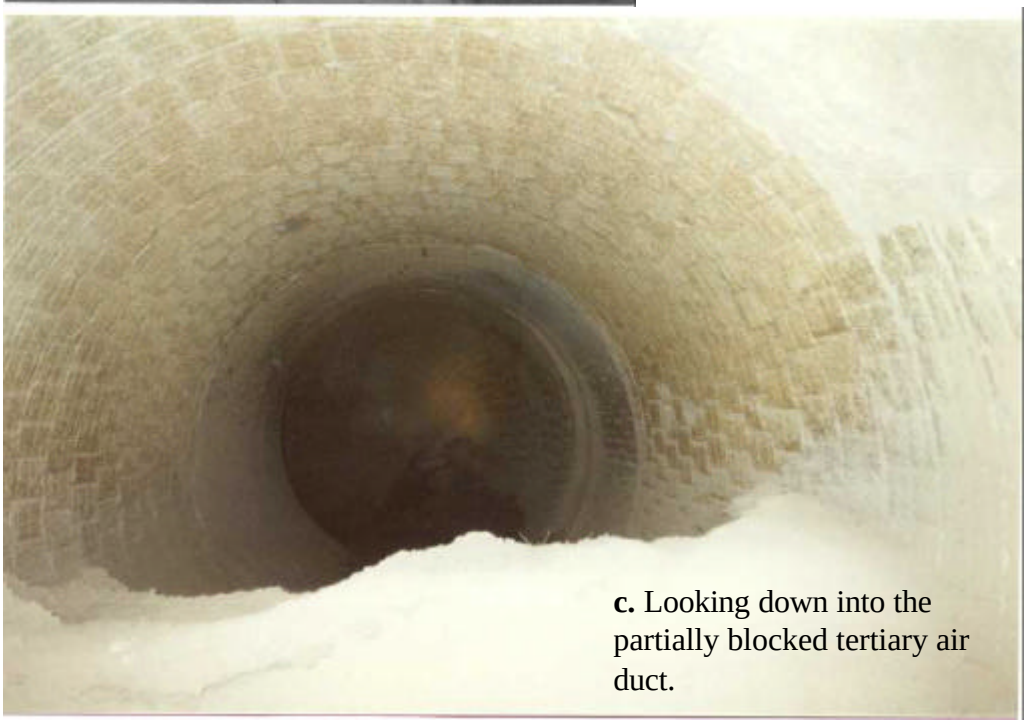

c. Looking down into the partially blocked tertiary air duct.

Fig. 1-5 Photographs of the tertiary air duct illustrating the blockage problem; (a) external photograph (b) external schematic diagram and (c) internal photograph.

2 Literature survey

This chapter gives an overview of and scientific basis for the work done during the course of the project.

Section 2-1. describes the development of the modern cement manufacturing plant, including descriptions of the wet and dry process and the preheater and precalciner plant.

Section 2-2. discusses the issue of pollution in cement manufacture. Typical fuel characteristics are described and difficulties associated with combustion in the precalciner presented. Current legislation world-wide is considered before a description of current pollution control techniques and a discussion of the production and control of NO_x emissions. The section ends with a discussion of the industry produced literature regarding NOx control.

Section 2-3. presents the issue of waste derived fuels and scrap tyre disposal. Some alternative fuels and their merits are presented. The "recovery" approach to scrap tyres is discussed as opposed to land-fill. Combustion of tyre waste in the cement industry is presented from several industrial surveys and research papers. Potential pollutants from tyre material are considered.

Section 2-4. presents the relevant features of limestone. The historical application of limestone is described and reactions for making cement considered. Thermal behaviour and mathematical modelling considerations are presented.

Section 2-5. describes the structure and chemistry of coal and considers mathematical modelling characteristics.

Section 2-6. considers the work of researchers into the characteristics of heating and oxidising tyre material. Products of combustion and pyrolysis are presented together with rates for oxidation and devolatilisation processes.

Section 2-7. presents the theory associated with non-spherical particle aerodynamics. Forces, the effect of shape and aerodynamic response times are considered.

Section 2-8. considers the effects of radiant heat transfer in the precalciner. The idea of a theoretically derived extinction coefficient and the effects of scattering and absorption by gases and particle clouds are considered.

Section 2-9. considers research models and measurements made on precalciners. Mathematical models and CFD models are described and the difficulty of making successful measurements is presented.

Section 2-10. concludes the chapter by describing ways in which the work presented in this thesis is original.

Notation for Chapter 2

A pre-exponential constant in Arrhenius rate equation (s^{-1})

Ar Archimedes number

C_D Drag coefficient

D_p diameter of particle (m)

E specific activation energy in Arrhenius rate equation (Jkg^{-1})

$\mathbf{g}$ acceleration due to gravity (ms^{-2})

k rate constant of limestone calcination rate equation (s^{-1})

K_l extinction coefficient of medium (m^{-1})

k_l optical thickness of medium (m)

k_{Oi} rate constant for devolatilisation of tyre particle (s^{-1})

l_m penetration distance of light beam in medium (m)

m mass of a raw meal particle (kg)

m_{CO2} mass of carbon dioxide available for release from raw meal particle (kg)

n (superscript) reaction order of tyre component material

N number of particles per unit volume in a suspension (m^{-3})

p pressure (Pa)

$\tilde{R}$ molar gas constant ($Jkmol^{-1}K^{-1}$)

Re Reynolds number

s surface area of particle (m^2)

S path length of radiant energy (m)

S_{sph} surface area of sphere (m^2)

s_l scattering cross section (m^2)

St_V Stokes number for a particle in a fluid

t time (s)

T temperature (K)

w total mass of a tyre particle (kg)

w_i mass fraction of a component of tyre material

a_l absorption coefficient of medium (m^{-1})

l wavelength of light (m)

m_f dynamic viscosity of fluid ($kgm^{-1}s^{-1}$)

x size parameter of particle in medium

r_f density of fluid (kgm^{-3})

r_p density of particle (kgm^{-3})

s_{sl} scattering coefficient of medium (m^{-1})

t_F characteristic time of flow (s)

t_V momentum response time of particle (s)

f shape factor of non-spherical particle

2.1 Cement manufacture

In this section a brief description of the development of the modern cement manufacturing plant is given, based largely on the work of Garret (1985) and highlighting the importance of the precalciner. In order for a cement manufacturer to remain competitive in the market, the industrial process should be as energy efficient as possible and it is this fundamental tenet that has driven the development process.

In the early days of cement manufacture the "wet" process was used for large-scale production. In this process, a slurry of limestone and shale in water is mixed to give a homogenous blend and then heated in a long kiln to evaporate the water and cause the calcining and cement clinkering reactions to occur in the one vessel. The need to evaporate large amounts of water made this process inefficient. This led to the development of the suspension preheater system, which enables the process to be done "dry", making the slurry unnecessary thereby eliminating mass

water evaporation. The suspension preheater system has become the most widely employed process technique for cement manufacture since Humboldt-Wedag first made it commercially viable in 1951. In addition to the kiln the process includes a preheater tower, which is typically in the order of 80m high and includes 4 to 6 cyclone separation vessels. The process was later further improved by the addition of a precalciner vessel.

Cauldon plant employs the preheater system, and Fig. 2-1 and 2-2 show schematic diagrams of the preheater tower configuration. Essentially, in the preheater system hot gases from the kiln pass upward at the same time as the pulverised raw meal travels downwards. The raw meal is pulverised, mixed whilst dry and supplied to the top of the preheater tower (cyclone stages 1A and 1B on Fig. 2-1). According to Perry, 1984, each cyclone acts as a co-current heat exchanger as the pulverised raw meal and hot gases circulate in the same direction during the separation process. The hot gases are generated by fuel combustion in the kiln (located at the bottom of the tower) and drawn through a duct from the top of the tower by a large fan mounted at ground level. Within the preheater tower, heat from the rising gases mixes with descending raw meal powder. The overall effect of the preheater tower is therefore to act as a counter current heat exchanger with heat passing from the rising gases to the descending raw meal.

Recent progress in development of the cement manufacturing process has focused on increasing throughput and improving emissions control. The development of the precalciner system has implications for application of waste derived fuels since the combustion vessel operates at high temperature and prolongs the residence time of the fuel.

Following the development of the preheater system, the introduction of the precalciner vessel, isolating the limestone calcination reaction in one vessel made a further improvement in energy efficiency. In the initial developments of the preheater system the calcination reaction occurred mostly in the kiln. When the new vessel was first introduced it was dubbed the precalciner as it is located immediately prior to entry to the kiln. Ishikawajima Harima Heavy Industries based in Japan developed the first commercially successful precalciner installation in 1972. The

preheater with precalciner is operated with fuel injection into the kiln and the precalciner and approximately $^2/_3$ of the total fuel requirement is delivered to the precalciner in a typical installation. In the Cauldon preheater tower, calcination of the raw meal occurs mainly in the precalciner, which is located between the kiln and the stage 4 cyclone (see Fig. 2-2).

Klotz (1997) gives a useful review of current precalciner technology and summarises the types of precalciner firing technique:

- Air Through – all air is supplied from the kiln;
- Air Separate – uses a tertiary air duct from the cooler to the precalciner (the Cauldon plant falls into this category);
- Separate Line – combustion occurs separately from the kiln gas stream.

According to Garrett (1985) the technology change brought about by development of the precalciner was quite radical in concept. It allowed effective doubling of kiln capacity and produced several other benefits including increased refractory life, reduced NO_x emissions and easier use of waste or lower grade fuels. The technology is applicable to large-scale manufacture (typically 1000 tonnes per day). Recent progress in the development of the cement manufacturing process has focused on increasing throughput and improving emissions control. The development of the precalciner system has implications for application of waste derived fuels since the combustion vessel operates at high temperature and prolongs the residence time of the fuel. This suggests that in future it may be possible to safely reclaim energy from waste products by using them to generate some of the heat required in cement manufacture. As Klotz (1997) shows, some of the most intensive research in the cement industry has been applied to the development of a more effective precalciner vessel, capable of greater throughput and improved emissions control.

2.2 Combustion pollution production and control

A survey of fuels used in the cement industry in Europe in 1995 produced the following summary: coal 38%; petroleum coke 36%; lignite 8%; fuel oil 7%; natural gas 2% and alternative fuels 9% (Bannon in Taylor, 1997). Coal is available in

different grades depending on the constituent moisture, volatiles, carbon and ash content (Smoot, 1993). Generally, higher fixed carbon indicates higher-grade coal, i.e. higher calorific value. With a precalciner and preheater tower arrangement, the combustion is performed at two points - at the kiln clinker exit end, in order to maintain the high temperatures for the clinker formation, and in the precalciner to complete the conversion of raw meal to calcined raw meal. The combustion in the kiln is outside the scope of this investigation.

Mullinger and Jenkins (1996) made the following observations about the complexity of combustion in the precalciner environment:

- changes to the air flow-patterns, such as moving the combustion nozzles and the tertiary air duct, have a "huge effect on the fuel/air mixing";
- the difficulty of maintaining a flame in the calcination region, due to the endothermic calcination reaction, can lead to "flame extinction";
- most heat transfer takes place by convection because the precalciner is a well-mixed system with gas and particles in intimate contact;
- unstable flow patterns within the precalciner will adversely affect the degree of calcination.

These observations are related to the commonest problems with precalciners, which are:

- incomplete combustion due to poor mixing of fuel and air streams and flame quenching by the strongly endothermic calcination of limestone; these problems are worse for fuels that are difficult to burn, e.g. gas with selective combustion temperature range and petroleum coke;
- unstable operation, with cyclic or random variation of degree of calcination, outlet temperature, and oxygen NO_x and SO_x formation;
- excessive NO_x formation due to the hot core where fuel is injected;
- material build up due to excessive residence times or overheating.

The calciner of this investigation is shown schematically in Fig. 2-2. These effects have been observed in the Cauldon precalciner under varying operating conditions.

Makroum and Mounir (1995) presented a study of a separate line calciner and kiln system, which delivered a qualitative analysis of some control characteristics

by using statistical process control. For this current work, the key points from the paper are that the division of fuel between the precalciner and the kiln affects the overall specific fuel requirement and that the precalciner operating temperature can be used to limit over-burning of the clinker produced.

2.2.1 Legislation

Research for improvement of the cement manufacturing process includes meeting the requirements of the legislation by applying improved control. Worldwide concern about polluting the environment has resulted in the new legislation and the progress made so far suggests that the legislative control is likely to get tighter.

The 1970 Clean Air Act in the USA has been updated with increasing understanding of emission effects and control technology. The EC has a directive to control emissions in Europe, and Germany, Japan and the Commonwealth of Independent States (CIS, i.e. what used to be mainly the USSR) all have legislation in place. The current legislating body in the UK is the Environment Agency (formed October 1996). Legal requirements are detailed in The Integrated Pollution Control (IPC) Guidance Notes Series 2 (SO, 1996) for Mineral Industry Sector and Waste Disposal and Recycling Sector. The legislation is aimed at the "criteria pollutants": CO, hydrocarbons (including aromatic hydrocarbons Furans and Dioxins), particulate matter, NO_x and SO_x (Smoot, 1993). Since the cement industry produces large scale combustion products, it is subject to the tightening legislation and must conform to the controls introduced.

2.2.2 Current pollution control in the cement industry

There are already a number of well-established controls (Perry, 1984). Increasing the efficiency of combustion can control hydrocarbon emissions (including CO). Furans and Dioxins are effectively destroyed at the high temperatures employed in cement production. It is the cooling gases at exit from the preheater tower that may be subject to production. It is important to quickly cool the exit gases through the temperature range 450°C to 200°C since Furans and Dioxins can be produced in this range. The gas-conditioning tower at the exit from the preheater is a cooling tower. It reduces the temperature from approximately 450°C to 150°C in the order

of a second. For more details see the IPC document (Environment Agency, 1997). The problems remain with NO_x and SO_x control, since control of these may inhibit efficient combustion and cause other emissions.

In practice, control of SO_x in the cement industry is not a problem as there is a naturally occurring reduction mechanism in the reactor. CaO produced in the calcination reaction absorbs the SO_2 converting it into $CaSO_4$, which can be removed from the stack gases by electro-static-precipitation as a solid particulate (Smoot, 1993). The temperature and residence time in the precalciner is ideal for this reaction to take place. Particulates can be collected by electro-static-precipitators (ESP).

2.2.3 NO_x production and control

Intensive research into NO_x control in the cement manufacturing process continues. The total stack volume exiting the typical cement works is in the order of 100,000 Nm^3/hour (i.e. volume of gas produced at Normal conditions, 0°C, 1 atmosphere). Anything more than a very small percentage of NO_x emissions will cause a major pollution problem in the vicinity of the plant. The Environment Agency monitors current legislation in the UK and operation restrictions are outlined in the Integrated Pollution Control (IPC) Guidance Notes series 2 (Environment Agency, 1997). NO_x emissions on cement manufacturing plant must be less than 900 mg/Nm^3 at the standard reference conditions (276K, 101.3 kPa, 11% oxygen and dry gas).

The mechanisms of NO_x production in combustion processes are described by Borman and Ragland (1998) and by Smoot 1993. The most significant production mechanisms for coal flames are:

- fuel NO_x (75-95%) in which fuel bound nitrogen oxidises,
- thermal NO_x, which is caused by temperatures in excess of 1400°C,
- Prompt NO_x, which is formed in the flame zone.

Control of NO_x can be approached using the following techniques.

- Nitric oxide recycle reactions, where NO is converted to HCN. This is known as "re-burning" and can be applied as control for NO_x using light hydrocarbon

gases or solid fuel with high volatile content in the post-burner flame - these are the suggested reaction schemes (Miller and Bowman in Smoot, 1993):

$$C + NO \leftrightarrow CN + O \qquad \textbf{Equation 2-1}$$

$$CN + H_2 \leftrightarrow HCN + H \qquad \textbf{Equation 2-2}$$

$$CH + NO \leftrightarrow CN + OH \qquad \textbf{Equation 2-3}$$

An alternative has been suggested in more recent literature as highlighted in the work by Tokheim et al (1998). They showed that employing plastic as the reburning fuel can reduce NO_x emissions.

- Air staging, where up to 25% of the supply air is delivered after the flame.
- Fuel staging, which makes use of re-burning. Part of the fuel is injected with the bulk of the air (fuel lean conditions) and then high volatile fuel is injected further on. This mechanism offers a 40-60% reduction of NO_x.
- Post combustion gas treatment with chemical reactants such as ammonia. These act as reducing agents and remove NO_x at appropriate temperatures.

2.2.4 Research into pollution control in the cement industry

Cement manufacture research on pollution consists of industrial scale experiments and surveys of techniques used by operators. The volume of industrial research indicates the importance and difficulty of controlling NO_x production. Several control techniques are effective. In particular, tyre combustion reduces NO_x production.

McQueen (1993) investigated the NO_x production and control problem in the cement industry in a critical analysis of available NO_x control technology. The kiln is an ideal zone for thermal NO_x production due to high temperature (1500°C) and fuel-lean conditions. Lower NO_x formation occurs in the precalciner due to the moderate temperature (850-900°C) and the fuel-rich conditions. The main control techniques available at that time were outlined and compared for effectiveness. They were divided into combustion technologies (i.e. controlling the NO_x production mechanism):

- combustion operational modifications (e.g. reducing excess air volume and temperature in the kiln combustion zone),
- low NO_x burners applied in the kiln firing zone,
- staged air combustion applied in the precalciner (firing 10-20% of precalciner fuel upstream of the tertiary air supply creating a reducing zone),

and post combustion technologies (i.e. reducing the NO_x already produced):

- selective non-catalytic reduction (injecting NH_3 in the temperature zone 870°C to 1040°C),
- and selective catalytic reduction.

The discussion described the high cost of controlling NO_x and the distinctly different combustion characteristics of the kiln and precalciner.

Syverud et al (1994) presented results of a trial, which showed the NO_x reducing effect of burning shredded car tyres in a precalciner. The tests were done on a Pyroclon™ precalciner at a Norcem site as part of an investigation into promoting post-combustion reduction by re-burn reduction of NO_x in the lower temperature zones of the process. NO_x was reduced by up to 30-45% by using chipped car tyres as a substitute for coal. Car tyre material is an ideal fuel for producing the re-burn effect due to the high volatile content of between 60% and 80% in comparison with coal, which has 10-30% volatiles. The checks on clinker quality and emissions in tests done showed no adverse effects. The sulphur cycle in the precalciner was observed to change but stabilised; an accumulation was observed in the precalciner due to alkali sulphate cycles, which was attributed to the reducing conditions locally around the tyre chips.

Jepsen (1997) demonstrated the concept of NO_x reduction in the precalciner by Staged Fuel Combustion, creating a reducing zone in the riser of the kiln before the injection of the combustion air. Tests showed that the effect was enhanced by operating at high temperature (1050°C) in the reducing zone. Tests were done on a laboratory scale on a low NO_x separate line calciner at Fuller Company. The purpose was to enhance combustion of fuels that are difficult to burn by creating a high temperature region not attainable in the in-line calciner. Having a separate line calciner enabled reduction of NO_x by up to 40%. The mechanisms of

NO_x reduction considered did not include the re-burn theory; they concentrated instead on the generation of a reducing zone at a temperature 900-1050°C.

Conroy (1997) described the successful implementation of KHD Humboldt Wedag Pyroclon^{TM} low-NO_x precalciners at three plants. The observations from these plants pointed the way to development of better low NO_x precalciners. The Pyroclon^{TM} low-NO_x precalciner is a tube calciner, which is fed from the tertiary air duct and the kiln exhaust gas. Fuel is introduced into the kiln exhaust gas to produce a reducing zone which encourages reversal of thermal NO_x. The CO rich stream produced is burned in the tertiary air duct flow through the precalciner. Introduction of a Pyrotop^{TM} swirl chamber at the precalciner exit encouraged complete combustion of CO at temperatures that are too low for thermal NO_x formation.

Bech and Gundtoft (1998) provided a more recent review of the NO_x, SO_x and CO mechanisms in cement manufacture based on actual plant data. The NO_x analysis described the effectiveness of burning tyre and waste material in the mid-kiln region. They proposed that poor mixing of air with the fuel creating a localised reducing zone caused the effect. The NO_x destruction benefit of a reducing zone is offset by promoted production of SO_x.

2.3 Tyre disposal and burning technology in the cement industry

The 1972 fuel crisis prompted investigation into the use of alternative fuels. Cement manufacture provides ideal conditions for waste combustion because of the long residence time in the process and high temperature involved. Waste fuels that have been considered as partial substitute fuels in cement manufacture include Refuse Derived Fuel (RDF, from domestic waste), and Secondary Liquid Fuels (SLF, solvents disposed of by industry). Used road vehicle tyres in particular possess high calorific value, typically 35 to 40 MJ/kg (Conesa, 1998), making them a prime candidate for use as a support fuel. Although this thesis focuses on combustion of scrap tyres the analysis of other waste fuels is useful and a brief catalogue of previous work is given in the following paragraphs before discussing use of tyres.

Petrie and Baldwin (1992) analysed a variety of waste fuels, comparing devolatilisation and combustion characteristics. They presented results of

combustion tests on mixed briquettes of high calorific value wastes (scrap coal and paper, scrap anthracite and molasses, paper and plastic, and bagasse). In particular they noticed that the devolatilisation rate is related to the volatile content and that the char activation behaviour is related to the binder used. They concluded that there is 'significant potential' for useful recovery of energy from these fuels.

The combustion of Refuse Derived Fuels (RDF) in the cement industry was analysed by Lockwood and Ou, (1993), in a study on a plant owned by Norcem in Norway. The study showed that the use of poor quality fuels such as RDF resulted in lower production levels, emissions problems and worsening chlorine salt build-up cycles due to high chlorine content of the fuel. They concluded that the upper limit for fuel substitution with RDF is 30%, and that there is no economical advantage in burning RDF in cement manufacture without subsidy due to the initial cost of investment in equipment and operation costs.

The combustion of tyres is advantageous to both the cement and waste disposal industries as it provides recovery of some of the usefulness of the waste and a cheap form of energy for the cement industry. The technology for tyre combustion in cement manufacture has been well developed and is used at a number of sites throughout the world. Schrama et al (1995) indicated tyre production of 275 million tyres per year in the USA, of which 14% went to the cement industry for use as a substitute fuel. Useful applications were found for a further 12%, but the remainder was sent to landfill. Recycling Week (1996) showed a similar situation in the UK, presenting a summary of a recent report by the DTI Scrap Tyre Working Group (1996). The Working Group found that of the 370,000 tyres scrapped in 1995 in the UK, the end uses were found to be as follows:

- 4% - useful landfill engineering
- 5% - put to use directly e.g., as boat fenders
- 11% - recycling
- 22% - energy recovery
- 30% - re-treading
- 28% - not recovered i.e. landfill refuse sites

Comparison of studies by Schrama et al (1995) and Blumenthal (1996), show that scrap tyre applications to useful purposes in the USA increased between 1995 and 1996 in order to dispose of the increasing supply, which had in the past been sent mainly for landfill. Schrama et al (1995) reported a survey on use of tyres as a substitute fuel in the US cement industry. Blumenthal (1996) described the techniques used for tyre combustion in the US cement industry. Chipped tyres were injected in to the kiln outlet end and whole tyres were injected in to the preheater tower at the level of the precalciner. From the experience of companies surveyed by Schrama et al (1995) in the USA, the maximum fuel substitution for whole tyre cases was 30% of fuel energy requirement while that for chipped car tyre cases was only about 10%. The reported experience from both papers showed that combustion of chipped tyres was more costly than using whole tyres due to the chipping requirement, despite improved feed control. Other problems associated with burning scrap tyres that were reported were build up of tyre deposits, maintaining regular supply of tyres, worsening of alkali salt ring formation in the kiln (due to alkali sulphate condensation in certain temperature zones within the kiln), and an increased oxygen supply requirement. The reported benefits were higher calorific value than coal and lower emissions. The preheater with precalciner installations surveyed by Schrama et al (1995) indicated that when tyres substitute more than 10% of fuel, problems become too large to justify the benefits.

Blumenthal (1996) indicated the scale of use in the US cement industry. Twenty-seven producers at that time used scrap tyres as a partial substitute for fossil fuels in the USA. Twenty others had permission to substitute and thirteen were conducting tests. The estimated potential use was projected to be 75-100 million scrap tyres out of a yearly production of 253 million. 69% of Tyre Derived Fuel (TDF) in the US had found a useful outlet, suggesting that if the increase in useful applications continued tyre supply for cement plants may become unreliable.

Saito et al (1987) reported on gasification as an alternative to complete combustion to yield 95% of the fuel as gas. The project, however, was only on a small scale (manufacture less than 1200 tonnes per day - the hourly production of many large plants). It was reported that this technique is suitable for applications

where combustion of the complete tyre is not practicable due to coloration of white cement and unwanted excess air ingress, associated with injection of tyres, in smaller production units. It was further suggested that although it is apparently cleaner, this technique would be too costly to apply at a large-scale plant. An additional reported advantage of this technique was the liberation of the steel wire content of the tyres in a recyclable form.

The emissions from tyre derived fuel have been researched and compared with equivalent emissions from coal. Levendis and Courtemanche (1997) present a discussion of the generation of NO_x pollutants from tyre and coal. They showed by experiment that reducing conditions lead to reburn reactions, that at temperatures less than 1230°C the majority of NO_x is from the fuel NO_x mechanism. NO_2 production was shown to increase as the equivalence ratio in fuel rich conditions increased. Levendis et al (1998) correlated CO and PAH (polynuclear aromatic hydrocarbons) showing that the CO and PAH yield from tyres was greater than that from coal in the temperature range 1000°C to 1300°C. PAH was reduced to almost zero at the highest temperature while CO emissions increased with temperature.

2.4 Limestone

Robert Herman Bogue (accredited with the development of the Bogue calculation - familiar to cement manufacturers) provides a good summary of the history of mankind's application of limestone in building (Bogue, 1955). It is apparent that the discovery of basic cement occurred in prehistory - limestone calcines to lime when strongly heated; lime forms a paste when mixed with water that hardens when dried. It was used in construction of the monumental pyramids of Egypt, and was extensively and methodically applied to construction work by Greeks and Romans in the respective classical periods.

The search for hydraulic cement (i.e. one that resists decomposition by water) led to the development of Portland cement (named after the renowned, high quality limestone found in Portland, Dorset) by adding clay. Limestone and shale are the naturally occurring minerals that are pulverised and dried and used to make

cement. Limestone is the fossilised remains of pre-historic shellfish and shale is sedimentary material formed from decomposed and fossilised vegetation.

When limestone is heated, the calcination reaction producing quicklime and carbon dioxide occurs:

$$CaCO_3 \rightarrow CaO + CO_2 \qquad \textbf{Equation 2-4}$$

This reaction is highly endothermic; a simple calculation of product and reactant formation enthalpies shows that the energy consumed is 1770 kJ per kg of $CaCO_3$. Cement production is therefore an energy intensive process. The process is well established and Taylor (1990) gives a good description. The process consists of two stages:

- On reaching 900°C at atmospheric pressure the limestone completely calcines to quicklime by the dissociation reaction. The reaction within a particle occurs at a reaction surface interface which moves inwards (Taylor, 1990). To achieve complete reaction, the high temperature 898°C must be attained throughout. In modern cement production, the limestone is pulverised before processing to promote heating efficiency. Taylor (1990) indicates an industrially standard particle size for the ground raw meal of 85% passing through a 90-μm size sieve.
- Further heating to the order of 1500°C causes the raw meal mixture to become semi-molten and the reactions that produce the main mineral constituents of cement - Alite, Belite, Ferrite and Aluminate - proceed. Cooling causes nodules of clinker to form, typically having a diameter in the order of 4 cm, which are then crushed and used to form the familiar cement powder. The constituents of cement are indicated in Table 2-1.

Inspection of a typical plant heat balance shows energy consumption in the order of 3.3 GJ per tonne of clinker produced with process temperatures reaching in excess of 1500°C in the rotary kiln.

Chemical composition

compound	chemical formula	% by mass
calcium oxide	CaO	62-67
silicon dioxide	SiO_2	18-24
aluminium oxide	Al_2O_3	4-8
iron oxide	Fe_2O_3	1-5

Mineral composition

Mineral name	Compound name	chemical formula
Alite	tricalcium silicate	$3CaO.SiO_2$
Belite	dicalcium silicate	$2CaO.SiO_2$
Ferrite	tricalcium aluminate	$3CaO.Al_2O_3$
Aluminate	tetracalcium aluminoferrite	$4CaO.Al_2O_3.Fe_2O_3$

Table 2-1 Chemical and mineral composition of cement.

The thermal behaviour of limestone is important since it determines how best to "burn" the limestone to form good quality cement. The chemical behaviour is well described by Boynton (1980). The important features are as follows:

- the partial pressure of CO_2 in the furnace atmosphere limits calcination if the temperature is below 900°C;
- the heat consumed during calcination varies from 1620 to 1955 kJ/kg depending on the nature of the limestone;
- the rate of calcination depends on the surface area to volume ratio.

From a modelling point of view it is important to know the rate of calcination to determine heat consumption patterns and CO_2 release patterns. Much of the work, which forms the basis of current calcination models, was completed during mid-1980. Borgwardt (1985), in particular working for the US Environmental Protection Agency, developed some key work building on previous research and producing useful data for activation energy and the Arrhenius rate equation for dispersed particles of limestone at temperatures and particle sizes equivalent to those in precalciner operation. Interestingly, a less obvious use for limestone is in pollution control from coal fired power generation and Borgwardt (1985) investigated the kinetics of calcining limestone in order to provide data for new pollution control research establishing both the rate of calcination and the rate limiting mechanism.

Previously established arguments about the calcination rate proposed three rate-controlling factors:

- heat transfer to the surface and then through the CaO product layer to the reaction interface;
- mass transfer of CO_2 away from the interface through the product layer;
- the chemical reaction.

In the case of small particles, as in this work, the resistance due to the reaction interface is negligible. Borgwardt demonstrated that heat and mass transfer in the particle determined the reaction rate, but in addition to previous work, that the surface area available for reaction was much larger than expected due to the porosity.

Borgwardt performed experiments on an entrained flow reactor and a differential reactor. A differential reactor applied to gas/solid reactions is one in which the difference between reactant gas concentration at inlet and outlet is not significantly affected by the reaction. The temperature ranges considered were 475°C to 710°C in the differential reactor and 775°C to 1000°C in the entrained flow reactor. Particle sizes were 1 to 90μm in the differential reactor and 10 to 90μm in the entrained flow reactor. The apparent activation energy of particles in these size ranges was estimated to be 2.05×10^{8} J/kmol.

The Brunauer-Emmett-Teller (BET method) surface area was found to be very important in determining the rate. A description of the BET method can be found in the text by Perry and Green (1984). It is used to measure the total surface area of a porous material. Borgwardt described limestone as having a porous nature with between 3% and 8% porosity. The BET surface area was found to be up to five times the area suggested by the external surface area. The particles studied by Borgwardt were similar to the particles in a typical precalciner and so it can be expected that similar behaviour will be exhibited. The reaction rate was found to be between 1.2×10^{-6} and 1.5×10^{-6} mol/cm^2.s. The rate calculation applicable to the code used for the work of this thesis was:

$$\frac{dm}{dt} = km_{CO_2} \qquad \textbf{Equation 2-5}$$

where m_{CO2} is the mass of limestone remaining in the particle that will be liberated as CO_2. k is determined by definition of the constants A and E in the equation

$$k = A\exp\left(-E/RT\right)$$ **Equation 2-6**

The constants used in this study were chosen to give reasonable agreement with the results presented by Borgwardt. Borgwardt found that A should be 3.81×10^{8} s^{-1} and E should be 2.05×10^{8} J/kmol. For particles between 20μm and 90μm, this resulted in equivalent rates of 0.528×10^{-6} mol/cm^2.s for a 20μm particle and 1.560×10^{-6} mol/cm^2.s for a 90μm particle.

Silcox et al (1989) developed a mathematical model of the calcination of limestone using the data of Borgwardt (1985). Dennis and Hayhurst (1987) performed experiments in a fluidized bed to find the effect of carbon dioxide partial pressure, variation of gas pressure above atmospheric, and temperature. They found a reaction rate constant in good agreement with Borgwardt (1985).

2.5 Coal Combustion Modelling

The coal combustion models available in Fluent use heating, devolatilisation and char combustion. The papers reviewed in this section were used to obtain realistic data for the models used in the precalciner and to verify the correct use of the data available from Fluent.

2.5.1 Structure and chemistry of coal

Coal is a fossil fuel, abundant supplies of which can supply energy at projected demands for up to 250 years. The structure of the coal is dependent upon the geology of the region from which it has been extracted. The quality of the coal determines its combustion characteristics and this is important for the smooth operation of the cement plant. Consequently it is within the scope of this thesis to understand the nature of the coals used at the Cauldon cement works.

The nature of coal is discussed in detail in the editorial compiled by Smoot (1993). Coal was formed over millions of years from partially decomposed flora and fauna in swampy environments. Decomposition was arrested by stagnant conditions as layers of this matter built up. As the depth of matter increased, pressure and temperature increased and first petrifaction and then the coal making process occurred. The structure of coals as we see them now was determined by

the nature of the constituent matter that was originally decomposed and on the history of the coal. The maceral content defines the type of minerals that were formed and indicates the predominant original ingredients.

It is not instructive to investigate further the detailed structure of coals here, but from the combustion engineer's point of view coal is classified by ultimate analysis, elemental analysis and proximate analysis. The ultimate analysis is the precise chemical composition of the coal in terms of carbon, hydrogen, oxygen, nitrogen, sulphur, and chlorine since these are the bulk constituent chemicals. Elemental analysis of the trace metals is important when considering pollution control. Elements include arsenic (As), cadmium (Cd), cobalt (Co), chromium (Cr), copper (Cu), mercury (Hg), manganese (Mn), nickel (Ni), lead (Pb), antimony (Sb), tin (Sn), thallium (Tl), vanadium (V), zinc (Zn). The behaviour of coals when heated is determined by the volatile content, the char or fixed carbon content, and the ash content which is the mineral matter that does not decompose when heated to flame temperatures. The classification, or ranking, of coal types is summarized in the Fig. 2-3 reproduced from Smoot (1993).

The oxidation of a solid fuel can be understood by considering the separate processes. Devolatilisation occurs as the temperature increases, by which components of the coal that change state from solid to liquid and from liquid to gas are yielded un-oxidized into the gas phase. This is followed by oxidation of those chemical species. Oxidation of the char component follows this. Char is the fixed carbon content of the fuel in the case of solid fuels. When devolatilisation occurs without combustion it is termed pyrolysis.

2.5.2 Devolatilisation

The devolatilisation of coal is described qualitatively and chemically in Smoot (1993). Heating the fuel causes the release of gases and tars , which then oxidize separately from the coal particle. The behaviour can include breaking hydrogen bonds to form a plasticised component called metaplast along with liquid components, evaporation of tars, further bond breaking to yield further tars and gases, and repolymerization to form char. Coal rank determines the behaviour

during devolatilization, and this has been investigated extensively. Research concerning devolatilization rate was of interest for this thesis and prominent papers are presented in this section.

Solomon et al (1992) produced a summary and cataloguing of experiments to determine the rate limiting factors. Experimental techniques were described which determine the rate of devolatilisation using heated grids, entrained flow reactors, thermo-gravimetric analysis and radiative heating, amongst others. The important parameters to monitor are the heating rate, the temperature attained, the size of the particles, and the ultimate and proximate analyses of the coal. Variation in the data of different researchers was found to vary by a factor of up to 1000 times, and possible causes of this were investigated. It was apparent that ranks of the coal and mass transfer effects were not the cause of the variation in devolatilisation rate. The essential factor in explaining rate kinetics differences between experiments was found to be the temperature history of the heated particle. All data presented in the paper is applicable to coal in the pulverised size range and the experiments were discussed critically to determine the potential error sources. The experimental results revealed characteristics of the composition and heating behaviour of the coals. These included rate of mass loss, and analysis of gases and tars evolved from the devolatilising particles. Detailed description of the mechanism of devolatilisation were presented including the authors' own theories. Primary pyrolysis occurs after 400°C. In the region 200°C to 400°C the chemistry of the coal changes as bonds change. Gases and lighter tars evolve first and then as the bond disruption proceeds, larger tar molecules are released.

There are many mathematical models of the devolatilization process and Solomon et al (1992) presented a summary of some that are used, including those used by Fluent. The devolatilization models rely on empirically determined constants. Those of Badzioch and Hawkesley (1970) and Kobayashi et al (1976) are used by Fluent. The experiments done by these researchers used entrained flow reactors (drop tube furnaces) and high heating rates in the order of 10,000 to 200,000°C/sec. The coals analysed were bituminous and lignite. The heating rates

and particle sizes were similar to those of the coal particles in the precalciner vessel, so that the devolatilization models should be applicable to the current study.

2.6 Tyre Combustion Rate Modelling

This section describes previous research work into the products and characteristics of tyre combustion.

Williams et al (1990) performed a detailed study of the pyrolysis products of tyre chips when heated in a nitrogen atmosphere. The results of that study showed the complex nature of product evolution as the tyre chip material reaches different temperatures at different rates of heating. The calorific value of the tyre material was assessed and the ultimate and proximate analyses were presented. The details are reproduced in the Table 2-2 together with the elemental compositions of Conesa et al (1998) and Schrama et al (1995). The proximate analysis and Gross Calorific Value were determined without accounting for the steel-wire-core present in tyres.

Elemental composition %

	Williams et al (1990)	Schrama et al (1995)	Conesa et al (1998)
carbon	85.9	83.5	78.4
hydrogen	8	7.8	6.6
nitrogen	0.4	0.4	0.2
sulphur	1	1.5	1.2
oxygen	2.3	6.8	1.2
ash	2.4	8.2	11.7

Proximate analysis %

	Williams et al (1990)
Volatiles	66.5
Fixed carbon	30.3
Ash	2.4
Moisture	0.8

Gross calorific value 40.0 MJ/kg

Table 2-2 Composition of scrap tyres from various researchers.

It is interesting to note that the calorific value (assuming removed steel wire) is greater than that for coal and that the sulphur content is similar to coal.

Using thermo-gravimetric analysis, Leung and Wang (1999) investigated the pyrolysis of tyre material in a nitrogen atmosphere for particle sizes is in the range of 0.5mm to 2.36mm. The tyre material was heated at a constant heating rate and the rate of weight loss as a function of temperature recorded. Figure 2-4a shows a sample result for the case where the heating rate was 10°C per minute and illustrates that mass loss rate occurred in three distinct regions. The size of the particle was found to not affect the pyrolysis rate, and the heating rate was found to have a small

effect. The cause of the three peaks was thought to be due to the behaviour of different components. The temperature range 150°C to 350°C caused evolution of oil, plastisizers and additives. The range up to 600°C causes evolution of the natural rubber, butadiene rubber and styrene-butadiene rubber, giving two characteristic peaks at 400°C and 470°C. The Arrhenius rate model that the researchers applied to the pyrolysis rate was therefore broken into three sections with three different rate controls for natural rubber, butadiene rubber and styrene-butadiene rubber. The data used and the results obtained from this model are seen in the Fig. 2-4a and show good agreement of the experimental data with the rate model applied.

The rate at which the tyres oxidise and how they will behave as they heat up is of particular interest to the work presented in this thesis. Experiments to find a kinetic model for combustion of tyre wastes were performed by Conesa et al (1998). Their work showing the effect of oxidation of the tyre material in 10% to 20% volume oxygen atmospheres with helium composing the remainder of the atmosphere, is of particular interest since it indicates the oxidation behaviour of the tyre material. Tyre particle size was less than 1 mm. As with Leung and Wang (1999) the characteristic mass loss was attributed to loss of natural rubber, butadiene rubber and styrene-butadiene reubber. Figure 2-4b shows a comparable result of Conesa et al to the work of Leung and Wang for 10°C/min heating in an inert atmosphere (Helium). Although the graph is inverted and the scale is different, the characteristic three regions can be seen. The reason for the difference in the two peak sizes between the two sets of results is not clear. It is important to observe the difference between the weight loss rate in an inert atmosphere and that in oxidizing atmosphere as seen by comparing Fig. 2-4b and Fig. 2-4c. It is clear that there are more peaks and that the temperature rate is no longer uniform due to the heat generated by combustion.

Conesa et al (1998) also determined the rate of decomposition of the mass by calculation. A 4 step reaction scheme was employed, in which the oil fraction, then the natural rubber then the styrene-butadiene rubber decompose followed by the mineral components (i.e. char). The rate equation used for each of the fractions was of the Arrhenius form:

$$\frac{dw}{dt} = \sum k_{0i} \exp\left(-\frac{E_i}{RT}\right) w_i^n \qquad \textbf{Equation 2-7}$$

Where w is the total mass, k_{0i} is the rate constant, E_i is the activation energy and w_i is the mass of the fraction and n is the reaction order. The data used is presented in Table 2-3 below with each of the F numbers representing on of the four reactions identified. The constants were determined by adjustment until the calculated weight loss curve matched the experimental result.

	F1	F2	F3	F4
k_{0i} (s^{-1})	2.84×10^{6}	4.64×10^{14}	4.15×10^{14}	3.79×10^{8}
E_i (kJ/mol)	83.6	245.6	201.7	223.2
n	2.445	3.905	1.456	0.692

Table 2-3 Rate constants for decomposition of tyre material from Conesa et al.

More recent work by Giugliano et al (1999) determined the combustion behaviour of tyre chips by holding them in suspension inside a precalciner in a zone having temperature 1050°C to 1150°C and oxygen 5 to 9% with a mean velocity of 20 to 22m/s. Tyre chip average weights were in the range 3.1 to 15.2 g. The rate of weight loss of the tyre chips was determined by assuming that it is initially by devolatilization only. This assumption is reasonable considering the gas conditions and the high volatile content of the tyre material. The calculated time for complete devolatilization of the chips was between 40 s and 100 s. The devolatilization process was completed in an average of 30 s in the experiments.

The chip sizes used at Cauldon are in the range of 5 g to 100 g. In assessing a rate of devolatilization, the most appropriate research regarding size of chip is the work by Giugliano et al (1999). Despite the more rigorous scientific approach determining Arrhenius rates with tyre granules sized in the order of millimetres, it is important to use like sized particles. The research reported in this thesis suggests that further experiments should be performed to determine the combustion behaviour of the tyre chips in the precalciner.

2.7 Non-spherical particle modelling

In order to model tyre chip aerodynamics, it is important to understand the mechanism of fluid forces on large non-spherical particles. No work specifically related to large chips with non-isometric (i.e. not regular) shapes was discovered in the literature, but the issue of predicting non-spherical small particle terminal velocity has received considerable attention.

The text by Crowe et al (1998) presents the basic principles of particle-gas interaction. For the momentum of the tyre chips, it is sufficient here to consider calculation of the drag force and gravity force only since other forces were not considered to have sufficient magnitude to merit attention for the following reasons:

- pressure gradients, buoyancy forces, unsteady Basset and virtual mass forces are all negligible because of the high ratio of particle density to gas density (in the order of 10,000)
- drag due to rotating particles in velocity gradient, lift forces due to Saffman and Magnus effects, and torque applied to the particle are not considered since they apply to spherical particles or iso-metric particles. Tyre chips are highly non-isometric and other techniques are required. For this reason, the non-spherical particle modification to drag is not considered.
- forces due to plasma effects and thermophoretic effects are negligible since the gas is not at plasma temperatures and temperature gradients are very small in the length scale of the particle diameter (25 mm to 150 mm in a 6.9 m diameter vessel.
- the Coulomb effect is negligible since there is no apparent electric field
- the "blowing" effect of reacting particles is considered negligible in all cases
- drag force due to density of the particle cloud is negligible due to the low volume fraction of the particles

Drag force on spherical particles has been well documented (e.g. Massey, 1989). Three regions defined by Reynolds number have been identified as affecting the behaviour of the drag coefficient. The Stokes' region (describing laminar flow

and named after George Stokes, 1819-1903) is the low Re region <0.05. The Transition region (describing the transition from laminar to wholly turbulent flow) is the intermediate Re region, 0.05<Re<2000. The Newtonian region (named after Isaac Newton, 1642-1727) is the initial fully turbulent region, 2×10^3<Re<2×10^5.

Although the tyre chips are highly non-isometric, it is useful to consider the approach of researchers into isometric non-spherical particles to get the relevant terms that are commonly used to describe the behaviour.

Considerable work has been done by other researchers in the determination of empirical data for isometric non-spherical particles. Hartman et al (1994) includes a summary of the work of several research papers describing the important arguments. A balance of forces when a particle is in free-fall results in the equation:

$$C_D \,\mathrm{Re}^2 = \left(4/3\right) Ar \qquad \textbf{Equation 2-8}$$

where *Ar* is the Archimedes number, the ratio of buoyant forces to viscous forces, defined as:

$$Ar = \frac{r_f}{m_f^2} D_p^3 g\left(r_p - r_f\right) \qquad \textbf{Equation 2-9}$$

C_D is related to Reynolds number and a factor that describes the shape of the particle. The most appropriate measure of shape is the sphericity developed by Wadell (1934):

$$f = \frac{s}{S_{sph}} \qquad \textbf{Equation 2-10}$$

Where *s* is the surface area of the particle and S_{sph} is the surface area of the sphere having the same volume. Several researchers have developed empirical correlations for the relationship of C_D to sphericity, (f), Reynolds number (*Re*). Haider and Levenspiel (1989) developed a generally applicable formula, in which the form of the drag coefficient was found to be:

$$C_D = \frac{24}{\mathrm{Re}}\left(1 + A\,\mathrm{Re}^B\right) + \frac{C}{1 + \frac{D}{\mathrm{Re}}} \qquad \textbf{Equation 2-11}$$

Where *A*, *B*, *C* and *D* are empirical functions of the sphericity determined by applying non-linear regression fitting software to experimental data. The sphericity is useful for consideration of particles that are isometrically shaped.

The important features of aerodynamic behaviour can be described by two parameters – the response time and the Stokes number, which are both clearly described by Crowe et al (1998). The momentum response time is developed from the equation of motion of the particle. It has the units of time and is shown in equation 2-12:

$$t_p = \frac{r_d D^2}{18m} \qquad \textbf{Equation 2-12}$$

Crowe et al (1998) show that the response time is the time taken for a particle to reach the free stream velocity when released from rest. Stokes number is defined as:

$$St = \frac{t_p}{t_F} \qquad \textbf{Equation 2-13}$$

t_F is a characteristic time of the flow field and is calculated using the velocity of the fluid and the length of a sensible cross section of the flow at the point at which the response time was calculated. If $St>>1$, then the particle will not be much affected by the momentum of the flow. If $St<<1$, then the particle will respond very quickly to momentum changes of the flow.

The Fluent software used in this thesis makes use of the work of Morsi and Alexander (1972) to calculate the drag coefficient of spherical particles. The drag coefficient is dependent on the Reynolds number of the particle in the flow. The equations developed for their work are presented in Table 2-4.

Ritter (1995) in previous work on the subject of this thesis, performed wind tunnel experiments on tyre chips to find the drag coefficient. Having the drag coefficient in a particular orientation of the chip and using the results of Morsi and Alexander, he was able to specify equivalent spheres to model tyre chips which had the same drag coefficient and mass as the tyre chip. This work will be built upon in this thesis.

Re	a_1	a_2	a_3
<0.1	0	24	0
0.1<Re<1.0	3.69	22.73	0.0903
1.0<Re<10.0	1.222	29.1667	-3.8889
10.0<Re<100.0	0.6167	46.5	-116.67
100.0<Re<1000.0	0.3644	98.33	-2778
1000.0<Re<5000.0	0.357	148.62	-4.75×10^4
5000.0<Re<10000.0	0.46	-490.546	-57.87×10^4
10000.0<Re<50000.0	0.5191	-1662.5	5.4167×10^6

Table 2-4 Morsi and Alexander equations for variation of sphere drag coefficient with Reynold's number.

Since the modelling of tyre chips must assume a highly non-isometric shape, it is questionable how accurately the drag coefficient can be determined by calculation. The research to date assumes either isometric shapes or simple geometries such as disks. It was therefore necessary to investigate aerodynamic behaviour of the tyre chips by experiment to determine drag and trajectory behaviour.

2.8 Radiant heat transfer modelling

At Cauldon it is possible to open an access port and look into the precalciner. On visual inspection it is apparent that radiant heat transfer within the vessel is significant. No more than a few centimetres depth is visible from any of the access ports before the sight becomes a thick, blurry-orange glow. The reason for this is the high particle loading and the concentration of gases, which absorb and scatter radiant heat energy.

Siegell and Howell (1992) describe the radiant heat transfer mechanisms in absorbing, emitting and scattering media. The following terms are useful for the description of the effects:

- extinction coefficient, K_l, combines the attenuation effects of absorption and scattering coefficients; units of reciprocal length;

$$K_l(l,T,p) = a_l(l,T,p) + s_{sl}(l,T,p) \qquad \textbf{Equation 2-14}$$

- penetration distance, which is the reciprocal of the extinction coefficient;

$$l_m = \frac{1}{K_l} \qquad \textbf{Equation 2-15}$$

- optical thickness, which is the product of extinction coefficient and path length and indicates the relation between the opacity of the medium and the dimensions of the boundary;

$$k_l(S) = K_l S \qquad \textbf{Equation 2-16}$$

Using the derivation of scattering coefficient for particle load, shown in equation 2-18 taken from Siegell and Howell (1992), it is possible to determine the scattering coefficient related to the particles in the Cauldon precalciner. The scattering coefficient can be calculated from the scattering cross section, s_l and the number of particles per unit volume, N:

$$s_{sl} = s_l N \qquad \textbf{Equation 2-17}$$

In the preclaciner, N is approximately 1229 cm^{-3} since the mean gas density is in the order of 0.3 kg/m^3 and the mass fraction of particles to gas is approximately 1:1. From Siegell and Howell, s_l depends on wavelength and the particle diameter. The wavelength of interest is the visible and near infra-red i.e. $l=10^{-7}$ to 10^{-4} m, and the diameter of the particles is in the order of 5.5×10^{-5} m so that $2\times10^{-3} < l/D_p < 2$. For $l << D_p$, scattering is by Fraunhofer and Fresnel diffraction plus reflection and s_l is determined by the formula:

$$s_l = 2\left(\frac{pD^2}{4}\right) \qquad \textbf{Equation 2-18}$$

Therefore, $s_l = 4.75\times10^{-9}$ m^2, and $s_{sl} = 5.84$ m^{-1}. This indicates a penetration distance of 17 cm. In addition to this, the work of Siegell and Howell indicates that for the Cauldon precalciner, surrounding particles will have no effect on scattering. Independence is determined by the particle size and the volume fraction in the gas and data for pulverised coal is displayed in Fig. 2-5. Since the combustion in the Cauldon precalciner is similar to pulverised coal combustion, the independence of scattering on surrounding particles can be inferred from this data.

The type of scattering is determined by the size parameter, ξ:

$$x = \frac{pD}{l_m}$$ **Equation 2-19**

In the Cauldon precalciner, $D_p \approx 55\mu m$ and so $1.6 < l < 1600$. For a size parameter of this magnitude, according to the data of Siegell and Howell (1992), diffraction does not have a significant influence and scattering is by reflection, mostly in the forward direction.

Absorption and emission in the precalciner gases have been considered as a secondary heat transfer effect compared when compared to that of the particles since the extinction due to particles is significant across all wavelengths of interest. Siegell and Howell (1992) described the vibrational and rotational transitions of the gas atoms and molecules in the moderate temperatures encountered in typical engineering applications. Gases absorb radiant energy at specific wavelengths. By Kirchoff's law, the emitted energy must equal this and be at the same frequency. Emission from a gas element is isotropic so the combined effect is to diffuse the radiant energy.

2.9 Survey of precalciner modelling research

2.9.1 Mathematical Models.

The ability to predict the behaviour of gases and particles inside a precalciner will contribute towards effective design of new calciners and improvement of existing installations. Early predictions were based on simple mathematical models and these have increased in complexity as modelling sophistication has progressed. The modelling approach culminates with Computational Fluid Dynamics (CFD), which was used for the work reported in this thesis, but it is important to examine the development of the mathematical technique to understand what information can be drawn from the current model.

Rosemann (1986) considered reaction kinetics in a plug flow model of a typical precalciner vessel. Kinetic data for the raw meal calcination was based on

gas temperature and partial pressure of CO_2. Coal combustion was modelled as devolatilisation and oxidation of volatiles followed by oxidation of the char component. Data for the rate of raw meal calcination was used from previous work (Kainer, 1982). An investigation was performed on the effect of staging raw meal addition (i.e. injection at more than one height in the precalciner) and it was found that the temperature of the gases in the vessel might be controllable using this technique. The one-dimensional model provided a useful indication of reaction progression but did not consider the fluid dynamics and detailed reaction kinetics.

Kolyfetis and Vayenas (1988) built upon the idea of Rosemann (1986) by including the effects of the coal pyrolysis, adding a char reaction rate scheme taken from Govind and Shah (1984), and calculating the rate of coal devolatilisation according to the model of Badzioch and Hawkesley (1970). A one dimensional plug flow model was used, divided into three sections: heating and mixing; pyrolysis; combustion and calcination. Comparison was made between the model results and temperature measurements from an existing installation and good agreement was observed. Fluid dynamics was not accounted for and the radial temperature field was not described. The effect of nine different types of coal on the process was assessed and this showed that increasing volatile content enhances coal combustion but creates lower temperatures and therefore reduces calcination.

Belot et al (1993) performed a mathematical analysis of the global process and used it to optimise process control and to consider the material flow and reaction kinetics. The model allowed analysis of the effect of staging injection of raw meal to the precalciner.

Mullinger and Jenkins (1996) used a mathematical heat transfer model, originally developed by Hottel (1961) for radiant heat transfer in a well-stirred reactor, to predict temperatures to consider the effects of heat transfer in a precalciner. The model was used in conjunction with other techniques to give the overall behaviour of the precalciner. The work is discussed further in the next section.

2.9.2 CFD modelling

Very little CFD modelling of precalciners has been reported in the literature. Belot et al (1993) reports work, in which a precalciner was modelled using CFD. The modelled precalciner operated in downflow mode with coal and raw meal inlets. A 2-D schematic of the precalciner, which had been developed for use with liquid fuels and only subsequently changed to burn coal, is shown in Figure 2-6a. Using Fluent version 3 a three-dimensional model of the precalciner was created, with modification for modelling two reacting species, the coal and the raw meal. As the grid was not body-fitted, steps are apparent at sections that are inclined to the grid axes. Combustion was modelled using the eddy breakup model and stochastic tracking was used to include the effects of local turbulence on the particle tracks. The results obtained showed close agreement with physical measurements made on site. However, Belot (1993) concluded that the computational method was too expensive in terms of the time required to get results, despite its usefulness as a diagnostic tool.

In another study of interest, Mullinger and Jenkins (1996) used three modelling approaches – mathematical, CFD and scale – to model a precalciner and the results were used to argue that no one model alone was sufficient to indicate the full picture of reactions and flows within the precalciner. The CFD model employed the commercial CFD code PHOENICS to investigate particle tracks and residence times in a precalciner. A 2-D schematic of the precalciner is shown in Figure 2-6b. The grid, as with Belot et al (1993) was not body-fitted. The results were used to resolve instability in the flow pattern, where switching between two flow patterns was observed; the problem was resolved by repositioning the burners. Mullinger and Jenkins (1996) argued that CFD should be used to optimise particle trajectories, concentrations and residence times by suitable adjustment of modelling variables. The analytical model of Kolyfetis and Vayenas (1988) had previously shown that fuel characteristics affect the performance of a precalciner. This results was confirmed by the work of Mullinger and Jenkins (1996) who also found that this effect could be modelled computationally.

2.9.3 Installation Measurements and Scale Modelling

It is both difficult and costly to obtain measurements on a precalciner installation as illustrated by Belot et al (1993). Two types of water-cooled probe were used - a suction pyrometer (Smoot, 1996) for the temperature profile and a gas sampling probe for CO, CO_2, O_2 and unburned gases. The probes were inserted through 5 holes in the precalciner wall at 3 different heights.

Mullinger and Jenkins (1996) used an acid/alkali scale model made from Perspex to show the general form of the combustion flows. This is a well-established technique for combustion modelling, and is used for prediction of the mixing of the oxidizing stream with the fuel. Models are expensive to construct and extracting results is time consuming.

2.10 Conclusions from the literature review

Cement processing efficiency was significantly improved by introduction of the preheater tower and the precalciner vessel of which there are various configurations. The Cauldon precalciner can be defined as Air-Separate, since it has a tertiary air inlet, and combines air from the clinker cooler with the kiln gases. There is no swirl mechanism in the Cauldon precalciner.

Several problems associated with combustion products were identified. Notably, the recognition of the need to control combustion pollutants has improved with increasingly strict legislation by governments world-wide. Pollution controls in the cement industry address all key pollutants including CO, NO_x, SO_x, PAHs and particulates. A great deal of attention has been addressed to the issue of NO_x production and control. There are several methods of control available, and interestingly using tyre material as a support fuel is one of them.

Scrap vehicle tyres pose a disposal problem. The literature indicates large volumes of scrap tyres sent to land-fill, and that this disposal route is not sustainable in the environment. Tyre material has a higher calorific value than coal and disposal by incineration provides a means of recovering the energy of the material. The cement process provides ideal combustion conditions for disposal by this route.

In order to develop a fully representative model of the precalciner, the chemical reactions must be realistically modelled. Limestone calcination reactions can be simulated using an Arrhenius rate equation for the liberation of CO_2. Data was found from relevant work for use in the model. Coal combustion behaviour depends on the characteristics of the particular coal. It is important to correctly represent the rate of release of the volatile material. Data was found in the literature in support of the model coal used for the work described in this thesis. Tyre material has particular combustion characteristics dependent on the composition. Researchers have identified three distinct peaks in the mass loss versus temperature behaviour of tyre material. The features correspond to the yield of oil, natural rubber and styrene-butadiene rubber. The small size of the granules tested in the literature indicated the need for some experimental work to determine the behaviour of larger tyre pieces.

The literature provided no direct research into the aerodynamic properties of objects similar to tyre chips. Much work has been done with regular shaped non-spherical particles, but the characteristics of random shaped, flat objects have not been described. Previous work on this research project indicated that the tyre chip drag may be modelled in two orientations – face and side presentation to the flow. The lack of literature indicated the need for experimental investigation in this area.

Radiative heat transfer is significant in the precalciner. Information was found in the literature that indicated scattering by the suspended particles caused the medium to be optically thick so that the mean free path of radiation was quite short. The estimate of path length was used to model radiant heat transfer in the precalciner.

In order to demonstrate the uniqueness of the project, other modelling work in the cement industry was reviewed. Although research was done on precalciners, the type of precalciner at Cauldon has not been modelled. The geometry and grid used were not body-fitted since the approach had not been developed at the time and so inclined walls in the computational mesh were not smooth but had steps in them. No work was done with block-structured or fully unstructured meshes. The modelling of tyre chip combustion and aerodynamic characteristics have not

previously been attempted according to this literature survey. The work is therefore original.

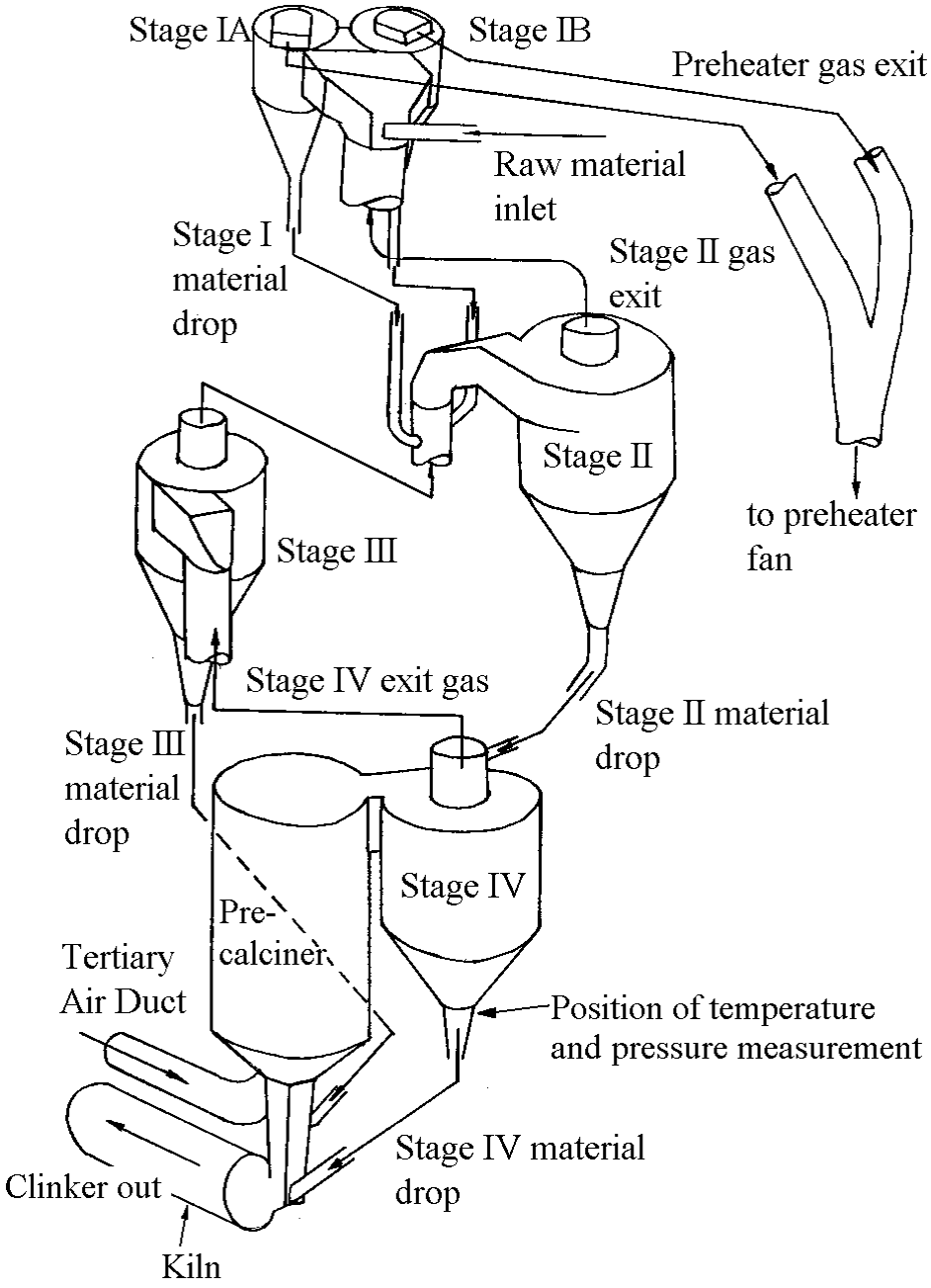

Fig. 2-1 Schematic of the Cauldon preheater tower. The components have been exploded for clarity to show the flow of gases and raw meal. Raw meal enters at the top of the tower in cyclones IA and IB. Hot gases rise from the kiln and from the tertiary air duct, which both draw air through the clinker cooler. Individual cyclones act as co-current heat exchangers, but the overall operation of the tower is as a counter-current heat exchanger. The precalciner is located just before the kiln. It receives coal and raw meal and serves to complete the calcination reaction of the calcium carbonate in the limestone of the raw meal.

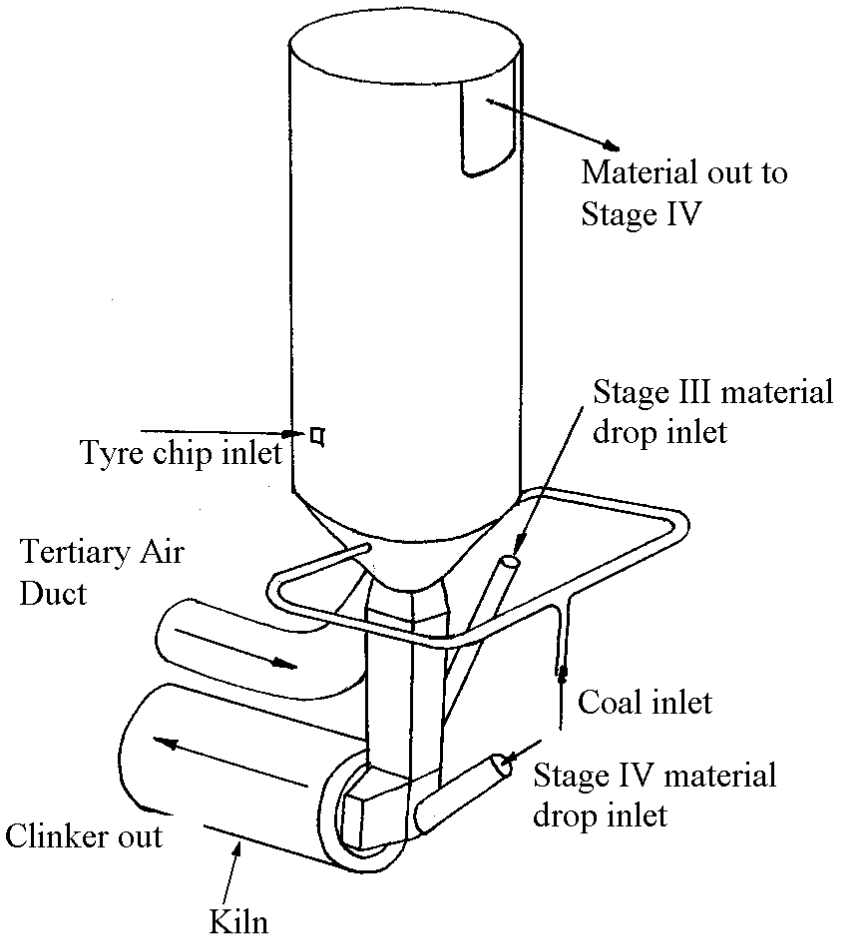

Fig. 2-2 Schematic drawing of the Cauldon precalciner vessel. Connections to the surrounding vessels are indicated. Raw meal falls from the stage III material drop inlet at the rate of 200 t.p.h. Gases from the kiln at 18 m/s and 1100°C carry the raw meal up the lower section of the precalciner before the tertiary air injection at 30 m/s and 900°C. The material is supported in the cylindrical section whilst calcining and heat is added by injecting coal at two inlets and tyre chips at a higher position. The overall height of the precalciner is 26m and the diameter of the cylindrical section is 6.9m. The gases and reacting particle cloud proceed out of the top of the precalciner to the stage IV cyclone before entering the kiln.

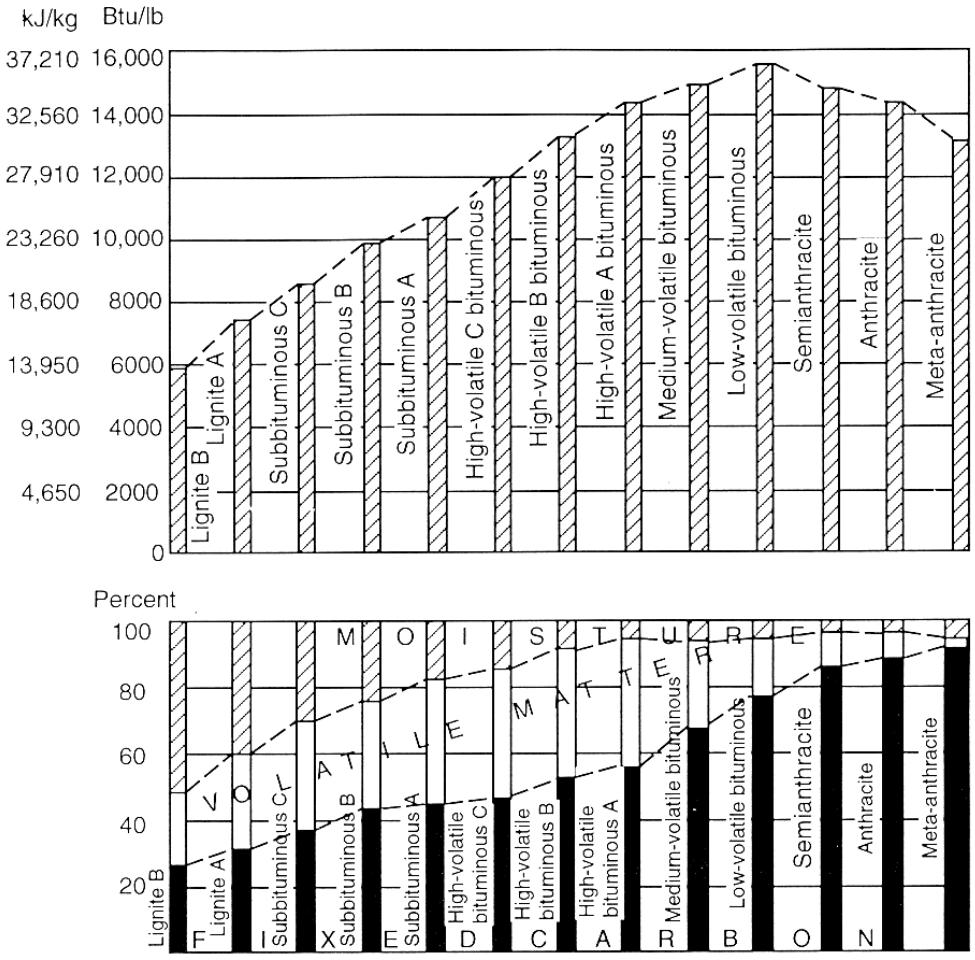

Fig. 2-3 Proximate analysis and heating value of various grades of coal reproduced from the American Society of Testing Materials Classification (1974) in Smoot (1993). Coal is characterised by the Gross Calorific Value and the proportions of fixed carbon (char), volatile matter, and moisture content. The type of coal used at Cauldon is similar to medium or high-volatile bituminous.

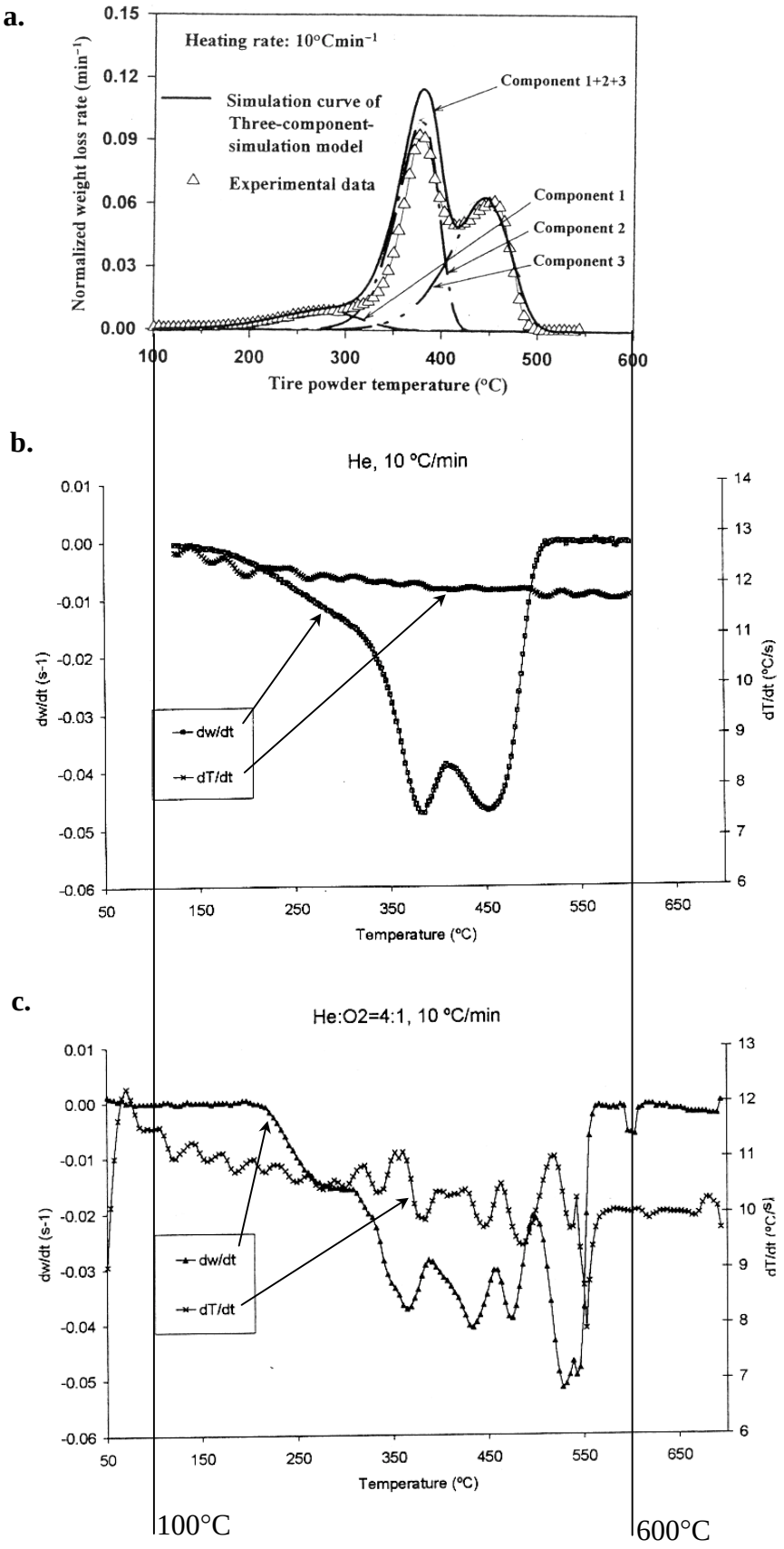

Fig. 2-4a-c Results of a. Leung and Wang (1999) tyre pyrolysis in nitrogen, b. Conesa et al (1998) tyre pyrolysis in helium, c. Conesa et al (1998) tyre combustion in 20% oxygen atmosphere. The temperature scales are consistent.

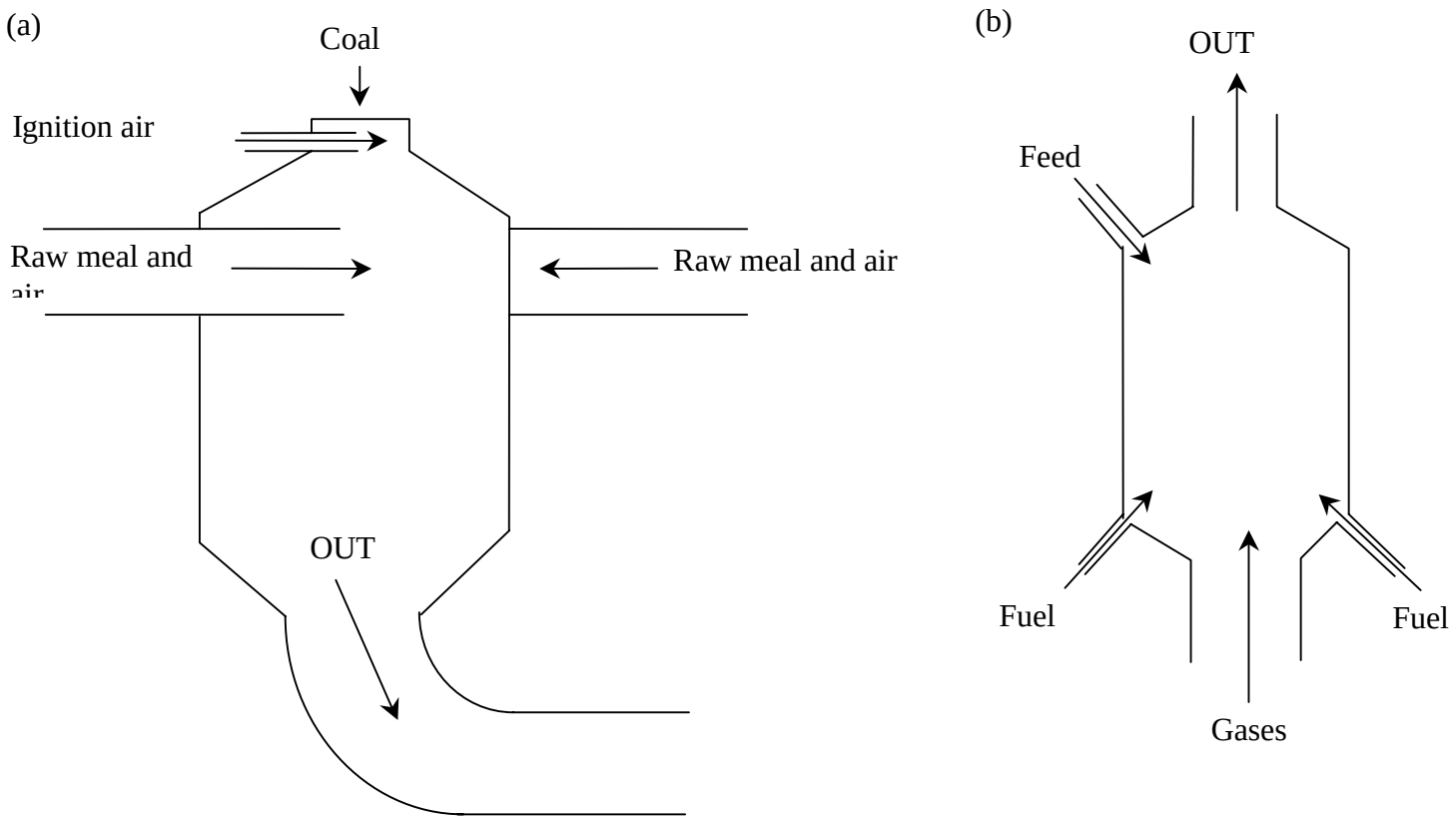

Fig. 2-6 Schematic 2-D diagrams of precalciners modelled by Belot et al (a) and Mullinger and Jenkins (b). Precalciner (a) is a downflow type with swirling air and raw meal injection, and precalciner (b) has feed from the top of the precalciner and is of the air-through type. The precalciner at Cauldon is of the upflow type with air separate and does not have swirl inlets and is thus significantly different from precalciner (a) and (b).

3 Application of Computational Fluid Dynamics (CFD)

The complex, non-linear fluid flow equations developed by C.Navier (1785-1836) and G.Stokes (1819-1903) are difficult to solve and "until now only a few particular solutions have been found" (White, 1991). These equations are solved using numerical techniques in CFD. The finite-volume technique is used. This involves dividing the volume of the subject fluid in to discrete volume cells in which simpler, linear algebraic equations are solved to approximate fluid flow parameters (velocity etc.) at discrete points in the flow region. A system of finite-difference equations is developed relating the changes in variables between cells according to the partial differential equations describing the transport of properties in the flow. The equations are formulated from the Navier-Stokes equations for continuity and momentum, from the energy balance equation based on the first law of thermodynamics and upon transport equations for scalar quantities such as chemical species and turbulence. The equations have been highly developed and the techniques for solving them in practical situations are continuously being developed. An indication of the equation formulation is presented in Appendix 1. The theory was clearly stated by Tannehill et al (1997). Versteeg and Malalasekera (1995) published a good introductory text.

CFD solutions to fluid flow behaviour is performed in three stages - pre-processing, solving and post-processing.

- Pre-processing defines the physical domain of the flow, developing a realistic geometry in a 2 or 3-dimensional coordinate system which is then divided into a number of volumes (cells) at which the flow parameters (eg pressure, velocity) can be calculated and related to surrounding cells. The boundary conditions (at inlets and walls and outlet) are specified at the start of the calculation. The solution of the set of second-order partial differential equations is parabolic when time dependency is not considered.
- Solving calculates the flow parameters numerically at each cell, using the finite volume method, which is an adaptation of the finite difference method.
- Post-processing analyses the results of the solution.

Notation for Chapter 3

C_p	specific heat at constant pressure ($Jkg^{-1}K^{-1}$)
h	height above datum (m)
g	acceleration due to gravity (ms^{-2})
I	turbulence intensity
k	turbulent kinetic energy (m^2s^{-2})
L	characteristic length (m)
Pe	Peclet number
Re_{DH}	Reynold's number based on hydraulic diameter
t	time (s)
u	velocity component (m/s)
u'	velocity component fluctuation (m/s)
U	fluid velocity (m/s)
$\vec{V}$	fluid velocity vector (m/s)
G	characteristic viscosity (kg/ms)
e	turbulent kinetic energy dissipation rate (m^2s^{-3})
r	fluid density (kg/m^3)
r_{op}	operating density (kg/m^3)

3.1 Mesh generation

Structured and unstructured meshes were developed during the course of the work. Body fitted co-ordinates were used, which follow the exact contours of the physical geometry of the model using spatial relation functions to map the cells from the computational co-ordinates to the physical co-ordinates.

A structured mesh has grid lines on 3-coordinate directions, which although they are unlikely to be orthogonal in physical space are orthogonal in computational space. Each cell is topologically a hexahedron. This can make mesh generation practically impossible for meshes that are required for other than simple geometry. An unstructured mesh is not restricted in this way and cell shapes can be hexahedral, tetrahedral or wedge shaped since the computational domain is not orthogonal. Structured meshes are less

computationally intensive than unstructured meshes, so it is advantageous to use them where possible. The multi-block approach is a sensible compromise that uses a block structured grid, i.e. made of blocks of structured grid regions that are joined together to make the whole. It is thus possible to develop meshes for complex shapes that are structured in blocks, which are joined together and solved using an unstructured solver.

Three geometries were generated for this work. To simplify the first model created, the mesh was constructed in the block-structured form as illustrated in Fig. 3-1. Six blocks were used; five in the main vertical section with a cross section as illustrated which persists throughout the height. The 'view A' shows the position of the inlets and the outlet duct on the model. One coal inlet is not visible, but it is located directly opposite the coal inlet that is visible on the conical section.

The grid in the region of the coal inlets was "refined"; i.e. the cell density was increased. This was necessary due to the rapid changes of gas velocity and temperature in that region. Coal secondary air enters at 25 m/s directly across the flow in the precalciner at 75°C compared to the mean temperature of 900°C of the precalciner gases at that point. Increasing the number of cells in the region reduced the gradient of each field variable from cell to cell. The hanging node method was used to refine the cells in that region. The method divides each hexahedral cell in the region in to eight new hexahedral cells as illustrated in the schematic at the top left of Fig. 3-1. The cells were refined in the region encompassed by three concentric spheres with coincident centres at the centre of the coal inlet. The three refinement regions are distinctly visible on the surface of the model.

The 'view B', from the top of the precalciner, shows the connection of the five blocks that were used to construct the model, and the addition of the outlet duct. The connectivity of the five main blocks of the model persisted throughout the entire length, changing in shape in proportion to the outside boundary. A total of 48,000 cells were used in the mesh. The height of the model was 25.84 m and the diameter of the main cylindrical section was 6.9 m.

The outlet duct was added to allow the flow to develop before the exit. It was found in development of the initial models that the pressure and velocity

field near to the outlet of the cylindrical section was unrealistic without a duct. In addition to this problem, using a structured mesh throughout on the model without the duct was unreliable since it resulted in highly skewed cells (cells which deviated significantly from orthogonal) at the walls at the four corners of the computational mesh mapped using body fitted co-ordinates. With the duct added it was impossible to make a structured mesh without highly skewed cells.

Using an advanced mesh generation package, a fully unstructured mesh was constructed on a precalciner geometry with more faithful representation of the actual geometry of the physical installation. In Fig. 3-2 the features of this mesh can be seen to include an improved tertiary air duct and coal pipes. The exit duct was included as in the earlier model to achieve near-fully-developed flow at the outlet. The fully unstructured nature of this mesh can be seen from the surface mesh.

It was discovered during the generation of the unstructured model that the outlet duct on the initial model was 25% too high, a misinterpretation of drawings being the cause. An improvement was made to the initial model when a new feature was added to the vessel in accordance with plant modifications. The duct was modified at the same time and the solutions compared. The third model, which was block structured, is illustrated in Fig. 3-3.

3.2 Solution technique

Solution of the equations governing convected scalars (e.g. temperature, pressure, species concentrations) requires a discretisation scheme (Versteeg, 1995). The two schemes relevant for this work are:

- First Order Upwind, in which cell face values are set equal to the cell-centre value in the cell up-stream, and
- Second Order Upwind, in which the cell face values are calculated using a Taylor Series expansion to give an increased range of influence of the surrounding cells.

The Fluent User Guide (Fluent Incorporated, 1996) advises that the First Order scheme will give a stable solution with a good rate of residual convergence, with the limitation that the accuracy of the solution may not be satisfactory. It

is subject to numerical diffusion for grids in which cells are not aligned with the flow. That is always the case for a mesh that has been built using tetrahedral cells. Numerical diffusion is the term used for the combined effect of numerical dissipation (otherwise known as artificial viscosity since it effectively increases the viscosity of the fluid in the calculation) and numerical dispersion (Tanehill et al p.106, 1997).

The technique used to obtain convergence with accurate results was:

- use First Order Upwind on all variables to start until a convergent solution was obtained, and
- apply Second Order Upwind to achieve accuracy.

The discretization scheme was specified separately for each variable calculated. Diffusion terms in the discretised transport equations are always central difference, second order and accurate to first order. Convective terms are calculated by a number of schemes available in Fluent: first order upwind, second order upwind, central, Quadratic Upwind Interpolation for Convective Kinetics (QUICK), and Power Law. Power law is used when the cell Peclet number, $Pe = \frac{rUL}{\Gamma}$ is large and is useful for pure diffusion type cases.

For the block structured grid, the discretisation scheme used for pressure was PRESTO! (PREssure STaggering Option as described in Fluent Incorporated, 1997) as the flow was considered to be subject to high-pressure gradients and body forces. This technique is only applicable for models with hexahedral cells. For the meshes with tetrahedral cells, the discretisation scheme for pressure was the Body Force Weighted model, which is used for cases where large body forces are expected.

The solution algorithm applied by Fluent is illustrated in Fig. 3-4. The key points of the solution technique applying in this case are the settings of under-relaxation for some variables and the settings of the Algebraic Multigrid. It was found necessary to do some grid adaption by region, volume and variable gradient.

3.3 Boundary Conditions.

The details of boundary condition values are presented in Chapter 4, where the development of the precalciner model with reference to available plant data

and literature research papers is explained. In this chapter, the type of boundary condition for each of the physical boundaries of the precalciner domain is explained.

3.3.1 Inlets

Velocity inlets were specified on all the inlets since the mass flow rate, gas composition and temperature at each inlet were known from the mass balance done on the installation. k and ε were specified at the inlet and wall boundary conditions. The specification of k and ε was by hydraulic diameter of the inlet and turbulence intensity. The hydraulic diameter was calculated from continuity and the turbulence intensity was derived from Equation 3-1, from the Fluent User Guide (Fluent Incorporated, 1997).

$$I \equiv \frac{u'}{u_{avg}} \cong 0.16(Re_{DH})^{-1/8} \qquad \textbf{Equation 3-1}$$

where Re_{DH} is the Reynolds number for the inlet calculated using the hydraulic diameter of the inlet area. Usually turbulence intensity is in the range 1% to 10%.

3.3.2 Fluid exit at the duct end

The type "outflow" was specified on all models. It is the appropriate outlet boundary condition for cases where the flow is fully developed, i.e. where there is no significant variation of the flow variables in the flow direction.

3.3.3 Walls

Conducting wall condition was used at the solid boundaries of the precalciner, except for the exit duct wall, which was subjected to adiabatic constraint since it is not a real part of the geometry.

Two techniques were available in the Fluent software for calculating the effect of walls on the aerodynamics of the flow. Standard Wall Functions (developed by Launder and Spalding, 1974) are used when the Reynolds Number of the flow is expected to be high. The technique is briefly described in Appendix 1. A fuller description is available in standard texts on CFD (e.g. Versteeg and Malalasekera, 1995).

3.4 Models used

In the case of this study, with two reacting particles, gaseous reactions, combustion and heavy particle loading, to introduce all aspects of the calculation procedure at once led to an unstable solution. By introducing new aspects of the physical situation separately, and obtaining a converged numerical solution for each step, the "picture" of the flow pattern was built up and the effects of different aspects of the flow were observed separately. The result of performing the calculation in this way was a converged solution with meaningful data. It was necessary to build the solution in steps like this to prove the accuracy of each aspect of the solver introduced. The model was constructed in three steps. The first stage modelled the gas phase, setting the conditions for the continuous phase in the vessel. Several model specifications were made at this stage to prepare for the development of the successive models. The second stage introduced the limestone particles as a discrete phase coupled to the continuous phase. This was done in stages of increasing mass injection of the particles. The third stage applied a combusting particle with devolatilization and char combustion and full gas reactions to simulate coal combustion and limestone calcination.

3.4.1 Turbulence

The *k-e* turbulence model of Launder and Spalding (1974) was used with the constants described in that paper. Other turbulence models are available in the Fluent software: Spalart-Almaras, Renormalization Group *k-e* (RNG), Realizable *k-e*, Reynolds Stress Model (RSM), and Large Eddy Simulation (LES). The last method is a turbulence scale filtering method, the others are Reynolds Averaged Navier Stokes methods (Fluent Inc. 1997). For the type of model required in this work only two of the models were considered to be appropriate: the standard *k-e* and the Realizable *k-e* models. For a full description of these models see the Fluent manual (Fluent Inc. 1997). The realizable model is advantagous for use with separated flows, free jets and mixing layers. A brief description of the formulation of the turbulence transport equations for the standard *k-e* and the Realizable *k-e* models is given in Appendix 1.

3.4.2 Pressure Velocity Coupling

The techniques available in the Fluent code are SIMPLE (Semi-Implicit Pressure Linked Equations), SIMPLEC (SIMPLE-consistent), PISO (Pressure Implicit with Splitting of Operators). The SIMPLE pressure-velocity-coupling scheme of Patankar (1980) was used.

3.4.3 Buoyancy

Calculation of the buoyancy effect on turbulence dissipation rate is available in Fluent software, but the model is not considered reliable. It was not used in any of the models in this thesis.

Buoyancy effects on the flow are modelled by defining the direction of action of gravity and an operating (reference) density.

The effect of buoyancy is calculated in the momentum equation. The density of the continuous phase is calculated by the ideal gas law and using an ideal gas mixing law. The operating density (r_{op}) is defined to allow calculation of the buoyant effect. In this case the operating density is set to atmospheric air density at the altitude of the vessel being modelled. Static Pressure in the continuous phase is then indicated by $(r-r_{op})gh$.

3.4.4 Heat transfer

The energy equation used in Fluent is described in Appendix 1.

The conservation form of the energy equation (also known as conservation law form, conservative form and divergence form, see Tanehill, 1997) was used in order to improve stability of the calculation in regions of high heat exchange (i.e. where the fastest rates of reactions occur). In this form of the energy equation the coefficients of all derivatives are constant, or if variable, derivatives of the coefficients do not appear elsewhere in the equation. The non-conservative form may lead to difficulties where the coefficients are discontinuous. Simply put in terms of the continuity equation, the forms of the conservation and non-conservation forms are respectively: $\frac{\partial r}{\partial t} + \nabla.(r\vec{V}) = 0$ and $\frac{Dr}{Dt} + r\nabla.\vec{V} = 0$. The reason for the effectiveness of this technique is given in the Von Karmen Institute lecture notes (Anderson, 1990).

Conducting walls were applied at all solid boundaries except the outlet duct, which had adiabatic walls. A constant heat flux was determined from the heat balance of the vessel for the conducting walls as described in Chapter 4. Fluent makes use of the Reynolds analogy applied to turbulent momentum transfer for heat transfer with the walls.

Radiative heat transfer was modelled in a sensitivity analysis to observe the effect on the temperature field. Radiation is modelled in Fluent using four schemes: discrete transfer radiation model (DTRM), P-1 radiation model, Rosseland radiation model and the Discrete ordinates (DO) model. The Rosseland model was used in this work. Since the concentration of particles in the precalciner results in a mass loading of approximately 1.2:1 in the main body of the precalciner, the absorption of heat by the particles is a significant heat transfer mechanism. A uniform absorption coefficient was assumed over the entire domain of the model. The justification of the assumed values for α are presented in Chapter 6. For a brief description of the Rosseland model as described by Fluent Inc. (1996), see Appendix 1.

The P1 model can model the effect of scattering by particles and absorption by gases separately, but it was not used in this case since scattering was regarded as negligible as discussed in Chapter 2 (section 2-8).

Radiation was not calculated initially in order to simplify the calculation. Since the gas and particle mixture is at fairly homogeneous temperature the simplification was a reasonable first assumption. Radiation modelling was done to check the effects of radiation as described in Chapter 6.

3.4.5 Materials

The constituents of the operating fluid and the material of the solid walls were specified. Materials were selected from a database stored within Fluent/UNS. Further properties were required to represent tyre material and Fluent allows specification of these by the user. The material of the walls in the models was aluminium since the sensitivity of the flow to heat transfer with the walls was considered to be small due to the large volume of the gases and the dense optical thickness.

The operating fluid was specified as a mixture-template, in which the user defines the component gases. Mixture-template is required where distinct gases, evaporating species, and user defined gaseous reactions are modelled.

The viscosity was set at a constant value since the domain is essentially isothermal, at temperatures in excess of 900°C. The reference temperature was 1100K (827°C). The values of *Cp* and thermal conductivity were similarly specified.

The discrete phase materials (coal, raw meal and tyre) were selected from a database of combusting particles. Standard materials were selected from the database and altered to correspond to the physical properties of the desired materials. Details of the raw meal and coal composition are presented in Chapter 4, and the tyre material is described in Chapter 7.

3.5 Discrete phase model

The Discrete Phase Model (DPM) used by Fluent has 3 particle types: inert, droplet, and combusting. Six physical laws applied by the code determine behaviour of the particles. The laws that are applied to the combusting particle type are:

- Law 1 Inert Heating – which calculates particle heating up to the continuous phase temperature.
- Law 4 Devolatilisation – which evaporates all the volatile content of the particle at constant temperature.
- Law 5 Surface (char) combustion – which oxidises the char content of the particle. A specified proportion of the heat released is absorbed by the particle to cause particle heating.
- Law 6 Inert Heating – following release of the volatile content of the particle.

The mass ratio of particles to gas (1.2:1) and the energy of the reactions mean that particles will have a significant effect on momentum and enthalpy of the gas. This is accounted for in the CFD by a coupled solution, in which interaction of the discrete phase (the particles) with the continuous phase (the fluid) is considered. The solution technique known as the particle-source in cell model is described in the paper by Crowe et al (1998).

The sensitivity of the solution to the discrete phase is dependent on the mass loading on each particle track calculated. If it is too high, then the solution becomes unstable. It was found that increasing the number of particle tracks, spreading the initial injection and employing stochastic effects helped stability. The particles in the precalciner are driven upwards against gravity by the gas velocity. Properly representing dispersion of particles into the gas stream gives better, more realistic interaction between the phases. It means that the result is less dependent on many particles following a particular path. Stochastic dispersal of the particles was employed, using the Fluent Discrete Random Walk (DRW) model (Fluent Inc., 1996), in which random changes are made to the turbulent component of the velocity vector, u', in each computational cell to alter the trajectory of the particle track. The total mass for each injection is then divided equally between the number of stochastic attempts. In this case 20 stochastic attempts were found to be necessary.

The Rossin-Rammler size distribution was applied to the particles. The size distribution is described in Chapter 4.

The Fluent software provides under-relaxation on the DPM source to limit the effect of mass, momentum and heat exchange to the continuous phase. The default setting of 0.5 was changed to 0.1 to obtain stable solutions.

The distance travelled by a particle before the next calculation of its trajectory is termed the "characteristic length". It is possible that particles will be caught in a recirculating region of the flow. To forestall wasted calculation time, the "maximum number of steps" for each particle is fixed. The product of number of steps and characteristic length is the maximum distance a particle will travel before its calculation is terminated.

3.6 Combustion model

3.6.1 Gas Combustion

Reaction mechanisms were simulated using the Magnussen-Hjertager (1976) eddy-mixing model. Six chemical species were included in the model: CO_2, CO, N_2, O_2, H_2O and lv-vol (the volatile of the coal). The tyre chip models included a volatile species for the tyre material defined as styrene-butadiene (C_4H_6).

3.6.2 Char Combustion

Coal combustion was included in the model. The devolatilisation rate was set according to the data of Badzioch and Hawkesley (1970) - the standard data available in the Fluent/UNS code. Combustion of carbon (char) was considered as a two step reaction (Borman and Ragland, 1998, explain the meaning of two step reaction), first to CO, then to CO_2. The diffusion-limited rate was used, whereby the diffusion rate of the gaseous oxidant to the surface of the particle determines the oxidation rate of the char.

3.7 Methodology for obtaining a stable solution

During the course of the CFD work, problems were experienced in obtaining a stable solution. Successful modelling was performed in the following steps once the mesh for the calculation had been generated:

- include all gases in the model gas mixture that will be used to model all reactions to be represented
- include all combustible particle materials that will be used
- specify all inlet boundary conditions as velocity inlets with gases representative of plant gases
- specify wall heat transfer rate for the precalciner main body
- turn off energy, particle tracking and reaction calculations
- solve gas flows in non-reacting conditions
- specify injection of coal and raw meal for partial load, say 10% of raw meal
- turn on particle tracking and solve coupled solution without reactions
- turn on reactions and energy and re-solve

increase raw meal injection rate in steps of say 10% and solve at each step.

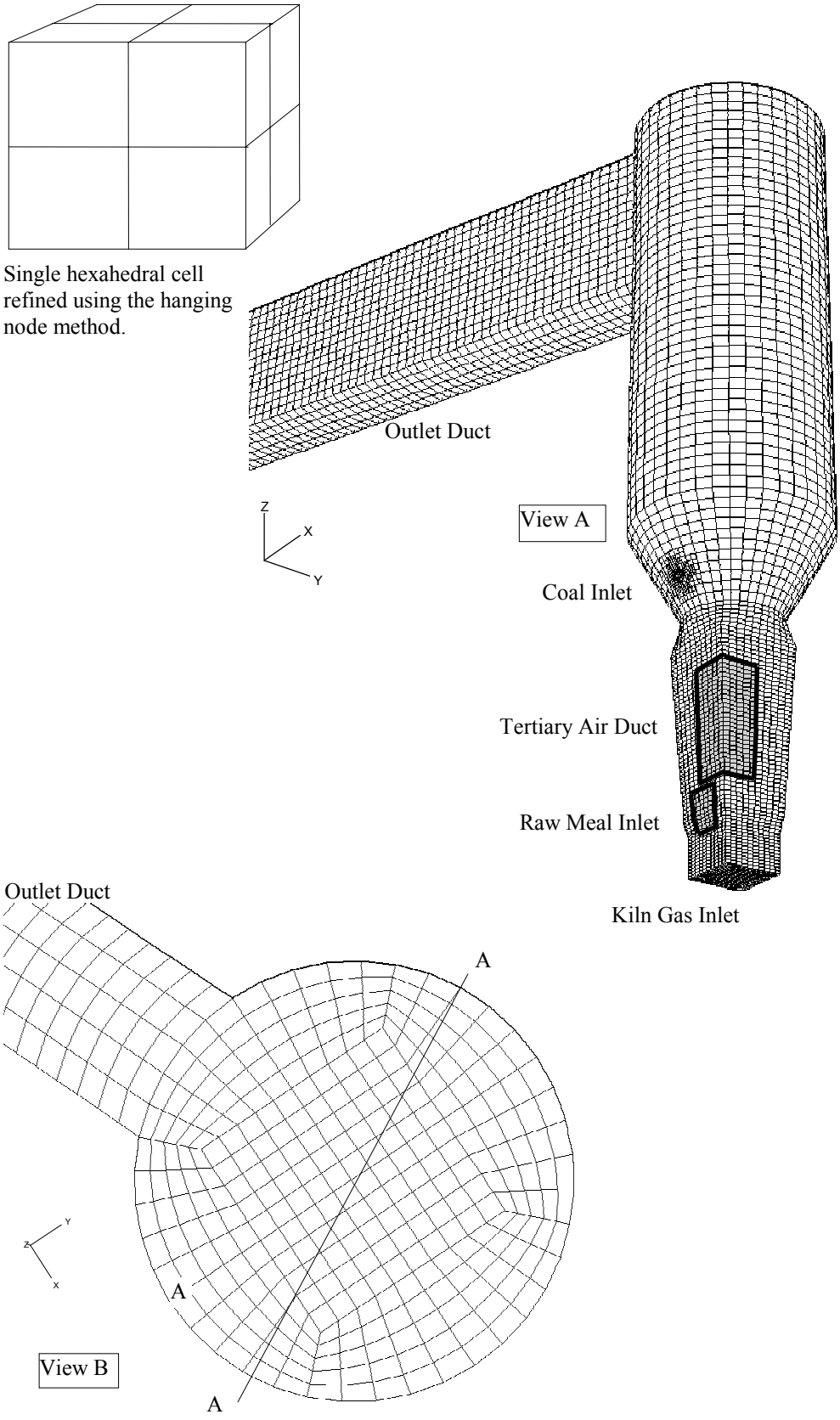

Fig. 3-1 Geometry and mesh of the initial precalciner model. Inlets are indicated in the View A. Results were inspected and compared on the vertical plane A-A indicated in View B. Hanging node cell refinement, shown in the top left diagram, divides each cell into eight smaller cells.

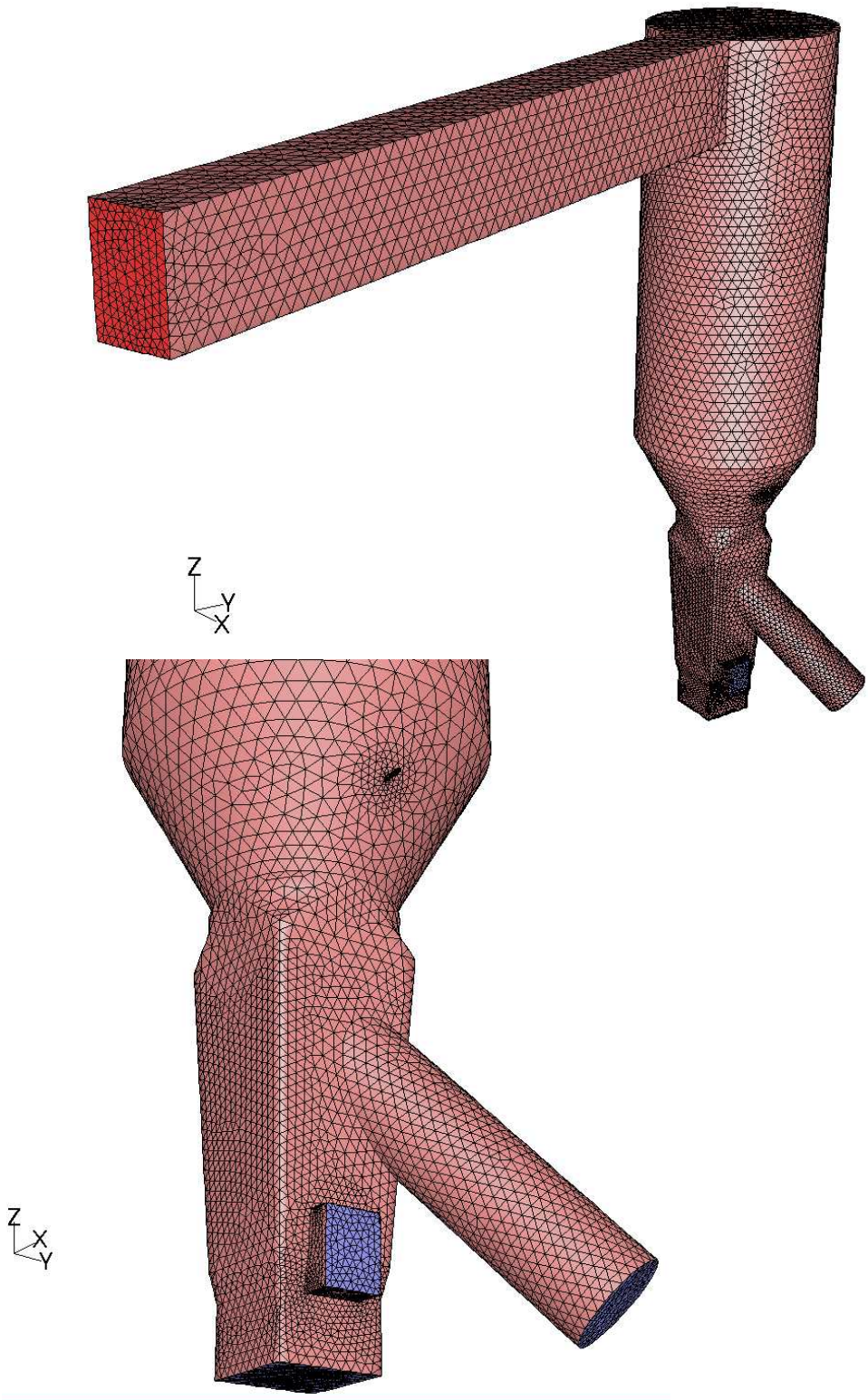

Fig. 3-2 Geometry and mesh of the unstructured mesh model, in which accurate representation of the tertiary air inlet, coal inlets and the raw meal inlet are made. Each cell in the mesh is tetrahedral.

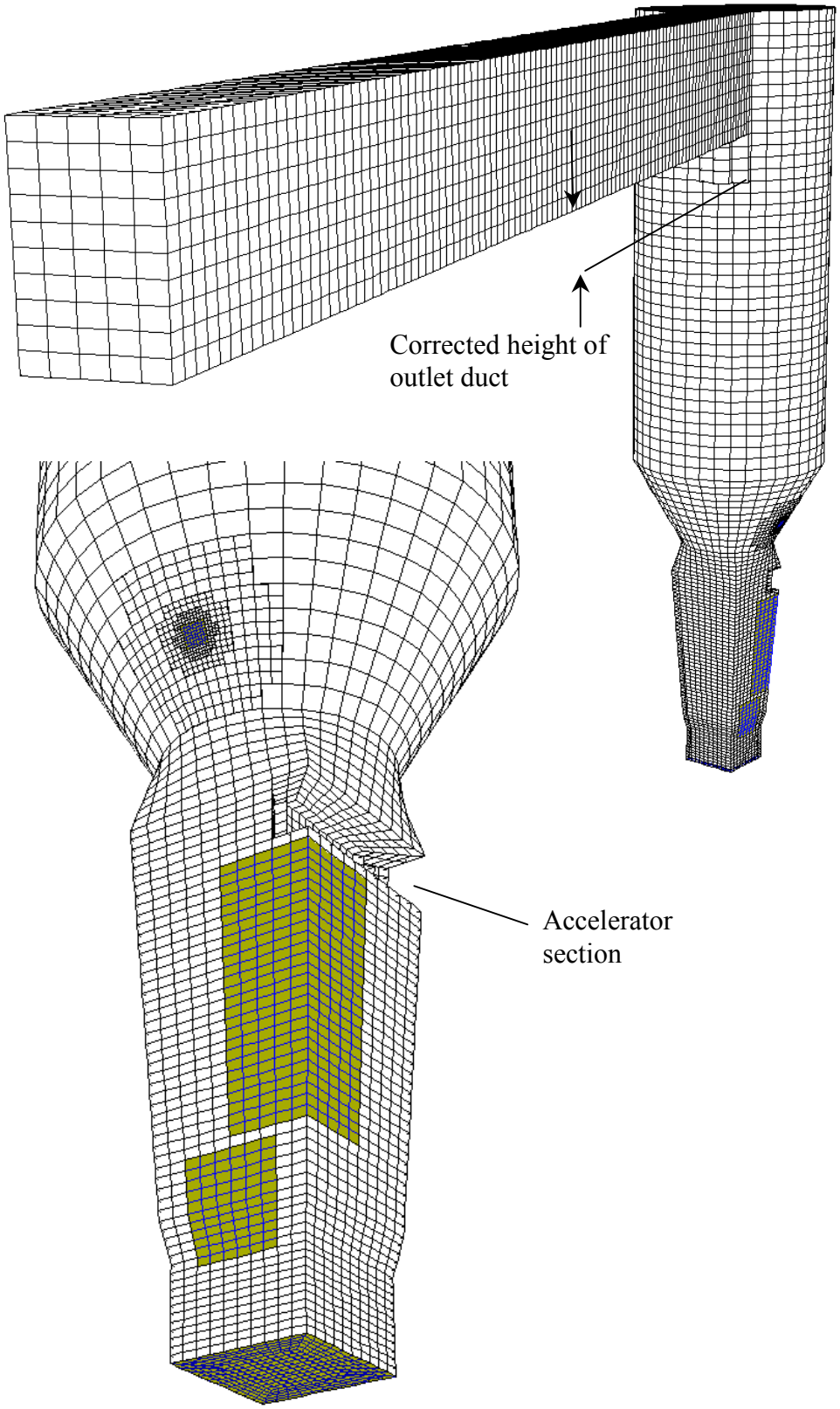

Fig. 3-3 Block structured model of the precalciner with accelerator section at the "throat" and corrected outlet duct height.

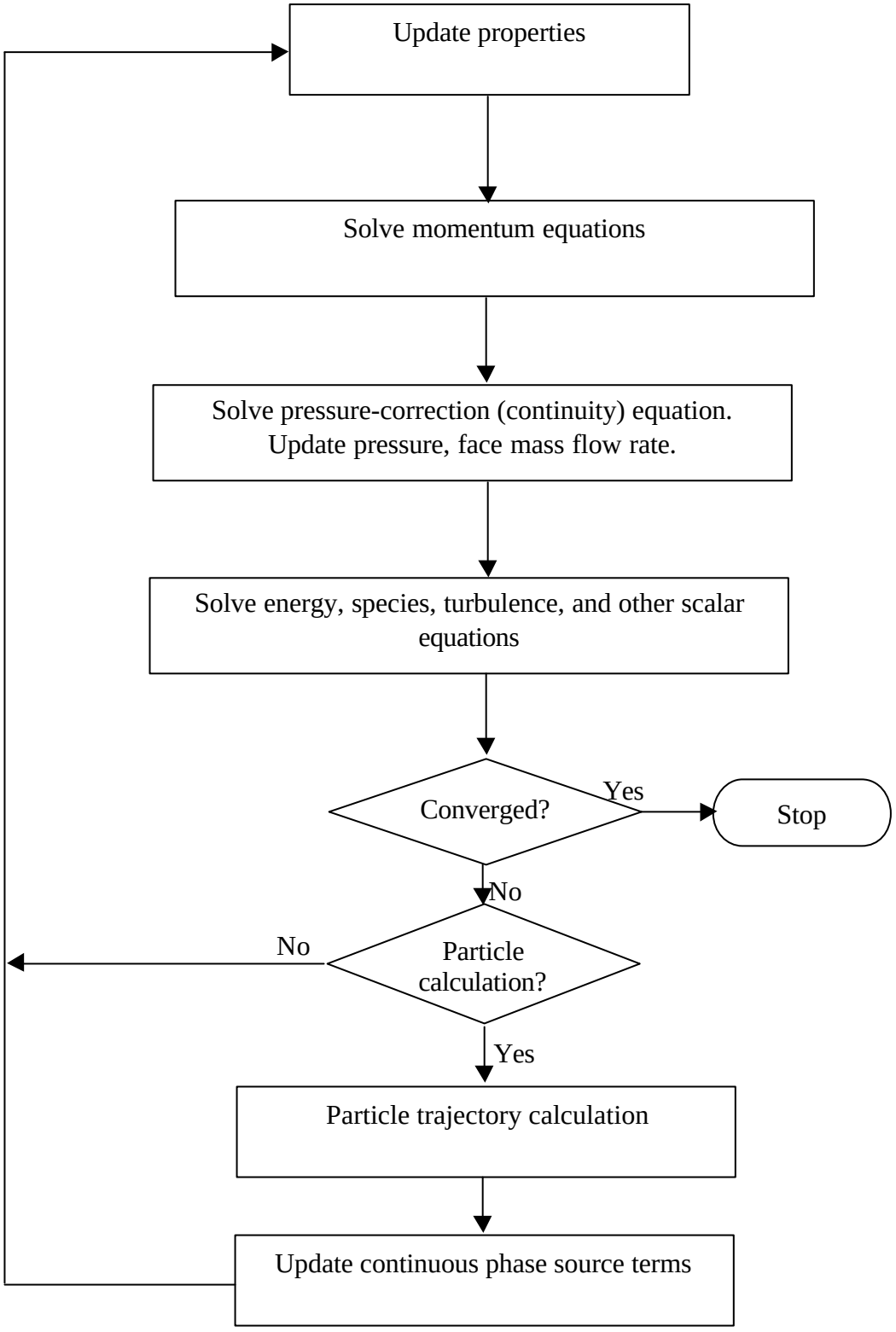

Fig. 3-4 Fluent solver calculation routine. Each of the continuous phase calculation loops is performed a fixed number of times between particle trajectory calculations. In this way the continuous phase solution adapts gradually to the injection of particles.

4 Boundary conditions, validation, and data collection

Key data for the model are presented in this chapter. This includes the determination of the boundary conditions for the CFD model, the coal data, raw meal data and any validation data that was collected from the plant in the course of the work.

Much of the data referred to in this chapter was derived from the annual production statistics and the heat and mass balances at the Cauldon plant for the year 1996. The data includes:

- composition and consumption of the coal and raw meal,
- the clinker production rate,
- emissions from the stack,
- heat loss to surroundings.

Since the production statistics and heat and mass balances do not explicitly define the precalciner boundary conditions, it was necessary to deduce the mass and heat boundary conditions for the precalciner from the available information. Since the deduction was not intuitive, it was necessary to present the method used to ascertain the boundary conditions in this chapter.

Characteristics of coal and raw meal are included in this chapter, since the behaviour of a particle in the precalciner determines its effectiveness in the real vessel. A great deal of heat exchange and mass transfer from solid to gas is involved. Correctly defining the characteristics of the particles in the model will encourage a realistic solution.

A desirable outcome of the project was to validate the data from the model against whatever features of the precalciner flows were measurable. Some limited measurements were performed at the Cauldon works and they are described in this chapter.

Notation for Chapter 4

Bi	Biot number
C1	calcination completed in cyclone 1 (kg s^{-1})
C2	calcination completed in cyclone 2 (kg s^{-1})
C3	calcination completed in cyclone 3 (kg s^{-1})
C3	calcination completed in cyclone 4 (kg s^{-1})

C_p specific heat capacity at constant pressure (J kg^{-1} K^{-1})

D particle diameter (μm)

F Raw meal feed to the preheater tower

Fo Fourier number

f_v volatile fraction of combusting type particle

f_{v0} initial volatile fraction of combusting type particle

h_{fr} enthalpy of formation of reactant species (kJ $kmol^{-1}$)

h_{fp} enthalpy of formation of product species (kJ $kmol^{-1}$)

$h_{f0,lv\text{-}vol}$ enthalpy of formation of volatile component (kJ $kmol^{-1}$)

IN1 raw meal injection to cyclone 1 (kg s^{-1})

IN2 raw meal injection to cyclone 2 (kg s^{-1})

IN3 raw meal injection to cyclone 3 (kg s^{-1})

IN4 raw meal injection to cyclone 4 (kg s^{-1})

k_{tc} thermal conductivity W m^{-1} K^{-1}

k_r devolatilization rate (s^{-1})

k_s devolatilization rate per unit area of particle (mol cm^{-2} s^{-1})

M_D proportion of particle sample by mass having diameter greater than D

$\dot{m}$ mass flow rate (Kg s^{-1})

m_p mass of particle (kg)

m_{p0} initial total mass of particle (kg)

n spread parameter of Rosin-Rammler particle size distribution formula

p fluid pressure (Pa)

R specific gas constant (J kg^{-1} K^{-1})

$\tilde{R}$ molar gas constant (J $kmol^{-1}$ K^{-1})

r_0 radius of infinite cylinder (m)

S_g BET surface area of particle (cm^2 mol^{-1})

s characteristic dimension (m)

T temperature (K)

t time (s)

t_i start temperature (K)

t_1 temperature of surroundings (K)

t_0 end temperature (K)

x ratio of current to initial volatile fraction of particle, f_v / f_{v0}

a thermal diffusivity ($m^2 s^{-1}$)

r fluid density ($kg m^{-3}$)

$h1$ separation efficiency of cyclone 1

$h2$ separation efficiency of cyclone 2

$h3$ separation efficiency of cyclone 3

$h4$ separation efficiency of cyclone 4

q_0 temperature difference at end of heat exchange (K)

q_i temperature difference at start of heat exchange (K)

4.1 Heat and mass balances for inlet conditions of the model

Correct specification of the model boundary conditions to represent accurately the physical precalciner is essential. This section describes the boundary condition assessment in detail.

The conditions at the precalciner inlets are not explicitly measured as part of the plant data analysis. It was necessary to deduce these details from the balance of mass using the continuity principle. The deduction of this data was done thus:

- The oxygen analysis measured at the base of the precalciner and at the exit from the preheater tower was noted.
- The coal delivery to the precalciner and in the kiln was determined from the operation data.
- The only gases that delivered to the precalciner at the kiln gas inlet were considered as due to the coal combustion and associated excess air.
- Negligible leakage of gases in the tower was assumed.
- Overall gas composition at the preheater outlet was calculated, assuming:
    - — complete coal combustion,
    - — complete calcination of the raw meal,
    - — the measured oxygen content at the outlet and
    - — the nitrogen induced with the combustion air.
- Combustion product gases in the kiln were calculated, taking into account:
    - — the oxygen content at the kiln back end, which indicates the excess air requirement and

— Nitrogen induced with the combustion air.

This directly provided the composition of the gas stream entering the precalciner at the kiln gas inlet.

- Air supplied to the tertiary air duct was calculated by considering the difference between the combustion air consumed overall and the kiln and coal inlet air supplied.

	T°C	m kg/s	%CO_2 mass	%N_2 mass	%O_2 mass	Volume rate m^3/s	Cross section area m^2
kiln gas inlet	1000	18.88	23	74	3	66.58	3.44
raw meal inlet	827	3.67	23	74	3	11.64	1.29
tertiary air duct	900	31.40	0	79	21	106.21	2.44
coal	70	0.34	0	79	21	0.34	0.01

Table 4-1 Summary of inlet boundary conditions for the model.

The inlet conditions considered for the calculation of the 1996 operation case are presented in Table 4-1. These data correspond to plant operation at 111 tonne per hour clinker production rate. The production rate can vary between 100 and 140 tonne per hour.

The development of the process analysis, which led to this summary, is detailed in the following sections.

4.2 Data used for the calculation of boundary conditions

Data from the 1996 plant production summary and heat and mass balances were used to calculate the precalciner boundary conditions (Appendix 2). The data used comprised:

- Excess O_2 at the preheater tower exit, 4.1%.
- Excess O_2 at the back end of the kiln, 3.2%.
- Mass rate of raw meal delivery to the preheater, 47.71 kg/s.
- Loss on Ignition of raw meal (CO_2 yield), 34%. This is the amount of mass loss of the raw meal when all the limestone has calcined.
- Total process mass rate of coal, 14 tonne per hour.
- Ash content of coal as received, 7.9%.

- Moisture content of coal as received, 10.6%.
- Mass ratio of O_2/N_2 in atmospheric air, 3.292.
- ratio of coal supplied to kiln and precalciner 2:3 respectively.

4.3 Cyclone mass balance for raw meal delivery to the precalciner

The delivery rate of raw meal to the precalciner from the material drop chute of the stage III cyclone is determined by the separation efficiency of the cyclones. The plant manufacturer supplies an indication of the efficiency of each cyclone.

Figure 4-1 indicates the flow of raw meal through the preheater tower, cyclone efficiencies and percentage calcination at each cyclone. Raw meal feed is *F* kg/s at the entry to stage 1. There is a dust loss, which is estimated to be 15%, from the top of stage 1. The efficiency values are stated on the diagram for each cyclone. Percentage of calcination at each stage is indicated by values C1 to C4, but no values are stated. The raw meal flows through the preheater system were calculated by a simple spreadsheet. It is important for the model boundary conditions to know how much raw meal enters the precalciner and what percentage of that feed has calcined. Calculating the continuity of raw meal through each of the cyclones and then solving the four resulting simultaneous equations gave the continuity for the whole circuit. The equations are:

$$
\begin{aligned}
IN1 &= F + (1 - h2)(IN2 - C2) \\
IN2 &= h1(IN1 - C1) + (1 - h3)(IN3 - C3) \\
IN3 &= h2(IN2 - C2) + (1 - h4)(IN4) \\
IN4 &= h3(IN3 - C3) - C4
\end{aligned}
\qquad \textbf{Equation 4-1}
$$

The solution of the simultaneous equations is quite protracted. The results of spreadsheet solution is shown in Table 4-2. The Data section describes:

1. the raw meal feed to the preheater tower,
2. the Loss on Ignition (i.e. mass lost by calcination of the limestone content),
3. the “decarb” or calcination state at exit from each cyclone and the cyclone efficiency (i.e. the proportion of particulates that are successfully separated from the gas stream and fall into the “drop-out” of the cyclone).

47.47 kg/s corresponds to 170 tph of raw meal, of which approximately 20% is shale.

Data:	
Raw meal feed rate	47.47 kg/s
Loss on Ignition (CO_2 content)	34 %
Shale content (inert)	10.8 kg/s
calcination at stage 1	0 %
calcination at stage 2	0 %
calcination at stage 3	11 %
calcination at stage 4	95 %
cyclone 1 efficiency	90 %
cyclone 2 efficiency	85 %
cyclone 3 efficiency	85 %
cyclone 4 efficiency	75 %
Composition:	
Initial Calcium carbonate	36.7 kg/s
Loss on Ignition (released CO_2)	16.1 kg/s
CO_2 release at stage 1	0.0 kg/s
CO_2 release at stage 2	0.0 kg/s
CO_2 release at stage 3	1.8 kg/s
CO_2 release at stage 4	14.4 kg/s
Calculation of mass flow rate:	
In to cyclones:	
In to cyclone 1	56.4 kg/s
In to cyclone 2	59.3 kg/s
In to cyclone 3	59.0 kg/s
In to cyclone 4	34.3 kg/s
Drop out of cyclone:	
Cyclone 1	50.7 kg/s
Cyclone 2	50.4 kg/s
Cyclone 3	48.6 kg/s
Cyclone 4	25.7 kg/s
Escape top of cyclone:	
Cyclone 1	5.6 kg/s
Cyclone 2	8.9 kg/s
Cyclone 3	8.6 kg/s
Cyclone 4	8.6 kg/s

Table 4-2 Spreadsheet calculation of cyclone raw meal continuity.

The calculation of composition section presents the initial mass of calcium carbonate, the potential carbon dioxide release from the calcium carbonate, and

the expected CO_2 release at each cyclone. The mass flow rate section shows the particle mass flow rate into the cyclones, exiting the drop out of the cyclone (i.e. the separated proportion) and exiting the top of the cyclone (i.e. not separated out of the gas stream). Calcination at stages 1 and 2 is negligible. The calcination at exit from stages 3 and 4 was measured. It can be seen from the "Drop out of cyclone" mass flow rate that the amount of material entering the precalciner (drop out from stage 3) is slightly greater than the overall raw meal injection to the preheater tower. This is despite the 11% reaction completion (i.e. 11% of the 34% LOI) by entry to stage 3 cyclone. Sensitivity studies on the cyclone spreadsheet model showed that the calcination or efficiency at cyclones 1 and 2 did not affect the mass entering the precalciner. Cyclone 3 and 4 significantly affect the precalciner, especially the efficiency of the stage 4 cyclone, since it feeds a large proportion of calcined limestone back into the stage 3 cyclone. The mass flow into cyclones 1, 2 and 3 is significantly larger than the total injection to the tower because of the cyclone separation efficiencies.

The mass flow rate into the precalciner used in the CFD model was 55kg/s, i.e. 6.4 kg/s or 13.5% more than the cyclone model predicted. This was due to an early assumption that the 75% efficient cyclone 4 fed 25% of the calcined feed back into the stage 3. This was shown to be an over-estimate by the spreadsheet, but the high value was carried through into the CFD work. It is equivalent to 53.7 kg/s (or 193 tph) of raw meal injection to the tower, which is within the operational capacity of the plant.

4.4 Calcination energy requirement and CO_2 release rate determination

The energy consumption of the calcination reaction was incorporated into the devolatilisation model of the combusting particle type applied to the raw meal particles. The energy consumption per kg of CO_2 released from the raw meal in the model was calculated from cement plant data for the 'heat of reaction' of $CaCO_3$ at 20°C, which is 422 kcal/kg of reactant. This indicates 4.017 MJ/kg of CO_2 released required to support the reaction. Balancing the formation enthalpies of the components of the reaction yields a similar figure, as indicated in the following development:

$CaCO_3$	$\rightarrow$	CO_2 +	CaO	
-1,212,079		-393,776	-635,138	kJ/mol

The reaction energy balance produces –183,165 kJ/mol of reactant. This is the energy requirement per mole of CO_2 produced, or 4,162,840 J/kg of CO_2. The discrepancy of 3.5% is probably due to truncating errors in the plant data.

The rate at which the carbon dioxide is released from the raw meal by the calcination reaction is determined in reality by the temperature and the partial pressure of carbon dioxide in the surrounding atmosphere (refer to Boynton, 1980). At temperatures exceeding 900°C, the partial pressure of CO_2 does not affect the calcination rate and only the temperature is relevant. The data for the Arrhenius rate equation used in the Fluent model was determined by reference to the results of Borgwardt (1985). The effect of the partial pressure of CO_2 was considered to be negligible due to the temperature in the precalciner being generally in excess of 900°C.

4.4.1 Calculation of the rate determining factors in the limestone reaction rate

Fluent uses the following formulae for devolatilisation:

$$-\frac{dm_p}{dt} = k(m_p - (1 - f_{v0})m_{p0}) \qquad \textbf{Equation 4-2}$$

which can be solved as shown in Appendix 3 to give:

$$\ln(1 - x) = -kt \qquad \textbf{Equation 4-3}$$

Borgwardt contains the relationship:

$$\ln(1 - x) = -k_s S_g t \qquad \textbf{Equation 4-4}$$

The equivalence between the two formulae is obvious. In this way it is possible to adapt the results of Borgwardt's paper to the form that Fluent requires to perform a sensible rate calculation. The activation energy of the limestone reaction from Borgwardt is 2.05×10^8 J/kmol. Relating this to the Arrhenius rate equation:

$$k = A\exp\left(-E/\tilde{RT}\right) \qquad \textbf{Equation 4-5}$$

with $\tilde{R}$ =8314.5 J/kmol (the universal gas constant) and T is the temperature at which the reaction occurs. Borgwardt stated the result of experiments conducted at 670°C. The rate for the model was determined from that data as shown in Appendix 3. According to the values from Borgwardt's paper, then at 670°C the rate is 3.81×10^{8} s^{-1}. At 900°C, in the Equation 4-5, the rate k is 0.28, which results in a time to decompose 95% of the limestone of 10.7 s.

Subsequent to conclusion of the project, the rate value was reviewed and closer inspection of the results of Borgwardt highlighted an overlooked aspect of the paper. This new information led to the calculation of a new rate, which gives a time to decompose 95% of the limestone at 900°C of 14 s. The determination of this rate is presented in Appendix 3; it is reasonably consistent with the rate used in the CFD models.

4.5 Coal analysis

The coal used at Cauldon is frequently analysed to determine whether the properties are suitable for the process. A typical analysis was used to develop the characteristics of the model coal. Two model coals were developed with high and medium volatile contents. The medium volatile coal was based on Upper Freeport MVD in Smoot (1993), which is a standard coal for the first models. The high volatile coal was formulated to represent the Cauldon coal as closely as possible. The technique used to formulate the model coals is presented in this section. The process was to:

- Calculate consumption rate.
- Calculate the calorific value.
- Determine the coal compositions.
- Formulate the volatile composition.
- Calculate the volatile formation enthalpy to be consistent with the calorific value of the coal.

The typical coal analysis was:

- proximate analysis:
    - — Volatile 33.7%
    - — Char 56.5%
    - — Ash 9.8%

- ultimate analysis:
    - carbon 71.1%
    - hydrogen 4.1%
    - sulphur 1.5%
    - oxygen 3%
    - nitrogen 1%
    - moisture 10.8%
    - Ash 8.5%

4.5.1 Consumption rate and calorific value calculation

The coal consumption rate of the precalciner operating without tyres is approximately 2.03 kg/s and the mean Gross Calorific Value is 30.22 MJ/kg. These values were determined from the process data for the plant for 1996 adjusting the coal consumption to be moisture free since the coal is dried prior to firing and using the G.C.V.

In 1996, the amount of as-received coal consumed was 94,640 tonnes in a total operation time of 6,896 hours. This is equivalent to 13.72 tonnes per hour (t.p.h.) of as-received coal. Since the moisture content of the coal is 10.8% of the as-received mass, the dry coal consumption rate is 12.24 t.p.h or 3.4 kg/s. Of this, approximately 60% is delivered to the precalciner, which is 2.03 kg/s.

The mean value of Gross Calorific Value for the dry coal is 7,218 kcal/kg or 30.22 MJ/kg according to the process data.

4.5.2 Proximate and ultimate analyses of the coals used in the CFD models

The characteristics of the model coals and the Cauldon coal are compared in Table 4-3. "Coal 1", the medium volatile coal, was used in the initial stages of the project before a full analysis of the plant coal had been considered. "Coal 2", the high volatile coal, reflects the change to conform the model to the plant coal. The G.C.V. is the dry gross calorific value, h_f^0 is the symbol for formation enthalpy and M_r is the molar mass symbol.

		Cauldon coal	Coal 1	Coal 2
	G.C.V. MJ/kg	30.22	31.0	30.37
Ultimate, %	C	90.9	81.4	90.9
(D.A.F.and	H	5.2	4.5	5.2
N and S free)	O	3.9	7.1	3.9
Proximate, %	Volatile	33.7	18.6	34.5
	Char	56.5	74.4	57.5
	Ash	9.8	7	8
Volatiles	M_r, kg/kmol		19.98	99.98
	Formula		$C_{0.625}H_{4.8}O_{0.48}$	$C_{5.89}H_{13.3}O$
	h_f^0, J/kmol		-1.18×10^8	-5.89×10^8

Table 4-3 Characteristics of Cauldon coal and the two model coals.

The formulation of the coals used in the models was simplified in order to make the numerical calculation simpler. Sulphur and nitrogen content were eliminated from the ultimate analysis. Although modelling NO_x and SO_x is possible it may detract from more important features of the flow. The gases modelled for coal combustion included carbon monoxide, carbon dioxide and water. The coal delivery was therefore modelled as consisting entirely of C, H, O and ash only at equivalent rate to the real coal (2.03 kg/s). The relative proportions of the C, H and O were maintained and the ash content was the same as the Cauldon coal.

The hydrogen and oxygen content can only be considered as residing in the volatile content of the coal since char is composed of carbon only in the Fluent model. The volatile constituents were determined from this supposition.

The formation enthalpy of the volatile material was calculated by the residual energy required from the coal after char combustioin and the conversioin to CO_2 and H_2O had been accounted for.

Char reaction was modelled as first oxidising to carbon monoxide:

$$C + \frac{1}{2}O_2 \rightarrow CO = -110{,}530 \text{ kJ/kmol of C}$$

or 9.21 MJ/kg of char.

Then the carbon monoxide oxidises to carbon dioxide:

$$CO + \frac{1}{2}O_2 \rightarrow CO_2, \text{which yields } -282{,}990 \text{ kJ/kmol of } CO$$

or 10.107 MJ/kg of carbon monoxide.

4.5.3 Volatile composition and formation enthalpy of the medium volatile coal

The calculation of the formation enthalpy of the volatile component for "Coal 1" was done in the initial stages of the project, and the technique used was somewhat laborious. It is presented here for completeness.

"Coal 1" was assumed 20% volatile and 80% char, ignoring ash at this stage. The calorific value of Lower Freeport M.V.D. was taken from Smoot (1993).

The D.A.F. composition of the coal is 87.5% C, 7.7% O and 4.8% H.

74.4% of the coal is char, and this is 80% of the D.A.F. composition. The relative proportion composition of the volatile was determined by assuming its mass to be 20% of 1 kg of the D.A.F. composition, thus:

$0.2 = \frac{4.8}{100}H + \frac{7.7}{100}O + \frac{X}{100}C$, from which X is 7.5%. The composition was then: $C_{7.5/12}H_{4.8}O_{7.7/16} \rightarrow C_{0.625}H_{4.8}O_{0.48}$, which has the molecular mass of M_r=20.02 kg/kmol.

The formation enthalpy of this new compound was determined using the residual calorific value of the coal after char was allowed for.

The energy released by the char from 1 kg of the coal 1 is:

$$0.744 \times (110{,}530 + 282{,}990)/12 = 24.398 \text{ MJ/kg}$$

The overall energy in the coal was taken as 30.98 MJ/kg (in the range of high to medium volatile bituminous coal from Fig. 2-3). The remaining 6.581 MJ/kg of energy must be released from the volatile reactions. The formation enthalpy of the volatile component was required such that the complete combustion of the combustion products released from it per kg of coal was 6.581 MJ. The reaction was perfomed in two steps:

- Enthalpy balance of the oxidation reaction of the volatile component, lv-vol:

lv-vol + $1.273O_2 \rightarrow$ $0.625CO_2 + 2.4H_2O$

h_f^0 lv 0 -393,520 -241,830 h_f^0 kJ/kmol

-245,950 -580,392 h_f^0 kJ/kmol of lv-vol

- The required energy of volatiles is 6,581 kJ/kg of coal, or

$-\frac{6{,}581}{0.186} = -35{,}380$ kJ/kg of lv-vol. Multiply by M_r to get -708,308 kJ/kmol

- the enthalpy balance of the reaction is:

$\sum h_{fp} - \sum h_{fr}$ = (-245,950+-580,392)-($h_{f0,lv\text{-}vol}$) = -708,308

$\Rightarrow h_{f0,lv\text{-}vol}$ = -118,034 kJ/kmol

4.5.4 Volatile composition and formation enthalpy of the high volatile coal

The derivation of the properties of this coal were determined in accordance with the average properties of the Cauldon coal in 1996. The G.C.V. was taken as 30.22 MJ/kg of coal from Fig. 2-3.

In order to calculate the volatile constituents ratio of C, H and O, it was necessary to consider what proportions of the elements were attributable to the parts of the proximate analysis. Table 4-4 shows the ultimate moisture free analysis, the D.A.F. analysis, the proportion of coal constituents that are part of the volatile content, the relative proportions of volatile constituents in the volatile content, and the char content of the coal.

	With ash %	D.A.F. %	Volatile % of coal	Volatile % of volatile	Char, %
C	81.9	89	24.4	70.7	57.5
H	4.6	5	4.6	13.3	0
O	5.5	6	5.5	16	0
Ash	8	0	0	0	0

Table 4-4 analysis of the model coal 2.

From Table 4-4, the volatile % of volatile of each element was divided by its atomic mass to give the relative molecular composition as $C_{5.89}H_{13.3}O$. The molecular mass of this contrived "molecule" is then 99.98 kg/kmol.

The enthalpy of formation was found by the same method as the medium volatile coal.

- Char oxidation to CO_2 produces 32,793 kJ/kg of carbon or 18,856 kJ/kg of coal.
- The total G.C.V. of the dry coal is 30,370 kJ/kg, so the energy required of the 34.5% volatile component is (30,370 – 18,856) = 11,514 kJ/kg of coal.
- The reaction enthalpy $H_{REAC} = \Sigma(h_{f\ products}^{0}) - \Sigma(h_{f\ reactants}^{0})$
  - for 1 kg of coal, there is 0.345/99.98 = 0.00345 kmol of volatiles.
  - $\Sigma(h_{fp})$ = 0.00345×(5.89×⁻393,530+6.65×⁻241,830)
    = ⁻13,545 kJ/kg coal
  - $\therefore \Sigma(h_{fr})$ = ⁻13,545 - ⁻11,514 = ⁻2,034 kJ/kg of coal.
- For 1 kmol of volatiles then, the formation enthalpy is:
  - ⁻2,034×99.98/0.345 = ⁻588,552 kJ/kmol of volatiles.

4.5.5 Devolatilisation constants for the coals used in the CFD models

It was important to establish the devolatilisation rate with regard to the experimental results of other researchers. Referring to the collection of research by Solomon et al (1992), the closest simulation of the coal combustion happening in the precalciner was done by Badzioch and Hawkesley (1970).

Of the model types available for the rate of devolatilisation in Fluent, the single rate Arrhenius type simulation was used in the work throughout. This relates to the work of Badzioch and Hawkesley (1970), and the constants from that paper were used.

The rate equation is:

$$-\frac{dm_p}{dt} = k(m_p - (1 - f_{v0})m_{p0}) \qquad \textbf{Equation 4-6}$$

and the rate constant k is determined by the equation:

$$k = A_1 \exp\left(-E/RT\right)$$ **Equation 4-7**

where A_1 (=312,000 s^{-1}) is the pre-exponential constant and E (= 7.4×10^7 J $kmol^{-1}$) is the activation energy of the reaction.

4.5.6 Size distribution of the pulverised coal particles

For the modelling work, two approaches were taken for the coal and raw meal particle size: a constant size particle, and a Rosin-Rammler size distribution. The size was based on particle size distribution data for the coal from Cauldon in Table 4-5.

dia, D (mm)	M_D, (%)	n
500	0	
250	0.1	1.28
125	4.8	1.35
90	**13.4**	1.42
63	**27.2**	1.94
45	**40.3**	0.48
40	**45**	0.71
30	**53**	0.75
20	**67**	0.90
15	72	0.86
10	80	0.88
5	90	0.94
2	96	0.97
Average value of n,		1.04

Table 4-5 Size distribution of Cauldon coal sample.

In the table, M_D is the proportion of the sample by mass with diameter greater than D, and n is the spread parameter. These values are defined in Equations 4-8.

$$M_D = \exp\left(-\left(D/\overline{D}\right)^n\right)$$
$$n = \frac{\ln\left(-\ln M_D\right)}{\ln D/\overline{D}}$$ **Equation 4-8**

Where the Rosin-Rammler size distribution was used in the model, the parameters set were according to data obtained from the cement works:

- minimum diameter, 20μm

- maximum diameter, 100μm
- mean diameter, 55μm
- spread parameter, n, 1.04

and where constant particle size was used, the mean particle size was taken, 55μm.

4.6 Measurements made on the real precalciner

This section describes collection of data from the plant that was used to provide some validation of the CFD model data. Measurements described in this section were devised for the project and performed as part of the work for the thesis.

No routine measurements are performed at the plant within the main section of the precalciner of gas velocity, pressure or temperature. The data that is available from the plant is from measurements made at the inlet to the tertiary air duct and in the stage 4 cyclone, where pressure and temperature are monitored constantly. These measurements are of limited value to this work. Some measurements of velocity, temperature and calcination of the limestone were performed at access ports in the precalciner wall using methods devised as part of the work of this thesis.

4.6.1 Position of the access ports

There are 6 inspection ports on the cylindrical section of the precalciner, which are used for inspection during shutdown. The position of the holes is illustrated in Fig. 4-2.

The figure shows the height of the ports at 11.4m and 20.4m from the position used as the base of the model. The ports are identified in the plan view as 1, 2 and 3 and this sense of numbering is maintained throughout this section. Since the access ports are not regularly used, they had been blocked by refractory lining so 1½-inch holes were drilled through the 23 cm of refractory lining for insertion of measuring probes.

4.6.2 Measurement of velocity and temperature

Velocity was measured approximately with an S-type Pitot tube that was purged of particle build-up between measurements using compressed air from

the on site air supply. Figure 4-3 shows the apparatus used to do this. The Pitot tube length was 1.8m and the inside diameter of the tubes was 3.5mm. The S-type Pitot tube has apertures facing 180° away from each other.

Calibration was performed in the lab to determine the relationship between the dynamic pressure measured using the S-type Pitot tube and that measured by a standard Pitot tube. For the standard Pitot tube, the dynamic pressure and velocity are related by:

$$p = \frac{1}{2} \rho U^2 \qquad \textbf{Equation 4-9}$$

where p is the pressure difference measured by the Pitot tube, ρ is the fluid density, and U is the free-stream fluid velocity parallel to the Pitot probe. The dynamic pressure for the precalciner measurements were then calculated from the relationship established in the lab. The gas composition was regarded as hot air; since the temperature was measured concurrently with the dynamic pressure, the density was then calculable and so the velocity by rearrangement of equation 4-9.

Temperature measurement was done using a thermocouple attached to the Pitot tube, thus getting simultaneous velocity and temperature measurement. The type of thermocouple was industrial mineral insulated probe type K, 2m long, diameter 3mm and temperature range 0-1100°C.

The measurements from the single campaign attempted are presented in Fig. 4-4. The error bars indicate the estimated limit of accuracy of the measurements.

An unusual phenomenon was noticed at Hole Position 1 at the upper measurement level, in that from time to time the differential pressure measured from the S type Pitot probe increased by over an order of magnitude. This corresponded to a noticeable upward force on the end of the probe and a sound that suggested that a stream of small particles was bombarding it.

The temperature of the precalciner shell was measured during the same campaign using an infra-red thermometer. Measurements were made at the heights of the access ports around the entire circumference of the precalciner. The measurements are illustrated in Fig. 4-5. The emissivity of the precalciner

shell surface was assumed to be 0.95, which is acceptable for an oxidised steel surface. This value was required for calibration of the thermometer.

Discussion of these measurements has been reserved for the validation sections of succeeding chapters with reference to the CFD model results.

4.6.3 Measurement of the calcination of limestone

The raw meal analysis is monitored at the plant hourly, since it critically affects the quality of the clinker, which is produced at a rate in excess of 100 tonnes per hour. The sample is taken before injection to the process and at the bottom of the stage 4 cyclone (i.e. just before entry to the kiln from the preheater tower). The constituents and Loss On Ignition (L.O.I.) are recorded. The constituents include: SiO_2, Al_2O_3, Fe_2O_3, CaO, MgO, SO_3, Na_2O, K_2O, and Cl. The model raw meal constituents were greatly simplified by assuming an inert CaO and shale component and a volatile CO_2 component.

The Loss On Ignition (LOI) is measured from the mass loss when a 1g sample is maintained at 1000°C for 10 minutes. The LOI is 35% according the annual process summary. The LOI of the raw meal at the raw meal inlet and at the exit from the precalciner can be used to set the initial condition of the raw meal and to validate the data.

There is an access port at the bottom of the stage 3 cyclone material drop chute which allows collection of a sample just before entry to the precalciner. The next suitable access port in the process is positioned at the bottom of the stage 4 cyclone material drop chute, which allows sample collection just before entry to the kiln. These are the closest to the two required data.

It was important for the reaction of the limestone to be arrested as soon as possible after collection. To do this, the standard sample collection pot was fitted with a heavy steel insert with a number of holes of small diameter. The detail drawing of the collection pot is shown in the Appendix 4. The expected rate of heating of the heavy insert was calculated to be sufficiently low that less than 50°C temperature rise would occur in the sampling time. The calculated rate of cooling of the sample of limestone was in the order of one second to below 500°C when reaction is effectively arrested. The calculation of the heat exchange in the sample pot is detailed in Appendix 4.

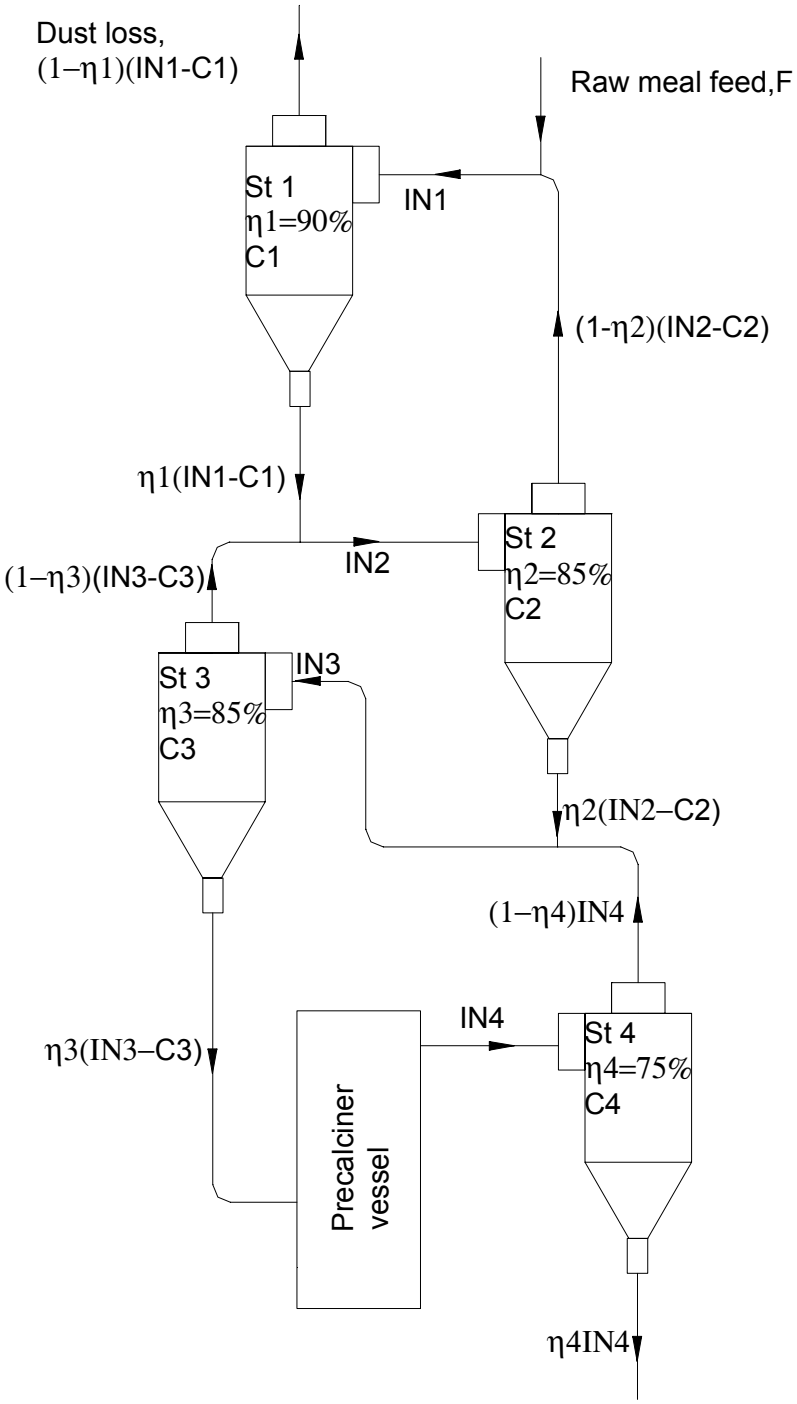

Fig. 4-1 Schematic showing the preheater tower with 4 cyclones and the precalciner vessel. The kiln is excluded for clarity. Each cyclone has a separation efficiency, η, an influx of particulates, IN, and a degree of calcination completed inside, C. The solution of the simultaneous equations was performed in an Excel spreadsheet.

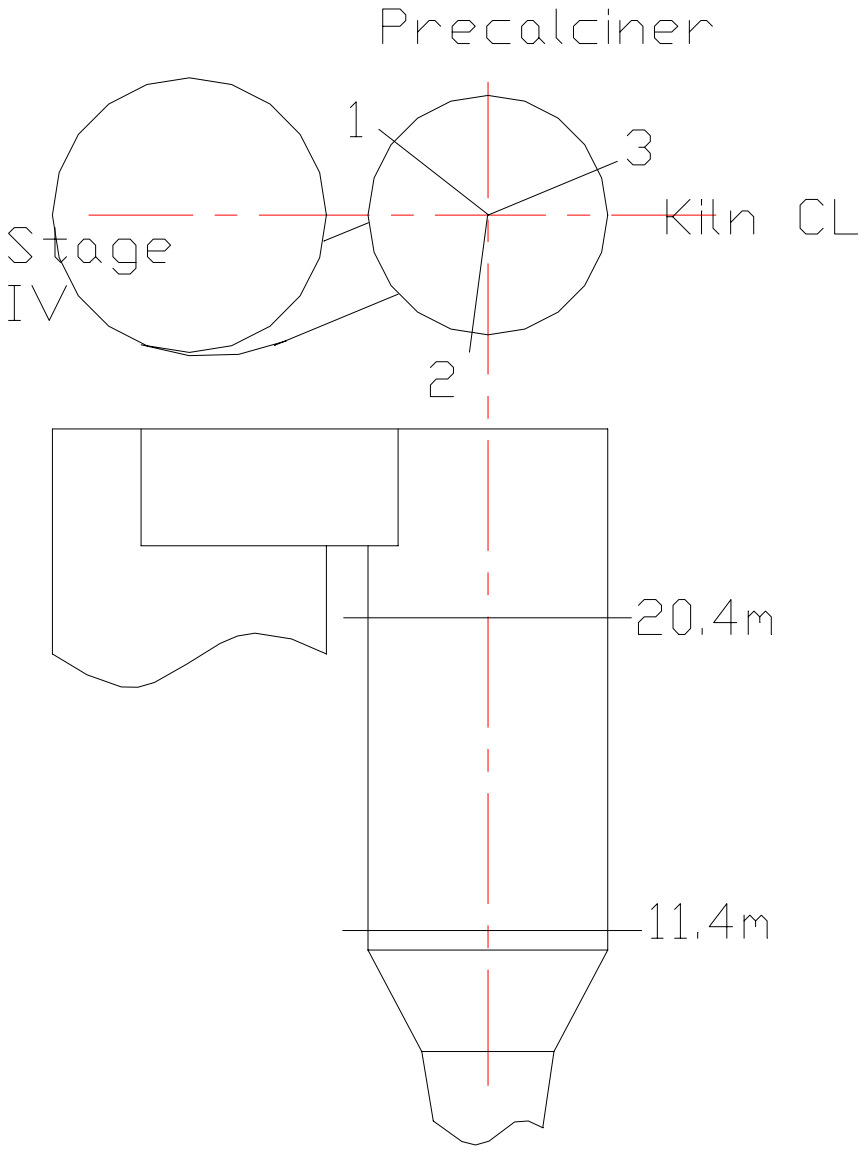

Fig. 4-2 Position of the access ports in the precalciner cylindrical section. The height indication is relative to the zero height datum on the CFD models. Three ports positioned in the same circumferential positions are available at each level. The diameter of the access hole was 1.5 inches.

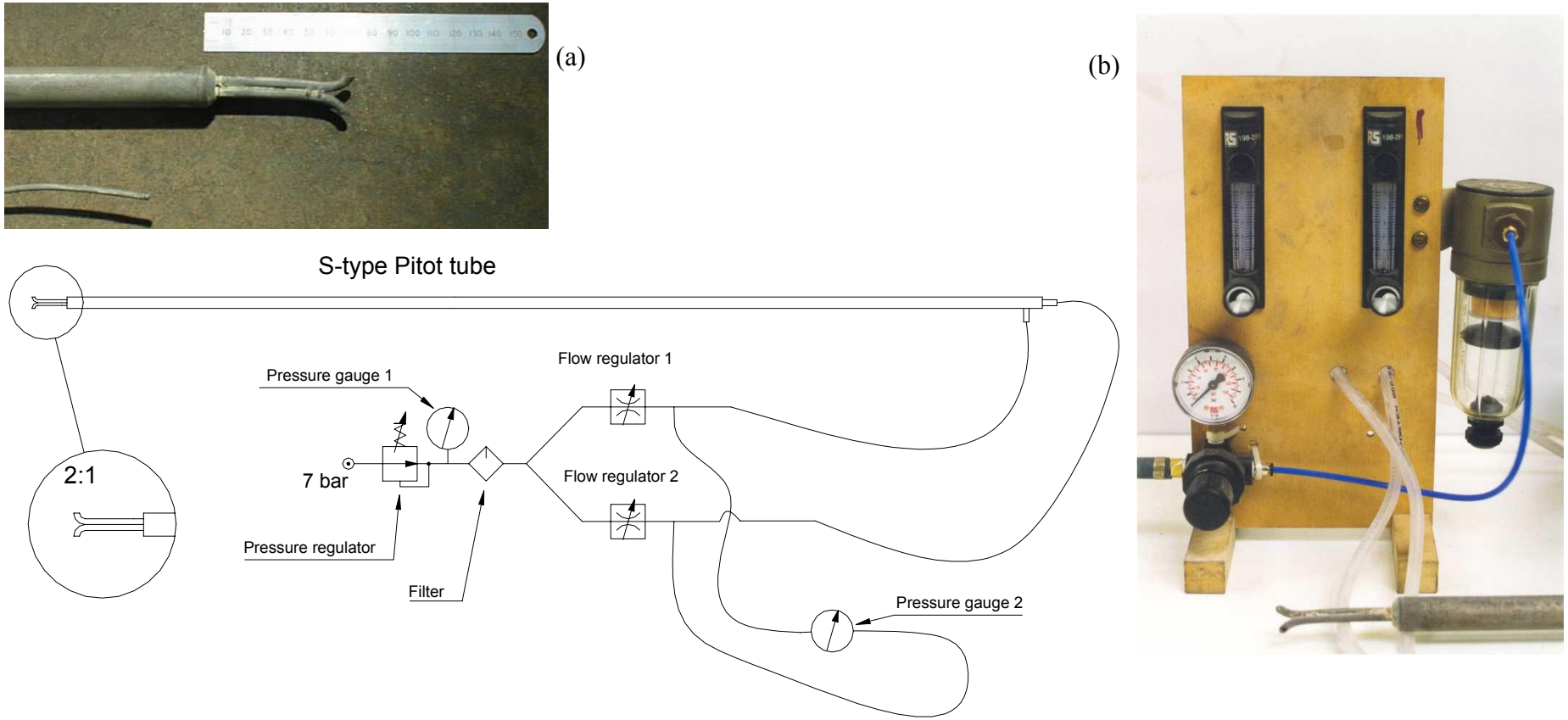

Fig. 4-3 S-type Pitot tube and thermocouple apparatus. The length of the Pitot tube is approximately 1.8m. Compressed air from the plant air line at low flow rate was used to purge the probe of blockage intermittently. Inset (a) shows the end of the Pitot probe and the tip of the 2m long thermocouple that was attached to the probe. Inset figure (b) shows the purging air circuit.

(a)

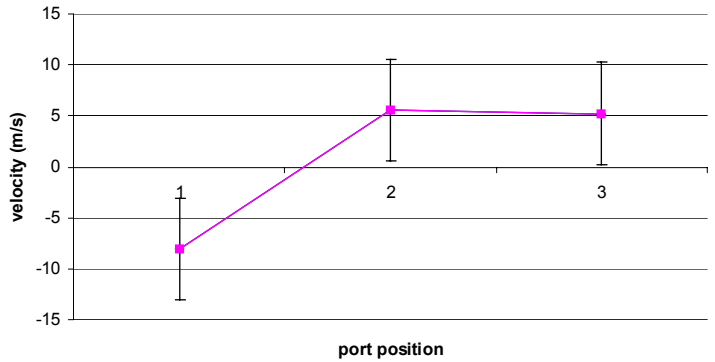

(c)

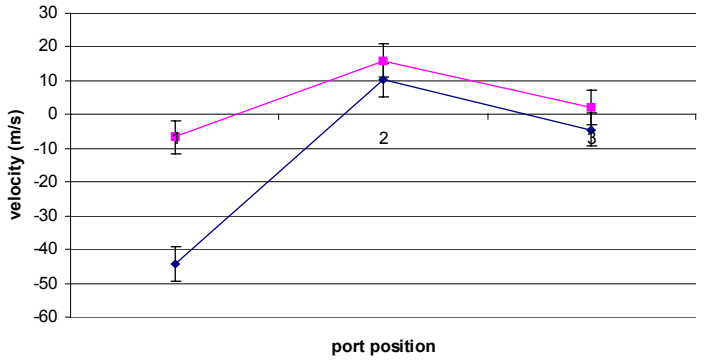

(b)

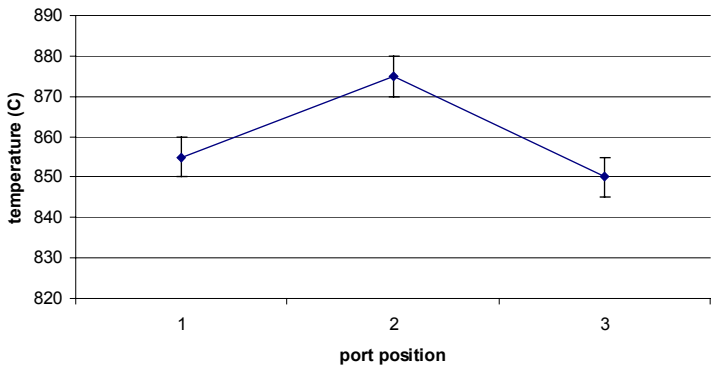

(d)

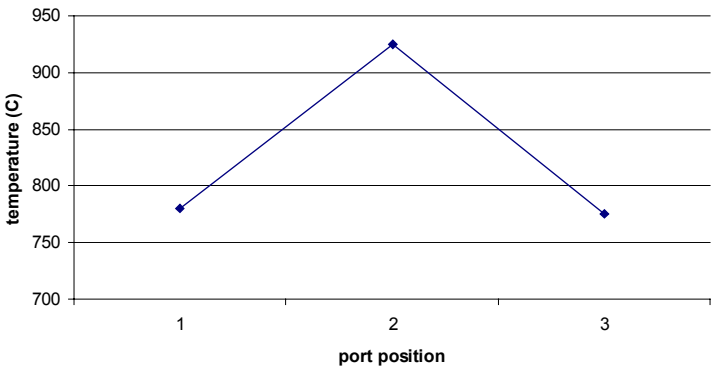

Fig. 4-4 Validation data from the precalciner of velocity and temperature measured at the port positions. Data was collected approximately 30 cm into the precalciner from the inside wall. Graphs of velocity, (a) and (c) show the vertical component, positive being upwards velocity.

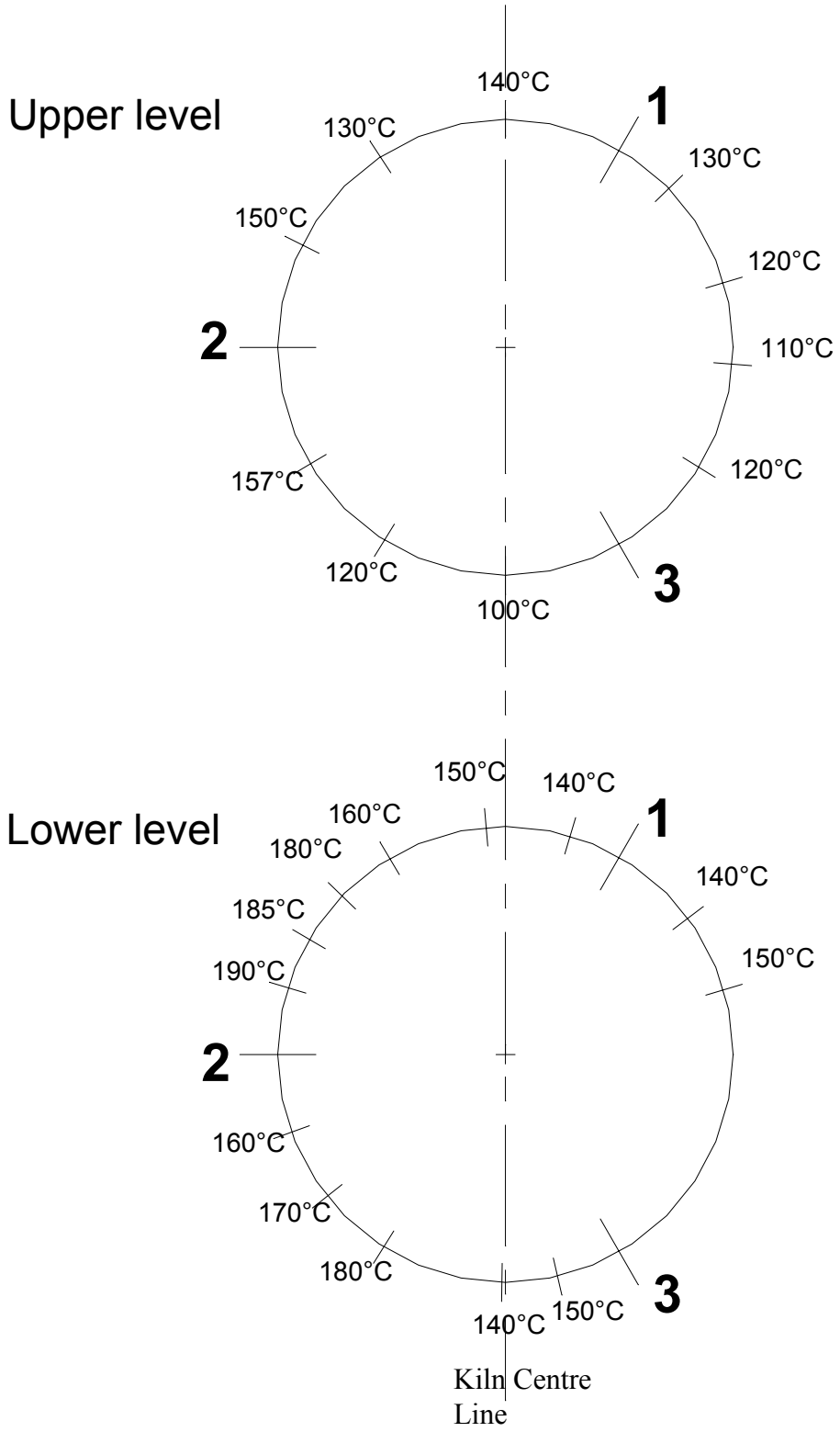

Fig. 4-5 Precalciner shell temperature measurement showing surface temperature measured with an infra-red thermometer. The surface emissivity was assumed to be 0.95 since the surface was partially oxidized steel.

5 Block structured mesh using Fluent/UNS version 4.2

The model developed for use with Fluent/UNS version 4.2 is presented in this chapter. The important features of model development are discussed and the results of the numerical solution are presented. Comparison is made between the results collected from the model and the measured features from the real precalciner.

The chapter presents the development of the initial stages of modelling with this commercial code. The characteristics observed in this model were used to develop subsequent improved models using improved commercial code. This model also formed the basis of the tyre chip models since the solutions obtained were found to be very stable.

Notation for Chapter 5

I	Turbulence intensity
u'	turbulent velocity fluctuation (m s^{-1})
u_{avg}	mean velocity component in turbulent flow (m s^{-1})
Re_{DH}	Reynolds number calculated using hydraulic diameter

5.1 Features of the model

Fluent Unstructured (version 4.2.5) was used to develop the model described in this chapter. It is used to solve the steady state, three dimensional, fully viscous Navier Stokes equations. The k-ε turbulence model of Launder and Spalding (1974) is used with the constants described in that paper. Reaction mechanisms are simulated using the Magnussen-Hjertager (1976) eddy mixing model and finite rate devolatilisation models of Badzioch and Hawkesley (1970) using the standard Arrhenius-type rate equation. The discretisation scheme used was PRESTO! (PREssure STaggering Option, Fluent Inc. 1996) for pressure as the flow was considered to be subject to high-pressure gradients and body forces. The SIMPLE pressure-velocity-coupling scheme of Patankar (1980) was used. Radiation was not calculated in order to simplify the calculation. Since the gas and particle mixture is at fairly homogeneous

temperature the simplification is a reasonable first assumption. The mesh is illustrated in Figure 3-1 and the mesh development was discussed in Chapter 3.

5.1.1 Gas composition

Six chemical species were included in the model: N_2, CO_2, O_2, H_2O CO, and lv-vol (the volatile of the coal). These are listed in order of decreasing partial pressure according to estimates of the relative proportions of the gases in the precalciner. The sources of these gases were the precalciner inlets and the reacting particles.

5.1.2 Boundary conditions

The heat and mass balances of the process were used to determine the heat and mass transfers at the boundaries of the model (Chapter 4). Three boundary types were modelled: inlets, walls and the outlet. Details of the heat and mass transfer used in the model at the boundaries are presented in Table 5-1.

Name	**Abbreviation**	**Temp. °C**	**Mass flow rate kg/s**	**%O_2 by volume**	**%N_2 by volume**	**%CO_2 by volume**
Tertiary Air Duct	TAD	900	27.4	21	79	0
Coal inlet on LHS	Coal A	75	0.43	21	79	0
Coal inlet on RHS	Coal B	75	0.43	21	79	0
Raw Meal Inlet*	RMI	827	3.6	21	79	0
Kiln Gas Inlet	KGI	1100	16.5	4.7	78	17

Table 5-1 Velocity inlet boundary conditions, showing gas flows only.

WALLS

The boundary at the walls of the main section (not including the outlet duct) was modelled as a conducting wall with wall heat flux, Q=1,293 W/m^2 as calculated in section 4.1.4. Considering the interaction of the particle with walls, the coefficient of restitution at the walls was set to 0.5 in both the

* Note that the Raw Meal Inlet boundary condition is formed from an estimate of the gas bypass through the stage 3-cyclone dropout duct.

tangential and normal directions. The outlet duct, as a non-real part of the geometry, was considered to produce no heat loss and so the duct wall condition was adiabatic.

OUTLET

The condition at the outlet from the computational domain was set to OUTFLOW, which allows exit of the gases from the domain without specification of pressure or velocity. The requirement for this boundary condition to be applied is that the flow is near fully developed at that point so that the field variable gradients are near zero for all except pressure; hence the long duct was added.

VELOCITY INLETS

Turbulence parameters for the velocity inlets were set according to the hydraulic diameter of each inlet and the turbulence intensity, *I* calculated from the standard formula:

$$I = \frac{u'}{u_{avg}} \cong 0.16(\mathrm{Re}_{DH})^{-\frac{1}{8}} \qquad \textbf{Equation 5-1}$$

5.1.3 Particulate modelling

The two particulate types modelled represent coal and raw meal, and both are modelled using the Lagrangian frame of reference (Fluent Inc. 1996). The aspects of particle modelling that are applicable to both types of particle involved in this model are described in this section.

The mass injection rate of raw meal particles to the domain was 55 kg/s and the coal injection rate was 2 kg/s. The raw meal was injected at 1056 points across the Raw Meal Inlet. It was found necessary to disperse the particles with diverging velocity components in order to obtain a stable solution. The dispersion is illustrated in Fig. 5-1.

The coal was injected at 24 points across both of the coal inlets.

The Rossin-Rammler size distribution was applied to the particles. The parameters were set according to Table 5-2.

Minimum particle diameter	20μ
Mean particle diameter	55μ
Maximum particle diameter	100μ
Spread parameter	1.04
Stochastic attempts	20
Interval length of tracking steps	10 mm
Number of tracking steps	15,000

Table 5-2 Particle size and stochastic settings.

5.1.4 Calcination modelling

The devolatililisation model of the combusting particle type was used to simulate the calcination reaction. The single rate model was used of the Arrhenius form, $k = A\exp-(E / RT)$. The activation energy (E = 2.05×10^{-8} J/kgK) and the pre-exponential constant (A = 3.81×10^{-8}) were determined by reference to the work of Borgwardt (1985). The amount of reaction estimated to have occurred prior to injection to the precalciner was 20%; this was established from the efficiency of the Stage 4 cyclone (post precalciner) which feeds 25% of the particles entering it back into the Stage 3 cyclone and therefore back into the precalciner. This condition was subsequently checked by measurement and found to be 12%. When the new value was used in the cyclone spreadsheet model described in section 4.2, it gave a flow rate into the precalciner of 48.6 kg s^{-1} compared to the 55 kg s^{-1} used in the model. The effects of this will be assessed in the subsequent discussion.

5.1.5 Combustion modelling

Coal combustion was included in the model. The devolatilisation rate was set according to the data of Badzioch and Hawkesley (1970) - the standard data available in the Fluent/UNS code. Combustion of carbon (char) was considered as a two step reaction (Borman and Ragland, 1998), first to CO, then to CO_2. The diffusion-limited rate was used, whereby the diffusion rate of the gaseous oxidant to the surface of the particle determines the oxidation rate (Baum and Street, 1971).

Data for the composition of a medium volatile coal was obtained from Smoot (1993). The coal simulated was based on Upper Freeport MVD. The composition of the model coal is stated in Table 5-3.

		Model coal
Proximate analysis (by mass, %)	volatiles	18.6
	char	74.4
	ash	7
Ultimate analysis (by mass, %)	carbon	87.5
	hydrogen	4.8
	oxygen	7.7
Calorific value (kJ/kg)		30,985

Table 5-3 Analysis of coal applied to CFD model.

5.2 Modelling results from the full model

Post-processing the results from the converged Fluent/UNS model showed some interesting features of the flow, which aided understanding of the operation of the plant and suggested ways in which the process could be improved. Some of the more significant features of the flow demonstrated by the model are illustrated using plots of particle tracks, contours and velocity vectors in Figure 5-2a-e. The same views of subsequent precalciner models will be used for comparison of data in the following chapters. Each figure shows the same view of the precalciner model, which is described with reference to the Fig. 3-1 in view B on the section indicated as A-A. The outlet duct is on the side of the precalciner farthest from the point of observation. All walls and other boundaries are transparent in order to render the internal features of the flow visible with only the outline of all boundaries visible. The inlets are labelled on the Fig. 5-2b for clarity. A brief description of each figure is as follows:

Fig. 5-2a. The trajectory of a single raw meal particle injected at the centre of the raw meal inlet. Six tracks are visible, each one representing a different stochastic attempt. Particles recirculate in the vessel before exiting through the outlet duct.

Fig. 5-2b. The trajectory of eight coal particles is shown; four are injected from Coal A on the left-hand side (the same side as the tertiary air duct) and four injected from Coal B on the right hand side. The trajectories appear to be smooth because the mean trajectory of each

particle is shown without the stochastic attempts that were calculated.

Fig. 5-2c. Temperature contours on a single plane through the centre of the precalciner vessel.

Fig. 5-2d. Discrete phase devolatilisation rate, indicating yield rate of volatiles from both the coal and the raw meal per unit volume. The model regarded the calcination of the raw meal as a devolatilisation reaction; the volatile being released was CO_2.

Fig. 5-2e. Velocity vectors on ten lines through the centre of the precalciner vessel, indicating a maximum vertical velocity of 39.6 m/s.

Further features of the model are illustrated in the following figures:

Fig. 5-3 Details of the raw meal behaviour in the precalciner.

Fig. 5-4 Details of the coal behaviour in the precalciner.

Fig. 5-5 Raw meal trajectories from groups 1, 11 and 16.

Fig. 5-6 Raw meal trajectories from groups 21, 26 and 31.

Fig. 5-7 Model data for comparison with plant measurement data.

Fig. 5-8 Data from measurements made on the precalciner.

Fig. 5-9 Profiles of vertical velocity.

Fig. 5-10 Velocity vectors through the centre line of the TAD.

Fig. 5-11 Raw meal particle track and vertical velocity interaction.

Fig. 5-12 Tertiary air velocity vectors.

Useful data is available from the gas composition at the exit from the cylindrical section as presented in Table 5-4.

Gas component	Mass flow rate at exit (kg/s)
carbon dioxide, CO_2	19.680
oxygen, O_2	2.892
lv-vol, $C_{0.625}H_{4.8}O_{0.48}$	0.000
carbon monoxide, CO	0.016
water vapour, H_2O	0.801
nitrogen, N_2	38.270
Total	61.659

Table 5-4 Gas composition at exit from the cylindrical section.

5.2.1 Raw meal particle trajectories and calcination

The model shows that particles injected at the raw meal Inlet, (RMI), are strongly influenced by the gases injected at the Tertiary Air Duct (TAD). Of the mass of raw meal injected approximately 85% is driven across to the further side. The momentum of the gases from the TAD (27 kg/s at 30 m/s) is similar to that of the raw meal (55 kg/s at approximately 15 m/s). Figure 5-2a shows this behaviour for one particle only. The effect of turbulence in the real installation tends to disperse the particles in random patterns; this has been modelled in CFD and is displayed in this figure. CFD shows that the initial common trajectory is toward the right hand side of the precalciner in the conical section, despite turbulence effects. The effect of turbulence is significant in dispersing the particles following their passage beyond the throat of the conical section. There is then significant recirculation of some particles in the main cylindrical section before exit. The single particle with 6 stochastic attempts in Fig. 5-2a illustrates this behaviour, showing that particles starting at the same point are directed to such different destinations that some rise and exit directly and others recirculate for some time before exiting. The time a raw meal particle will take to traverse from inlet to exit thus varies considerably; an average of 5 seconds is apparent from Fig. 5-3a, with some taking as little as 2 seconds and as much as 38 seconds. The momentum of the gas mixture drives the particles. Therefore the model flow field illustrated in Fig. 5-2e by velocity vectors shows why the particles are observed to behave as they do. Recirculation of the gas on this plane is strong. On the left-hand side of the precalciner, the downward velocity reaches 11 m/s and on the right hand side the upward velocity reaches 20 m/s. An interesting feature shown in the velocity vectors is in the region of the RMI in that the vertical velocity is completely depressed close to the raw meal injection, and next to the inlet there is a small downward velocity as particles “fall on to” the gas stream.

Figure 5-3b suggests that the injected raw meal is 74% calcined before exit from the precalciner. Some care is required in interpreting this value since the limestone content on injection was considered to be 20% reacted. Referring to Fig. 5-3a and 5-3b, the residence time and degree of calcination by exit depend on the release position. The release positions of the groups and the

trajectories are shown in Fig. 5-5a-f and 5-6a-f. Group 1 (Fig. 5-5a & b) is furthest from the centre line of the tertiary-air-duct, and Group 31 (Fig. 5-6e & f) is closest to it. Particle groups closer to the centre line of the tertiary-air-duct have longer residence times and hence have calcined more before leaving the precalciner. No measurement on the real installation has yet been performed that can verify this. The post-processing available showed (Fig. 5-2d) the discrete phase devolatilisation rate per unit volume from the coal and the raw meal in one field variable. This included the *lv-vol* from the coal and the CO_2 from the raw meal, which was modelled as a volatile despite the true nature of the reaction. Since the volatile content of coal was only 2.5% that of the raw meal, the effect of raw meal volatiles, *lv-vol*, can be expected to dwarf the effect of the coal. Interpreting the Fig. 5-2d with this assumption suggests that calcination occurs mainly toward the wall at the right hand side of the precalciner, i.e. on the side furthest from the TAD above the conical section. Since calcination is a highly endothermic reaction, an associated region of relatively low temperature would be consistent with a high rate of calcination. This is what is observed in the model in Figure 5-2c, in which the region corresponding to high calcination rate in Fig. 5-2d shows a depression to the range 900°C to 1000°C. Energy supplied by the coal combustion reactions maintains the temperature until the calcination reaction is complete.

5.2.2 Coal particle trajectories and combustion

The behaviour of the coal illustrated in Fig. 5-2b was consistent with the above discussion. Coal from the inlet on the same side as the Tertiary Air Duct (Coal A) rises and exits without recirculating; coal from the other inlet (Coal B) rises to the ceiling of the precalciner and recirculates in the full length of the main cylindrical section. Residence times were 0.6 to 1.0 second for coal A and 5 to 18 seconds for coal B (Fig. 4a). Volatiles were released very quickly due to the high temperature of the gases into which the relatively cold (75°C) coal air stream entered, and the conversion to CO and H_2O was completed before exit from the main body of the precalciner. Char oxidation was completed before exit from the precalciner for Coal B; 20% of the char from Coal A was not oxidised before exit. Some CO was present at the exit from the precalciner at 0.46 ppm, confirming the presence of reacting char. The effect of the different

residence times on the coal combustion is illustrated by Fig. 5-4b, in which the residual mass of coal for inlet Coal A is greater than that for inlet Coal B.

5.2.3 Pressure and temperature validation

The static pressure on the model decreased from the top of the conical section to the exit from the precalciner by 350 Pa. Measurement on the installation indicated 400 Pa between the conical section in the precalciner and the vortex finder (i.e. the gas outlet) of the stage 4 cyclone. The similarity suggests that the model calculated pressure drop is the correct order of magnitude.

Temperature at the exit from the precalciner was approximately 927°C on the model. The temperature measured in the stage 4 cyclone was approximately 870°C under similar operating conditions (see Figure 2-1 for position of the Stage 4 cyclone with respect to the precalciner. The heat balance for the model precalciner indicated that there was just sufficient coal to support the calcination reaction. It can be expected that the temperature at the outlet from the precalciner will be slightly higher than 900°C as suggested in the discussion about calcination in section 5.2.1.

5.2.4 Validation of the CFD results

Validation of CFD results is important to give confidence to the modelling. Limited measurements are made for process control. These do not indicate how accurately the model has predicted the process inside the precalciner main body since there are no probes for pressure, temperature or gas composition installed. The high temperature makes measurement inside the precalciner difficult and there is heavy particle loading so that probes suffer blockage. A campaign of measurements was developed to measure flow direction by using an S-type Pitot, and temperature using high temperature thermocouples as described in Chapter 4. Another important measure is the state of the raw meal at the RMI and at the exit from the precalciner. A quenching collection pot was constructed to collect suitable samples for this purpose in order to arrest the reaction progression in the collected sample as quickly as possible.

Initial measurements show promising correlation with the model. Six access ports are present on the cylindrical section of the precalciner as shown in Fig. 4-2. Three are equally spaced on the circumference at two heights; 0.6

m above the conical section (elevation 11.42m on the model) and 5m below the top (elevation 20.42m). The data from the model at these two heights is presented in Fig. 5-7. Position of access ports (1,2, and 3) is indicated on the circumference of the precalciner in the top left diagram of Fig. 5-7a. The outlet duct is shown bottom left of each contour plot. The view is from the top of the precalciner. Contours of velocity in the vertical (z) direction (m/s), temperature (°C), and particle concentration (kg/m^3) are shown. Probes were inserted approximately 0.3 m into the flow from the edge of the refractory lining.

All temperature measurements show good correlation to within 60°C (Fig. 5-8a).

Accurate measurement of gas velocity inside the precalciner is very difficult on account of the very high particulate loading. However for the purposes of initial validation, an S type Pitot probe was used to give and indication of flow direction in the precalciner.

The results of the flow measurements are shown in Fig. 5-8b. There is considerable uncertainty in the actual velocity measurements because of the time varying nature of the flow although greater relevance can be attached to the relative magnitude at each measurement port and flow direction as it is extremely unlikely that these would be wrong. Error bars on the measured values are used to give an indication of the estimated uncertainty from the size of the observed fluctuations. The probe blocked up with particles after a few seconds and had to be cleared by purging with air. There was significant unsteadiness in the velocity measurements from the probe. Nevertheless it can be seen from Fig. 5-8b that there is generally good agreement between the prediction of the flow velocity and the direction and relative magnitude of the velocity indicated by the measurements.

An unusual phenomenon was noticed at Hole Position 1 at the upper measurement level, in that from time to time the differential pressure measured from the S type Pitot probe increased by over an order of magnitude. This corresponded to a noticeable upward force on the end of the probe and a sound that suggested that a stream of small particles was bombarding it. It can be seen from Fig. 5-7f that the measurement point is close to a region in which a

high concentration of particles occurs locally. It is possible that this region of high particle concentration moved from time to time where the probe was measuring.

The collection of quenched raw meal from the inlet and outlet of the precalciner showed that the calcination reaction was 11% complete at inlet and 95% complete at the base of the stage 4 cyclone, which is in agreement with the energy balance for the precalciner assuming complete coal combustion. The inlet condition for the model raw meal was 20% completed. Although the degree of completion at the exit from the precalciner was 74 % according to the model, this is not comparable to the measurement at the base of the cyclone. The additional path length to the base of the cyclone allows further reaction. This path length is equivalent to the length of the duct on the model. The degree of calcination at the exit from the duct is 85%. Predicted calcination at exit was considered to be acceptable at this stage of the work, although since the model indicated only 85% calcination, compared with a measured value of 95%, causes of this behaviour were sought. Full discussion of this point is made in Chapter 6, section 6.9.

5.2.5 Further visualisation of the flow

Other interesting features of the model became apparent as the visualisation techniques available in Fluent improved. These features are illustrated in the last four figures of this Chapter (Fig. 5-9 to Fig. 5-12).

Figure 5-9a and b show vertical velocity on a selection of planes in the riser section of the precalciner. The changes to the flow in this region are significant. The raw meal entering at the raw meal inlet causes a significant depression of the initial upward flowing gases, which persists up the height of the riser into the conical section. The higher velocity gases are displaced toward the wall on the opposite side. When the tertiary air enters, a second high velocity upward travelling gas stream is introduced. The two high velocity peaks persist into the conical section. When the gases enter the conical section, this model shows that in addition to the downward recirculation from the larger scale flow in the cylindrical section on the same side as the tertiary air inlet, there is also a smaller recirculation in the conical section opposite the tertiary air inlet. This is more clearly shown in Figure 5-

10 where velocity vectors are shown on lines parallel to the tertiary air inlet centre line at various heights. A third smaller scale recirculation zone is apparent in the section between the tertiary air inlet and the start of the conical section.

Figure 5-11 shows how raw meal particles and the vertical gas velocity relate together. The particles sit neatly in the depression observed in Fig. 5-9 and then are carried up in the fastest upward moving gases and then downwards on the other side of the precalciner in the highest downward velocity gases.

Figure 5-12 shows planes inclined at the same angle as the tertiary air inlet at four heights to show the three-dimensional nature of the recirculation zone.

5.3 Discussion of the modelling results

An interesting observation follows from the foregoing analysis of the CFD results. The coal injected at Coal A and that at Coal B follows very different trajectories (Fig. 5-2b) and as a result behaves very differently. Coal B is directed up the right hand side of the precalciner vessel, in the same region where the raw meal is seen to react at the highest rate. This coal burns at a relatively low temperature, 900°C to 1000°C. Coal A rises through the hottest region of the precalciner, reaching temperatures in excess of 1500°C. It follows a general trajectory that takes it directly out of the exit and well away from the right hand side of the vessel where the raw meal is reacting at the highest rates. Temperatures of this order can lead to production of thermal NO_x. Coal B appears to "work harder" than Coal A to support the raw meal reaction. By injecting all coal at one of the two inlets the interaction of the region of maximum heat release from the coal and the region of maximum calcination rate of the raw meal might lead to improved heat transfer and more efficient operation. Sensitivity analysis based on this observation was performed as described in Chapter 6.

The recirculation of the flow and the particles in the model indicated that the reaction time within the precalciner might be prolonged by the ensuing increased gas residence time. Prolonged residence is beneficial for approaching complete reaction of the raw meal in the precalciner. The rate of

reaction was determined according to the research of Borgwardt (1985, described in section 2.4) which was done with similar sized particles and at similar temperatures. The reaction level of the raw meal going into the precalciner and at the base of the stage 4 cyclone on the plant was measured. At inlet the CO_2 released was 11% and at the stage 4 exit it was 95%. The model used 20% at inlet and indicated 90% at exit from the duct. The plant produces 83% of the CO_2 release and the model produced only 70%. This may be attributable to the exit duct on the model providing less mixing than in the cyclone that stands at the exit of the real precalciner. It may also be attributable to the finite cooling time of the samples collected, which would allow for further reaction.

5.4 Conclusion and further study

The work done in the model of this chapter demonstrated that CFD can be used to indicate the likely behaviour inside the Cauldon precalciner vessel.

Investigating the causes of the behaviour observed in the model suggested alternative operation of the precalciner by injecting all coal from one inlet may lead to improvement in NO_x reduction. Further CFD models were thus suggested to test the sensitivity of the model to this and other changes, which are presented in Chapter 6.

Combining the information provided by the temperature field, the coal and raw meal trajectories and the calcination rate produced an interesting picture of the interdependency of their behaviour. In the model, there was a temperature field depression opposite the TAD, which was related to the strongly endothermic reaction of raw meal since 85% of the raw meal passed through the region. Raw meal will yield CO_2 to a 100% CO_2 environment at 900°C. The model temperature field was drawn to 900°C in the region of high raw meal concentration. The coal in this region, which was released from the inlet Coal B, burned at a lower temperature than the coal released from the other inlet. The coal inlet on the cooler side supported the most intense region of raw meal calcination rate.

A large scale recirculation zone was identified in the model in the main cylindrical section of the precalciner. Coal from the inlet opposite the TAD and raw meal were carried into this zone and their residence times were

increased. This zone was directly caused by the tertiary air inlet and it dominates the flow pattern in the precalciner. Smaller scale recirculation was observed in the region by the coal inlet on the side opposite the TAD (Coal A in Fig. 5-2b).

Limited measurements of velocity and temperature in the real precalciner vessel showed reasonable agreement with the observations made with the model results. The measurements of velocity in the upward direction through access ports showed the same trend of behaviour as the model. An interesting feature was observed during the measurements, which led to the conclusion that the particle trajectories might suffer "roping" as observed in coal conveying pipes.

There was a significant difference between the calcination achieved in the model precalciner compared to the measured calcination. Full discussion of this point is made in Chapter 6.

The work in this chapter illustrated some important characteristics of the behaviour in the precalciner vessel, which cannot be practically measured. The usefulness of the CFD tool for this work is proven in its ability to make clearer the behaviour of the vessel. Validation of results can be done by making measurements at key positions through the precalciner wall to verify the information produced by the model at those locations.

(a)

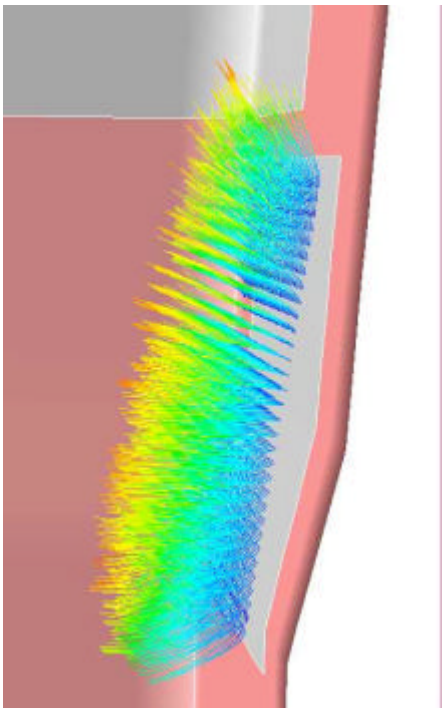

(b)

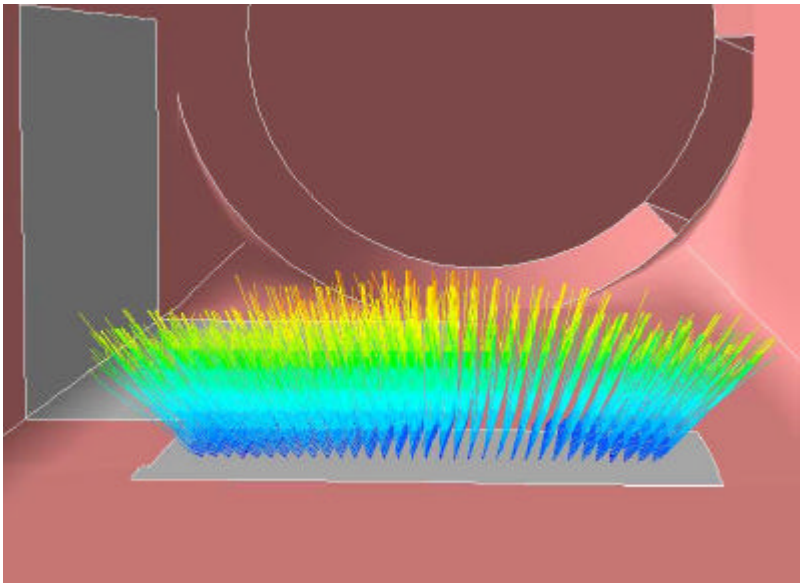

Fig. 5-1 Showing the dispersion of the raw meal injections at inlet (a) from the side and (b) looking up from the kiln gas inlet. The dispersion of the particles at injection was necessary for stability of the CFD solution, and was considered to realistically represent the way that the raw meal enters the real precalciner.

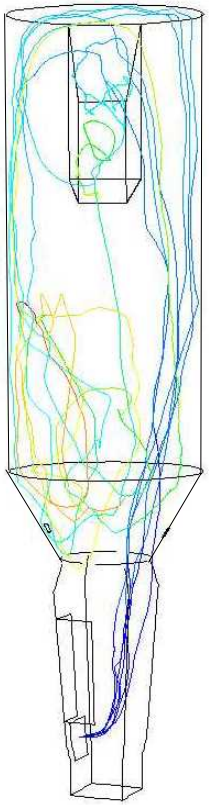

Fig. 5-2 (a) Single Raw Meal particle, showing 6 stochastic attempts.

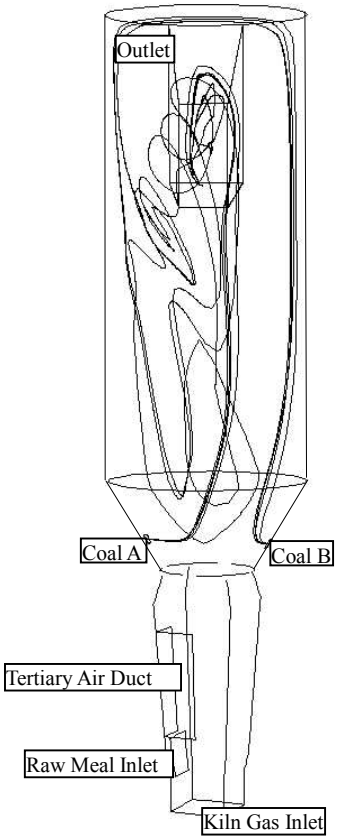

Fig. 5-2 (b) Coal injection from the two inlets, A and B. Mean path only.

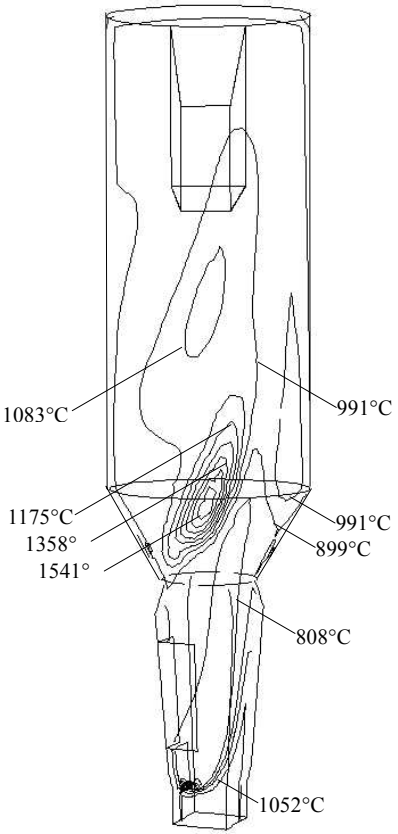

Fig. 5-2 (c) Contours of temperature (°C) showing high temperature core.

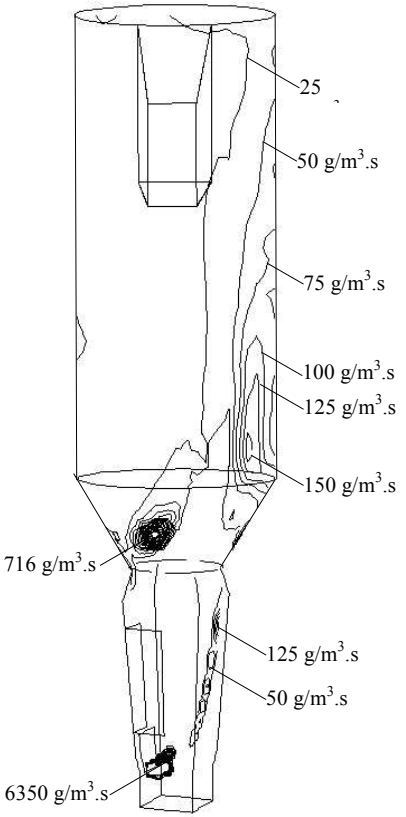

Fig. 5-2 (d) Contours showing release of volatiles (grammes/m^3.sec).

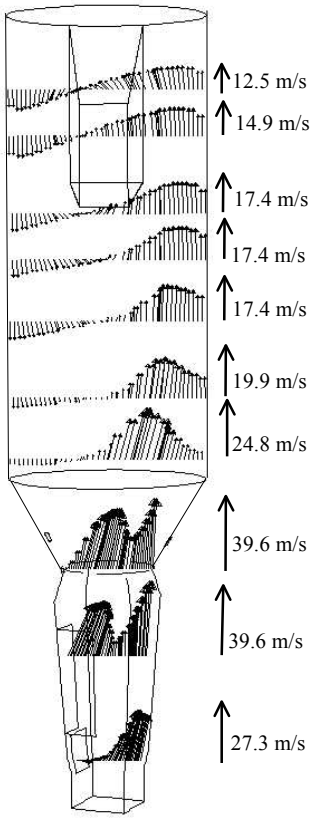

Fig. 5-2 (e) Velcoity vectors on selected lines through the precalciner.

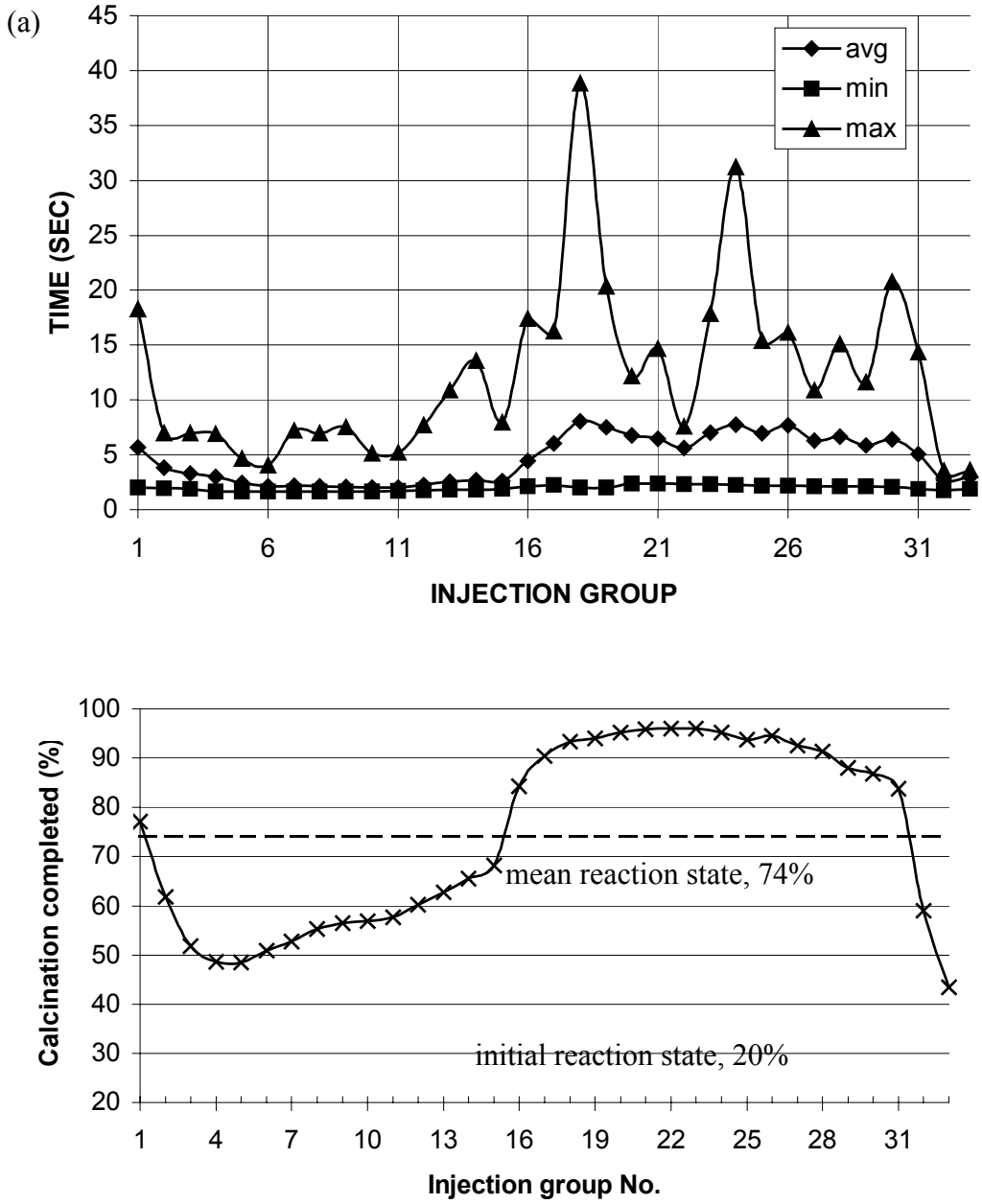

Fig. 5-3 Behaviour of the raw meal in the precalciner vessel between injection at the raw meal inlet and exit from the main cylindrical section into the exit duct. Residence time is presented in (a) and the degree of reaction achieved by exit in (b). There are 33 injection groups across the width of the raw meal inlet each with 32 injection streams in vertical lines. Group 1 is furthest from the centreline of the TAD and Group 33 is closest as illustrated in Fig. 5-5 and Fig. 5-6. Residence times were analysed over each group to show the minimum, maximum and mean value of the group. Inspection of graph (b) gives an approximate mean reaction completion of 70%.

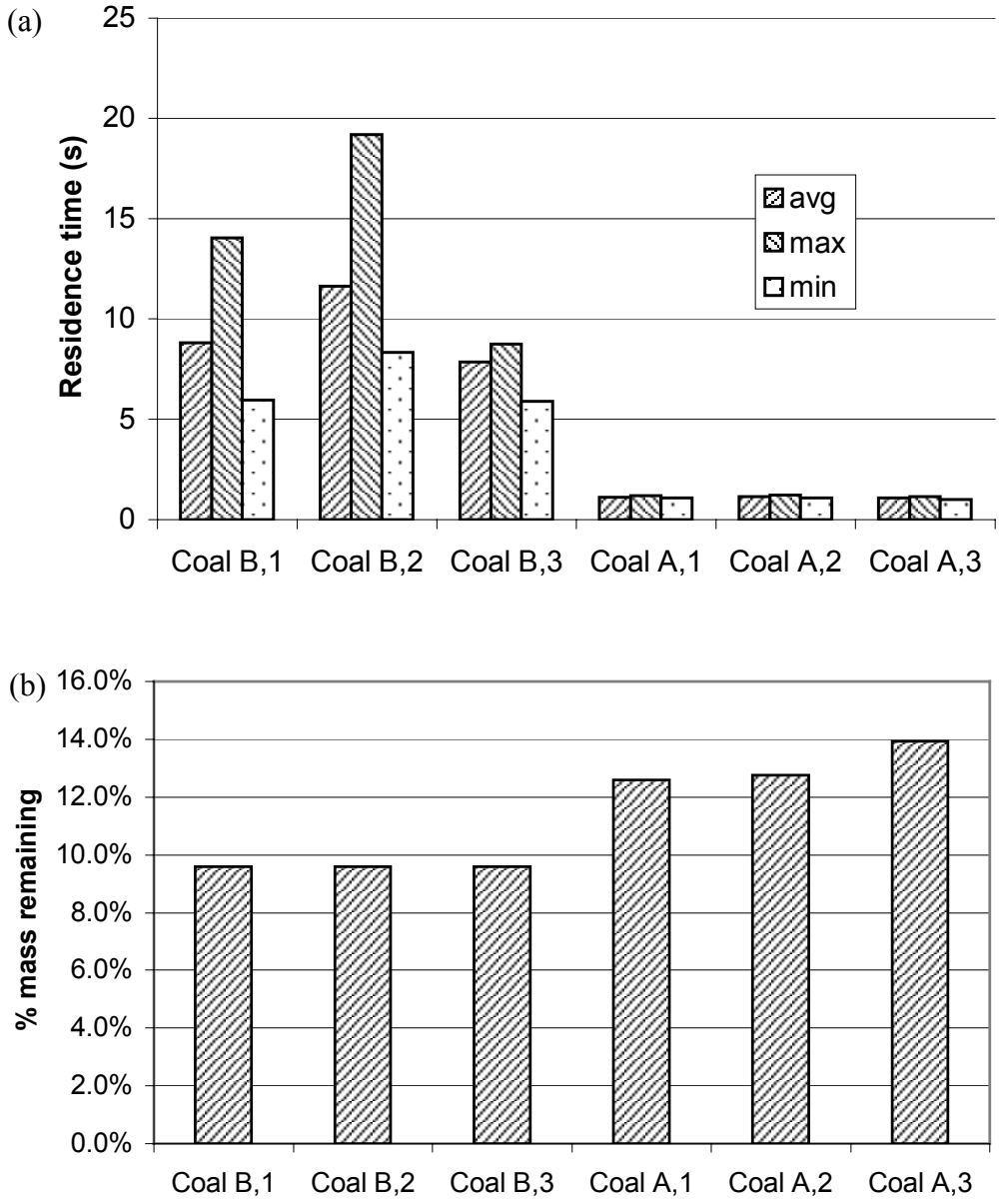

Fig. 5-4 Coal behaviour in the CFD model. Coal B is on the side opposite the tertiary air inlet and Coal A is directly opposite Coal B. Each coal injection group had four injections and graph (a) indicates the average, maximum and minimum time spent in the precalciner for each group. The shorter residence times indicated for groups in Coal A inlet are reflected in the residual mass at exit. The coal has not finished reacting until only the ash content, 7%, remains.

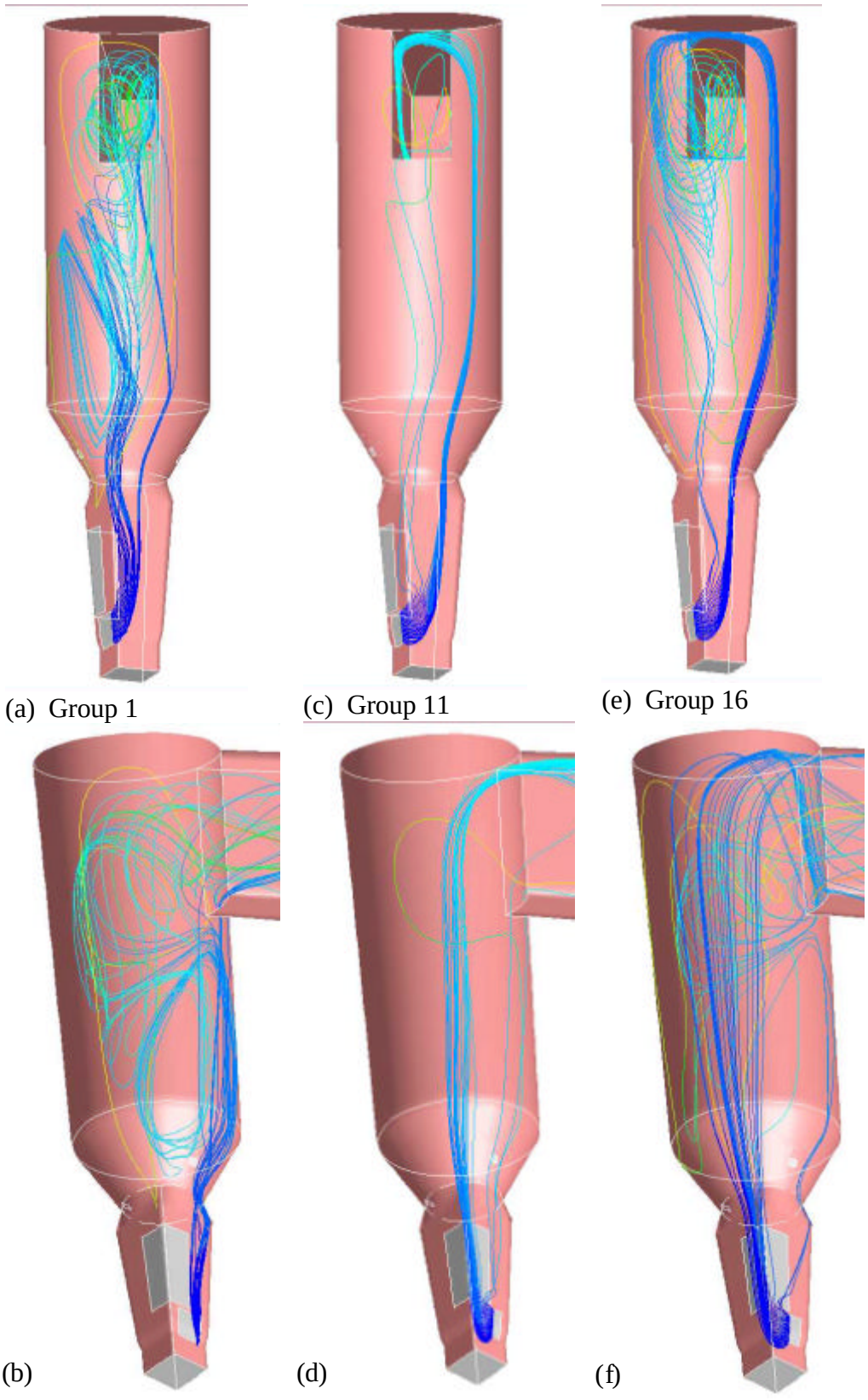

Fig. 5-5 Raw meal trajectories of groups released on the side of the inlet furthest from the tertiary air inlet centre line viewed from two directions. (a) and (b) show Group 1, (c) and (d) show Group 11, (e) and (f) show Group 16.

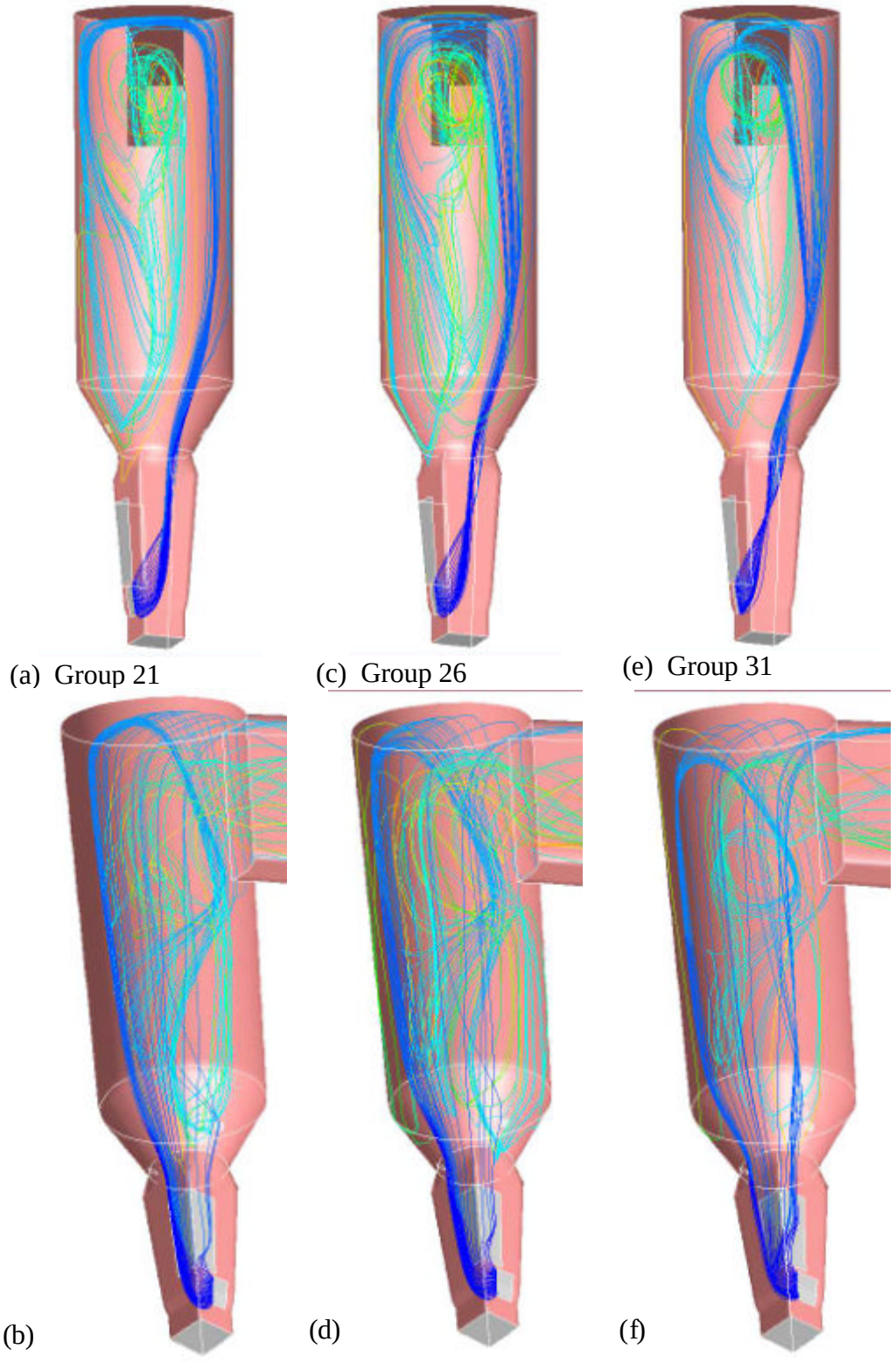

Fig. 5-6 Raw meal trajectories of groups released on the side of the inlet furthest from the tertiary air inlet centre line viewed from two directions. (a) and (b) show Group 21, (c) and (d) show Group 26, (e) and (f) show Group 31.

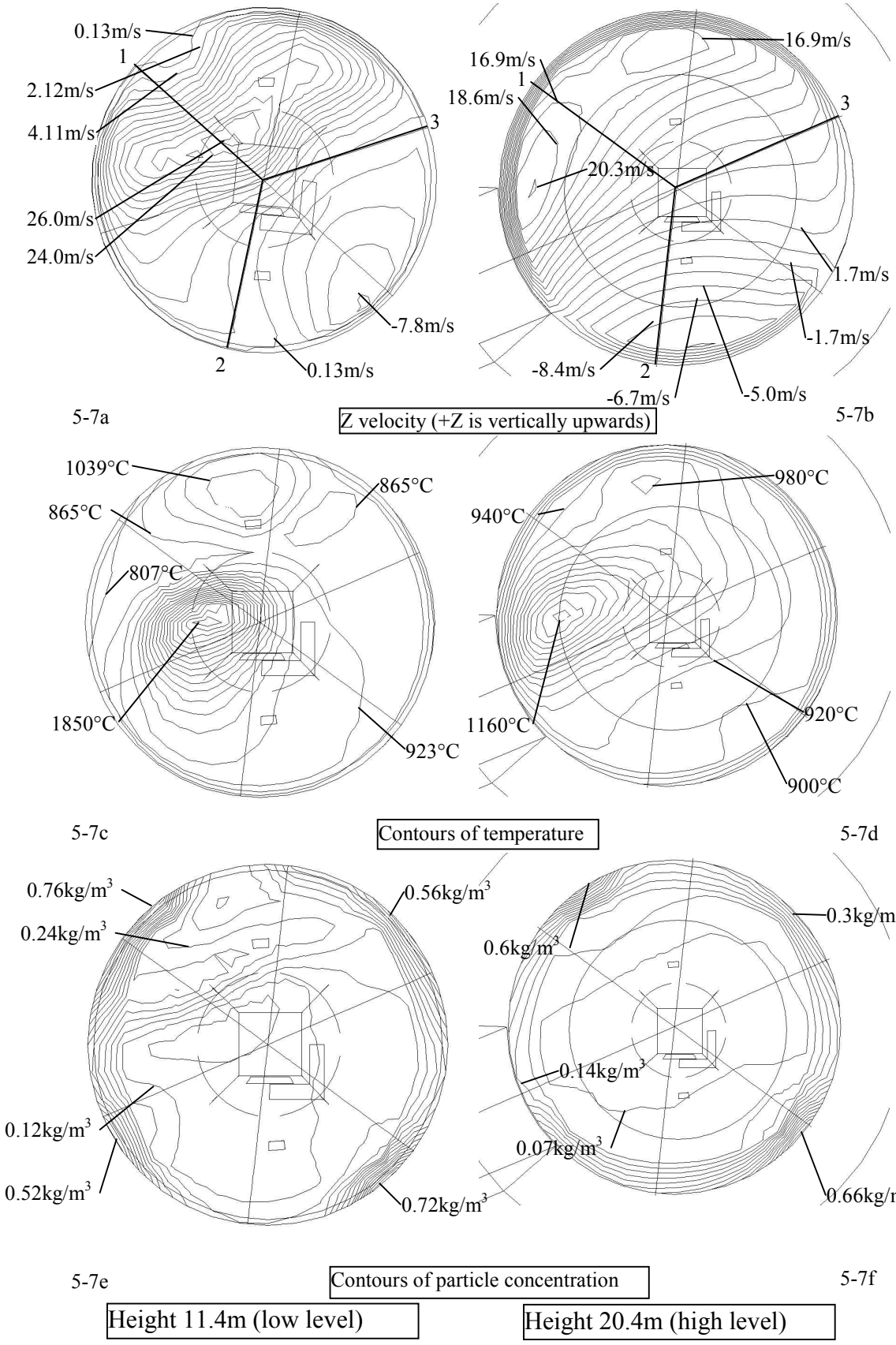

Fig. 5-7 CFD predictions at high (20.4m) and low (11.4m) measurement positions on the precalciner.

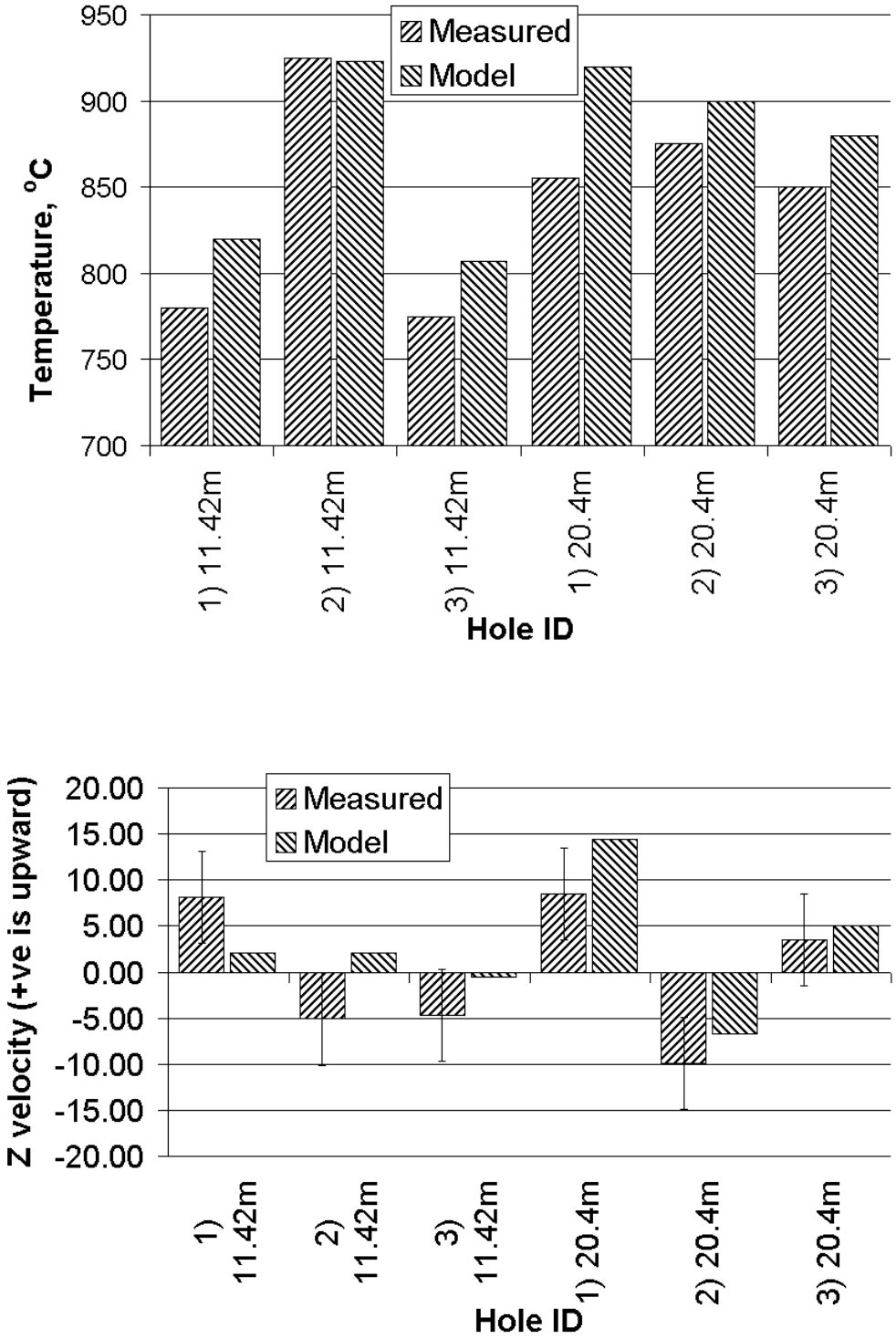

Fig. 5-8 Comparison of site measurements and CFD results for (a) temperature and (b) velocity with error bars applied to the velocity measurements. Measurements were made approximately 30cm into the flow from the inside surface of the precalciner wall at the hole positions indicated in Fig. 4-2.

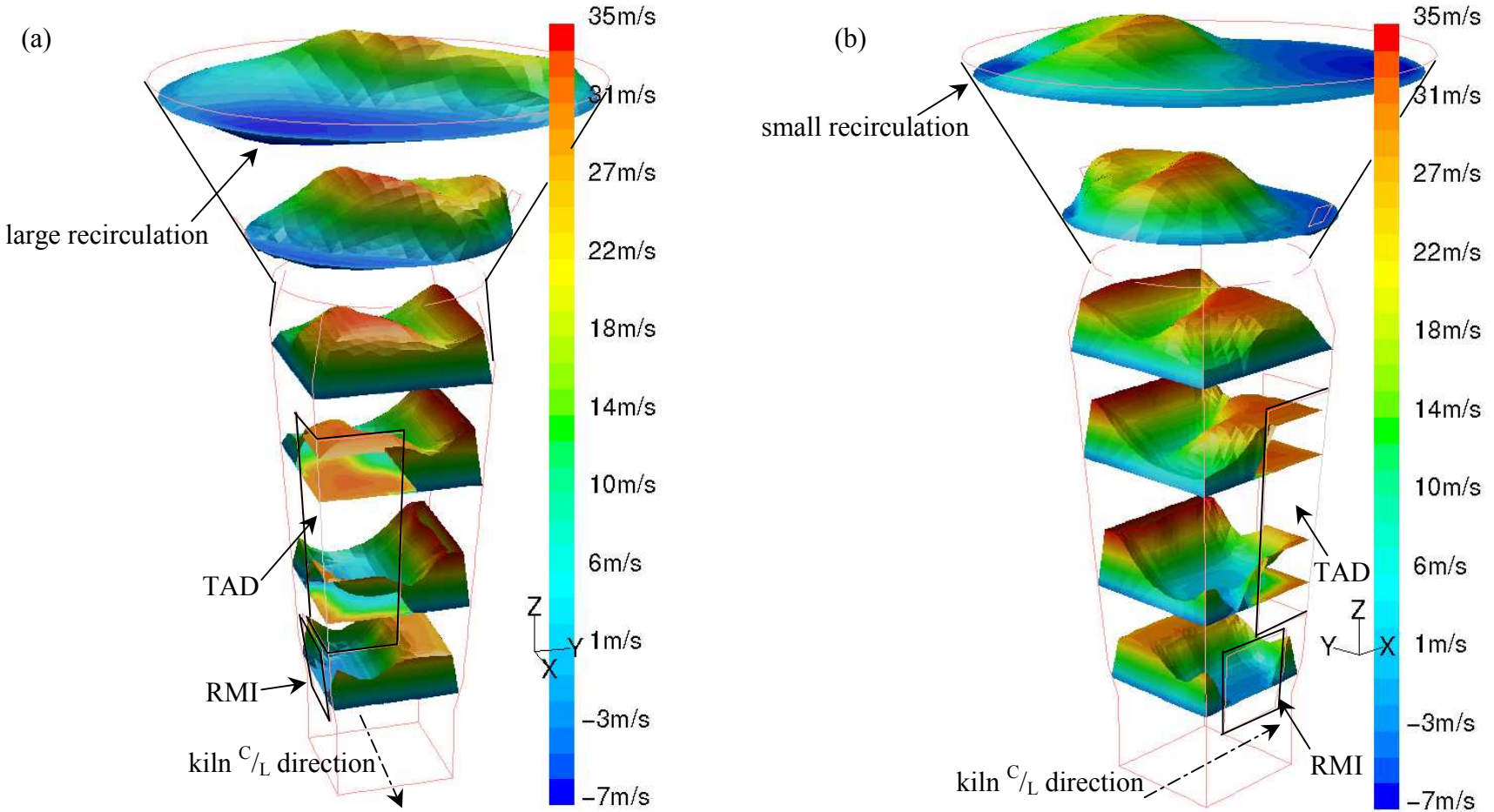

Fig. 5-9 Views of profiles of vertical velocity on several horizontal planes in the riser section (a) looking from the kiln centreline and (b) looking toward the kiln centreline.

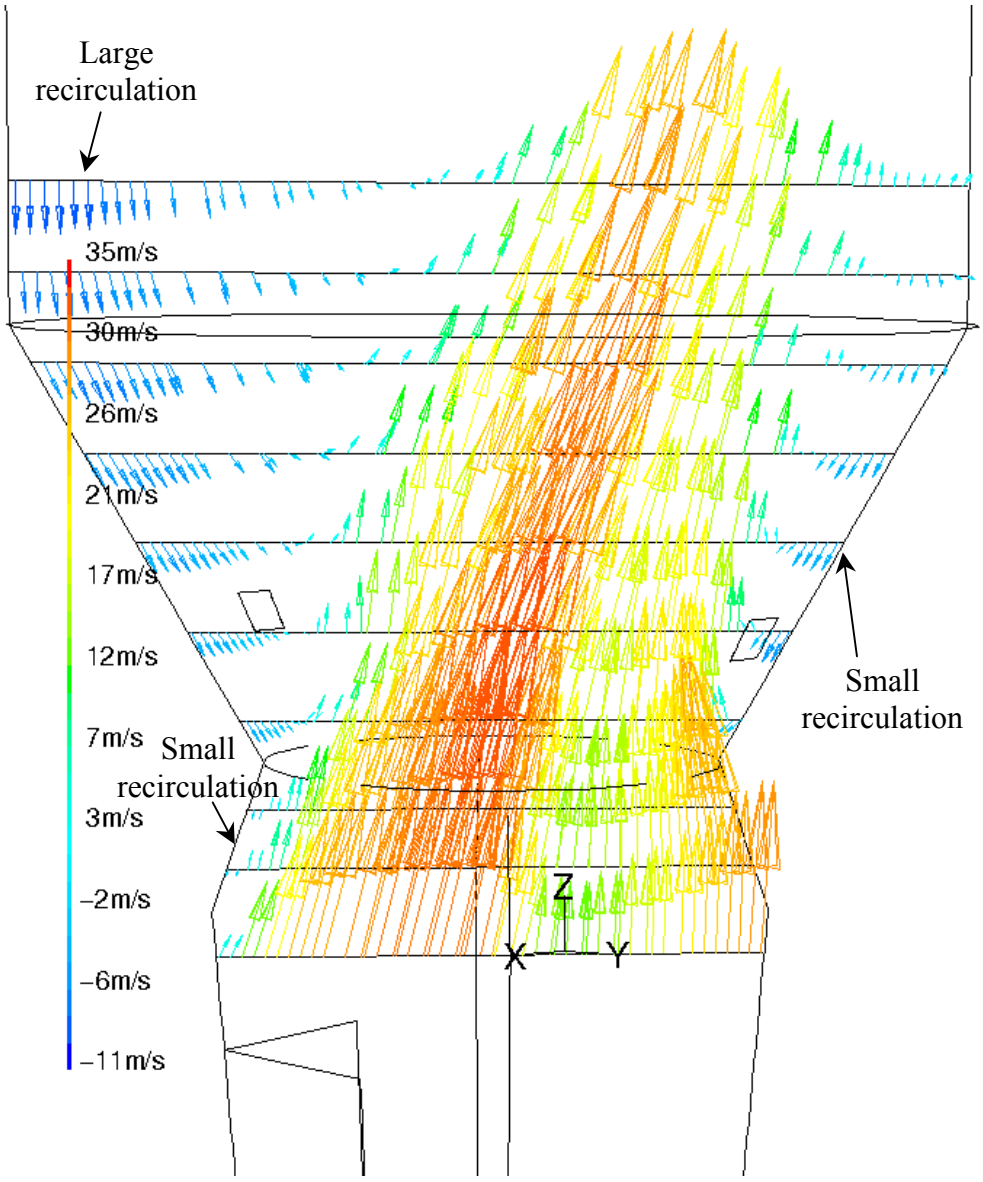

Fig. 5-10 Velocity vectors on several lines in the plane through the centre of the tertiary air inlet. Obvious large and small recirculation zones are apparent on the same side as and on the opposite to the tertiary air inlet.

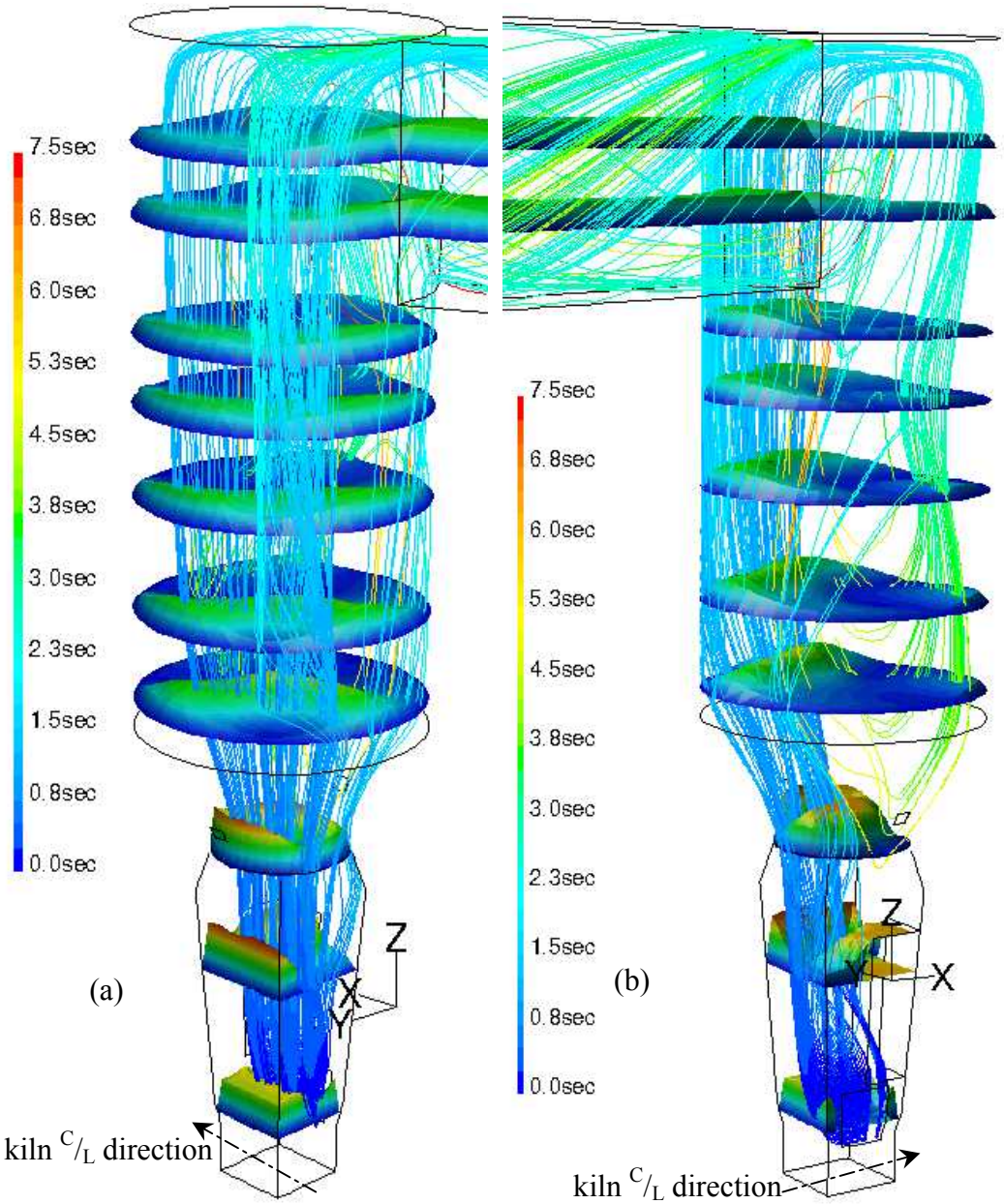

Fig. 5-11 Raw meal particle trajectories superimposed on velocity profiles on horizontal planes up the height of the precalciner. View (a) is looking toward the TAD, which is on the opposite side from the viewpoint and view (b) is looking toward the raw meal inlet with the RMI on the closest right hand side.

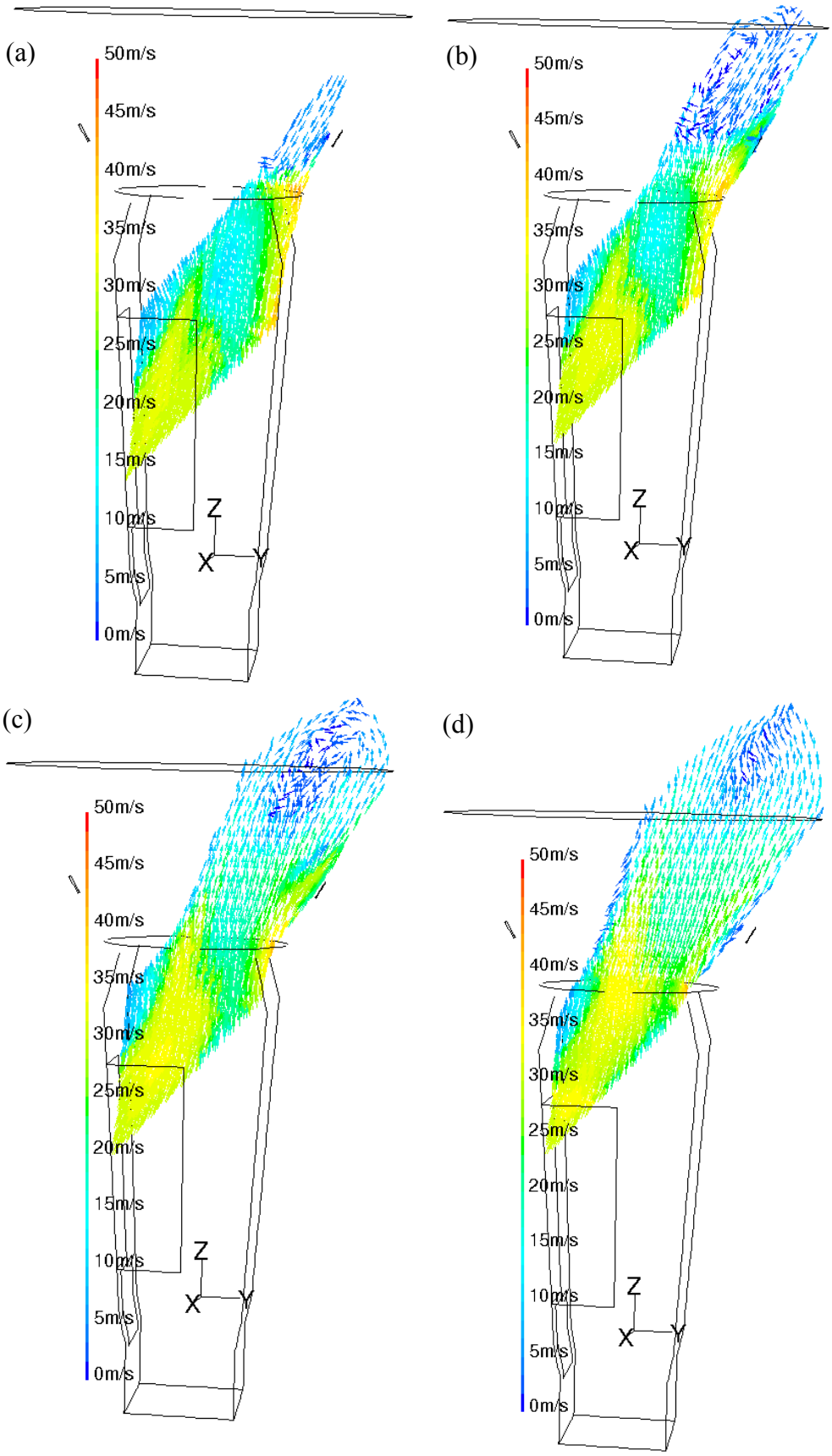

Fig. 5-12 Isometric views of velocity vectors on four planes inclined at the same angle as the tertiary air duct and progressively higher in the duct from (a) to (d). The 3-D nature of the small recirculation of Fig. 5-10 can be seen.

6 Sensitivity analysis

It is important in establishing the validity of the results presented by the model to ensure that the conditions imposed at the boundary conditions are realistic and that the mesh that has been used is sufficiently refined. For this case several sensitivity cases were constructed to test the modelling conditions and to establish the reliability of the data from the initial model.

Sec. 6-1. The mesh was refined and grid independence of the solution presented in Chapter 5 was established from the data obtained.

Sec. 6-2. The effect of radiant heat transfer was considered to assess the effect of the particle scattering and gas absorption.

Sec. 6-3. Carbon dioxide yielded from the raw meal was identified separately from that of combustion products to inspect where the raw meal reactions were taking place more closely.

Sec. 6-4. Coal was injected entirely at the inlet opposite the tertiary air duct to test the hypothesis that the core temperature of the flame would be reduced.

Sec. 6-5. The sensitivity of the solution to the manner of raw meal injection was checked by injecting all raw meal at the kiln gas inlet with a velocity equivalent to the gas rising from the inlet.

Sec. 6-6. The coal injection angle was changed to more accurately represent the real precalciner.

Sec. 6-7. Modifications were made to the shape of the vessel to more closely represent the shape and to accommodate new developments in the real precalciner.

Sec. 6-8. An entirely new geometry was developed using new mesh generation software. This model more accurately represented the shape of the real precalciner vessel.

The conclusion of the sensitivity analysis is that the first model showed all the important features of the fluid dynamics, the particle trajectories and the reactions inside the precalciner when operating with coal only.

Notation for Chapter 6

$D_{i',m}$ diffusion coefficient for oxidant in the bulk (m^2/sec)

D_p particle diameter (m)

h_i specific enthalpy of species *i* at final temperature (J kg^{-1} K^{-1})

h_{i0} specific enthalpy of species *i* at 25°C (J kg^{-1} K^{-1})

Δh_0 specific enthalpy of combustion at 25°C (J kg^{-1})

$\dot{m}_f$ mass rate of fuel (kg s^{-1})

$\dot{m}_i$ mass rate of species *i* (kg s^{-1})

m_O local mass fraction of oxidant in the gas

m_p particle mass (kg)

N number of particles per unit volume (m^{-3})

p gas pressure (Pa)

$\dot{Q}$ heat input from complete coal combustion (W)

R specific gas constant (J kg^{-1} K^{-1})

S_b stoichiometry of the char reaction equation.

t time (s)

T gas temperature (K)

T_p particle temperature (K)

$T_¥$ free stream temperature (K)

r_g gas density (kg/m^3)

r_p particle density (kg m^{-3})

m fluid viscosity (kg m^{-1} s^{-1})

6.1 Features of a refined mesh on the same geometry

An important feature of good CFD modelling is that grid independence of the solution is established. If the mesh is refined (i.e. the cells are made smaller so there are more of them), then the behaviour observed by the post processing should not change if the solution is grid-independent.

To establish grid-independence for the precalciner vessel model, a finer mesh was developed as seen in Fig. 6-1 compared with the initial mesh in Fig. 3-1. Cells in the main section of the precalciner only were refined and the total number of cells in the refined model was then 138,717, compared with

previously 48,000. Mesh refinement was not performed in the exit duct, since it has no important flow features. Refinement was also not performed in the lower section, since the mesh there was already relatively densely packed compared to the cylindrical section.

Results were compared with the original model. The Fig. 5-2a-e illustrated the significant features of the flow in the original model. Similarly comparison of these features with the refined mesh model is presented in Fig. 6-2a-e. Two further comparisons were made considering the gas composition and the raw meal and coal characteristics at the exit from the precalciner cylindrical section.

Inspection of the Fig. 6-2e shows the effect of increasing the number of volume cells in the main body of the precalciner. The velocity vectors in the model with refined mesh are denser than on the unrefined mesh. Referring to Fig. 5-2e, the features of the velocity field have been preserved between the two models. The same maximum velocity is evident within 1 m/s and the recirculation noted in the previous section is still very obvious. The maximum upward components of velocity on the ten lines from each figure are presented in Fig. 6-3 for comparison and significant differences in the maximum velocity on some lines can be seen. Line 1 is the lowest line on Fig. 5-2e and Fig. 6-2e and 10 is the highest. From the figures there is a slight difference in the pattern of velocity vectors on the lower three lines. The larger vectors are concentrated in to a smaller area on the original model. An obvious conclusion from this is that “grid independence has not been proved”. However, using a second-order “upwind” discretization scheme suggests that since the mesh refinement is downstream of the conical section, another cause might be responsible. Another plausible cause is the instability of the raw meal particle tracks in the lower region as illustrated by comparing the original model in the Fig. 5-5 and 5-6 to the refined model in Fig. 6-6 and 6-7. Inspection of the early part of the raw meal trajectories shows significant differences. In particular, group 16 (Fig. 5-5e,f and Fig. 6-6e,f) is more spread out across the width of the riser duct in the original model than in the refined mesh model. This represents the raw meal that arrives in the riser duct across the centre-plane, so it is reasonable to assume that this behaviour is the cause of the velocity vector differences across the central plane of Fig. 5-2e and 6-2e.

The other flow variables in the model indicate that grid independence has in fact been established since the differences from the original model are not significant.

Comparing the temperature field, Fig. 5-2c and 6-2c, shows that the pattern of the temperature field is similar and that the maximum temperatures differ by only 73°C.

Fig. 5-2a,b and 6-2a,b show that general pattern of raw meal and coal trajectories are similar. The overall behaviour of the coal and raw meal is best compared by the summary of all particles' characteristics at the plane where the cylindrical section meets the outlet duct. These data are presented in Fig. 5-3 and 5-4 and Fig. 6-4 and 6-5. Referring to figures 5-3b and 6-4b, the raw meal reaction state at this point is similar for each model. Groups 15 to 32 show more reaction due to longer residence times, which are evident from figures 5-3a and 6-4a. Coal behaviour is apparently identical in figures 5-4a and 6-5a, showing that coal released from the side opposite the tertiary air duct has a short residence time of 2 seconds compared to between 5 and 18 seconds for coal released from the other side. The corresponding level of reaction is indicated by the mass remaining, 7% being the ash content.

Figure 5-2d and Fig. 6-2d illustrate the raw meal reaction. The release rate of volatile components is very concentrated on the right hand side of the figures, showing the same characteristic in each model. The overall level of reaction in the original model was 74% complete and in the refined model it was 71% complete. This means that 11.0 kg/s of carbon dioxide is released in the original model and only 10.5 kg/s in the refined model.

Useful data is available from the gas composition at the exit from the cylindrical section as presented in Table 5-4. Comparing the gas composition at the same plane, Table 6-1 shows little difference between the two models. The CO_2 content of the models appears to not balance but the difference is accountable by the stochastic attempts. A summary of the mass with all stochastic attempts shows that the raw meal yields 10.797 kg/s in the original model.

In conclusion, the observed differences between the models appear to be due to the raw meal being driven upwards against gravity. Since the changes

occurred in the unrefined section of the mesh, "upstream" of the refined section, these results suggest that the original mesh was sufficiently refined to illustrate the flow features and that the variation between the two models was due to changes in the raw meal particle flow patterns.

Gas component	Refined model rate (kg/s)	Mass flow rate at exit (kg/s)
carbon dioxide, CO_2	8.573	19.550
raw meal CO_2	9.540	
total CO_2	**18.113**	**19.550**
oxygen, O_2	2.803	2.945
lv-vol, $C_{0.625}H_{4.8}O_{0.48}$	0.000	0.000
carbon monoxide, CO	0.012	0.023
water vapour, H_2O	0.693	0.805
nitrogen, N_2	38.799	38.482
Total	**60.420**	**61.805**

Table 6-1 Gas composition comparison at exit plane.

6.2 Features of radiant heat transfer effects

Radiation heat transfer in the precalciner is affected by the high concentration of particles. Looking into the precalciner through view-ports reveals a short distance before the limit of vision is reached. This is because the particle suspension is optically thick. This is a term from radiative heat transfer theory described in Chapter 2. The mass ratio of solid to gas is 1.2:1, and the density of the particle material is approximately 2880 kg/m^3. The depth of vision can be estimated by considering the average volume of gas occupied per particle. Consider the side of a cube of this volume and find how many particles arranged side by side would fill the area and assume that each of those particles is stacked to make the depth of vision. The calculation is done as follows:

- mean gas density is from the perfect gas law (assuming air only),

$$r_g = \frac{p}{RT} = \frac{10^5}{287 \times 1173} = 0.297 kg/m^3,$$

- the concentration of particles is 1.2×0.3=0.36 kg/m^3.
- the mean diameter of the particles, 55μm,

- the mass of the particle is

$$\frac{pD_p^3}{6} r_p = \frac{p \times (55\times10^{-6})^3}{6} \times 2880 = 2.51\times10^{-10} kg$$

- the number of particles per m^3 is, $N = \frac{0.36}{2.51\times10^{-10}} = 1.434\times10^9$.
- the volume of gas per particle is $1/N = 697\times10^{-12}$ m^3.
- a cube of this volume has side 0.9 mm
- dividing the area of the cube face by the projected area of the particle gives an indication of the number of particles to obscure vision, $(0.9\times10^{-3})^2\times4/(55\times10^{-6})^2\times\pi = 340$
- the depth of vision is therefore 340×0.9mm = 30 cm.

This was considered to be an over-estimate due to the turbulent flow. Absorption coefficient values were changed in the model to alter the radiant heat transfer equation in Chapter 3, section 3.4.4 in the form of reciprocal-mean penetration distances, to see the effect on the temperature field. The mean penetration distance was assumed to be between 10 and 25 cm, which is the perceivable distance by looking into the vessel and is of similar magnitude to the values suggested by the above calculation and in section 2.8. Results were taken from the 10-cm case.

The temperature field is illustrated in Fig. 6-8a-c and compared with the original model in Fig. 6-8d-e. Temperature has been reduced in the hottest zone at the core of the flame from 1909°C to 1561°C – a reduction of 348°C. The cases with longer penetration distance caused further reduction in the core temperature. The effect of the absorption coefficient is then to hinder heat transfer from the central hot core of the flame towards the walls, but to increase the effective heat transfer between gases and particles. This is not surprising, since radiative heat transfer between the gases and the particles is essential for effective reactor operation. It is apparent that the radiative heat transfer reduces the core temperature and so must be modelled in order to predict the reactor temperature. The temperature at the core of the model with radiation heat transfer was just lower than that required for thermal NO_x production, whereas the previous model showed temperatures suitable for NO_x production.

6.3 Named carbon dioxide issuing from the raw meal

This technique was adopted following the inspection of the original model results, which had a limitation in the effectiveness to show where and how much the raw meal CO_2 was being released. Fluent was able to calculate a second CO_2 species as a distinct gas. It differed from the combustion products CO_2 in name only, being called raw-meal-CO_2.

Figures 6-9a-e illustrate the behaviour of carbon dioxide in the two models and the difference between the combustion CO_2 and raw meal CO_2. Figure 6-9a is from the original model showing CO_2 mass fraction in contours on the centre plane looking in to the outlet duct. The region of high gradient toward the right hand side suggests that this is where most raw meal CO_2 is released. Figures 6-9b and 6-9c show the effect of separating the CO_2 from raw meal and combustion and the behaviour suggested by the first model is confirmed. Comparing the sum of the raw meal and combustion CO_2 from the new model to the CO_2 in the original shows that the total CO_2 content is unchanged. Iso-surfaces of the raw meal CO_2 are presented in Fig. 6-9d and 6-9e. Fig. 6-9e shows that the raw meal CO_2 is not directly opposite the tertiary air duct but is displaced to the left. This is due to the asymmetry of the raw meal injection relative to the tertiary air inlet, which caused significant effects in the velocity field as seen in Chapter 5, section 5.2.5.

6.4 Features of modelling all coal at one inlet

The behaviour of the raw meal reaction illustrated in the original model showed significant differences between the behaviour of coal injected at the two inlets. It suggested that the coal injected on the side opposite the tertiary air inlet was responsible for supporting the majority of the raw meal reaction. The coal on the tertiary air inlet side did not recirculate and so had a shorter residence time in the order of 2 seconds. This caused a hot core region with temperatures up to 1900°C in a nitrogen rich environment, which are suitable conditions for thermal NO_x production. The entire injection of coal in the model was therefore injected from the coal inlet on the side opposite the tertiary air inlet to see what effect this would have.

The most significant result of this model was to reduce the core temperature. Inspection of the coal condition at outlet showed that the coal

consisted of ash only (i.e. it had completed reacting). Inspection of the results indicates the reason for this behaviour. Looking at Fig. 6-10, the contours of oxygen mass fraction in the precalciner are presented at several heights with trajectories of coal released from the inlet opposite the tertiary air inlet for the original model (6-10a) and the one-coal model (6-10b). The coal rises through a low oxygen region from the inlet as volatiles are released and oxidised. It then passes over the roof and down the other side. The contours show a significant difference in the oxygen concentration on the coal downside. Since the contours in 6-10b show higher oxygen content, it can be seen that the coal oxidises more efficiently in this case than in the original. The CFD code models the oxygen consumption of the combusting-particle-char oxidation equation. The rate of char oxidation depends on the oxygen concentration in the surrounding fluid:

$$\frac{dm_p}{dt} = -4pD_pD_{i',m}\frac{m_O T_p r_g}{S_b(T_p + T_\infty)} \qquad \textbf{Equation 6-1}$$

In addition to this evidence of changed behaviour in the model, the average level of calcination of the raw meal at exit is found to be 78%, which is an improvement over the original model (74%). Fig. 6-11a-e presents the temperature distribution, volatile release pattern and velocity vectors in this model. The temperature (Fig. 6-11 a,b,c) shows a much reduced core temperature of 1150°C. The iso-surfaces (a and b) show that the hottest part of the flame is the in the region of maximum raw meal reaction seen in Fig. 6-11 (d). The volatile release shows that the raw meal reacts more consistently on the right hand side of the figure, i.e. on the side opposite the tertiary air inlet. The velocity vectors in Fig. 6-11 (e) show the same features as the original model showing that the flow configuration has not changed.

6.5 Raw meal injection at the kiln gas inlet

Since estimation and best guess determined the pattern of the raw meal injection, it is unclear whether the solution was then sensitive to the choice within reasonable limits. An alternative injection strategy was therefore developed which was significantly different from the initial injection, but still considered to be realistic. The alternative injection was vertically upward and

uniformly distributed over the base of the precalciner, i.e. from the kiln gas inlet, with velocity the same as the kiln gases. This was significantly different since the initial trajectory of the entire injection was uniform across the inlet so that there was no initial downward velocity and there was no initial spread of particles. The particle size for all injections in this case was 55μm.

Figures 6-12a-d show the vertical velocity on profiles. Figures 6-12a and 6-12b compared with Fig. 5-9a and 5-9b show that the large vertical momentum change in the inlet region by the raw meal inlet has been significantly reduced. This shows two things – that accelerating the raw meal at its injection point involves heavy momentum exchange with the gases entering at the kiln gas inlet, and that the gas injection at the raw meal inlet has an un-important role in the flow features of the precalciner. Figures 6-12c and 6-12d compared with Fig. 5-11a and Fig. 5-11b show that the flow in the cylindrical section of the precalciner is not significantly affected by the change in raw meal injection. This is confirmed by the residence time of the raw meal particles at the exit from the cylindrical section into the exit duct, which is 1.8 sec to 16.8 sec with mean value of 5.0 sec. This is similar to the original model (Fig. 5-3a). The level of calcination in this model is 78.7% at the exit from the cylindrical section compared to 74% in the original model. The difference is accountable by the more uniform interaction with the gases at 1100°C entering from the KGI.

6.6 Alteration of the coal inlet angle

This sensitivity analysis was done following new information about the coal inlets. In the previous models they were modelled as horizontal injections. The real precalciner coal inlets are angled downwards at 30° to the horizontal. This can be seen in the photograph in Fig. 6-13 showing the coal inlet that is on the same side as the tertiary air inlet and the raw meal inlet.

The changes caused by this modification of the physical shape of the precalciner were small. Figures 6-14a-f show the velocity vectors on the vertical plane intersecting both coal inlets and near to the wall of the precalciner in the conical section. Figure 6-14a shows the positions of the coal inlets. Figure 6-14b shows the typical trajectories of coal particles released at the two inlets. Little change can be seen compared with Fig. 6-2b, although it

is clear that there is an initial downward trajectory on both sides. Figure 6-15 shows the graphs of residence time and mass remaining at exit. There is an apparent anomaly in the behaviour of coal injection "Coal B,1", which being released from the same side as the raw meal inlet, should take a short while only to exit. The residence time of this injection stream can reach the same time as coal injected from the opposite side. This effect is due to the alteration of the injection angle. Inspection of the Fig. 6-14b shows that the particles do have a small recirculation in the middle of the cylindrical section, which did not previously occur. This suggests that the inclination of the coal inlet on that side encourages better mixing of the coal with the gases and that the combustion is more complete prior to exit.

Figures 6-14c and 6-14d show the velocity vectors in the original model and 6-14e and 6-14f show the same for the model with the changed injection angle. The differences between the velocity vectors can be seen. Firstly referring to Fig. 6-14c and 6-14e, the inlet is on the same side as the downward recirculation seen in Fig. 6-2f. Figure 6-14e shows that the initial trajectory has been altered, but that the effect is soon dissipated in the large-scale flow of the precalciner. On the other side (Fig. 6-14d and 6-14f) a similar small change can be seen. In this case the model with the injection inclined at 30° downwards directly opposes the fast stream of hot gases rising from the kiln so that the fast jet penetrates less distance towards the core of the precalciner.

Coal particles have a very short response time to the gases rising at the neck of the precalciner (i.e. the section at the base of the cone). Using equation 2-12 for calculation of the momentum response time:

$$\frac{r_p D_p^2}{18m} = \frac{2880 \times \left(55 \times 10^{-6}\right)^2}{18 \times 4.5 \times 10^{-5}} = 0.011 \sec$$

which is the time taken for the particle to attain 63% of the free stream velocity. Figure 6-14b bears out the evidence of the calculation since the particle trajectories at the new angle show only a small initial downward velocity before following very nearly the same trajectory as the original model.

6.7 Addition of an accelerator at the throat section

To keep up with the changes made at the plant an "accelerator" was inserted into the original model. Restricting the area at the throat section at the base of

the cone formed a section that accelerated the gas. The change to the geometry is illustrated in Fig. 3-3. The purpose was to reduce the amount of tyre chips falling into the tertiary air duct and so prolong the time between maintenance shutdowns due to TAD blockage. There were 47,358 cells in this model. In addition to the change in the throat section, a modification was made to the outlet duct height to change it from 5m to 3.5m. This restriction was made in order to adhere to the true shape of the precalciner. The previous dimension had been used due to error in interpretation of an unclear drawing to which no clearer drawing was found until the final year of the project. This causes a reduction in the outlet area of approximately 30%. That means the original outlet was 43% too big, which means the outlet velocity will be 43% too small. Despite the apparently worrying magnitude of this error, it should be remembered that the key features of the flow are determined inside the cylindrical section and in the lower section. Whether the increased velocity at the outlet causes significant change to the flow pattern and particle residence times in the precalciner was assessed and no significant changes were observed.

Referring to Fig. 6-16 and 6-17, the particle residence times and level of reaction by the time they exit from the cylindrical section is presented in graphs for coal and raw meal. Comparing these figures with Fig. 5-3 and 5-4, it is clear that there is significant change. The coal has hardly reacted compared to the previous model and this appears to be caused by the reduced residence time. The maximum temperature in the model is 1140°C. The response of the raw meal to this is that the reaction by exit is significantly reduced, on average it is only about 40% reacted compared to 74% for the original model. The pattern of the residence times is similar to Fig. 5-3a except that the behaviour is emphasised in the accelerator model such that groups 1-14 have slightly shorter residence and 15-33 slightly longer. The reasons for this behaviour can be deduced from the flow field. Figures 6-18 show the velocity profiles in the vertical direction and sample coal and raw meal trajectories. In the cylindrical section, the accelerator has induced a high-speed jet up to 60 m/s. This induces the strong recirculation zone. Due to the location of the coal inlets, the coal trajectories are similar to the original model, but travelling

faster, they exit more quickly. In the case of the raw meal, the sample trajectory is from injection group 15, and this shows the borderline condition between long and short residence times of the raw meal. The injections 1-14 tend to follow the same trajectory as the particles that exit when they reach the top of the precalciner. Injections 16-33 tend to follow a recirculation path above the accelerator.

The effect of the constriction in the exit duct cannot be eliminated as a cause of the low reaction levels within the vessel in this case, but the evidence is that the intensification of the recirculation zone in the cylindrical section results from the accelerator.

When tyre chips were modelled on this grid, the results show much improvement in the reaction by exit. That model is addressed in Chapter 7.

6.8 Complete geometry and mesh redevelopment

A newer version of the software became available during the course of the project, which made development of a realistically shaped model of the precalciner possible. This new model included:

- correct connection of the tertiary air inlet to the precalciner
- correct representation of the coal inlet pipe size
- addition of a raw meal "splash box"

The coal pipes were directed horizontally, since the correct coal inlet angle had not been recognised by this stage. The mesh structure was changed to entirely tetrahedral. It was constructed from three key sections – the coal inlets, the central core and the remainder. The model had 191,000 cells. Figure 3-2 shows the new geometry and mesh structure.

Some difficulties were encountered during the solution of this case due to high field variable gradients of temperature and velocity, and the heavy particle loading, which had been a problem in the original model. The problems were not entirely eliminated, and a satisfactory solution was obtained for a reduced flow rate of the raw meal of 60% of the full load. Without entirely changing the mesh, further improvement to the model was not thought to be possible. Since mesh development is time consuming, the model was not developed further.

The results from the successfully solved case on the new mesh showed some interesting features not highlighted in the original model. Coal trajectories (Fig. 6-19a) were observed to be drawn downward on the tertiary air inlet side of the model in to a recirculation zone at the neck and the hot flame core was drawn in to the same flow feature (Fig. 6-19b, c and d). The temperature range is higher due to the missing 40% of the raw meal, which would draw energy from the flame.

6.9 Consideration of the raw meal calcination at exit

The foregoing analysis showed incomplete calcination of the raw meal. At the immediate conclusion of the work, the reason for this was thought to be due to the rapid exit of some portion of the raw meal. Subsequent analysis has found a far more likely explanation for this. Scrutiny of the energy balance of the precalciner with 100% raw meal loading shows insufficient supply of coal to meet energy consumption. Briefly, the energy balance is presented in Table 6-2.

Energy source	**Heating value MW**
Energy for calcination	-59.652
Coal gas heating	-0.478
Raw meal gas heating	-0.334
Kiln gas heating	3.207
Tertiary air heating	0
Raw meal heating	-8.192
Energy to walls	-0.595
Energy from coal	62.537
Sum of energy	-3.507

Table 6-2 Energy production and consumption in the precalciner.

Calcination energy was calculated from the data in section 4.4, using the energy required per kg of CO_2 released. Gas-stream heating requirements were calculated from inlet mass flow rate, the difference between inlet and outlet temperature, and the specific heat capacity at the inlet temperature for an

approximate answer. The tertiary air was at 900°C at injection and therefore required no heat input to heat to the exit temperature. Raw meal particle heating was calculated similarly using injection mass, heat capacity, and the difference between temperature at inlet and outlet. The energy lost to the walls was calculated using the heat conduction rate determined in Appendix 2 and the surface area of the conducting walls. Coal provided the energy source to support the heat consumed. The heat added by the coal was calculated by equation 6-2. The G.C.V. at 25°C was taken from (Table 4-3).

$$\dot{Q} = \sum_{products} \dot{m}_i (h_i - h_{i0}) - \sum_{reactants} \dot{m}_i (h_i - h_{i0}) + \dot{m}_f \Delta h_0 \qquad \textbf{Equation 6-2}$$

The sum of all the energy produced and consumed, assuming full reaction is –3.507 MW, implying that insufficient coal was injected to support the complete reaction of the raw meal. The expected shortfall in reaction is calculable from the calcination energy: -3.507/-4.017 = 0.873 kg of CO_2. For 100% release, 14.85 kg/s of CO_2 would be produced. The shortage of coal will cause 5.9% reduction in reaction of the raw meal so that the maximum attainable reaction is 94.1% of the injected raw meal, or 95.3% total calcination allowing for the starting 20%.

It is interesting to note that the coal supply calculated from the production record of 1996 in section 4.5 as 2.03 kg/s is 60% of the total 3.4 kg/s delivered to the entire process. The required extra 3.507 MW would be made up by additional coal: 3.507/31=0.11 kg/s (approximately 5% of the supply requirement). The required total of 2.14 kg/s of coal is 63% of the total mass of coal supplied to the process. In practice at the plant, the balance of coal delivery between the precalciner and kiln is flexible. The ‘rule of thumb’ is to use approximately $^2/_3$ of the total coal delivered in the precalciner (as noted in the literature review section 2.1). The actual balance is determined by CO and O_2 concentration at the kiln back end, just below the precalciner. It could be argued that the value of 60% used in the modelling work was conservative, and the argument is supported by the calcination deficiency. Despite the error introduced by this, it is likely that the features of the model illustrated would not be significantly altered.

Alternatively, recalling the excess raw meal injection according to the cyclone spreadsheet balance, the coal would have been sufficient to completely calcine 51.8 kg/s of raw meal.

6.10 Conclusions of the sensitivity analysis

Results of this section showed that the key features of the real precalciner were represented well by the original model. The main characteristics of the flow observed in the first model were repeated in the sensitivity models.

The refined mesh model showed the same characteristics as the first model indicating that the initial sizing of the cells and the cell distribution was suitably chosen. The number of cells was increased from 48,000 to 138,770. Differences in quantities observed between the two models were attributed to the 'instability' of the raw meal trajectories in the lower part of the precalciner. The instability was indicated in the first model, and was the cause of difficulty in obtaining a stable numerical solution. Supporting the raw meal against gravity intuitively provides an unstable situation. The particles are likely to move on the supporting column of fast moving air, which sweeps in to the main body of the precalciner.

Radiative heat transfer affected the temperature field but other variables were unaffected. Including radiative heat transfer with an optical thickness assumed to be 10cm reduced the core temperature in the model by 348°C. Increasing optical thickness reduced the core temperature. The radiative scattering and absorption associated with the particles tended to hinder radiative heat dispersion to the walls. This suggests that modelling without radiative heat transfer gave a reasonable initial indication of the temperature field. The prediction of core temperature using 10cm optical thickness is likely to be more accurate. Measurements to determine the optical thickness using an infrared pyrometer were suggested toward the end of the project. The time available did not permit the work to be done.

The CO_2 release from the raw meal was successfully identified and illustrated separately from combustion CO_2. Most raw meal reaction occurred in the region by the wall opposite the tertiary air duct as suggested by the first model.

Injecting coal in the model from the side opposite the tertiary air inlet only changed the coal combustion characteristics and the oxygen distribution in the precalciner. The effect was to improve the combustion efficiency. Oxygen concentration in the region of the coal that supported most of the raw meal reaction increased, increasing the rate of combustion in that region and thus promoting faster calcination in the vessel. The temperature of the flame was reduced and the core of the flame was not so obvious, since the temperature in the entire cylindrical section was within 200°C. Making changes to the plant to verify this effect was discussed, but the cost of plant modifications to trial the effect was prohibitive.

Injection of the raw meal across the kiln gas inlet in the model showed two important aspects of the injection. The model is not sensitive to the way raw meal injection occurs, provided the particle streams are well dispersed from each other. The raw meal injection gas quantity that leaks through the stage 3 cyclone drop chute has only a minor effect on the flow momentum. The flow in the cylindrical section was more symmetrical about the centre line of the tertiary air inlet than the first model, but the change was not sufficient to cause changes in the reaction behaviour of the coal and raw meal.

Changing the coal injection angle in the model caused a small change to the velocity vectors in the immediate vicinity of the coal inlets. The effect was only local and caused no significant change to the overall flow pattern. The coal trajectories went down slightly at inlet but the residence time and reaction levels by exit were not affected significantly.

The temperature field was sensitive to the addition of the accelerator in the model and the raw meal and coal behaviour was significantly affected by this change. This model was further investigated in the tyre chip investigation (Chapter 7).

Changing the entire model geometry using the fully unstructured mesh technique affected the large recirculation in the cylindrical section, but the overall characteristics of the flow were preserved. The high temperature core of the flame was drawn lower due to intensification of the recirculation between the tertiary air inlet and the neck below the conical section. Coal from the inlet on that side was drawn down into this region. The reaction of the coal

and raw meal could not be assessed since the case was solved successfully for 60% of the raw meal loading before instability in the numerical solution stopped progress.

Coal supply to the precalciner was found to be short by almost 10% at the conclusion of the work. Raw meal maximum calcination at exit was 88.5% of the total due to this. A further interesting sensitivity analysis that should be done in future work is to check the sensitivity to fuel injection rate.

The alternative models performed for this chapter have shown that the model responded to:

- ✓ radiative heat transfer effects,
- ✓ injecting all coal at the inlet Coal A,
- ✓ changing the coal injection angle,
- ✓ adding the “accelerator”

but that it was relatively insensitive to:

- ✗ mesh refinement in the cylindrical section,
- ✗ injecting all the raw meal at the kiln gas inlet,
- ✗ change of mesh to refined tetrahedral cells throughout and
- ✗ adjusting the shape of the inlets.

The model is sufficiently sensitive to show changes that affect the operation of the plant, but is sufficiently robust against approximations used in the numerical analysis.

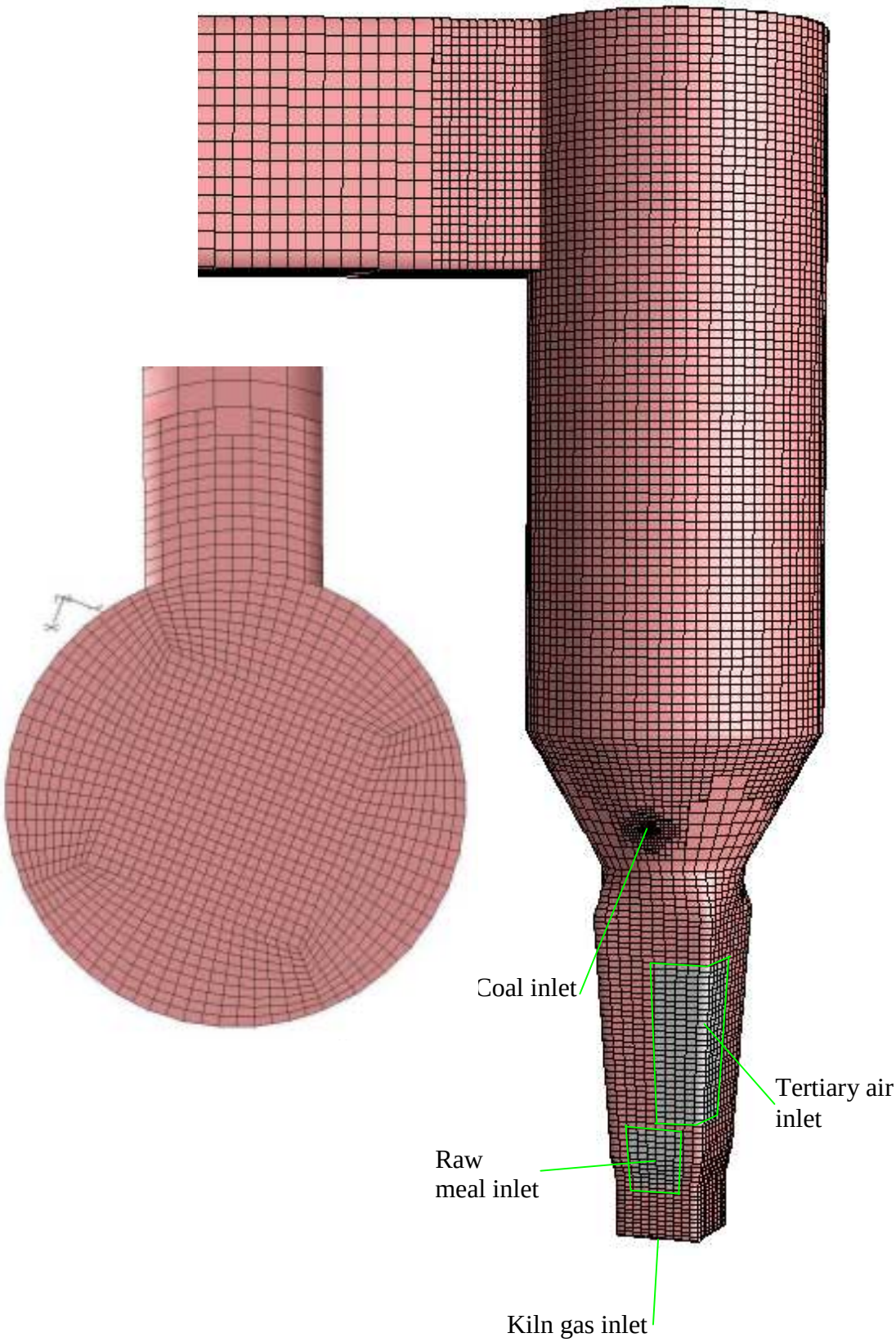

Fig. 6-1 Refined grid illustration. The mesh was refined such that cells of the size typically found in the cylindrical section only were altered. Each cell was refined by the hanging node method depicted in Fig. 3-1. The outlet duct was not refined, since the flow in the duct is not of interest and no complex flow features were found there in the previous model.

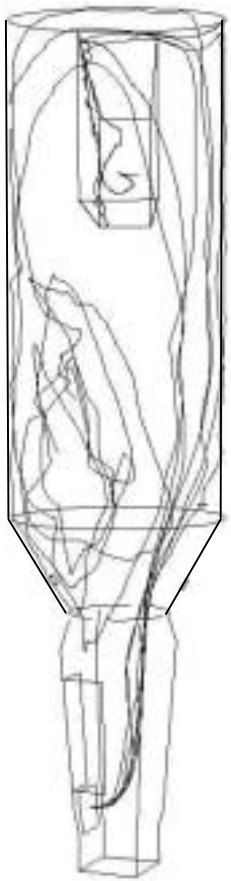

Fig. 6-2 (a) Single raw meal particle trajectory showing 6 stochastic attempts.

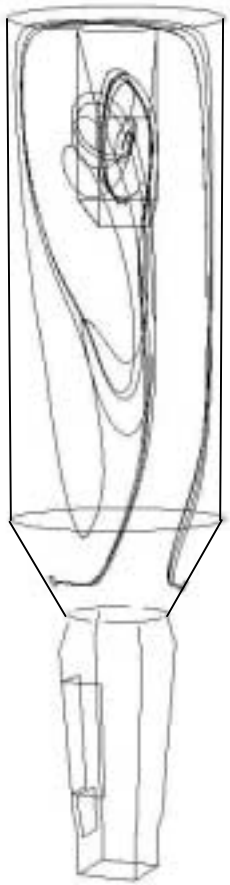

Fig. 6-2 (b) Coal injections from the two inlets A and B. Mean path only.

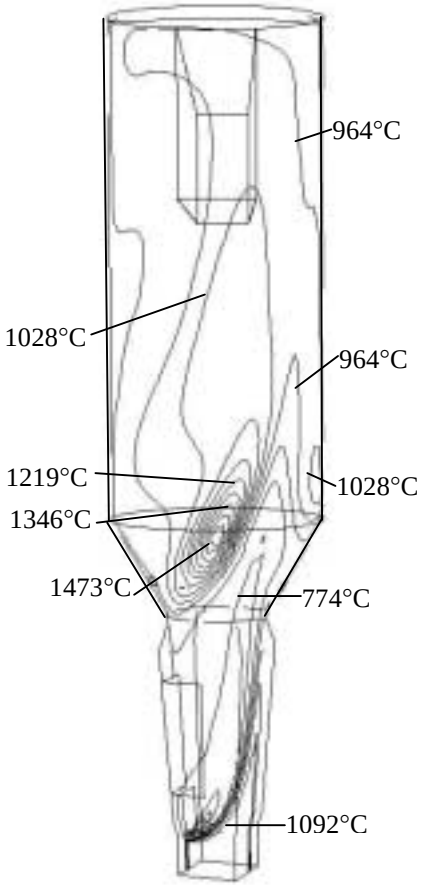

Fig. 6-2 (c) Contours of temperature (°C) showing high temperature core.

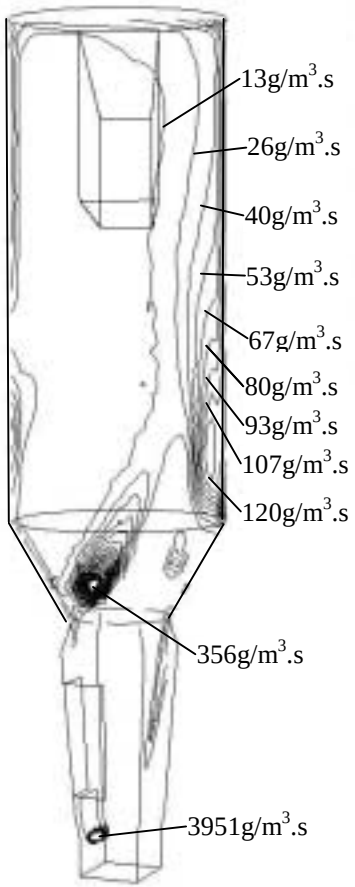

Fig. 6-2 (d) Contours showing release of volatiles (grammes/m^3.sec)

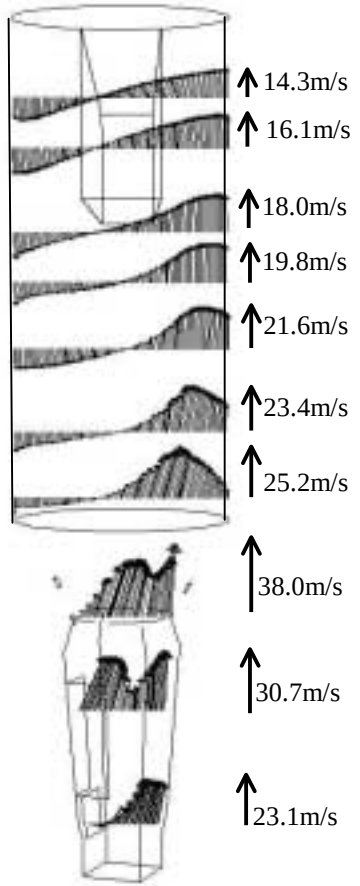

Fig. 6-2 (e) Velocity vectors on selected lines through the precalciner.

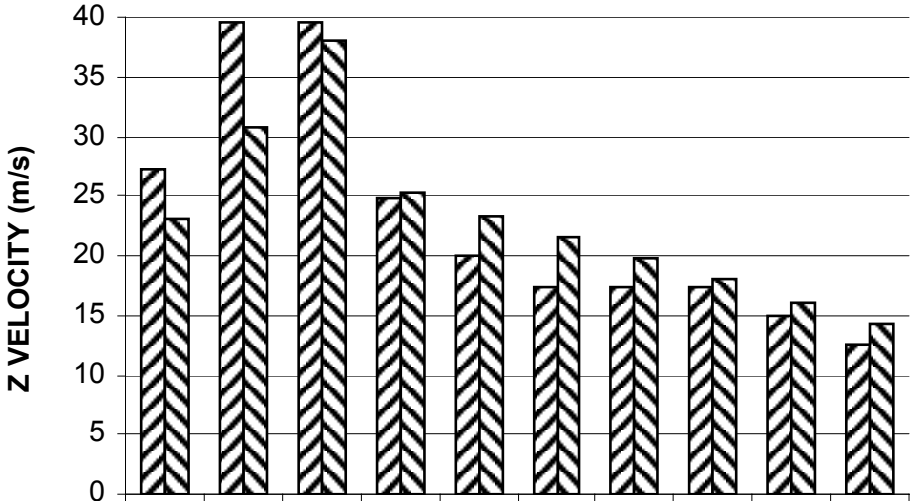

	1	2	3	4	5	6	7	8	9	10
Refined	27.3	39.6	39.6	24.8	19.9	17.4	17.4	17.4	14.9	12.5
Original	23.1	30.7	38	25.2	23.4	21.6	19.8	18	16.1	14.3

Fig. 6-3 Comparison of maximum vertical velocities on 10 lines up the height of the precalciner from Fig. 5-2e and Fig. 6-2e. Line 1 is the lowest line of on each figure and line 10 is the highest. There is significant difference between values on lines 1, 2, 5, and 6.

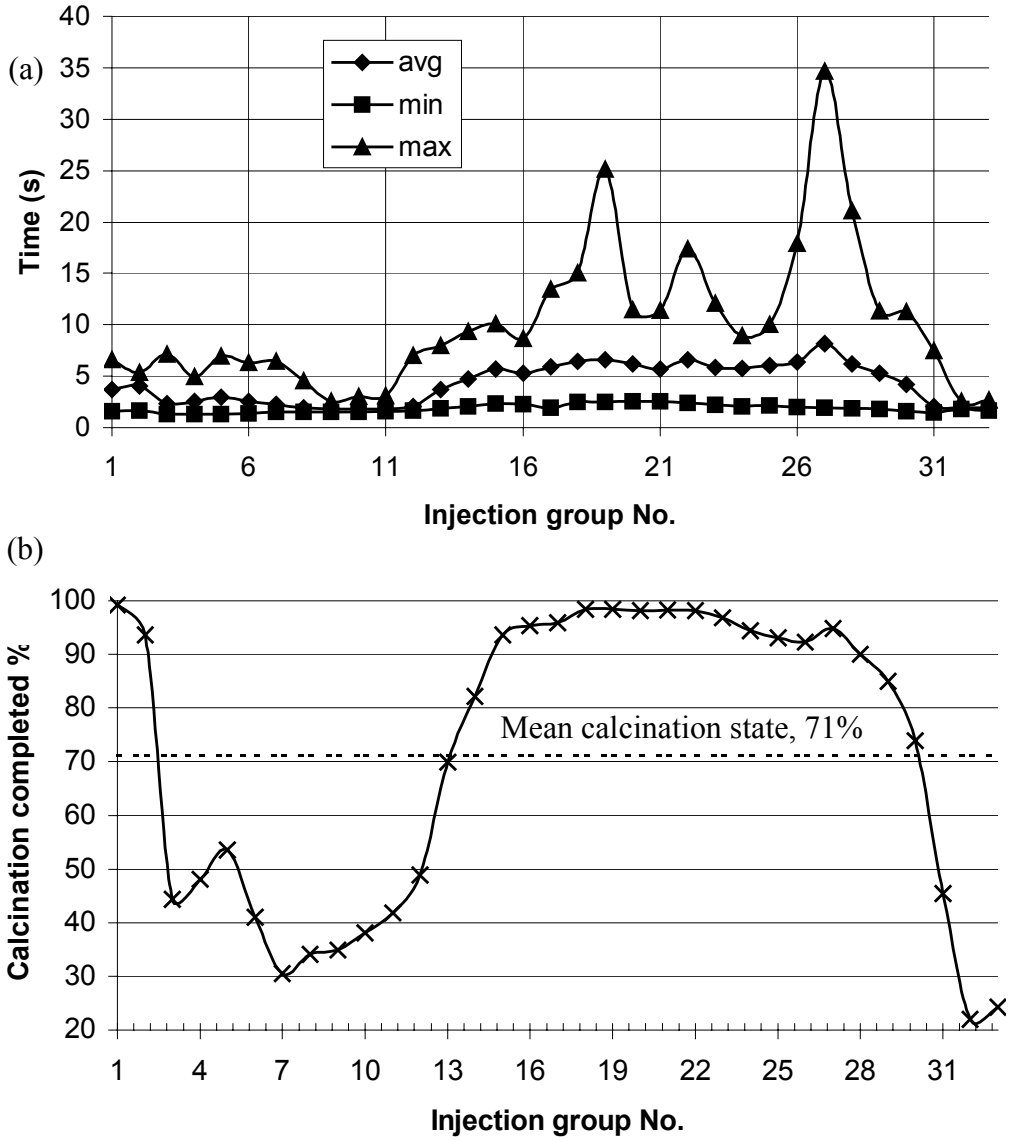

Fig. 6-4 Behaviour of raw meal in the refined precalciner model. Graph (a) shows the mean, maximum and minimum exit time of each of the 33 groups from entry at the RMI. Graph (b) shows the calcination state at exit from the main cylindrical section, including the mean state of calcination.

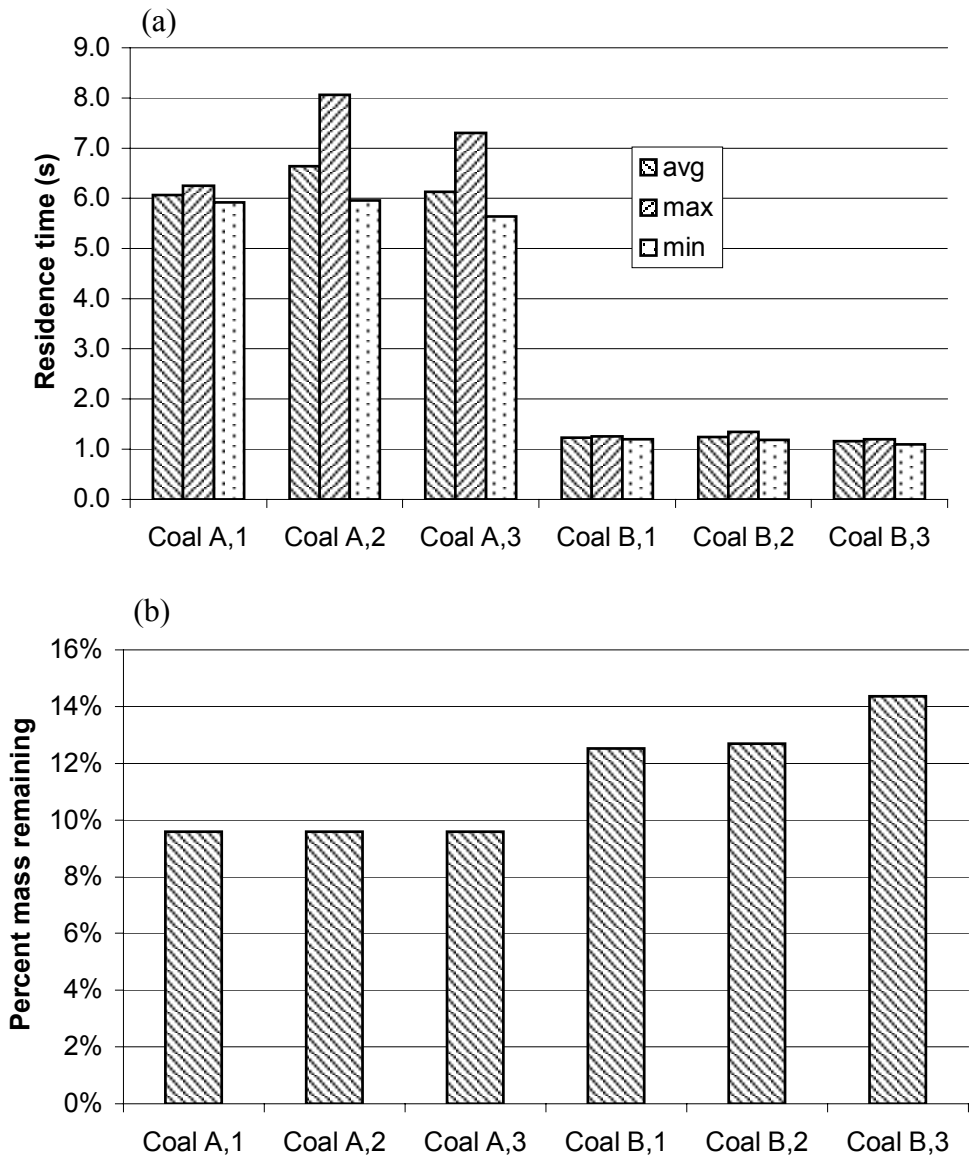

Fig. 6-5 Coal behaviour in the precalciner model with refined mesh. Coal was released in 3 groups of 4 particle streams at each of the coal inlets, Coal A and Coal B. Histogram (a) shows mean, maximum and minimum residence times from the inlet to the outlet from the cylindrical section and (b) shows the mass remaining at the exit.

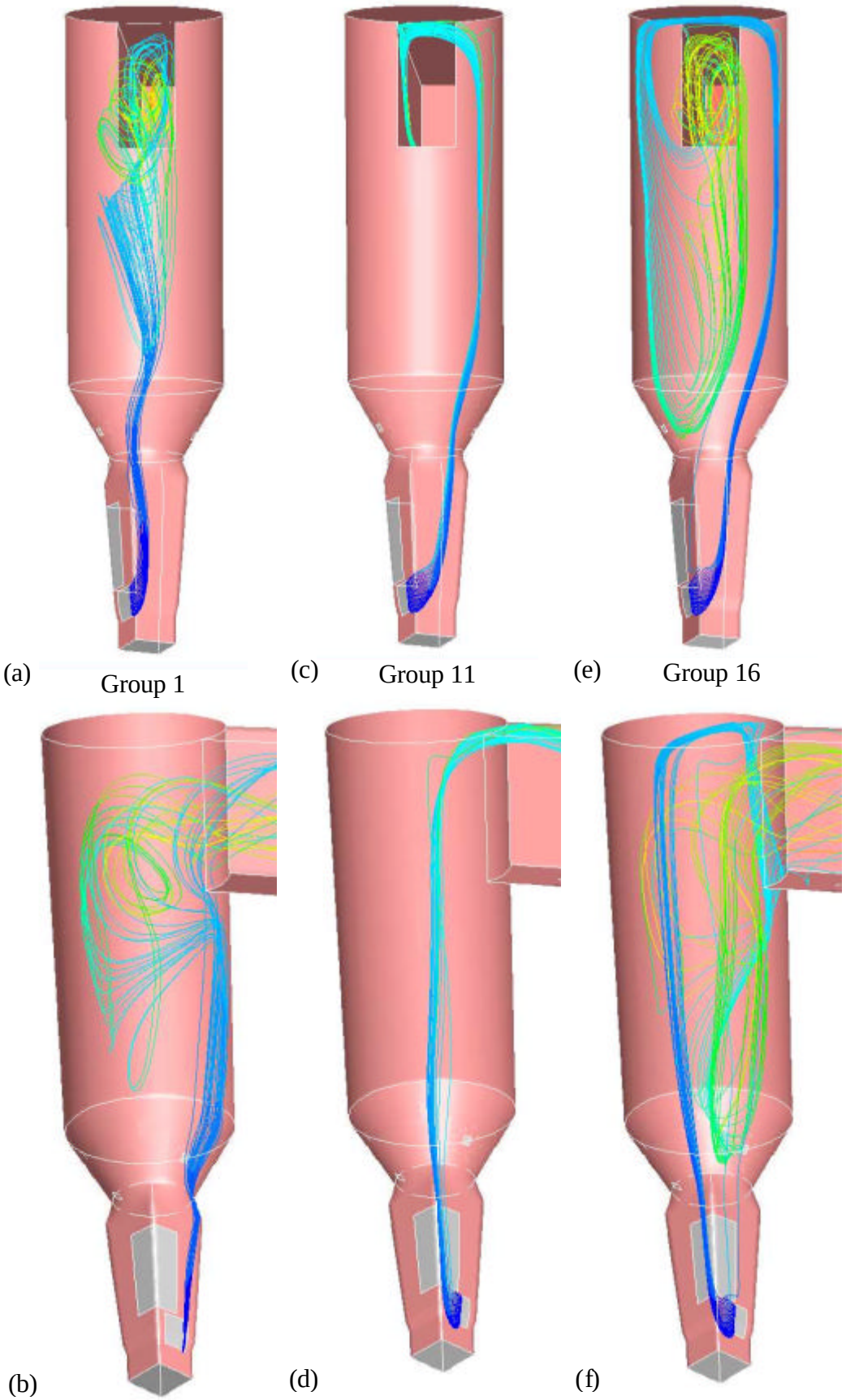

Fig. 6-6 Raw meal injection trajectories viewed from two directions. (a) and (b) show Group 1, (c) and (d) show Group 11 and (e) and (f) show Group 16. Coloured by residence time.

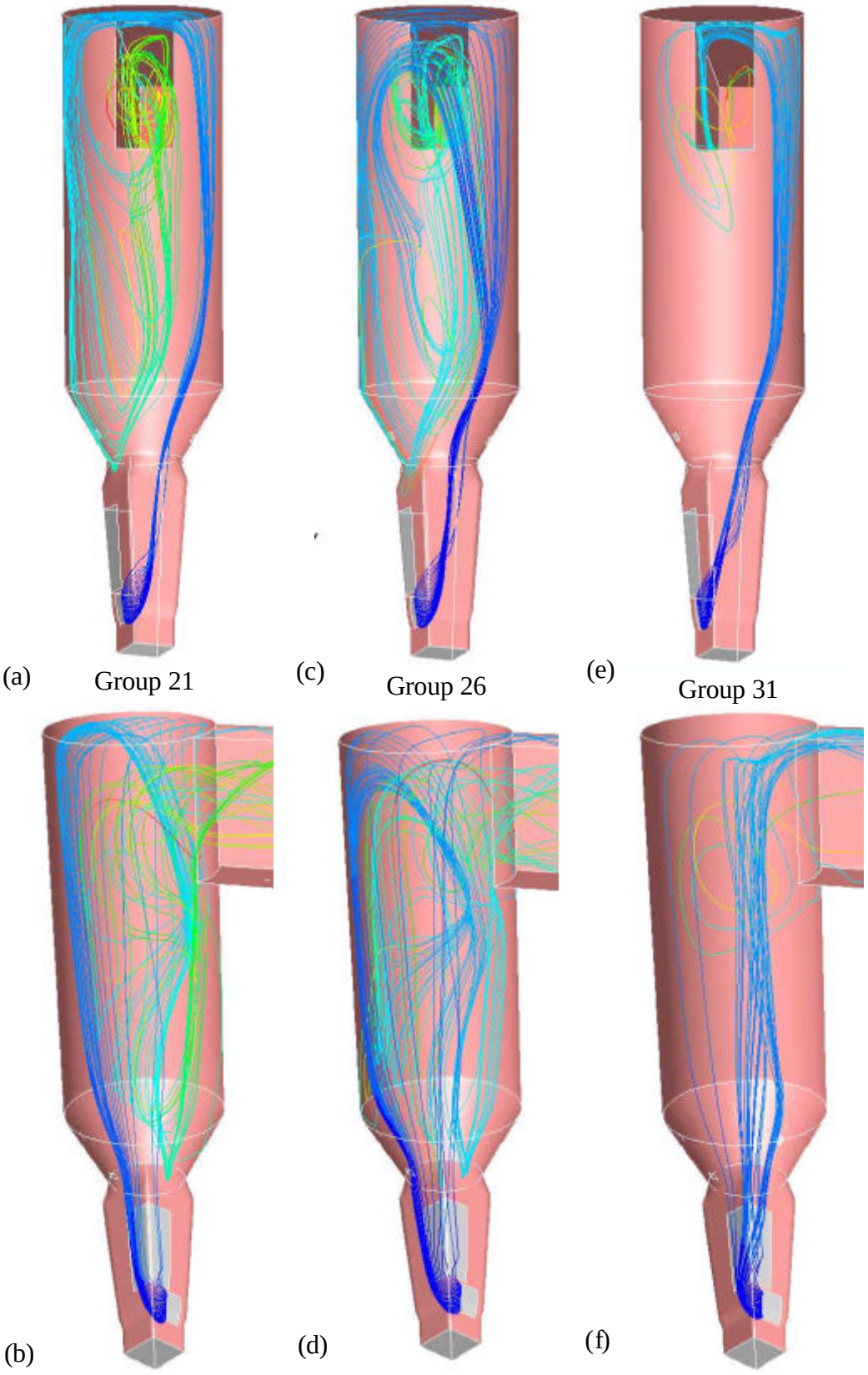

Fig. 6-7 Raw meal injection trajectories viewed from two directions. (a) and (b) show Group 21, (c) and (d) show Group 26 and (e) and (f) show Group 31. Coloured by residence time.

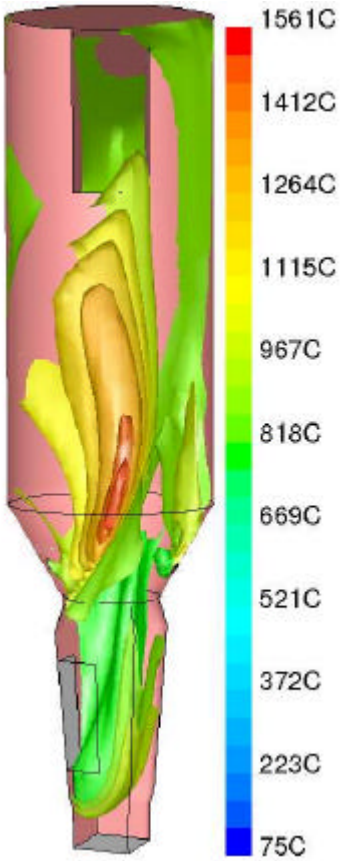

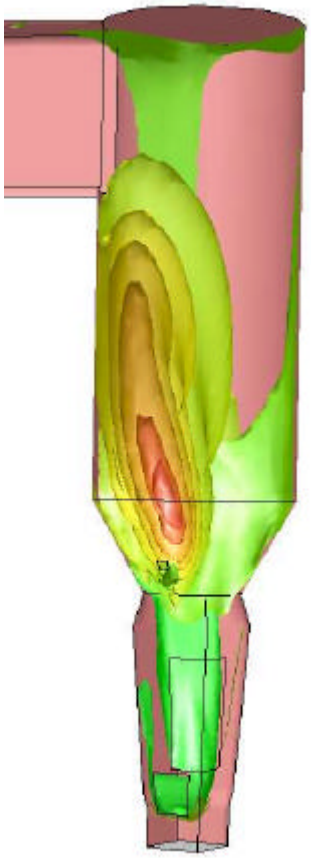

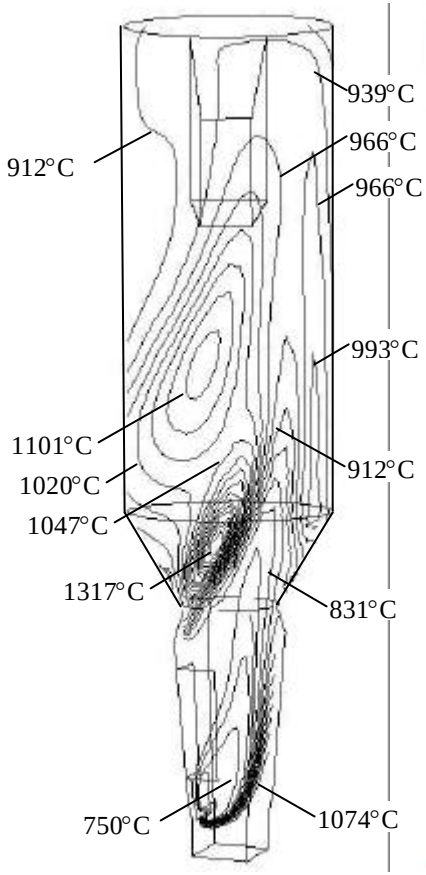

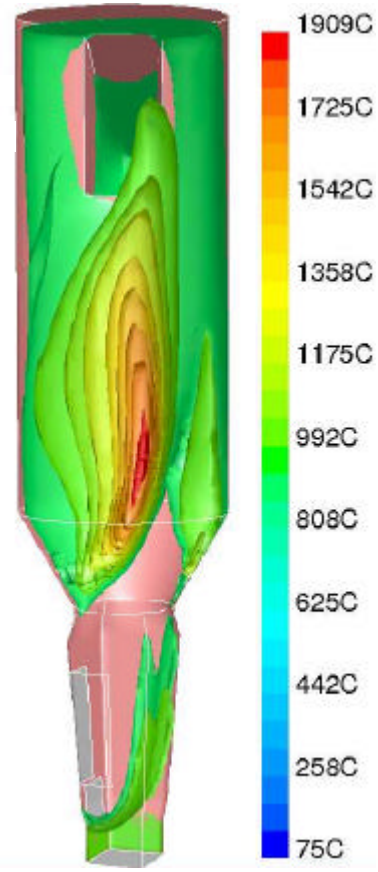

Fig. 6-8 (a) Temperature iso-surfaces on model with α=0.1 m^{-1} looking into the outlet duct.

Fig. 6-8 (b) Temperature iso-surfaces on model with α=0.1 m^{-1} looking perpendicular to the outlet duct.

Fig. 6-8 (c) Temperature contours on model with α=0.1 m^{-1} on the plane through the centre.

Fig. 6-8 (d) Temperature iso-surfaces on original model looking into the outlet duct.

Fig. 6-8 (e) Temperature iso-surfaces on original model looking perpendicular to the outlet duct.

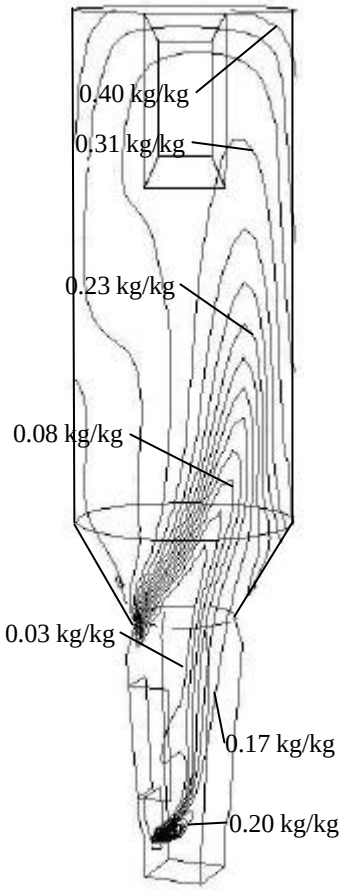

Fig. 6-9 (a) original model, mass fraction of CO_2 contours (kg/kg)

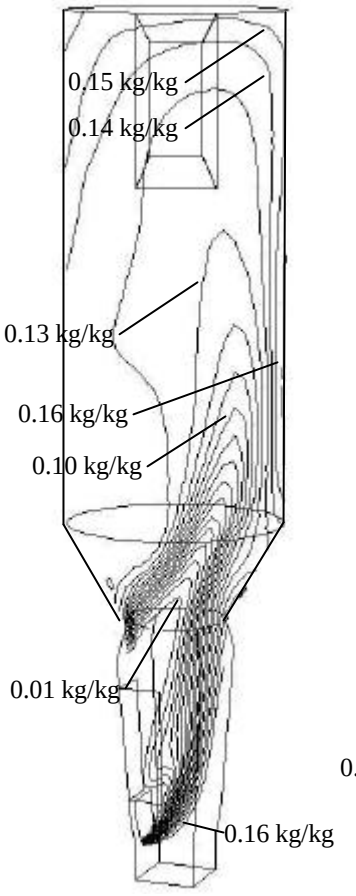

Fig. 6-9 (b) named CO_2 model, mass fraction of combustion CO_2 contours (kg/kg)

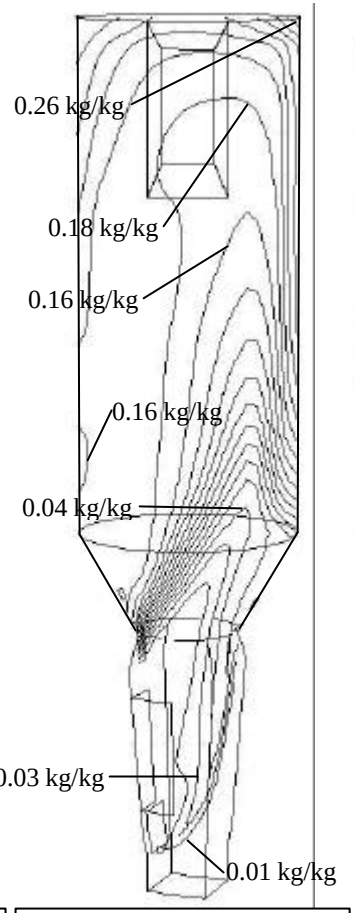

Fig. 6-9 (c) named CO_2 model, mass fraction of raw meal CO_2 contours (kg/kg)

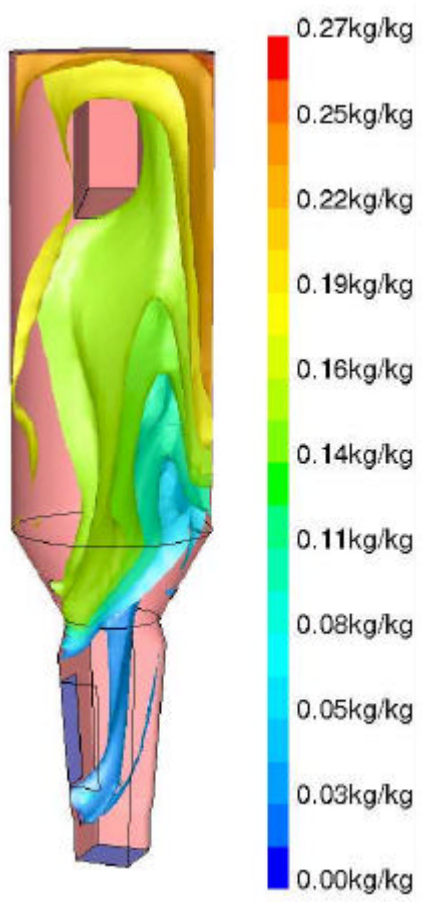

Fig. 6-9 (d) named CO_2 model, mass fraction of raw meal CO_2 iso-surfaces (kg/kg), looking into outlet duct.

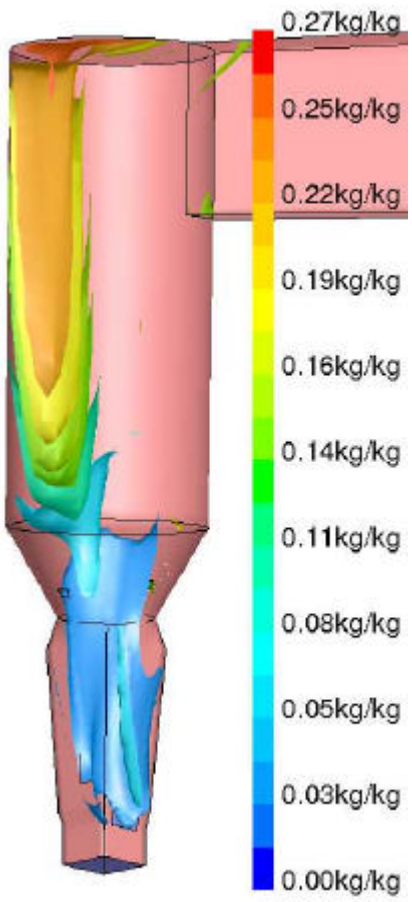

Fig. 6-9 (e) named CO_2 model, mass fraction of raw meal CO_2 iso-surfaces (kg/kg), looking into tertiary air inlet.

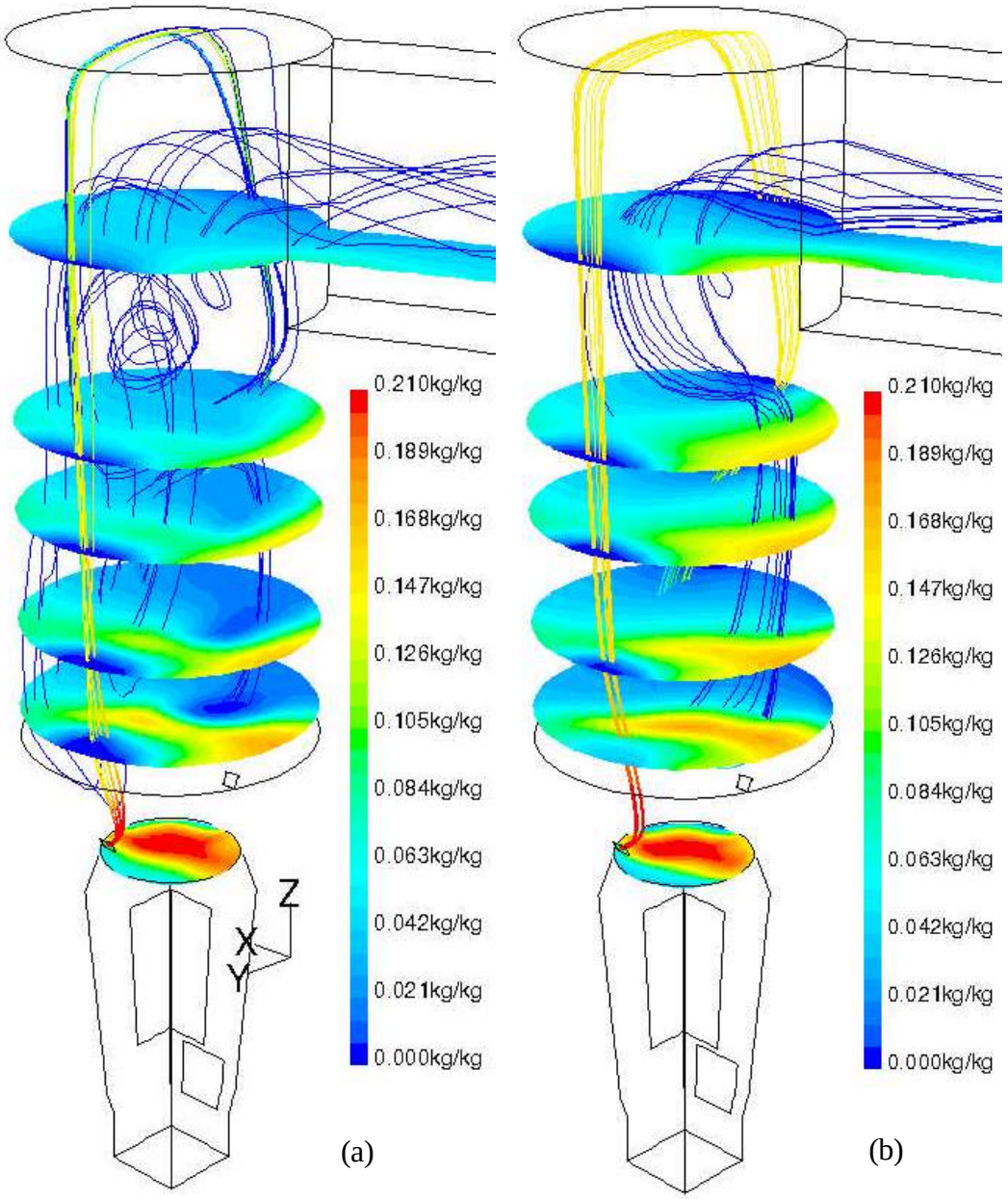

Fig. 6-10 Contours of oxygen mass fraction with coal particles from the coal inlet opposite the tertiary air duct for original case (a) and the one coal inlet case (b). The effect of removing the second coal source in (b) is to change the oxygen concentration pattern in the cylindrical section, thus making oxidation of coal injected at inlet Coal A easier.

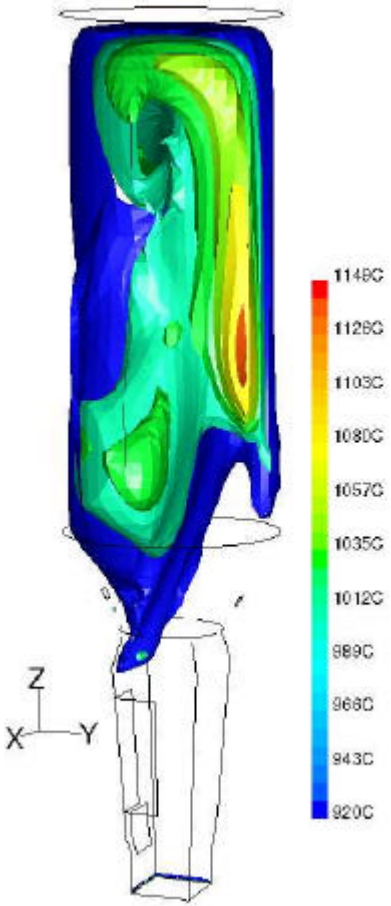

Fig. 6-11 (a) One coal model, temperature iso-surfaces on plane perpendicular to outlet duct.

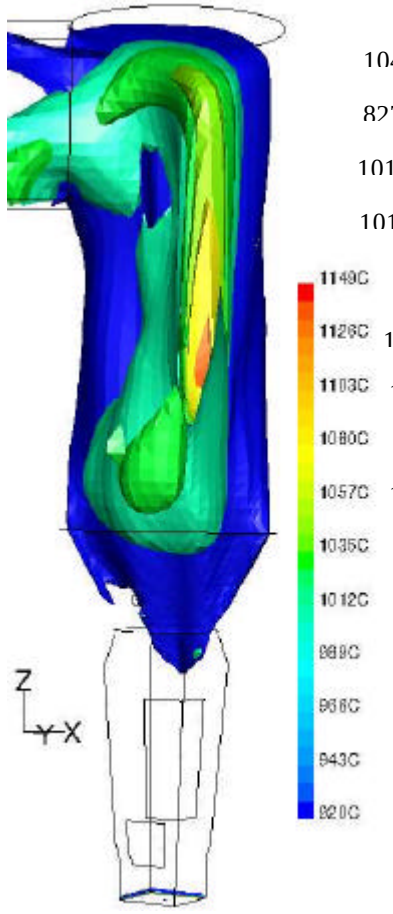

Fig. 6-11 (b) One coal model, temperature iso-surfaces on plane parallel to outlet duct.

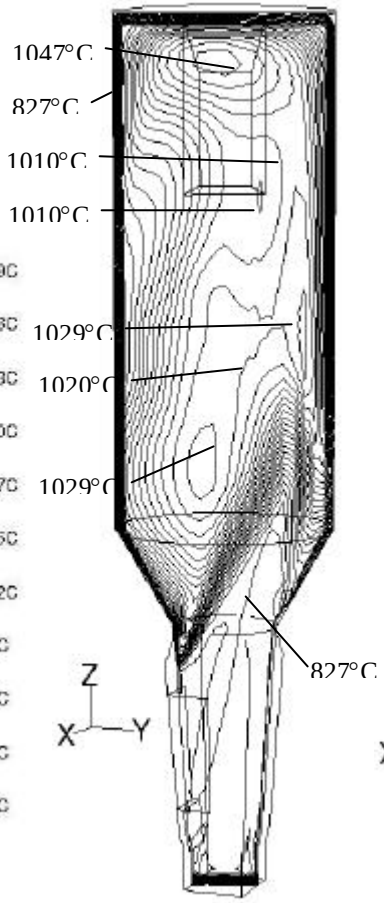

Fig. 6-11 (c) One coal model, temperature contours on perpendicular plane.

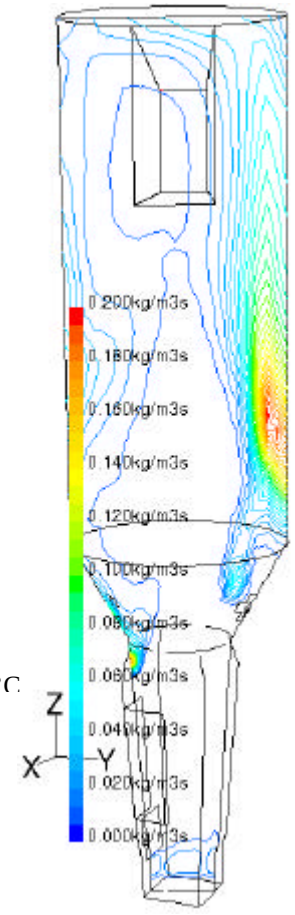

Fig. 6-11 (d) One coal model, release of volatiles contours on perpendicular plane.

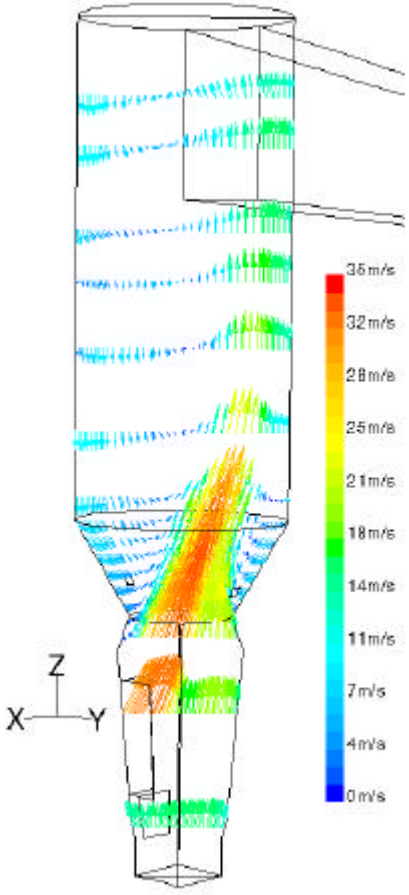

Fig. 6-11 (e) One coal model, velocity vectors on plane through tertiary air inlet.

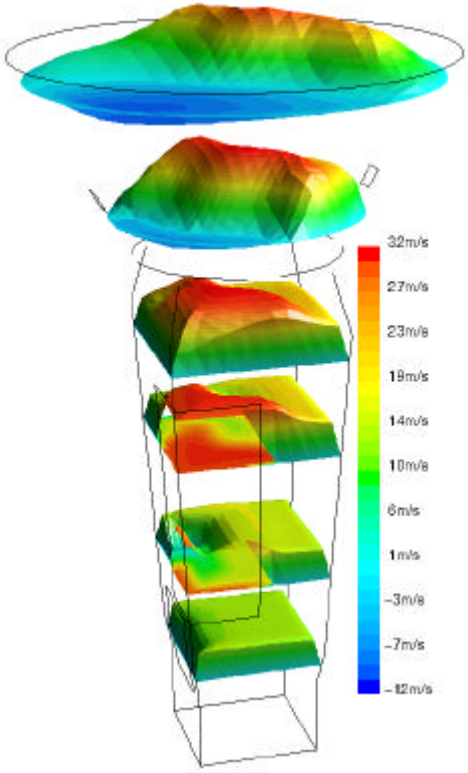

Fig. 6-12 (a) Profiles of vertical velocity close up with the tertiary air duct on the left-hand-side.

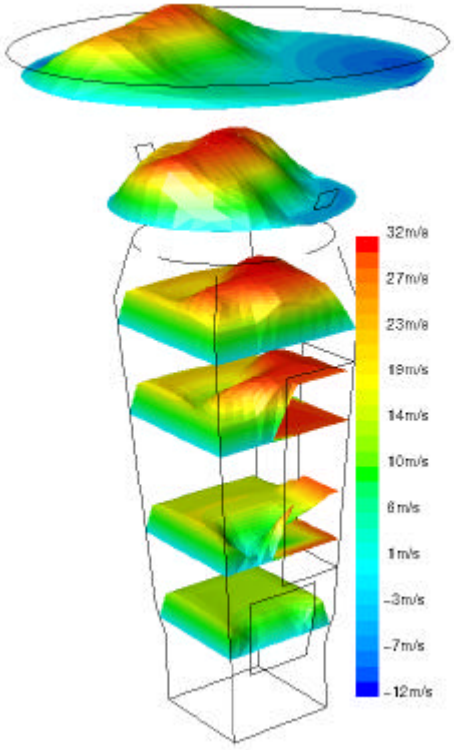

Fig. 6-12 (b) Profiles of vertical velocity close up with the tertiary air duct on the right-hand-side.

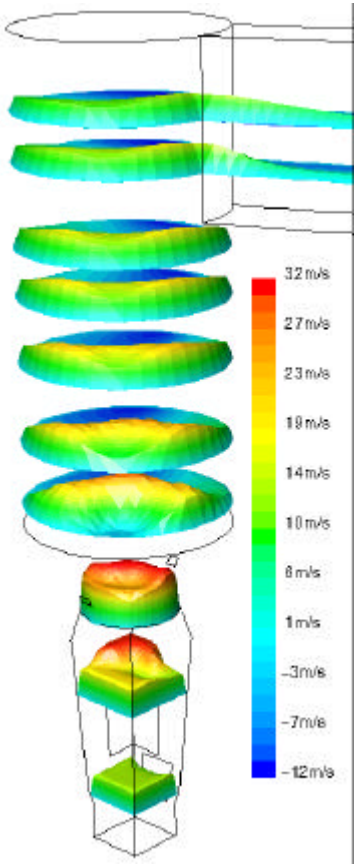

Fig. 6-12 (c) Profiles of vertical velocity looking toward the tertiary air duct.

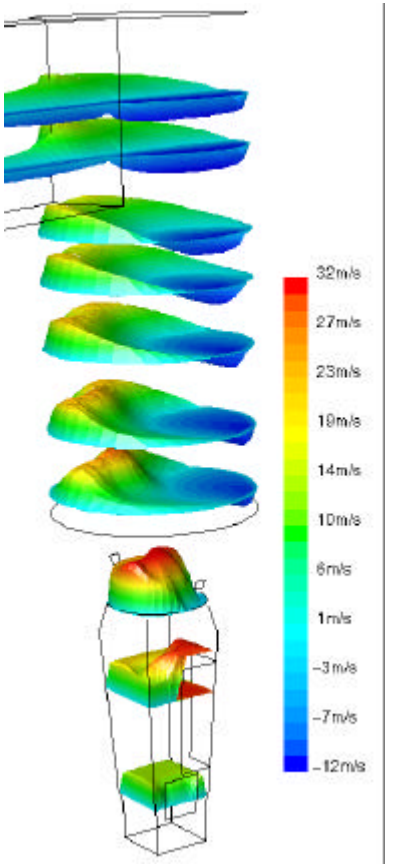

Fig. 6-12 (d) Profiles of vertical velocity with the tertiary air duct on the right-hand-side.

Fig. 6-13 Photograph showing the angle of the coal pipe entering the conical section of the precalciner wall. This section of the precalciner is approximately 26 m above ground level.

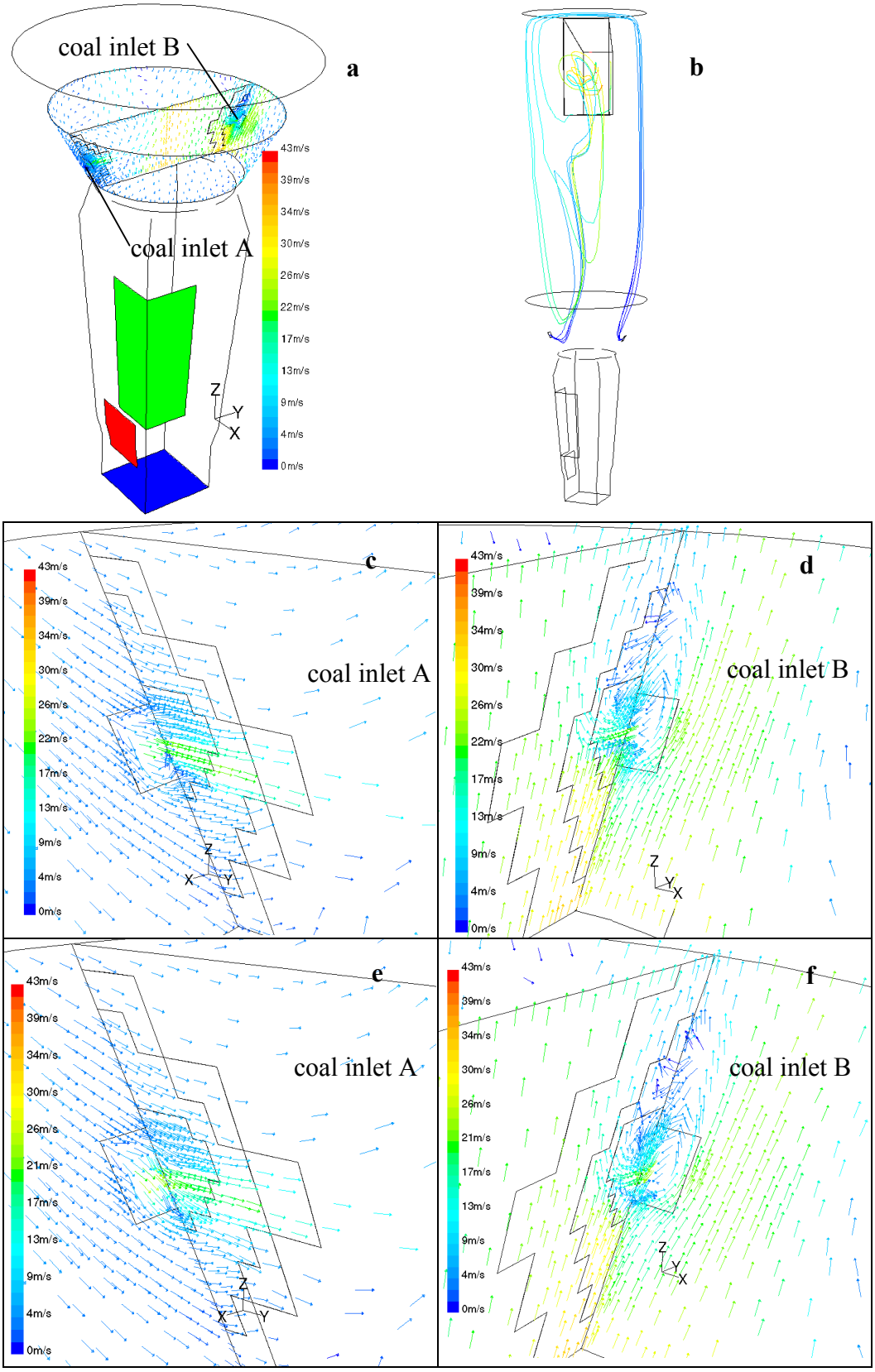

Fig. 6-14 Velocity vectors near the coal inlets: **a** showing the overview, **b** shows typical coal trajectories, **c** and **d** are from the original model and **e** and **f** are from the angled coal inlet injection model.

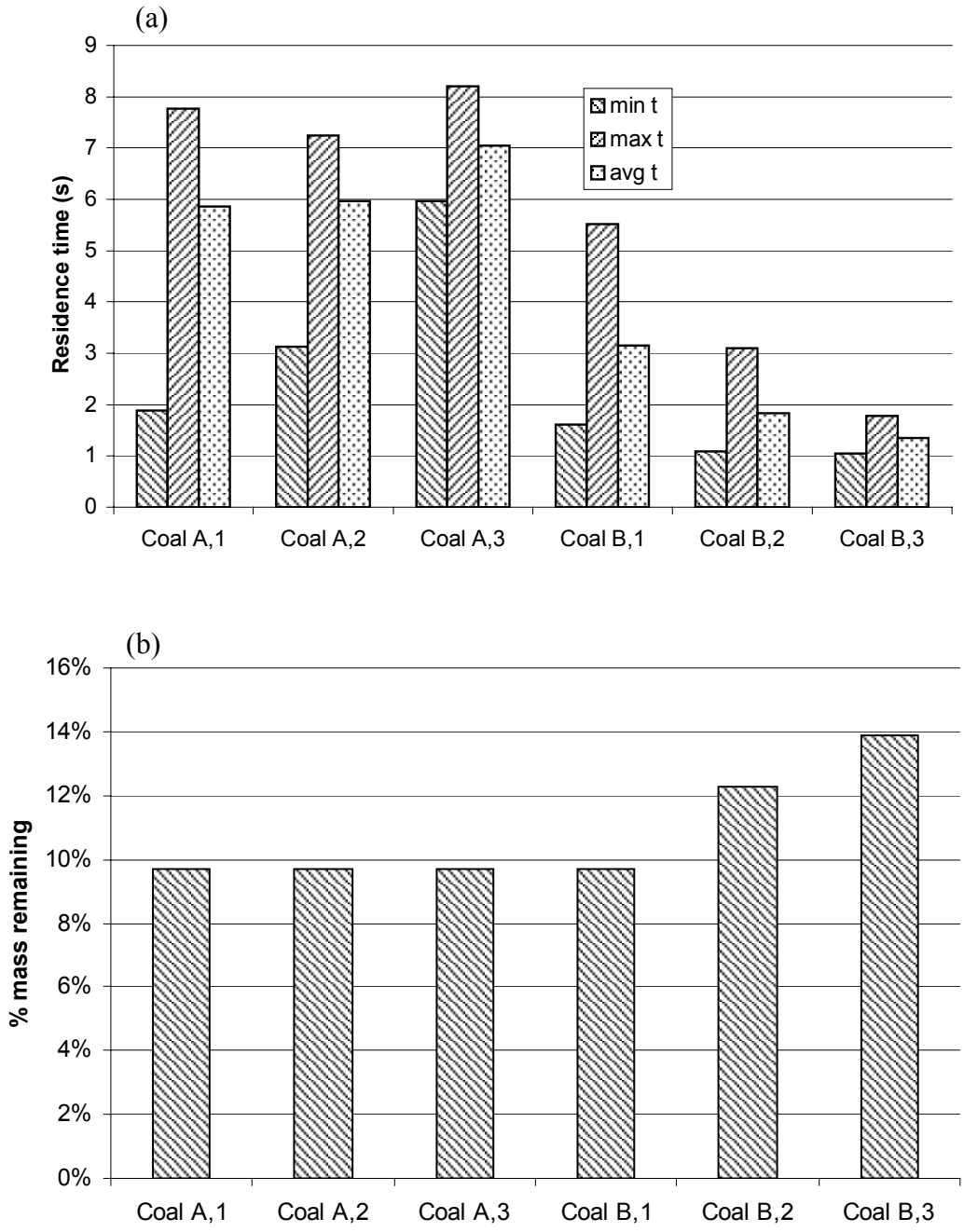

Fig. 6-15 Graphs showing (a) residence time and (b) mass remaining of the coal particles released from each of the coal inlets Coal A and Coal B shown in Fig. 5-2.

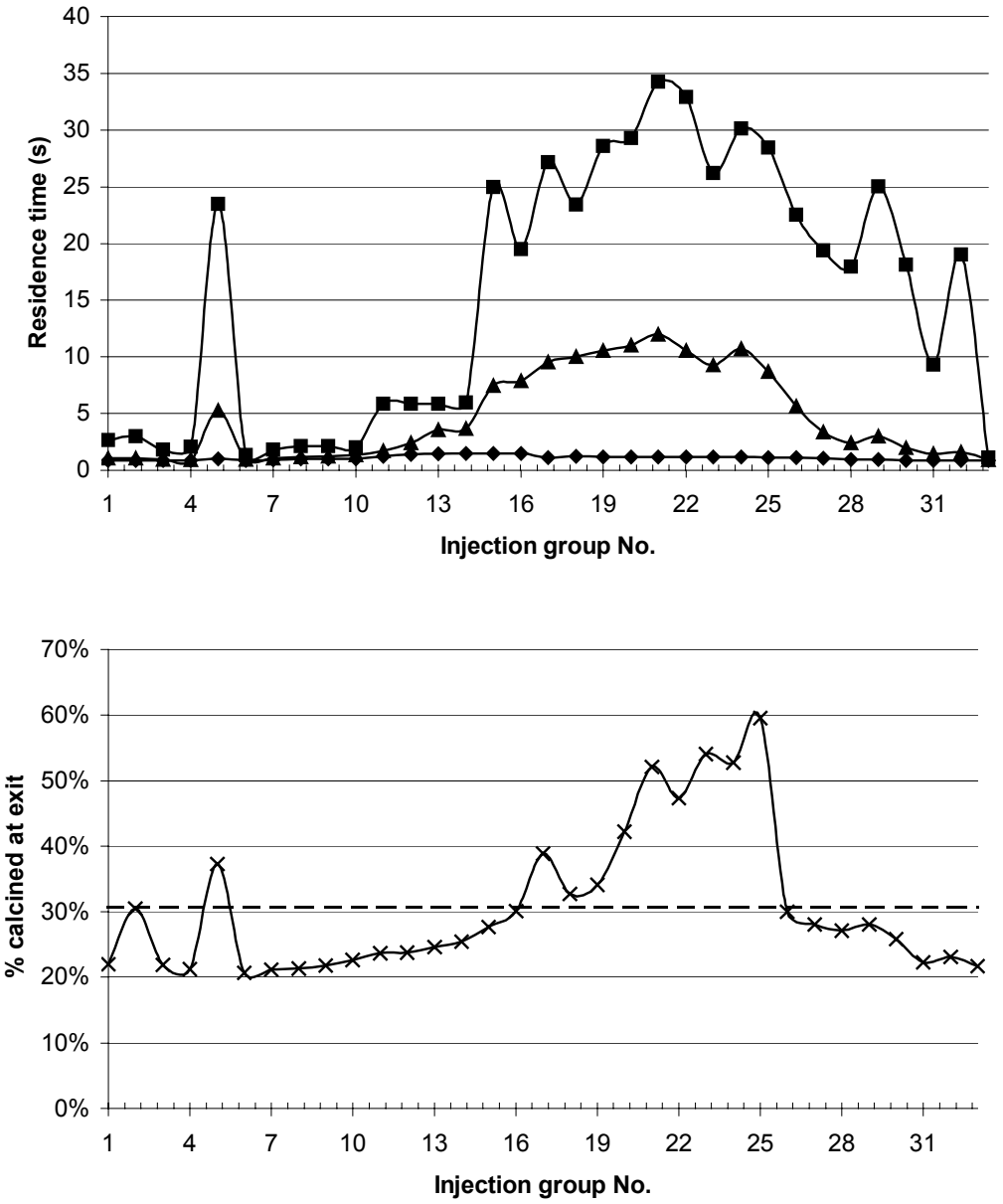

Fig. 6-16 Raw meal behaviour in the model with the "accelerator" section at the throat of the precalciner. Residence times are shorter than cases without the "accelerator" and the degree of calcination at exit is less.

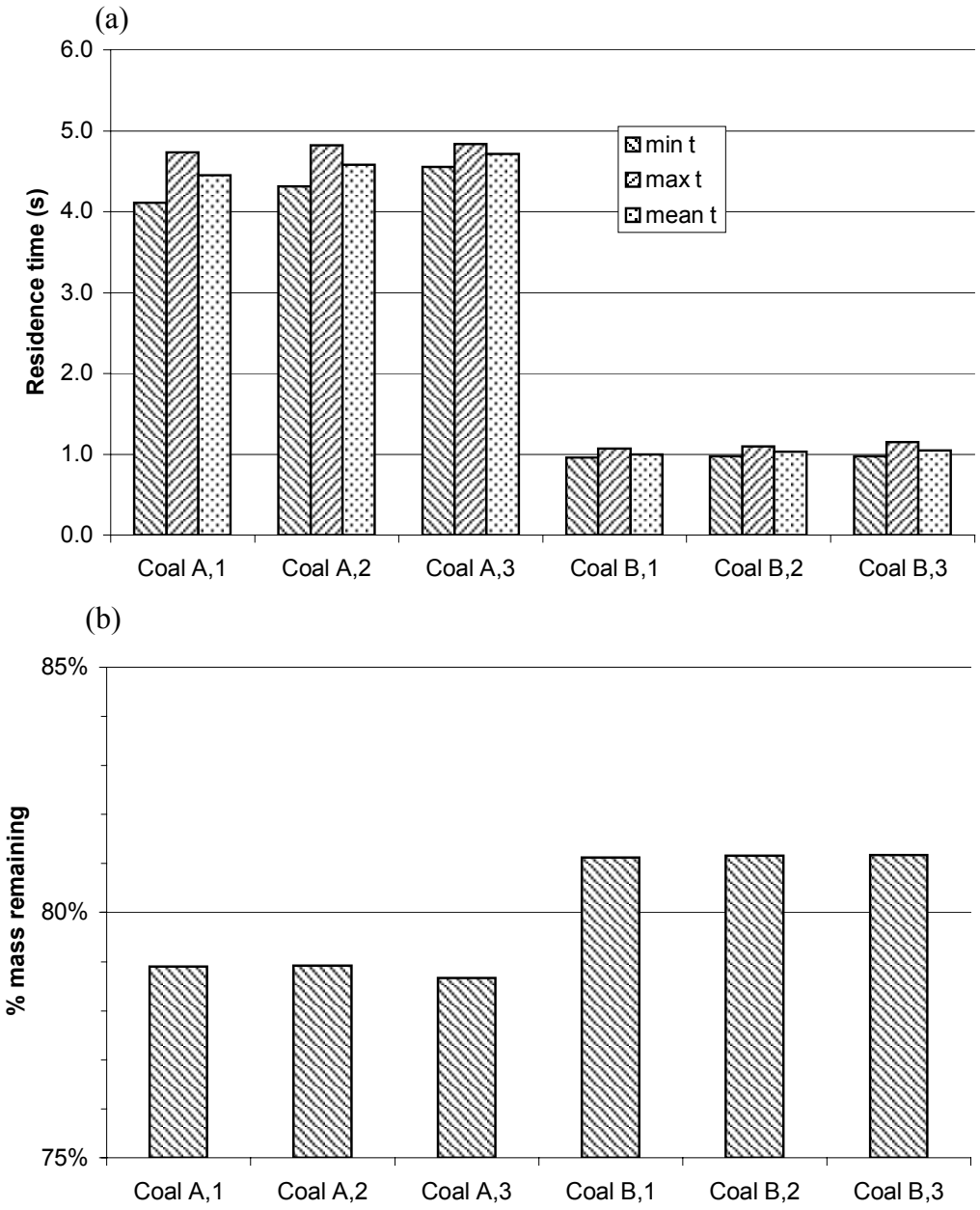

Fig. 6-17 Coal behaviour in the model with the accelerator section. It is clear from histogram (a) that the mean time coal particles spend in the main body of the precalciner is significantly less than in cases without the accelerator and from (b) that they are far less oxidized on exit.

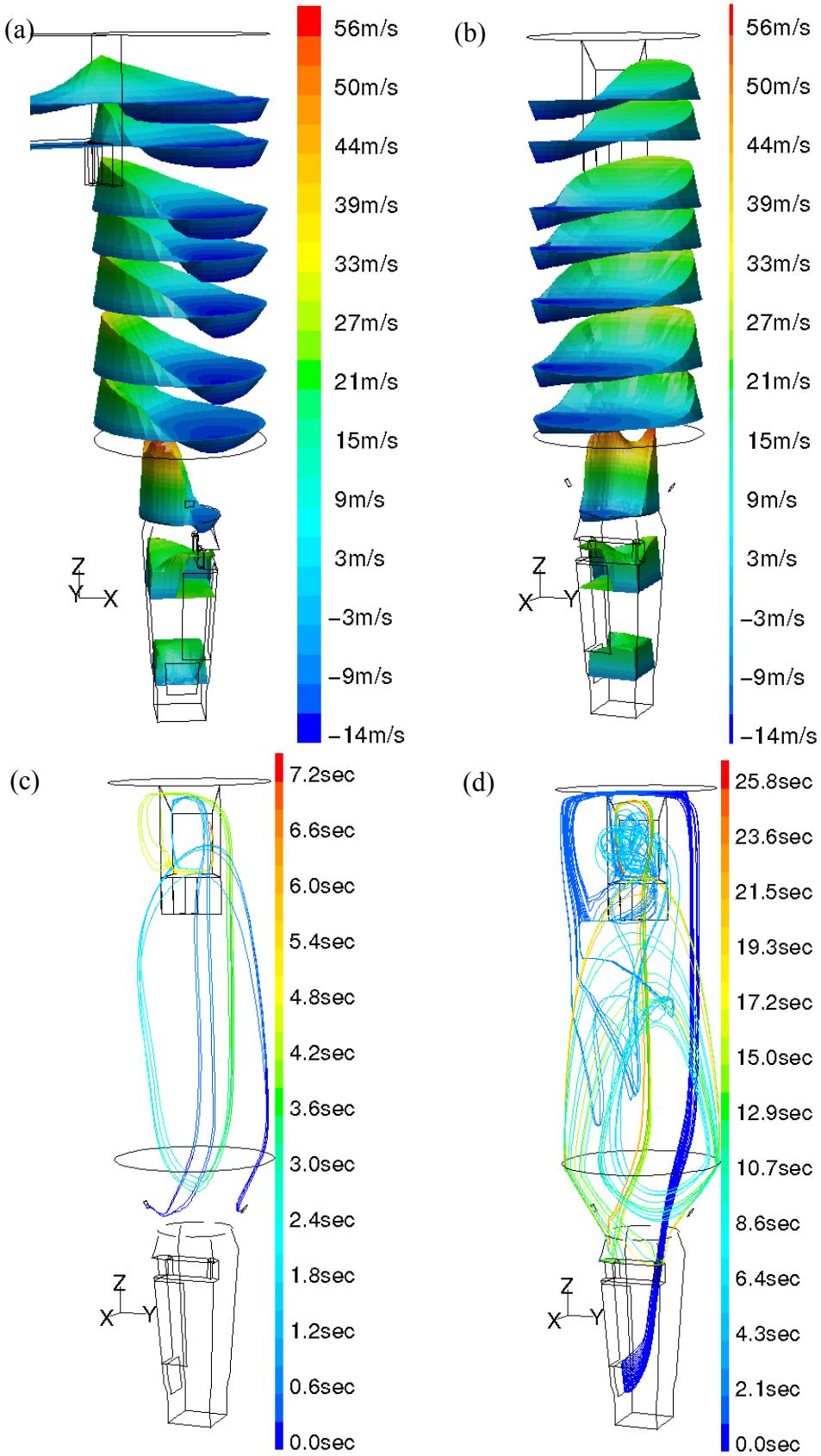

Fig. 6-18 Showing the vertical velocity profiles (a and b) in the accelerator model and the particle trajectories for coal (c) and raw meal (d).

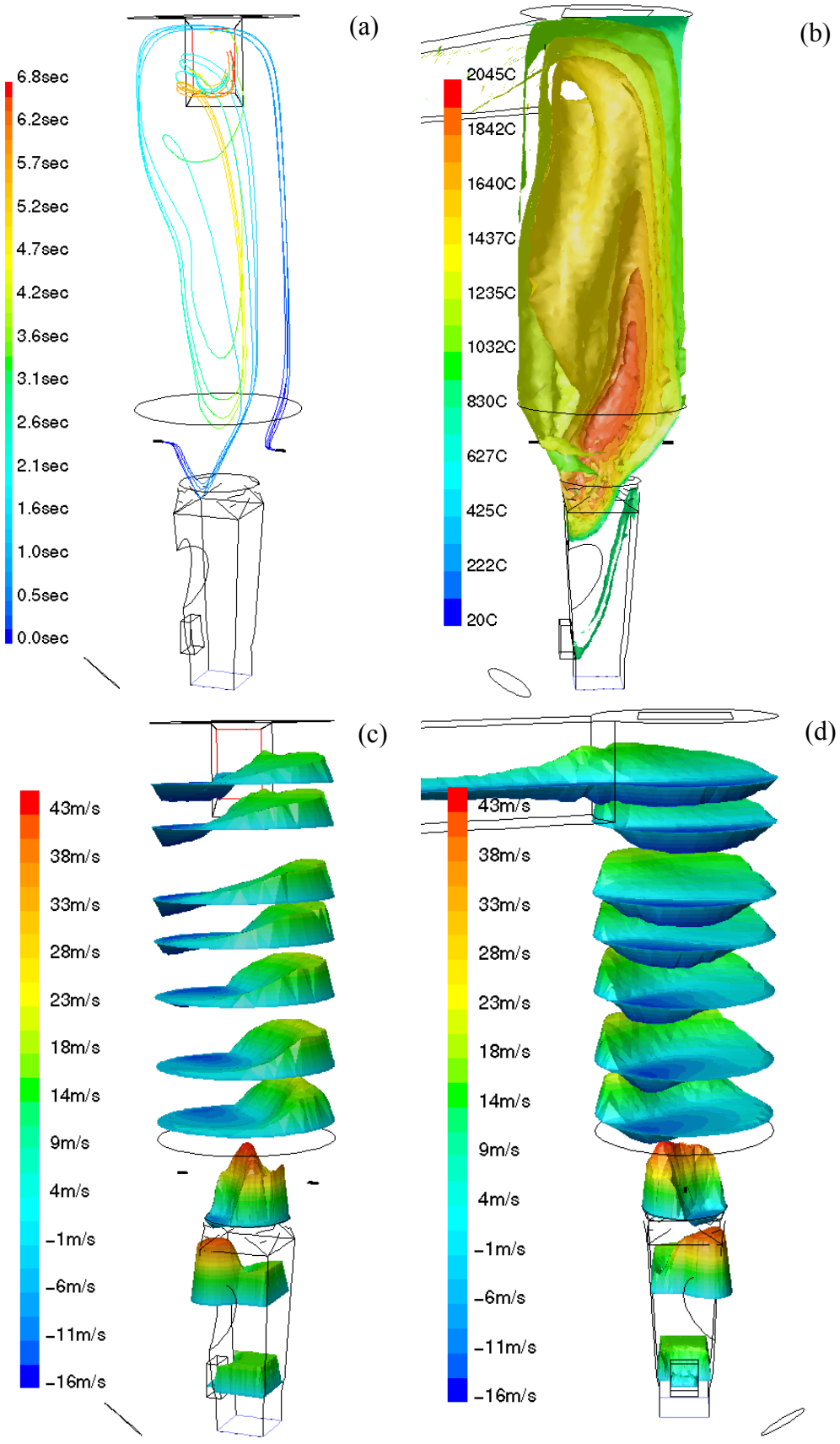

Fig. 6-19 Features of the improved geometry solution. (a) shows typical coal trajectories, (b) shows temperature iso-surfaces, (c) and (d) show profiles of velocity in the vertical direction. This model has only 60% raw meal load.

7 Modelling Tyre Chips in the Block Structured Model

Tyre chip modelling was carried out on the block structured model presented in Chapter 5 and subsequently on the model with the accelerator added, described in section 6.7. The sections in this chapter describe the modelling work and experimental work performed to model tyre chip behaviour in the precalciner.

Sec. 7-1. Information used to develop a good simulation of the tyre chip injection into the precalciner is presented. This was done by inspection of the precalciner and feeder mechanism and by experiment.

Sec. 7-2. Aerodynamic behaviour of the tyre chips was investigated in previous work and the results are presented here. Further experimental work was performed to determine the free-fall behaviour of tyre chips. The results of these experiments were used to determine the best technique for modelling tyre chip aerodynamics.

Sec. 7-3. Combustion experiments were performed to see how the tyre chips react in the conditions likely to be found in the precalciner. The experimental observations were used to develop devolatilisation and char combustion models for the tyre chips.

Sec. 7-4. The data for the tyre chips and injection information was used on the model from Chapter 5 to answer the initial question posed for the project about tyre chip fates in the precalciner.

Sec. 7-5. Due to developments made on the precalciner by addition of the accelerator presented in section 6.7, the tyre chips were modelled on this new geometry.

Sec. 7-6. The accelerator model was used to determine the best alternative injection point for tyre chips to make decisions about further alterations to the precalciner.

Sec. 7-7. Conclusions of the tyre chip investigation.

Notation for Chapter 5

A cross section area presented perpendicular to free stream (m^2)

$C_{d,sph}$ drag coefficient of sphere

F_d drag force (N)

R_e Reynolds number

U free stream velocity (m s^{-1})

r_g gas density (kg m^{-3})

7.1 Tyre chip injection

The tyre chip injection point was determined from drawings and photographs of the precalciner. The tyre chips are conveyed to the precalciner through a long delivery system comprising the following:

- tyre chip hopper at ground level, which receives chips from the chipper by a dumper truck
- bucket elevator to the height just above the conical section of the precalciner (approximately 28m above ground level)
- screw feeder horizontally to the wall of the precalciner
- drop feed to the inlet chute
- rebound from the wall of the chute into the precalciner.

Initial tyre chip trajectories were predicted from experiment and assumptions about the inlet chute.

7.1.1 Tyre chip inlet configuration of the precalciner

Visual inspection of the tyre chip injection chute was used to determine a range of suitable injection velocities for the tyre chips in the CFD model.

The tyre chip delivery chute is shown in Fig. 7-1a-d. The four photographs were taken on the floor at the plant just above the conical section of the precalciner. The important features have been highlighted with yellow lines. The views shown are illustrated diagrammatically in the Fig. 7-2a-b. Figure 7-1a and 7-1b show the wedge shape of the delivery chute, which has a 23 cm refractory lining similar to the rest of the precalciner vessel. Figure 7-1c shows the cover of the screw feeder leading to the precalciner wall. Figure 7-2b shows a schematic drawing of the tyre chip feeder with the top of the precalciner removed for clarity showing the refractory lining in orange. The position of the injection point of the tyre chips is indicated in Fig. 7-2a. The inclination of the chute wedge is approximately 60° to the horizontal. Tyre chips are dropped from the end of the feed screw approximately 1 m before

striking the side of the feed chute and rebounding into the precalciner. The entry height of the chips is between 1.2 and 1.6m.

7.1.2 Tyre chip dispersion experiments

Tyre chips enter the precalciner through the wall in the position shown in Fig. 7-1 and Fig. 7-2. The initial trajectory of the tyre chips is not known since they are dropped from a screw feeder approximately 1m before bouncing off of a refractory lined steel plate at 60° to the horizontal. Typical dispersion characteristics of tyre chips from a refractory lined surface are not available in the literature.

Assumptions were made about the coefficient of restitution of tyre chips on refractory, since the "bounce" depends on the shape of the chip as well as material properties. The coefficient of restitution was divided into components parallel and perpendicular to the incident surface. The parallel coefficient was chosen to be 0.85 and the perpendicular coefficient was chosen as 0.9 since it is likely that there is significant friction between the surfaces on impact and that the impact is elastic. The velocity is only slightly decreased in each direction. The shape of the tyre chips and the composition with wire and rubber mixed on the surface makes experimental determination impracticable since no uniform and realistic criteria can be specified.

Experiments were performed, as illustrated in Fig. 7-3, with a ¼" steel plate inclined at 60° to the horizontal on to which various sized tyre chips were dropped from a height of approximately 1m before striking the plate. A grid was marked on the floor immediately in front of the plate. The dispersion of the chips was determined by repeating drops and recording the point on the grid where the chip first struck. It is the angle of injection and the likely injection velocity that are of interest to determine the initial behaviour of the tyre chips. The calculation of the horizontal and vertical components of velocity assuming the 1m free-fall under gravity before striking the plate is detailed in the Fig. 7-3. The experiment showed the likely spread of the tyre chips and the random nature of the bounce as illustrated in Table 7-1.

Drop	h (cm)	l (cm)	α deg
1	10	5	8.4
2	5	10	19.0
3	20	5	6.5
4	10	5	8.4
5	10	10	16.4
6	15	0	0.0
7	10	0	0.0
8	20	5	6.5
9	25	10	11.5
10	15	5	7.3
11	15	5	7.3
12	20	5	6.5
13	15	0	0.0
14	5	5	9.8
15	15	5	7.3
16	10	10	16.4
17	5	10	19.0
18	10	0	0.0
19	30	5	5.3
		Average	**8.2**
		Max	**19.0**
		Min	**0.0**

Table 7-1 Dispersion of the tyre chips in the drop experiment.

The angle α is indicated in Fig. 7-3. It is the deflection of the initial trajectory of the tyre chip from the centre line of release perpendicular to the plate. It was determined from the point where the tyre chip first hit the ground at co-ordinates (h,l) from the strike point as indicated in Fig. 7-3.

There are many factors affecting the initial trajectory of the tyre chips:

- mass feed rate
- free wire on chip edges
- the surface of the delivery chute
- behaviour at the end of the screw conveyor

The model tyre chips were assumed to behave in two ways – they either dropped individually from the end of the screw conveyor then bounced off of the delivery chute, or slid down the delivery chute. The velocity after sliding 1m down a frictionless chute was determined by simple calculation. The dispersion of the tyre chips indicated by the experiment was used for the dropped chips. The chips were dispersed across a 34° arc from the chute entry point and the horizontal and vertical components of the velocity were

determined by considering the bounce from the 60° inclined plane with assumed coefficients of restitution in the parallel and perpendicular directions.

7.2 Combustion properties of tyre chips

7.2.1 Analysis of tyre material

The work done for Blue Circle by International Combustion (1993) included thermogravimetric analysis and trace metal composition analysis. The results show good agreement with the published data according to Williams et al (1990), Conesa et al (1998), and Schrama et al (1995) included in Chapter 2 (Section 2.6, Table 2-2). Since the temperatures in the precalciner are not sufficiently high to decompose the iron wire, it was considered for this work that the wire is part of the ash content. The ash content was disregarded altogether and only char and volatile decomposition was considered. The trace metals analysis is useful for emissions analysis, but was not of interest for this thesis and was disregarded. The model tyre material comprised 37% char and 63% volatile. The volatile was butadiene, C_4H_6.

7.2.2 Combustion air

No air was injected with the tyres in order to simplify the modelling process. In this way the block-structured mesh developed for Chapter 5 provided a suitable start point for the tyre chip model. To modify the mesh to add a tyre chute would require remodelling the geometry, which is time consuming. The assumption of no feed air with the tyre chips is reasonable since induction of air is restricted by enclosure of the feed mechanism all the way to ground level at the feed hopper. A bucket elevator is used to raise the tyre chips 30m and then an enclosed screw feeder transports them about 5m to the delivery chute.

7.2.3 Physical aspects of tyre chip combustion

As discussed in section 2.6, some there is little experimental data in the literature to determine a suitable model of tyre combustion rate. Experiments were performed as part of this work to establish the characteristics of tyre material in an environment as similar as possible to the inside of the precalciner vessel. Small tyre chip samples were analysed using an ashing furnace. Chips were put into the ashing furnace at 900°C with the door of the

furnace kept open for the duration of the test to cause circulation of air around the sample. The progress of the test is illustrated in Fig. 7-4a-e and Fig. 7-5a-c. It can be seen that for this 7.5-gramme sample, the flame has extinguished at approximately 2 minutes. The analysis of the material remaining after the test indicates that the lost fraction corresponds to the evolution of the volatile fraction of the tyre. A pile of wire and char granules remained. The disintegration was first to small granules of char of approximately 3-mm characteristic dimension. The char granules had a density of approximately 70 kg/m^3. Further decomposition of the char with a gas-solid reaction was observed for between 15 and 25 minutes depending on the sample thickness.

A sample of a 3.36-gramme chip, which was removed from the furnace to cool immediately after flame extinction, was inspected. The char granules were entirely free of the wire and the structure of the initial chip had completely disintegrated. The char granules are shown in Fig. 7-5(c). The proximate composition of this chip is detailed in Table 7-2.

chip	3.36g	100%
wire	0.62g	18%
char	1.00g	30%
loss	1.74g	52%

Table 7-2 Composition of test piece.

Based on the information from these experiments, the devolatilisation rate for the tyre material in the model was decided. Using the values of the devolatilisation constant in the available literature was not realistic since the size of the tyre chips in this work was so much larger. The maximum dimension of tyre material tested in the literature was less than 3-mm (Leung and Wang, 1999). It was decided to use the experimental observations to set the rate of volatile yield. Since the volatiles evolved in approximately 2 minutes in a relatively static atmosphere for all chips tested, the devolatilisation process in the precalciner with turbulent gases would occur more quickly as the heat transfer would be greater. It was thought that the rate of decomposition was dependent mainly on the chip thickness, which was usually within the

range 8 to 15-mm. These ideas suggest further experimentation, but time did not allow for this during the course of the investigation. The tyre chip devolatilisation behaviour was modelled as constant rate over 30 seconds for all chip sizes. Further investigations might involve the following: holding a tyre chip with tongs through one of the access ports in the precalciner wall and observing the increased oxidation activity; investigating the behaviour of a larger sample of tyre chips in the ashing furnace.

7.3 Aerodynamic properties of tyre chips

The size and shape of tyre chips were expected to determine aerodynamic behaviour. Samples were taken and analysed twice during the work. In 1996, the sieve size on the tyre chipper, which determines the maximum tyre chip size, was set to two inches. Figure 7-6a-f shows a typical sample of tyre chips at that time. Each figure shows a 6" rule at the centre (to give an indication of the scale), the mean mass of tyre chips in that size range, the mass used in the model and the mass found in the sample. In 1999, the sieve size was reduced to one inch. A further sample was taken at that time.

Tyre chip aerodynamic behaviour in the model was determined from experiment, theory and the features of the mathematical model available in Fluent. Prior to the commencement of this current work, experimental investigations had been performed in a wind tunnel to determine the drag coefficient of tyre chips (Ritter, 1995). The data was used in this project to provide initial modelling characteristics for the tyre chips. Further experimental work was done during this work to investigate how tyre chips behave when they are subject to free fall under gravity supported by a vertical stream of air. A novel technique for simulating the change from whole chip to char granule aerodynamic behaviour was developed. In the subsequent sections, the samples are described, previous work presented, char modelling is defined and the new experimental work presented.

7.3.1 Tyre chip size distribution

A sample of 5 kg of tyre chips was taken in April 1997. The chips had been cut when the knives on the chipper had been fitted for some time but were still sharp so that the edges were well defined and overhanging wire was not

excessive. The sample was sorted by maximum dimension and the following table of data was collected.

Tyre chip sizes

Size	Sample mass (kg)	%	No	Mass per chip (g)
6",48g	0.476	12	10	48
5", 31g	0.596	15	19	31
4", 30g	1.36	33	45	30
3", 16g	1.222	30	78	16
2", 5g	0.326	8	68	5
1", <5g	0.094	2		
total	4.074			

Table 7-3 Tyre chip size analysis

Various chips from each size category are displayed in Fig. 7-6 to indicate the random shape of the chips. It is clear that the mass of the chips varies from the mean since they have quite different shapes. The size data resulted in the distribution illustrated in Fig. 7-7a.

In addition to this sample data, a further sample in November 1999 resulted in a different size distribution illustrated in Table 7-4.

Size	Sample mass (kg)	%	No	Mass per chip (g)
6",30g	0.03	0.4	1	30
5",28g	0.056	0.8	2	28
4",19g	0.684	10.0	36	19
3",12g	3.562	52.1	294	12
2",6g	2.284	33.4	386	6
1",2g	0.226	3.3	94	2
	6.842			

Table 7-4 Tyre chip size analysis in November 1999

and this data is illustrated in Fig. 7-7b.

There was an obvious shift toward smaller chips in the later sample illustrating the effectiveness of the changes to the tyre chipper. The change

was made in an attempt to improve the combustion of the tyre chips, to reduce accumulation of tyre deposits.

This data was used in conjunction with the aerodynamic data to correlate tyre chip mass to aerodynamic behaviour. The injection rate of differently sized tyre chips was then determined together with the aerodynamic behaviour of that group of particles. The size distribution in Fig. 7-7a was used to set the proportion by mass of tyre chips in the initial models compared with the actual as illustrated in Fig. 7-6a-f.

7.3.2 Previous aerodynamic experiments and models available in Fluent

Ritter (1995) investigated the drag coefficients of various sized tyre chips in previous work on the Cauldon precalciner project. Experiments were performed in a wind tunnel to establish the drag coefficient. The drag was found to be maximum when the tyre chip was presented with the largest, flat face perpendicular to the flow ("face on" presentation) and smallest when the area presented was least ("side on" presentation). The two orientations are illustrated in Fig. 7-8a. The idea of the equivalent sphere, i.e. one having the same drag properties, is indicated in the figure. Ritter assumed that spheres having the same drag as the tyre chip in the two orientations could represent the behaviour of tyre chips. The density of the sphere was calculated from the volume to give it the same mass as the tyre chip. The details of the findings of Ritter's wind tunnel experiments are included in Table 7-5. The experiment was conducted for a sample of ten tyre chips. The mass was recorded and the maximum and minimum cross sections measured and recorded; the samples were mounted in the wind tunnel in the two orientations and the drag force measured for each. The terminal velocity of the tyre chip in each orientation is indicated in the column to the right of each set in blue text.

		face on flow					side on flow				
chip number	mass g	cross section cm^2	drag coefft	sphere diameter cm	density kg/m^3	Vt	cross section cm^2	drag coefft	sphere diameter cm	density kg/m^3	
6	8	12.5	1.34	6.8	48	10.1	3.0	4.33	6.1	69	11.4
3	8.4	23.0	1.31	9.0	22	7.7	4.5	3.20	6.4	62	11.1
10	15	19.2	1.51	8.9	41	10.5					
5	20.5	24.3	1.26	9.1	52	11.9	5.5	2.95	6.7	128	16.4
9	22	27.8	1.48	10.5	36	10.7	8.3	2.34	7.3	107	15.5
8	25	36.1	1.06	10.1	46	11.8	9.0	1.54	6.3	196	19.6
7	26	25.5	1.26	9.3	61	13.1	7.0	1.94	6.2	209	20.2
2	28	24.5	1.03	8.3	93	15.3	8.0	1.80	6.4	207	20.3
1	34	25.8	1.31	9.5	75	14.6	5.4	2.84	6.6	230	21.7
4	54	57.0	1.30	13.9	38	12.4	11.2	1.53	6.9	313	25.9

Table 7-5 Results of the investigation by H.Ritter at The University of Nottingham.

Equivalent sphere diameters were calculated using the Eq. 7-1:

$$C_{d,sph} = a_1 + \frac{a_2}{\mathrm{Re}} + \frac{a_3}{\mathrm{Re}^2} \qquad \textbf{Equation 7-1}$$

where a_1, a_2 and a_3 are constants presented in Table 2-3. The drag force on the tyre chips in the wind tunnel is represented by the equation 7-2,

$$F_d = C_d \frac{1}{2} r_g U^2 A \qquad \textbf{Equation 7-2}$$

Eliminating C_d from these equations and rearranging yields equation 7-3 for determining the diameter of a sphere having the same drag coefficient as the tyre chip (from Ritter, 1995).

$$D_p = \frac{-a_2 m + \sqrt{(a_2 m)^2 - 4 a_1 r_g \left(a_3 \frac{m^2}{r_g} - \frac{8}{p} F_D \right)}}{2 a_1 r_g U} \qquad \textbf{Equation 7-3}$$

Ritter's results were used in the initial stage of tyre chip modelling.

7.3.3 Tyre chip disintegration modelling

Particles in Fluent trajectory calculations are considered to be points with no length dimensions and take no volume in the modelled gas – the diameter is used only for drag force calculations. A swelling coefficient can be defined that determines the final size of the tyre chip after complete devolatilisation. The Fluent particle tracking routine increases particle diameter linearly with volatile component release. It is not possible using the standard code to

simulate particle break-up, so an alternative solution was found. Since the devolatilisation process converts the tyre chip from whole to char granule, the swelling coefficient can give a reasonable simulation of the behaviour. The char granules remaining after devolatilisation have approximately 3mm-diameter and 70 kg/m^3 density. Using the swelling coefficient, the drag coefficient of the tyre chip was altered to simulate the drag of the char granule.

The particle tracking routine caused a relatively high density sphere representing a single tyre chip to expand to a low density large sphere to represent the aerodynamic behaviour of a single char granule, but the mass of many. The acceleration response to the same flow had to be the same for the sphere and granule. The following section illustrates the procedure used to formulate an expression for the swelling coefficient.

Using the drag force and Newton's Second Law:

$$\mathrm{F}_D = C_D \frac{1}{2} rU^2 A \text{ and } a = \frac{F_D}{m_p}$$

Where F_D is the drag force and m_p is the particle mass. Equating the acceleration:

$$\frac{F_{Dp}}{m_p} = \frac{F_{Dg}}{m_g} \Rightarrow \frac{C_{Dp} \frac{1}{2} rU^2 A_p}{m_p} = \frac{C_{Dg} \frac{1}{2} rU^2 A_g}{m_g} \Rightarrow \frac{C_{Dp} A_p}{m_p} = \frac{C_{Dg} A_g}{m_g}$$

Where the suffix *g* indicates granule and *p* indicates the swelled tyre chip. Assuming a swelled diameter of approximately 0.4m as an initial estimate and approximate conditions of free-stream velocity and density, the appropriate Reynold's number for each "particle" was calculated.

$$\text{Granule: } \mathrm{Re}_g = \frac{rUD_g}{m} = \frac{0.3 \times 10 \times 0.003}{5 \times 10^{-5}} = 180$$

$$\text{Tyre chip: } \mathrm{Re}_T = \frac{rUD_p}{m} = \frac{0.3 \times 10 \times 0.4}{5 \times 10^{-5}} = 24{,}000$$

Drag coefficients were calculated using the appropriate form of the Morsi and Alexander equation for each Reynold's number (Table 2-3):

For the granule, 100<Re<1000,

$$C_D = \frac{98.33}{\mathrm{Re}} - \frac{2778}{\mathrm{Re}^2} + 0.3644 = 0.8249$$

For the particle, 12,600<Re<36,000,

$$C_D = -\frac{1662.5}{\mathrm{Re}} + \frac{5.4167\times10^6}{\mathrm{Re}^2} + 0.5191 = 0.459$$

The mass of the typical char granule was calculated from the approximate density, of 70 kg/m^3 and the approximate diameter of 3mm.

$$m_g = \frac{p}{6}0.003^3 \times 70 \text{ and } A_g = \frac{p}{4}0.003^2$$

The mass of the fully swelled tyre chip is the initial mass minus the volatile fraction, f_{v0}.

$$m_p = M_{p0}(1 - f_{v0}) \text{ and } A_p = \frac{p}{4}D_p^2$$

Inserting these values in to the equation 1 above:

$$D_p = \sqrt{16.34 M_{p0}(1 - f_{v0})} \qquad \textbf{Equation 7-4}$$

Equation 7-4 is the required formula for calculating the swelled diameter of a tyre chip of initial known mass and volatile content, which gives the same aerodynamic characteristics as the char granule.

Application of this formula produced the data in Table 7-6 for the tyre chips inspected by Ritter (1995). Tyre chips were selected to give a summary of the behaviour of the range of chips available. From the initial selection of ten tyre chips, the properties of five were used (highlighted in yellow/blue in Table 7-5) to represent each of the size ranges illustrated in Fig. 7-6. The method assumed that the tyre chip remained in the same orientation throughout its track history in the model. Although this is physically unrealistic, it is a simplifying assumption that illustrates the limiting behaviour of the tyre chips. The chips are arranged in sets of two in Table 7-6 having the same initial mass. The first of each pair is the face on presented chip and the second is the side on presented chip. Five groups of six side-on drag and five groups of five face-on drag tyre chips were injected.

Model chip identity	Initial diameter (mm)	density (kg/m^3)	Initial mass (g)	Final diameter Dp (mm)	Swelling coefficient Sw
tc1	88	23	8.2	209	2.38
tc2	61	69	8.2	209	3.43
tc3	89	56	20.7	332	3.73
tc4	65	142	20.4	330	5.08
tc5	81	102	28.4	389	4.81
tc6	61	230	27.3	382	6.26
tc7	93	80	33.7	424	4.56
tc8	63	255	33.4	422	6.70
tc9	137	40	53.8	536	3.92
tc10	67	344	54.1	538	8.03

Table 7-6 Calculation of tyre chip char granule model diameter and swelling coefficient.

The final diameter is the diameter after swelling has stopped. The mass of the char in the model tyre chip is far larger than a single char granule. The energy contribution to the gases as the char burns required dispersal from the single chip to simulate the release of many char granules. The issue was overcome to some extent by using the stochastic dispersal model with twenty stochastic attempts.

7.3.4 Experimental investigation of the whole tyre chip aerodynamics

Tests were performed in a specially constructed vertical air pipe rig. The construction of this is shown in Fig. 7-8b and photographs of the rig appear in Fig. 7-9.

The important features of the rig were:

- The test section, an 8" diameter perspex pipe, was designed to enable tyre chip behaviour to be seen
- An upward air stream velocity of 5 to 20 m/s
- A Pitot tube mounted on the top of the perspex section to measure flow velocity
- A gauze sheet placed near the top of the perspex section, where the flow was expected to be fully developed to support the tyre chip when the velocity was lower than the terminal velocity
- A speed controller attached to the motor powering the fan, which was a pulse-width modulator invertor

- Video equipment mounted close by to record the behaviour of the tyre chips.

Six tyre chips in each of the 6 size ranges illustrated in Fig. 7-6 were selected and tested in the rig. The results showed terminal velocity and qualitative aspects of the tyre chip behaviour. The quantifiable features measured are presented in Table 7-7.

Maximum dimension (inches)	Chip number	Chip mass (g)	Chip thickness (mm)	Face-on surface area (cm^2)	Observed terminal velocity (m/s)	Drag coefficient C_d	Terminal velocity at 900°C (m/s)
2	1	8.6	15	5.5	13.5	1.43	26.7
	2	5.1	12	5	12	1.18	23.8
	3	7.4	10	6	13	1.22	25.7
	4	6.2	10	6	13	1.02	25.7
	5	8.2	8	10	11	1.13	21.8
3	1	18.7		12.5	15	1.11	29.7
	2	11.6		19	11.5	0.77	22.8
	3	36.6		25	13.5	1.34	26.7
	4	19.6		16	13.5	1.12	26.7
	5	6.1		11.5	10	0.88	19.8
4	1	30.4	12	26	14	0.99	27.7
	2	28.4	10	26	11	1.50	21.8
	3	28.4	8	28	12	1.17	23.8
	4	16.5	5	23	10	1.20	19.8
	5	32.5	10	29	12	1.30	23.8
5	1	55.4	15	40	13	1.37	25.7
	2	22.8	5	37	11	0.85	21.8
	3	28	5	29	12	1.12	23.8
	4	29.3	2	40	12	0.85	23.8
	5	28.6	10	30	12	1.10	23.8
6	1	28	3	51	10	0.92	19.8
	2	30	7	27	12.5	1.19	24.8
	3	42.3	8	48	11.5	1.11	22.8
	4	65.8	10	52.5	12	1.45	23.8
	5	39.3	10	36	11	1.50	21.8

Table 7-7 Results from the tyre chip flotation rig.

Tyre chips were placed on the gauze in the perspex tube and the fan speed increased until the chip was just supported and floating freely in the air stream. Table 7-7 shows the velocities that were observed and the drag coefficients calculated from the velocity and the tyre chip mass and face area. The face area was used for the calculation of C_d since the chips presented the maximum area to the flow. The tyre chips "wobbled" on the supporting air stream, moved around the circumference of the tube and snagged in the gauze. Despite the instability of the motion, the general trend was that tyre chips

present the maximum area to the flow. This is a useful observation since it indicates that it is mainly the face area of tyre chips that determines drag in the precalciner.

Another interesting feature of the results was the terminal velocity range. The range in each group of tyre chips was the same across the whole size range, varying between 10 and 15-m/s. The estimated terminal velocity range in the precalciner at 900°C is 21.8 to 29.7 m/s, assuming air density calculated using the perfect gas law. The results were used to make predictions of tyre chip destinations within the precalciner.

7.4 Original model with tyre chips added

The initial model developed to include tyre chips was based on the model described in Chapter 5. The coal mass injection rate was reduced and tyre chips were added. The properties of the tyre chips were set according to the data in the preceding sections. The injection point was set according to Fig. 7-2. Tyre chip injection velocities were set to the sliding tyre chip velocity in one case and to the dropped tyre chip velocity in the second. The results of the CFD models showed the likely trajectories of the tyre chips in the two orientations with the two injection conditions.

The injection point of the tyre chips is illustrated in Fig. 7-10a-c. Figure 7-10a shows the point of injection from a side position. Figure 7-10b and c show the initial trajectories of the dropped and sliding injection respectively from the top. The first models assumed the tyre chips travelled in the direction of the feed screw. A spread of 34° was applied to the dropped chips to simulate the behaviour observed during the chip dropping experiment in section 7.1.2. Chips were injected with the characteristics in Table 7-6. The proportion of mass injection for each of the five sets of two chips was set according to Fig. 7-6 to give a size distribution similar to the first sample in section 7.3.1.

7.4.1 Temperature field effects of tyre chips

The temperature in the precalciner vessel modelled with tyre chips present was similar to the temperature with coal only as illustrated in Chapter 5. However the change due to the tyre chip injection is obvious in parts of the vessel. For

example, a new high temperature region can be seen, referring to Fig. 7-11 a high temperature region is present directly below the initial release point of the tyre chips in both cases with the sliding chips and the dropped chips (Fig. 7-11 illustrates the sliding entry case). The high temperature region is consistent with the initial trajectories of the tyre chips, which tend to roll around on the wall in the conical section. Figure 7-11 (c) shows the concentration of the tyre volatile material on six horizontal levels in the conical section showing that a large amount of volatiles is released in that region.

7.4.2 Model explanation of tertiary air duct blockage

The most interesting information from the results of the coupled CFD calculations was the trajectory history of each of the tyre chip group injections. Figures 7-12 and 7-13 show the trajectories of the dropped and sliding entry tyre chips respectively. For the dropped tyre chip injection, numbers 4 to 10 predicted that one trajectory entered the tertiary air inlet. Several other injection points were assessed using non-coupled tyre trajectories in order to determine whether tyre chips entered the tertiary air inlet under other circumstances. Once the tyre chips had gone past the initial trajectory and were influenced then only by the gas momentum, no tyre chips entered the tertiary air inlet regardless of initial injection point in the precalciner. The deduction from this observation is that tyre chips can only enter the TAD if they are directed toward it upon injection with sufficient velocity to overcome the drag of the tertiary air. The result of this is blockage after three-month's operation similar to that illustrated in Fig. 1-5c. The model suggested that one of the six trajectories of injections 4 to 10 went into the tertiary air inlet. This represents sizes 4" and above in Fig. 7-7, the amount of tyre chips falling into the tertiary air inlet is approximately 10.3%, of which about 12% is ash. Applying a realistic feed rate of 2 tonne per hour for three months, this indicates a build up of about 17 tonnes of tyre debris. Assuming this is wire of density 7000 kg/m^3, the volume is 2.5 m^3. With reference to Fig. 1-5c in the 1.8m diameter tertiary air inlet, this appears to be a reasonable estimation of the build-up.

7.4.3 Model explanation of tyre material build-up on walls

Inspection of the inside of the precalciner during shutdown also showed that tyre chip wire collected in “nest” shaped bundles on the conical section walls. The CFD model predicts this behaviour. Initially all dropped tyre chips first rebounded off of the conical section wall opposite the injection point before proceeding into the main stream of the precalciner gas flow. In practice, with a rough refractory surface, sticky, hot tyre chips yielding sticky volatiles might well stick to the surface until the volatiles were yielded and in this way a nest may build up. Smaller tyre chips tended to circulate on the conical section opposite the tertiary air inlet, illustrated in Fig. 7-12, while the volatile component was released. In the case of drop injected tyre chips, only injections 1 to 3 behaved in this way. Of the sliding entry chips (Fig. 7-13), all the face on presentation chips and the two smallest side on presentation chips circulated on the conical section wall. The initial trajectory in this case caused the chips to rebound from the conical section wall directly below the injection point. Thus there are three regions on the conical section wall where tyre chip build-up was predicted by the model. Further tyre chip wire deposition was evident at the exit duct connecting the precalciner to the stage 4 cyclone. Inspection of Fig 7-12 and Fig. 7-13 shows that this is likely to be caused by the tyre chips landing there after being carried upward by the main stream gases in the precalciner and dropping out into the exit duct.

7.4.4 Model explanation of reduced kiln NO_x due to tyre chips

A large proportion of the larger tyre chips penetrate the neck of the precalciner and fall into the kiln as shown in Fig. 7-12 when the drop tyre chip injection is considered. Measured NO_x level changes at the back end of the kiln indicate that this is likely. Process data shows that the introduction of tyre chips to the process resulted in an improvement of the back end NO_x as also noted at other plants (section 2.2.4). A decrease in NO_x measured at the back end is consistent with tyre chips falling into the kiln directly from the base of the precalciner. This is because of the large amount and rate of volatile release from each chip, which creates a local reducing environment, which converts NO_x products produced in the kiln into harmless combustion products (section 2.2.3).

7.4.5 Effect of tyre chips on calcination of the raw meal

The raw meal reaction level and residence times for the dropped entry condition are shown in Fig. 7-14 and those for the sliding entry condition in Fig. 7-15. The residence times are little changed by the addition of the tyre chips since the aerodynamic characteristics of the flow are not greatly affected by the changes in combustion. The reaction level in both cases was approximately the same as the model without tyre chips, i.e. 74% in the original model to 74% in the sliding entry case and 71% in the dropped entry case. The behaviour is of similar form. Some of the chips exit through the kiln

	average time (sec)	maximum time (sec)	minimum time (sec)	start mass (kg)	end mass (kg)	volatiles consumed (kg)	volatiles consumed (%)
1	18.6	26.8	10.0	0.020	0.012	0.008	62%
2	22.0	30.3	12.9	0.020	0.011	0.009	73%
3	16.9	24.7	3.6	0.083	0.045	0.038	73%
4	2.6	3.3	1.2	0.083	0.079	0.004	8%
5	2.9	4.0	1.3	0.083	0.079	0.005	9%
6	2.4	2.7	1.2	0.084	0.080	0.003	7%
7	5.0	14.2	1.3	0.036	0.033	0.003	14%
8	2.3	2.6	1.2	0.037	0.035	0.001	6%
9	9.9	16.4	1.4	0.029	0.023	0.006	32%
10	2.2	2.5	1.2	0.029	0.028	0.001	5%
			Overall	**0.504**		**0.079**	**25%**

(a) Dropped entry tyre chips

	average time (sec)	maximum time (sec)	minimum time (sec)	start mass (kg)	end mass (kg)	volatiles consumed (kg)	volatiles consumed (%)
1	19.7	50.0	11.1	0.020	0.011	0.010	77%
2	61.6	118.2	21.0	0.020	0.008	0.012	94%
3	37.1	52.2	22.6	0.083	0.033	0.050	96%
4	28.1	41.8	14.7	0.083	0.039	0.044	85%
5	24.1	46.6	18.0	0.083	0.046	0.038	72%
6	2.8	2.9	2.8	0.084	0.079	0.005	9%
7	23.3	46.5	14.2	0.036	0.021	0.015	68%
8	2.7	2.8	2.7	0.037	0.034	0.002	9%
9	29.1	45.0	24.5	0.029	0.013	0.016	89%
10	2.5	2.6	2.5	0.029	0.027	0.002	8%
			Overall	**0.504**		**0.194**	**61%**

(b) Sliding entry tyre chips

Table 7-8 Data for tyre chip exit behaviour.

gas inlet (chips 6, 8, and 10 in Fig. 7-13). The release of energy from those tyre chips is incomplete. Table 7-8 shows the exit behaviour of the sliding and

dropped entry tyre chips. Relating this table to the Figs. 7-12 and 7-13, tyre chip destinations were different in the two cases, and this affected the residence time, which affected the amount of reaction. Most tyre chips were in the precalciner for less than the 30 seconds for devolatilisation. The data shows that the overall volatile release in the precalciner is significantly less for the drop injected tyre chips. Inspection of the trajectories shows that more chips falling into the kiln in that case caused the effect. In practice, the tyre chips that fall into the kiln deliver their energy into the system as they will burn in the hearth of the precalciner, at the join with the kiln.

7.5 Accelerator model with tyre chips

The accelerator described in Chapter 6 was added to the plant at the same time as the alteration to smaller chip size described in section 7.3.1. The mass injection of the chips was changed in the model to reflect the change in the chip size distribution. In this case only tyre chips in the smaller size ranges up to 4" maximum dimension were considered and the size distribution illustrated in Fig. 7-7b was used in the model. The rate of tyre chip injection to the model was 1 kg/s with 1.5 kg/s of coal injection.

Operational changes at the plant were noticed when the accelerator was added and the tyre chip mean size was reduced. Less tyre chip material entered the kiln back end via the kiln gas inlet. Evidence of this was the reduction in tyre material build-up at the back end and an increase of the NO_x measurement at the back end probe since back end NO_x is effectively reduced by the presence of tyre material. More char and wire from the tyre chips was collected in the raw meal sample at the exit from the stage 4 cyclone than before, indicating greater carry-over of tyre material from the precalciner to the stage 4 cyclone.

Results from the model showed that the tyre chip reaction and aerodynamic behaviour in the vessel is different from tyre chips in the model of section 7.4. The table 7-9 compared with table 7-8 illustrates that for the dropped tyre chips in both models, the accelerator model improves the residence time and volatile release of the tyre chips. Figure 7-16 supports the data by showing that the first six tyre chip sizes circulated in the cylindrical section more than in the previous model illustrated in Fig. 7-12. Figure 7-17a

and b show how the accelerator tends to prevent tyre chips from entering the tertiary air duct. The right hand injection group is blocked from directly heading towards the TAD in Fig. 7-17a. It was found that the only way to get tyre chips into the tertiary air duct was along a very small range of likely injection trajectories based on the dropped chip data. Once chips were beyond the effects of the initial trajectory, they did not enter the tertiary air duct. Figure 7-17b shows that one injection of the group (on the right hand side) entered the tertiary air duct. Figure 7-16a shows that the chip was prevented from doing so by the accelerator being in the way.

	Average time (sec)	maximum time (sec)	minimum time (sec)	start mass (kg)	end mass (kg)	volatiles consumed (kg)	volatiles consumed (%)
1	19.3	40.6	7.6	0.1668	0.105	0.062	59%
2	22.5	41.2	6.2	0.1665	0.095	0.071	68%
3	27.9	40.1	17.1	0.2802	0.126	0.154	87%
4	6.3	12.1	1.3	0.28	0.245	0.035	20%
5	5.9	13.9	1.4	0.0498	0.044	0.006	19%
6	10.1	26.8	2.3	0.05	0.040	0.010	32%
			Overall	**0.9933**		**0.338**	**54%**

Table 7-9 Reaction of the dropped tyre chips in the accelerator model.

Additional improvement was caused by the shift of mass distribution to the smaller chips since larger chips were found to be harder to support against gravity. The carry over of tyre chip trajectories into the stage 4 cyclone is improved for the accelerator model, illustrated in Fig. 7-16, compared to the model without accelerator, illustrated in Fig. 7-12 and Fig. 7-13. Improved carry-over of tyre chips was indicated by observations at the plant of increased tyre debris found in the routine collection of raw meal at the base of the stage 4 cyclone.

Raw meal behaviour in the “accelerator” model is shown in Fig. 7-18. Coal and tyre chip residence times and reaction levels at exit are indicated in Fig. 7-19. The corresponding reaction and residence time of the raw meal in this case showed behaviour different to the previous tyre chip model (section 7.4) and the accelerator without tyre chip model (section 6.7 in Fig. 6-16 and 6-17). The residence times in the accelerator models are similar, but the level of reaction is quite different. In the cases with the accelerator, reaction is

significantly increased in the model with tyre chips (70%) compared with 30% for the model with coal only. The reason for this is the generation of energy caused by the tyre volatile material in the gaseous phase. The resulting increase in temperature from 1140°C (in the accelerator model without tyre chips) to 1470°C caused the coal to react fully in its short residence time.

7.6 Accelerator model with alternative tyre injection positions

The permitted rate of tyre usage at the works was increased by the Environment Agency during the course of this work, and methods of injecting increased amounts of tyre chips into the precalciner were sought. It was thought that an alternative injection position could be found using the CFD models. A number of alternative injection points for tyre chips were investigated in order to determine the best point of injection for additional tyre chips into the precalciner. The range of tyre chips described in section 7.5 was used and the injection was considered as dropped. The points of injection were decided before testing as follows:

- at the same height as the current tyre chip injection (approximately 1.5m above the start of the cylindrical section) at 8 equally spaced points on the circumference of the cylindrical section
- at an increased height of 5m from the current injection position at 8 equally spaced points on the circumference of the cylindrical section
- at 10 points on the roof 0.3m from the circumference of the cylindrical section with a downward velocity of 0.2m/s and a separating velocity between the first and last injection of each group of 0.1m/s.

These trial positions for the model were selected by considering the physical limitations of delivering the chips to the precalciner and by inspection of the CFD results with the current tyre position. The injections were performed un-coupled from the continuous phase on the model with tyre chips used in section 7.5. In this way the likely trajectory of the added tyre chips would be seen without the effect on the gases. A coupled solution was not attempted due to the large number of cases it would involve for each new separate injection in the short time scale of allowed for the work. Since the trajectory of each new injection and the resulting residence times were of interest and the total energy required for the balanced reaction was already present from the coupled

solution of section 7.5, the process used was the most efficient for the task. It was sufficient to show the features of interest, which were to investigate the likely trajectory of the chips, to see which would have a good residence time in the precalciner and would mix well with the raw meal.

Residence times and final destination of the tyre chips for each of the new injection points were analysed. A full list of the data is provided in the Appendix 5 to support the information supplied by the following figures.

A cursory examination of injection velocity variation suggested that it is not critical to final trajectory within the limits investigated. Further investigation is recommended.

Behaviour of chips injected at the current height (Fig. 7-20a-f)

Figures 7-20e,f show that the larger chips (about 10% of the tyres by mass) always enter the kiln. A good proportion of the 3" chips injected at points B, D, and I (Fig. 7-20c,d) escape through the outlet.

The following residence times and destinations were observed:

<2" chips	7-69 sec	all exit to St 4
<3" chips	7-71 sec;	D exits to St 4;
		B & I - 4 of 6 exit to St 4;
<4" chips	N/A	All exit to kiln.

Injection at current height indicated that all large tyre chips (10% of chips) exit to the kiln regardless of circumferential position. If the largest 10% are ignored then point D is a good injection point and points B and I may be acceptable.

Behaviour of chips entering at height +5m (Fig. 7-21a-f)

These results show that the 4" chips tend to exit through the kiln except for injection at points D, and F.

The following residence times and destinations were observed:

<2" Chips	6-50 sec;	all exit to St 4.
<3" chips	7-66 sec;	D & J exit to St 4;
		H & I - 5 of 6 exit to St 4;
		B, F & G - 4 of 6 exit to St 4.
<4" chips	8-43 sec	D exits to St 4; F - 4 of 6 exit to St 4

Injection at height +5m indicates that all chips exit St 4 from point D and that point F may be acceptable, including the largest chips. If the largest chips are ignored then points B, F, G, H, I and J may be acceptable.

Behaviour of chips injected at the roof (Fig. 7-22a-f)

The smaller chips (Fig. 7-22a,b) respond quickly to the gas flows; they "fall over" the high velocity region and head for the throat section. D and F injections "short circuit" to the exit duct. The results for the other two tyre chip sizes (3 and 4") show that the positions H, I and J result in chips falling into the tertiary air and raw meal inlet.

The following residence times and destinations were observed with exception of D and F injections:

<2" Chips	8-49 sec	all exit to St 4
<3" chips	9-83 sec	A, B, C, G & I exit to St 4
		E & J - 5 of 6 exit to St 4
		H - 4 of 6 exit to St 4
<4" chips	8-72 sec	C & G exit to St 4
		B - 5 of 6 exit to St 4
		I & J - 4 of 6 exit to St 4
		E - 3 of 6 exit to St 4
		A - 1 of 6 exit to St 4

Roof injection restricted the number of chips exiting via the kiln since the model shows that chips do not exit to the kiln. The results showed that tyre chips should never be injected in the region close to the stage 4 cyclone exit duct at the roof of the precalciner because chips <3" will short circuit to exit in 4-5 seconds. The central position on the roof is impracticable because of the relatively weak roof structure. Positions H, I and J should be avoided since chips released there fall to the kiln. The best injection points from the roof appear to be at G and C since all chips released from these points exit to the stage 4.

Injection in the raw meal inlet

Injection of chips at the raw meal inlet results in chips <2" rising to the St 4 exit and all others falling to the kiln.

Stochastic (random turbulence) effects

The height +5m injection was performed with 20 stochastic attempts, effectively multiplying the number of injections by 20 to 120 chips. The destination of these chips is recorded in Appendix 5 and can be compared with the data for the height +5m injection, to show that the proportion of chips exiting alternative boundaries is consistent with a larger sample. No residence times were determined due to time constraint of the project.

7.7 Conclusions

The results of the work described in this chapter demonstrated a successful technique for modelling tyre chips in the Cauldon precalciner.

- Tyre chip combustion characteristics were investigated experimentally in an ashing furnace at 900°C. Volatile material was completely yielded within 2 minutes. Observations suggested that it is the thickness of the tyre chip that determines the time for complete volatile release. Further experiments were suggested.
- Aerodynamic behaviour of the initially intact tyre chip was investigated experimentally using a purpose made tyre chip flotation rig. Observations showed that it is likely that the tyre chips prefer to face “into the wind”, i.e. to present maximum area to the flow.
- Tyre chips were added to the initial precalciner model. Several interesting observations were made including explanation of the reduced NO_x level at the kiln back end when burning tyre chips, the reason for tertiary air duct blockage and tyre material build-up on the walls.

- Tyre chips were also added to the model with the “accelerator” section. The accelerator improved the residence time of the tyre chips and prevented tyre chips entering the tertiary air inlet. Observations at the plant following the concurrent introduction of smaller mean tyre chip size and the accelerator section indicated good agreement with the model.

(a) (b)

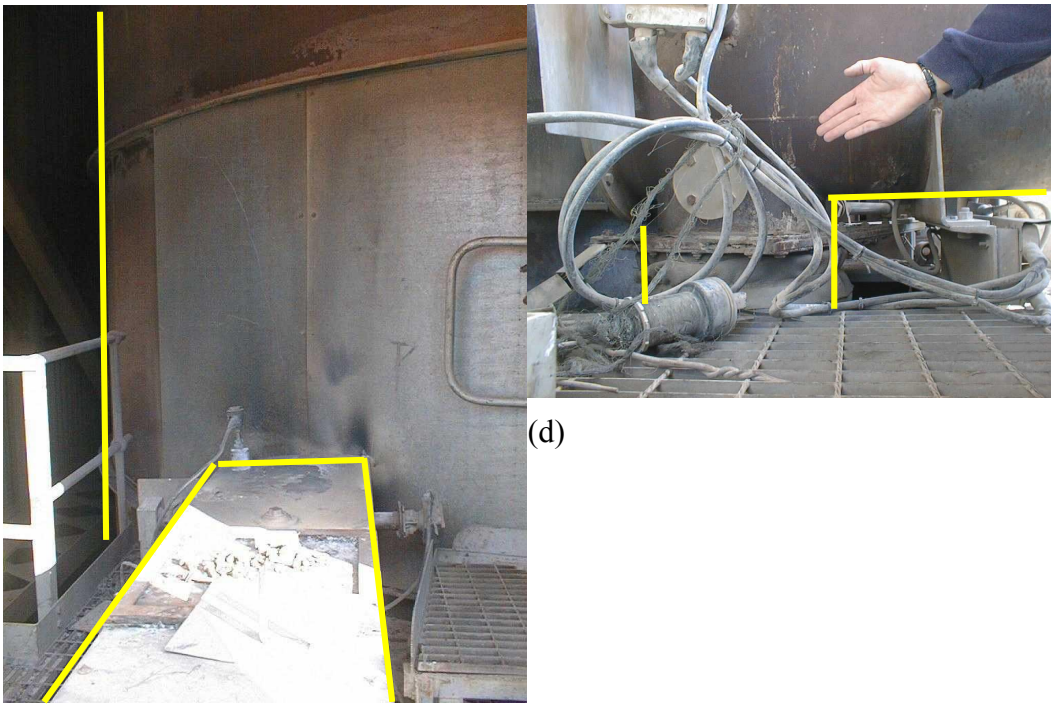

(c) (d)

Fig. 7-1 Photographs of the tyre chip feeder (a) looking from the kiln side (b) from the opposite side (c) along the screw feeder to the feed chute (d) the top of the feed chute.

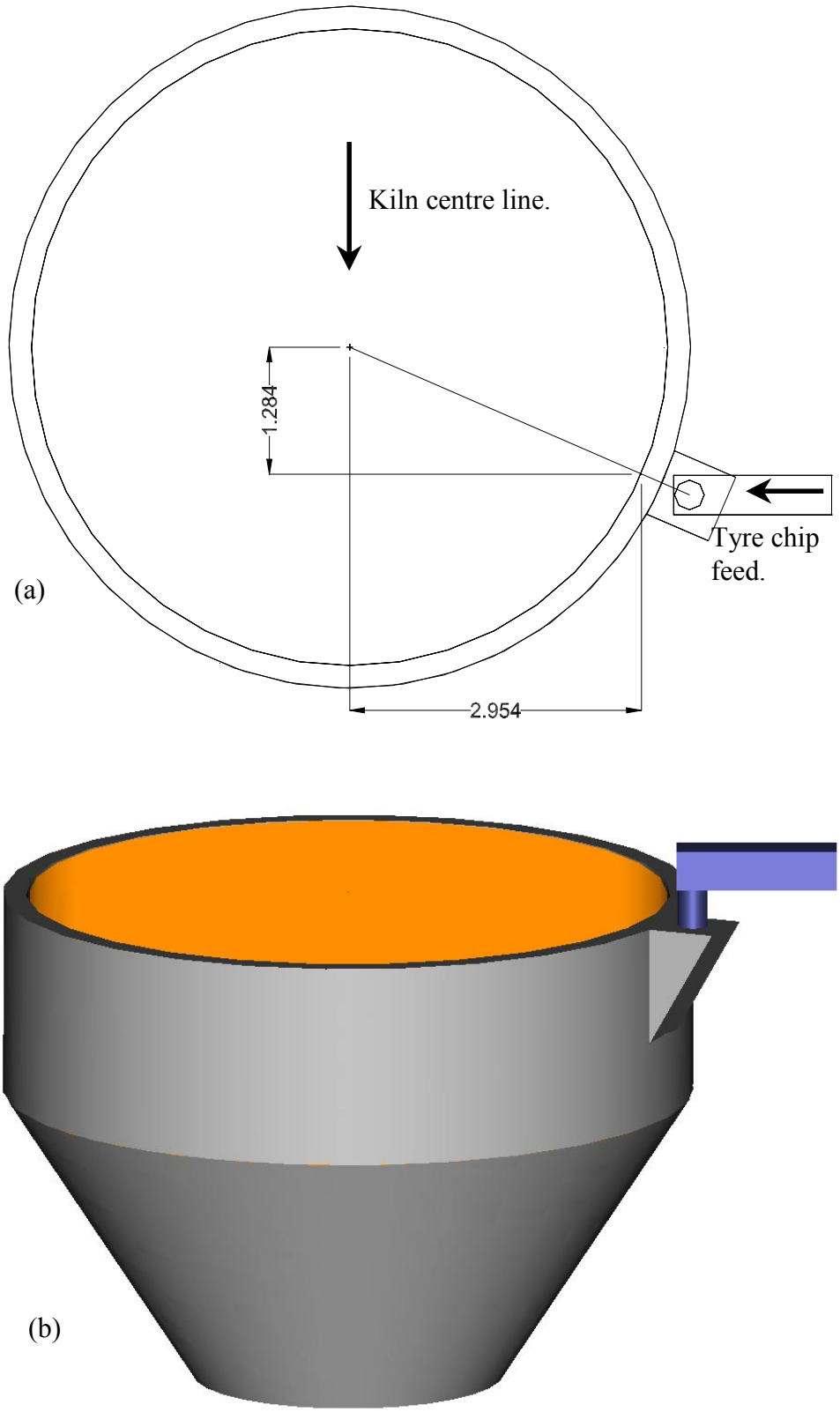

Fig. 7-2 Tyre feeder position – showing a plan view drawing and isometric section of the precalciner vessel with the cylindrical section removed (dimensions in m).

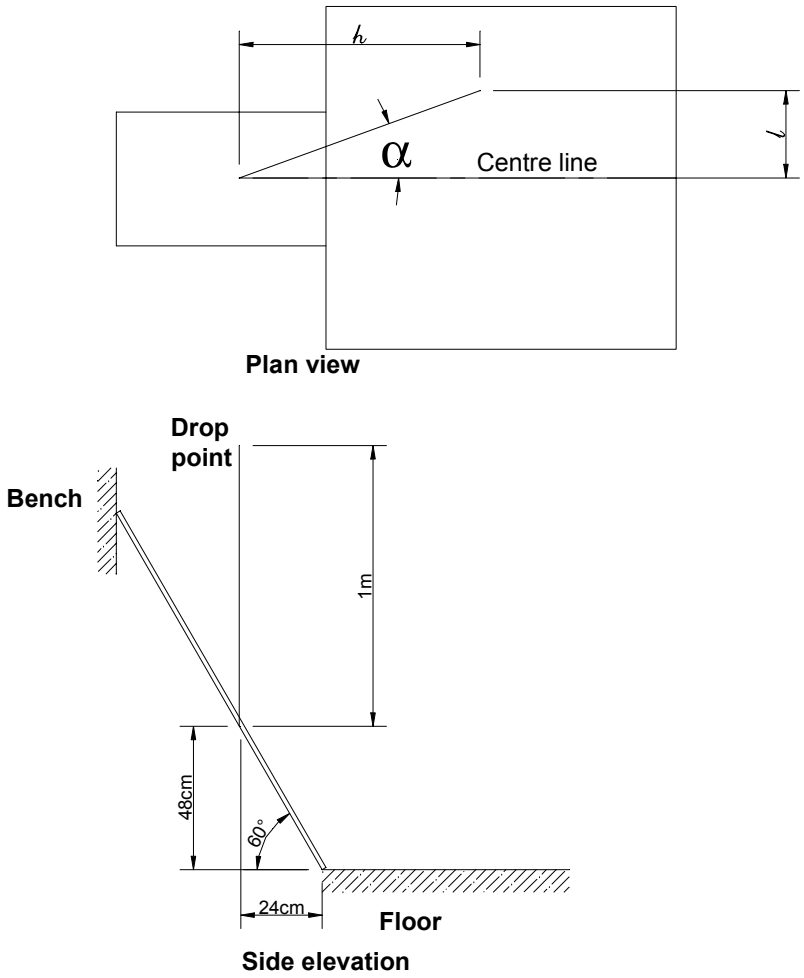

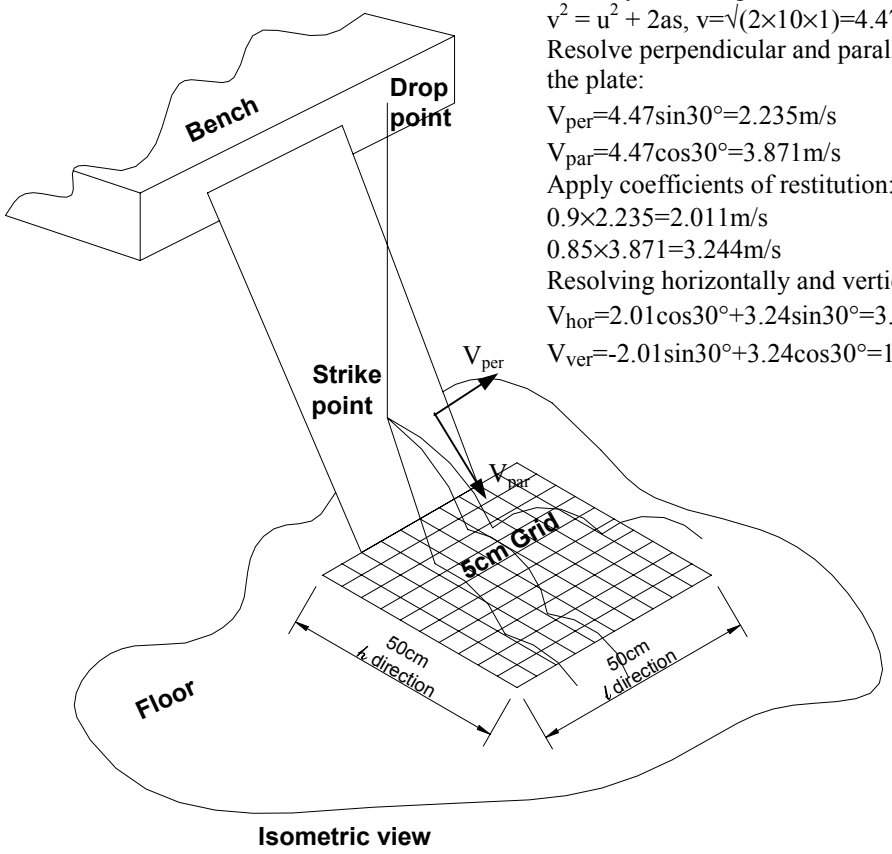

Calculation of vertical and horizontally velocity

Velocity at strike point:

$v^2 = u^2 + 2as$, $v=\sqrt{(2\times10\times1)}=4.47$m/s

Resolve perpendicular and parallel to the plate:

$V_{per}=4.47\sin30°=2.235$m/s

$V_{par}=4.47\cos30°=3.871$m/s

Apply coefficients of restitution:

$0.9\times2.235=2.011$m/s

$0.85\times3.871=3.244$m/s

Resolving horizontally and vertically:

$V_{hor}=2.01\cos30°+3.24\sin30°=3.37$m/s

$V_{ver}=-2.01\sin30°+3.24\cos30°=1.8$m/s

Fig. 7-3 Tyre chip drop experiment to assay the likely initial tyre chip trajectories.

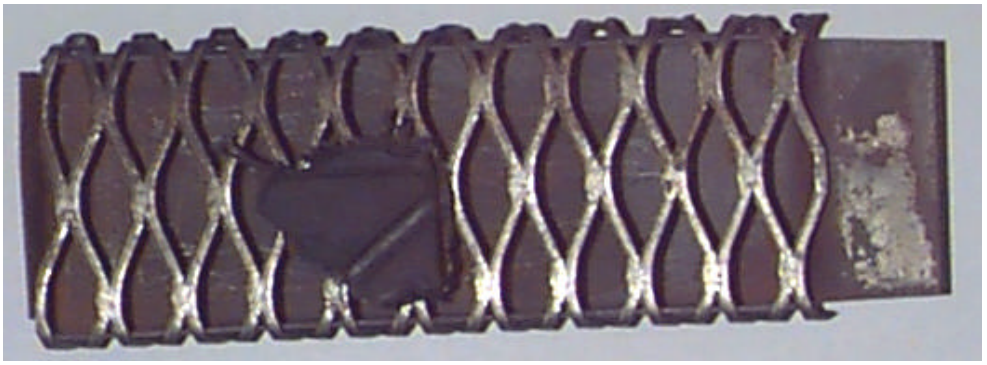

(a)

(b)

(c)

(d)

(e)

Fig. 7-4 Combustion of tyre chip at 900°C; (a) before test, (b) at ignition, (c) at ignition + 30s, (d) at ignition + 1 min, (e) at ignition + 2 min. A bright gas-gas flame was observed while the volatile components were released.

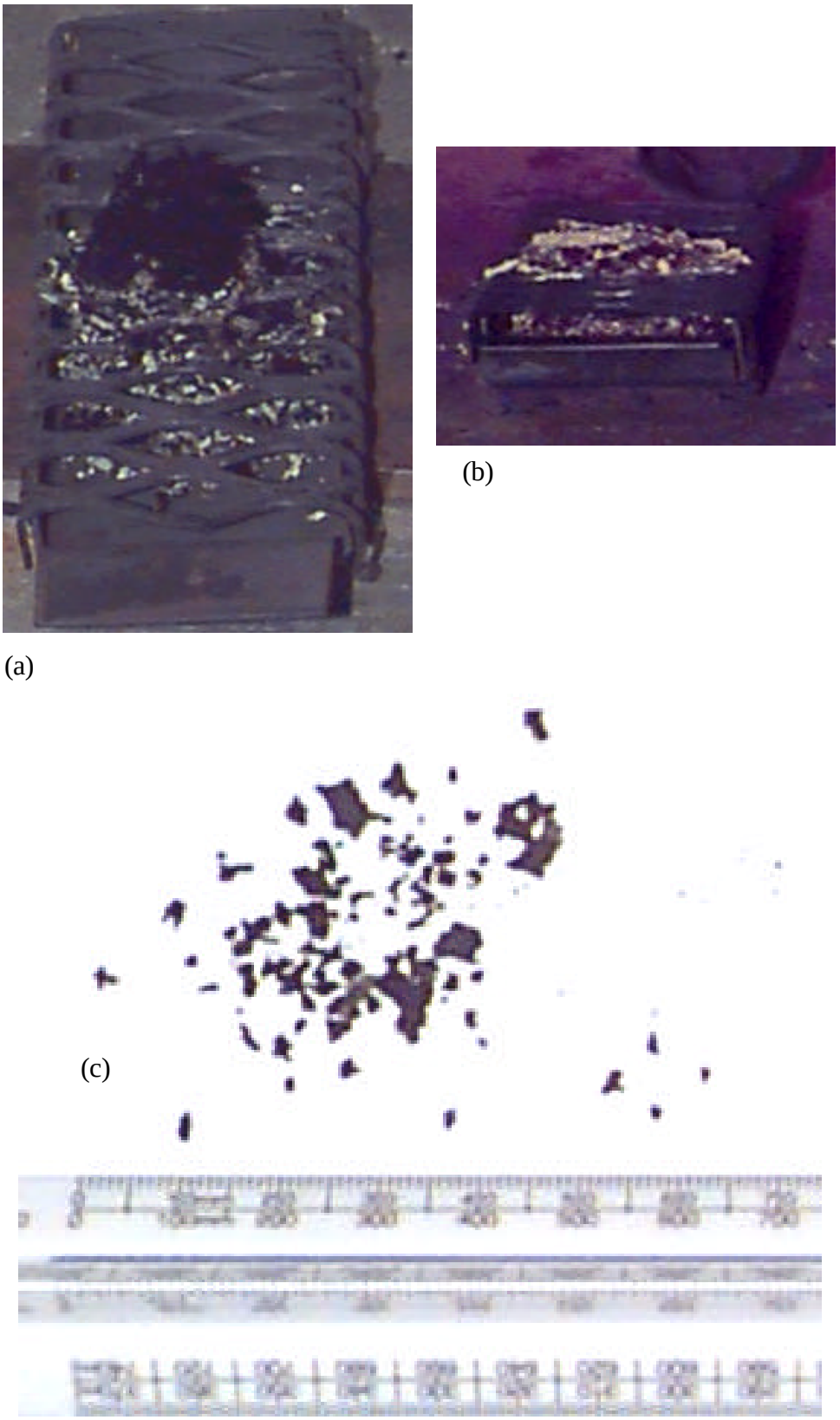

Fig. 7-5 Final stages of tyre chip combustion experiment (a) at flame extinction, (b) at complete oxidation and (c) a sample of char granules with mm scale.

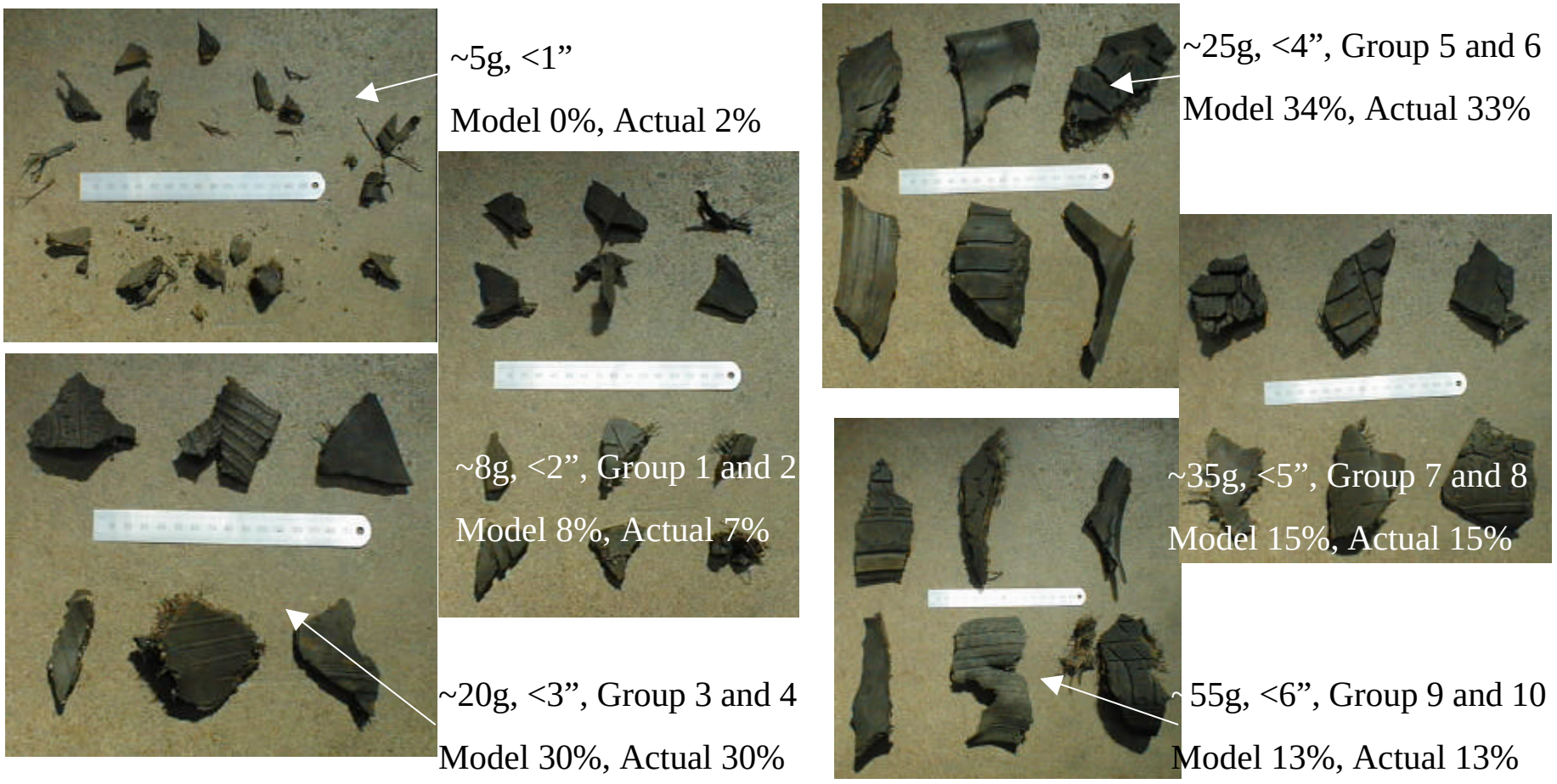

Fig. 7-6 Tyre chip size classification. Chips were grouped by maximum dimension (inches). The 6” steel rule indicates true size.

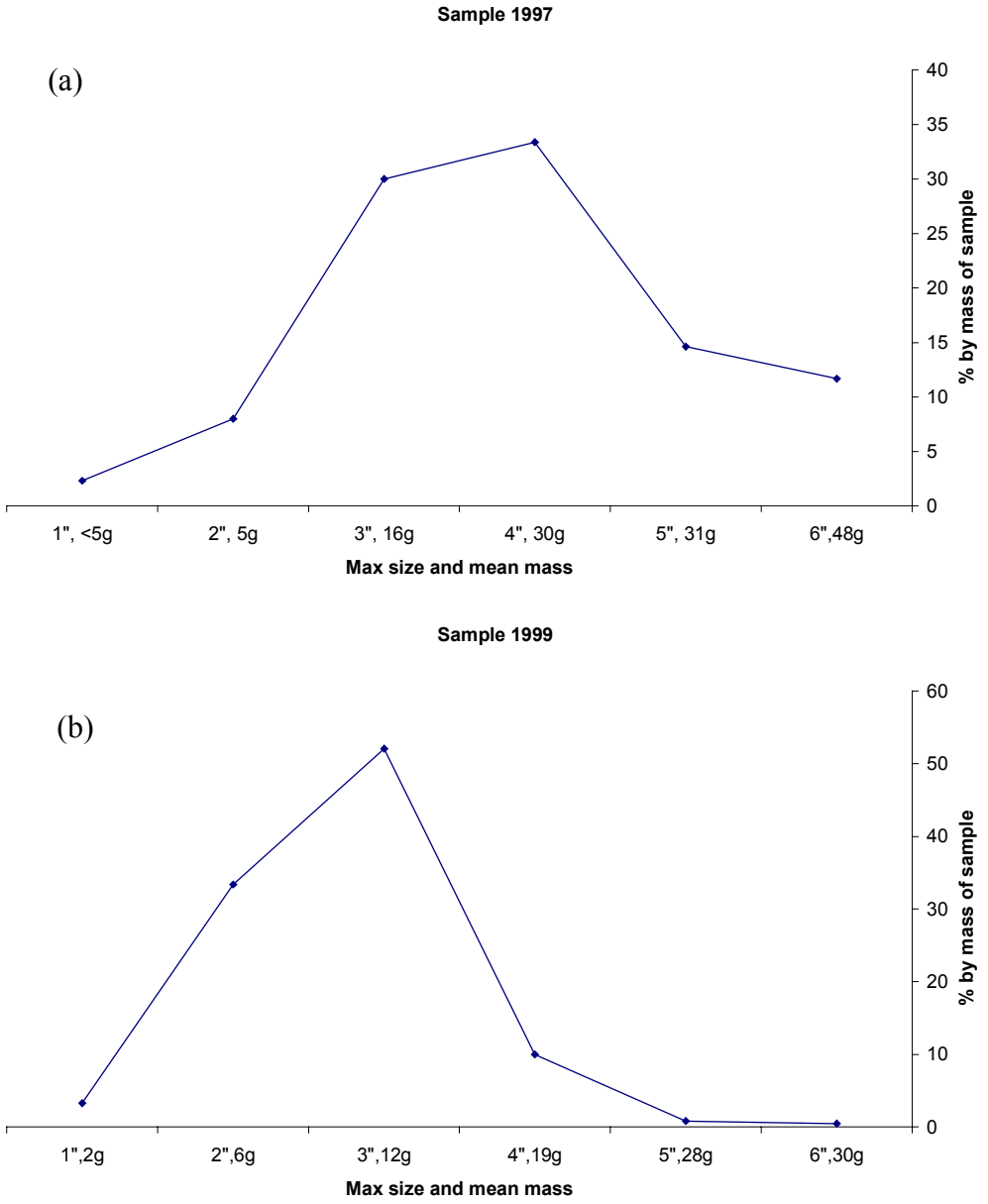

Fig. 7-7 Tyre chip size distribution analysis from two samples (a) taken 1997 and (b) taken 1999. The mean mass of tyre chips and maximum dimension in inches of each group is stated on the horizontal axis.

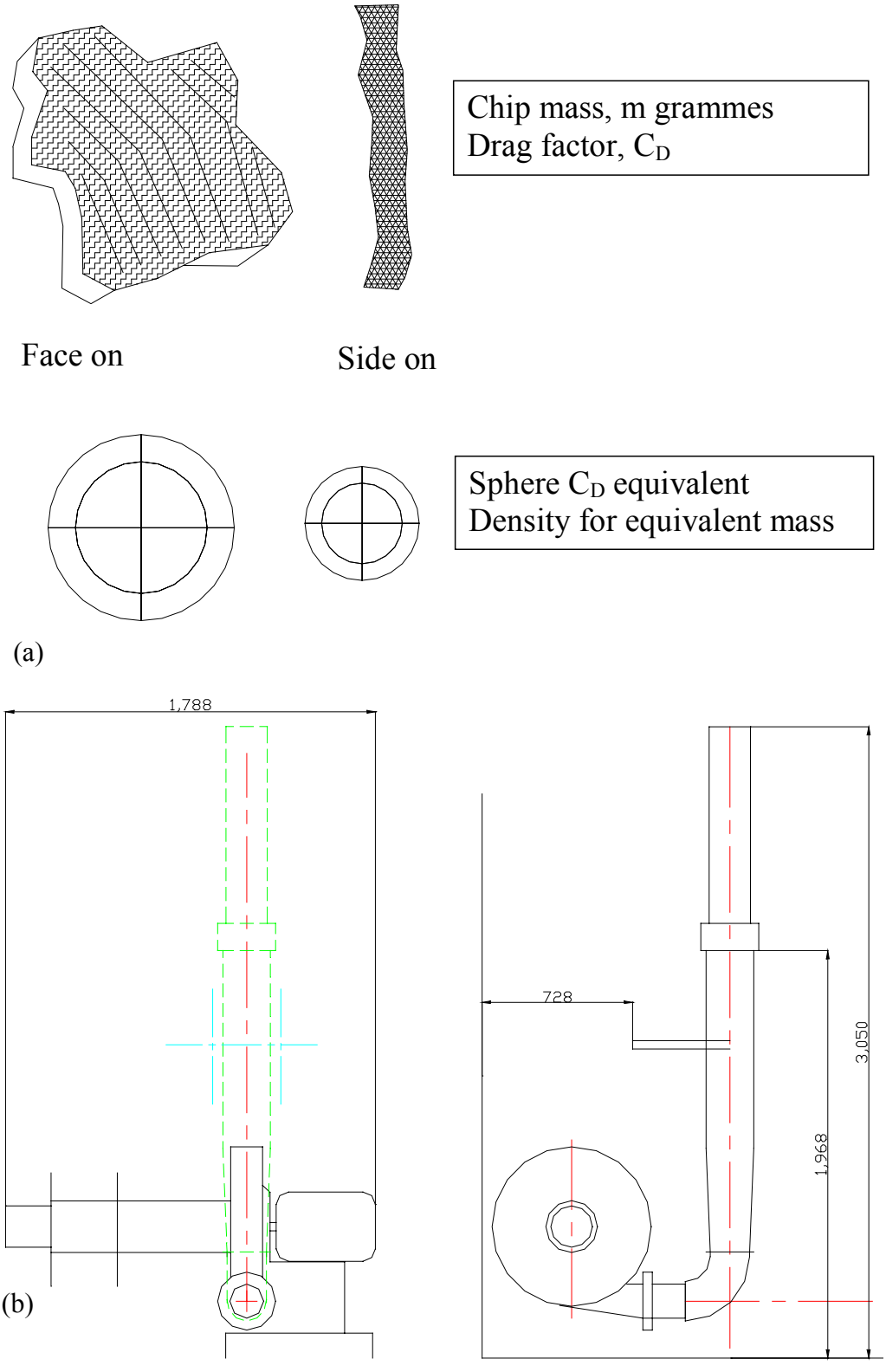

Fig. 7-8 (a) Illustration of side-on and face-on modelling technique (b) Tyre chip flotation rig design (dimensions in mm).

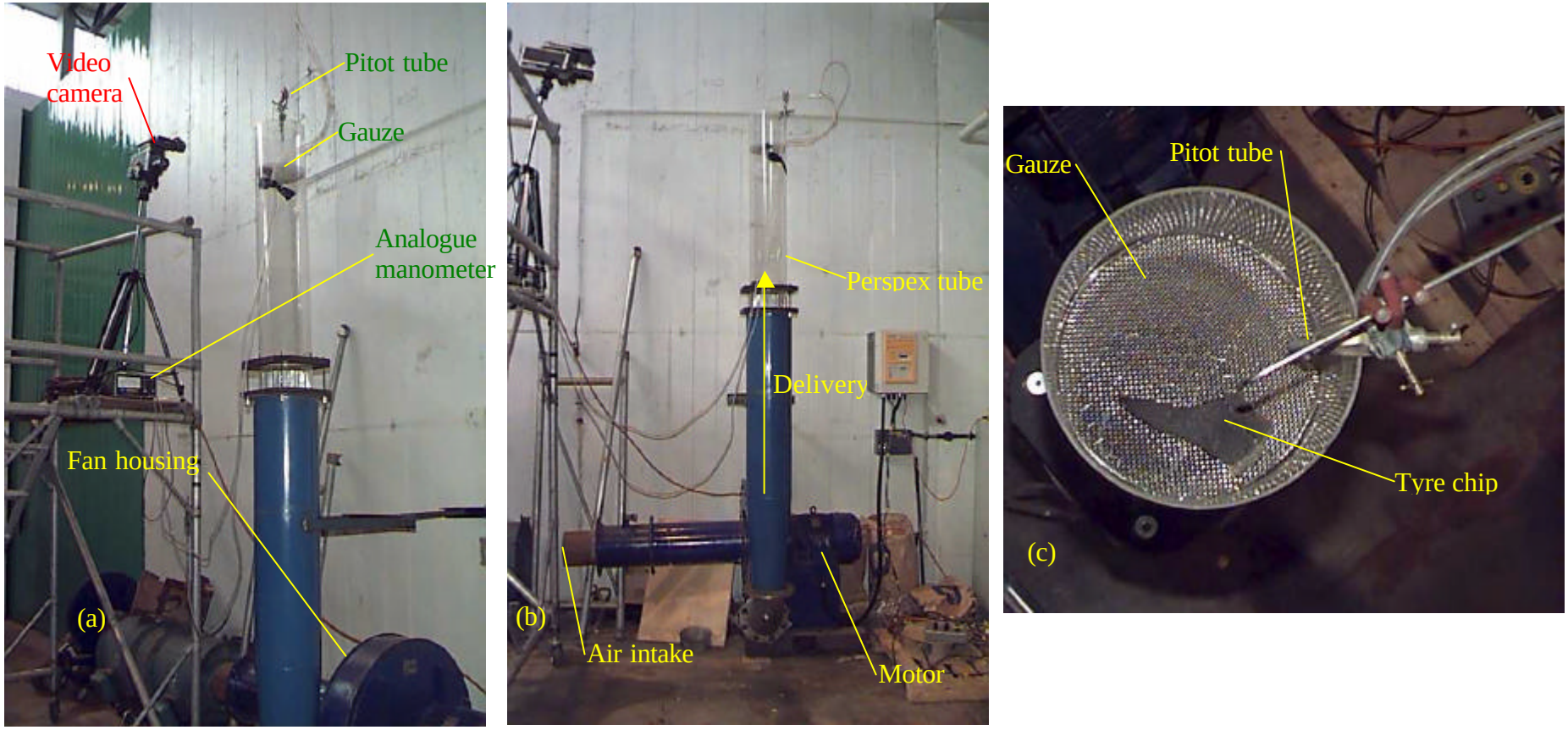

Fig. 7-9 Photographs of the tyre chip flotation rig. (a) and (b) show the riser from the fan to the test section and (c) shows the view above the test section looking down on the gauze with the tyre chip ready for testing.

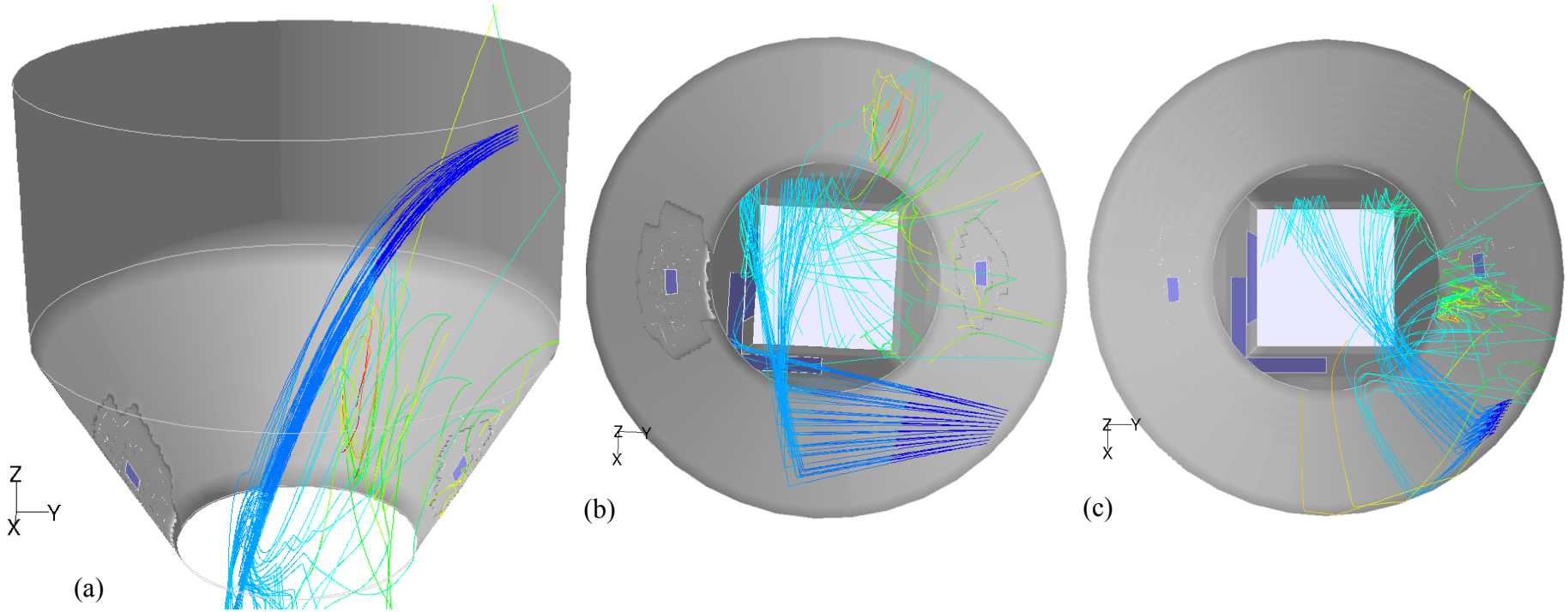

Fig. 7-10 Initial injection position and trajectories of tyre chips, (a) side view, (b) dropped chip trajectories, (c) sliding chip trajectories. Dropped chips bounce into the main body of the precalciner before hitting the conical section wall. Chips that have sliding entry trajectories fall directly on the conical section wall before bouncing into the main upward stream in the precalciner.

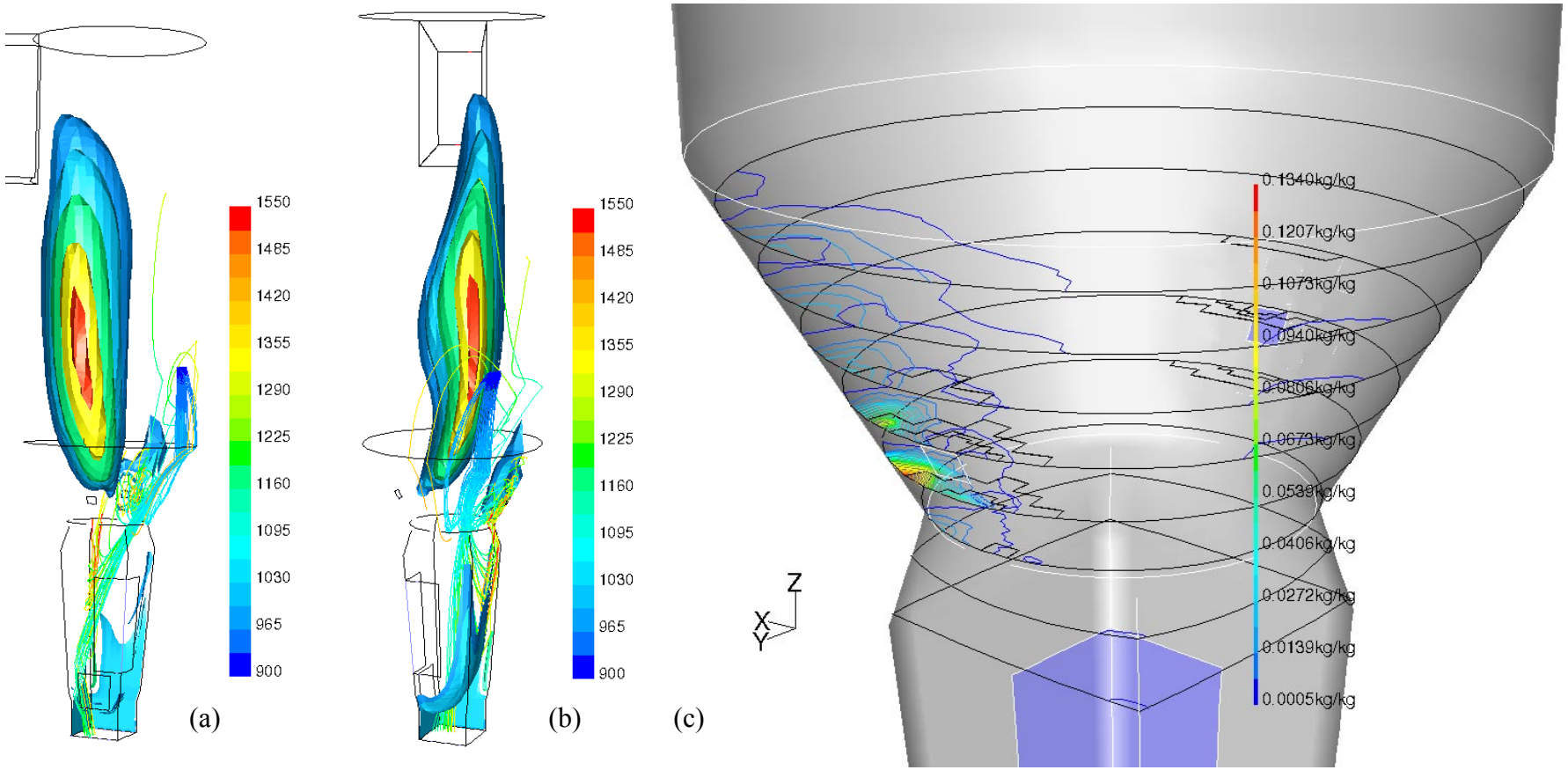

Fig. 7-11 (a) and (b) show temperature iso-surfaces and (c) shows contours of tyre chip volatile in the sliding tyre chip model. New high temperature regions are apparent compared to the models without tyre chips.

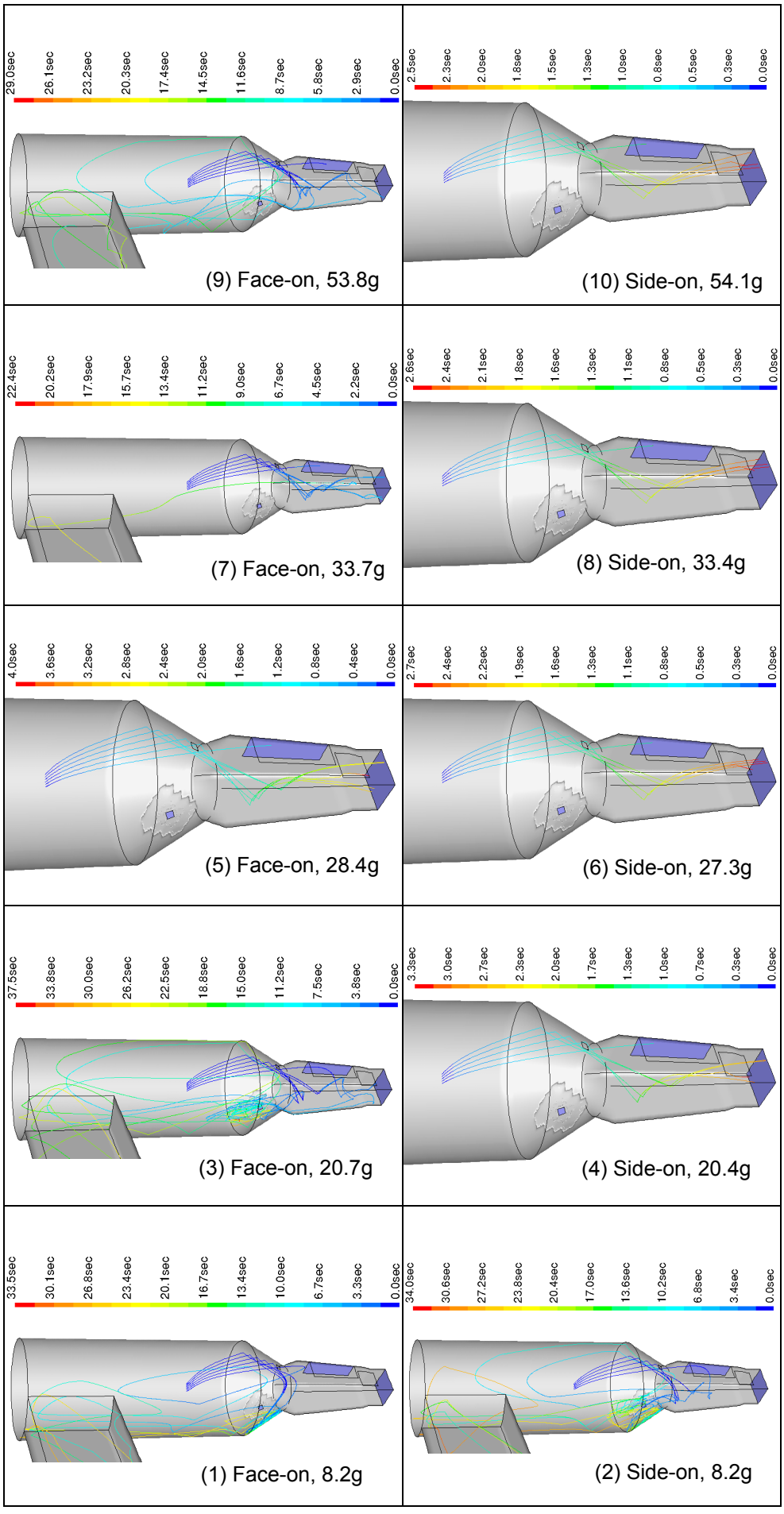

Fig. 7-12 Trajectories of dropped chips. Captions show tyre chip number and mean mass of the group it represents.

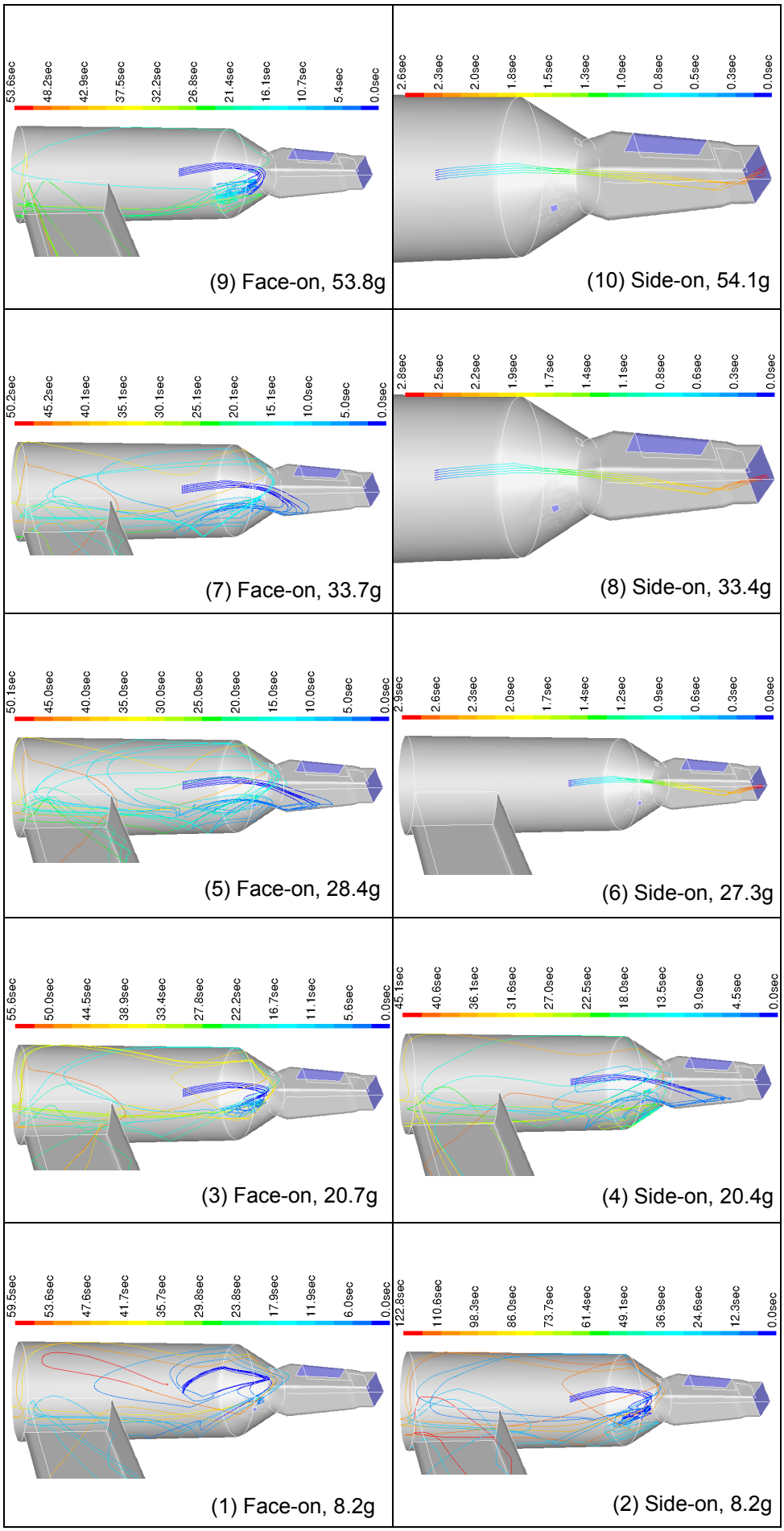

Fig. 7-13 Trajectories of sliding entry chips. Captions show tyre chip number and mean mass of the group it represents.

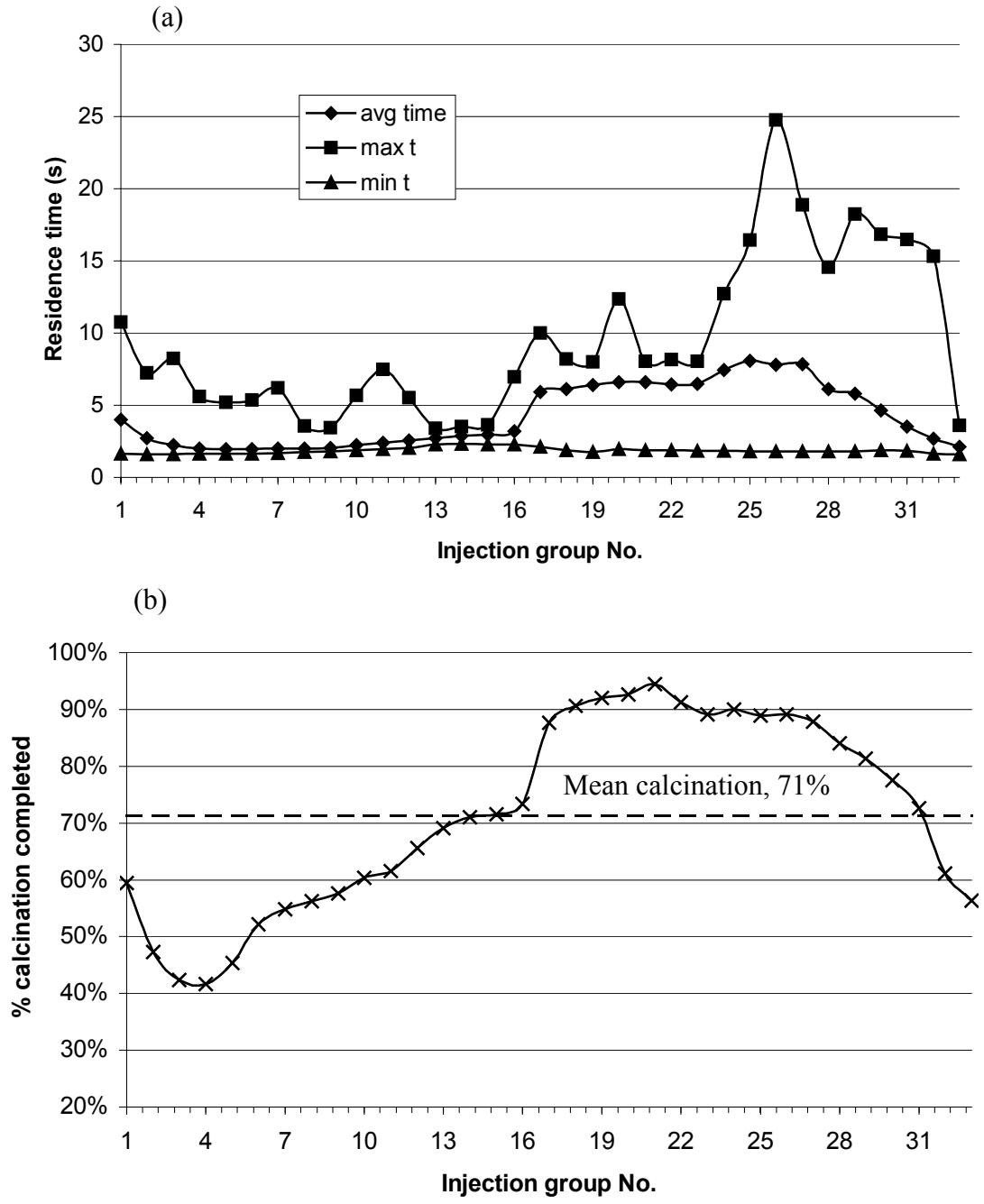

Dropped entry condition results.

Fig. 7-14 Behaviour of the raw meal in the precalciner model including tyres entering with the dropped entry condition. (a) shows the mean, maximum and minimum time of each group to traverse from RMI to the exit from the cylindrical section and (b) shows the calcination state at exit.

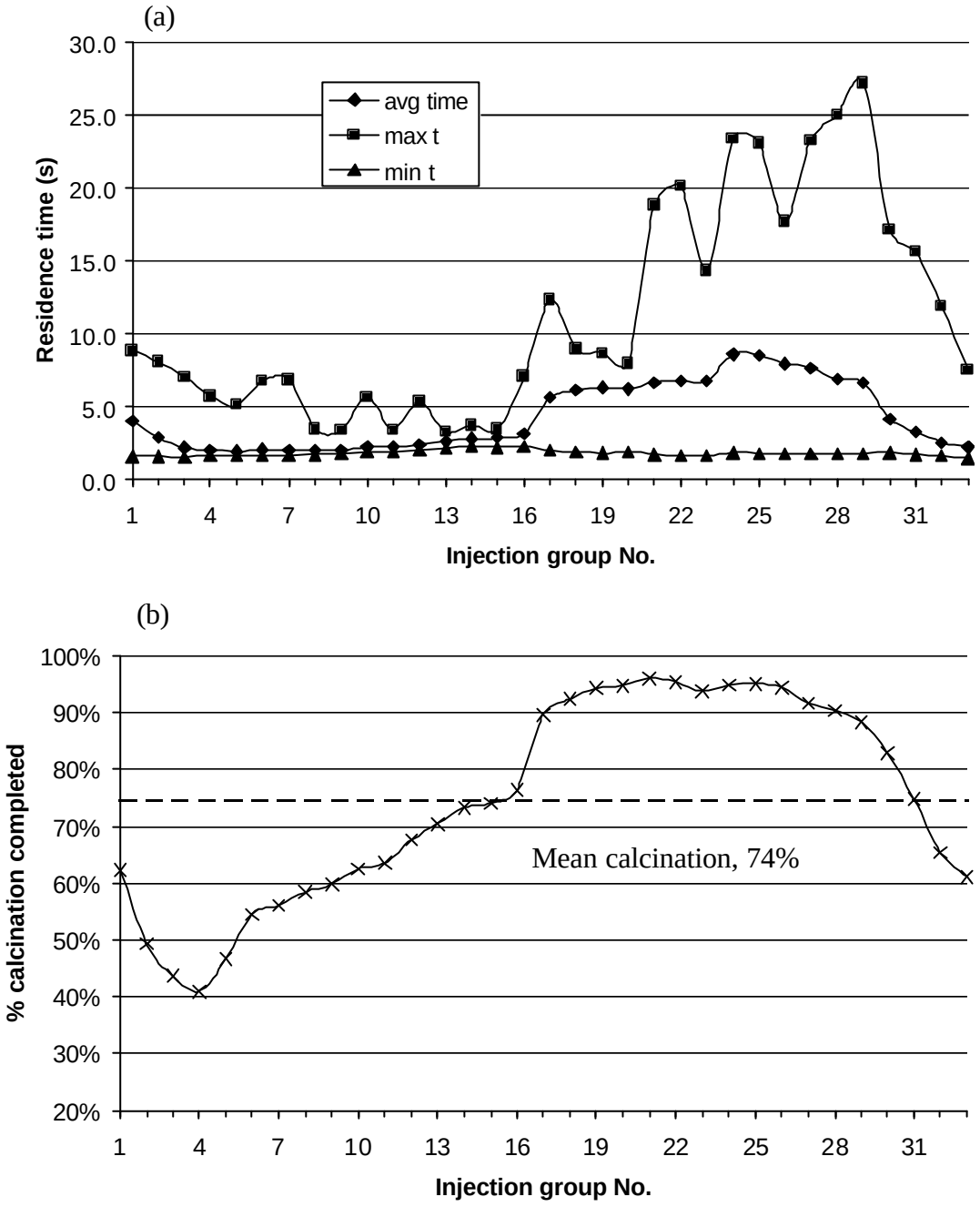

Sliding entry condition results.

Fig. 7-15 Behaviour of the raw meal in the precalciner model including tyres entering with the sliding entry condition. (a) shows the mean, maximum and minimum time of each group to traverse from RMI to the exit from the cylindrical section and (b) shows the calcination state at exit.

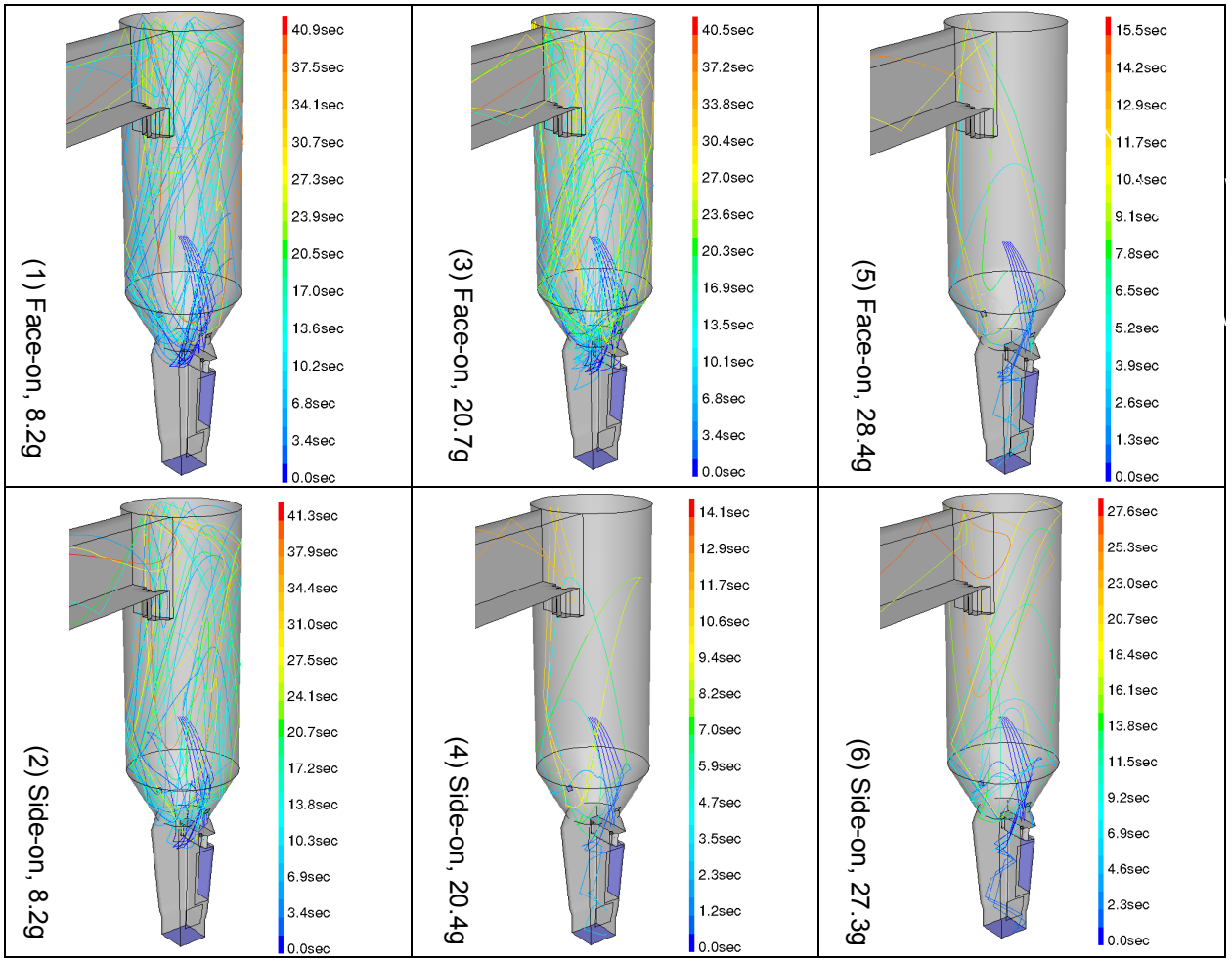

Figure 7-16 Trajectories of tyre chips in the "accelerator" model (tyre chip number shown in captions).

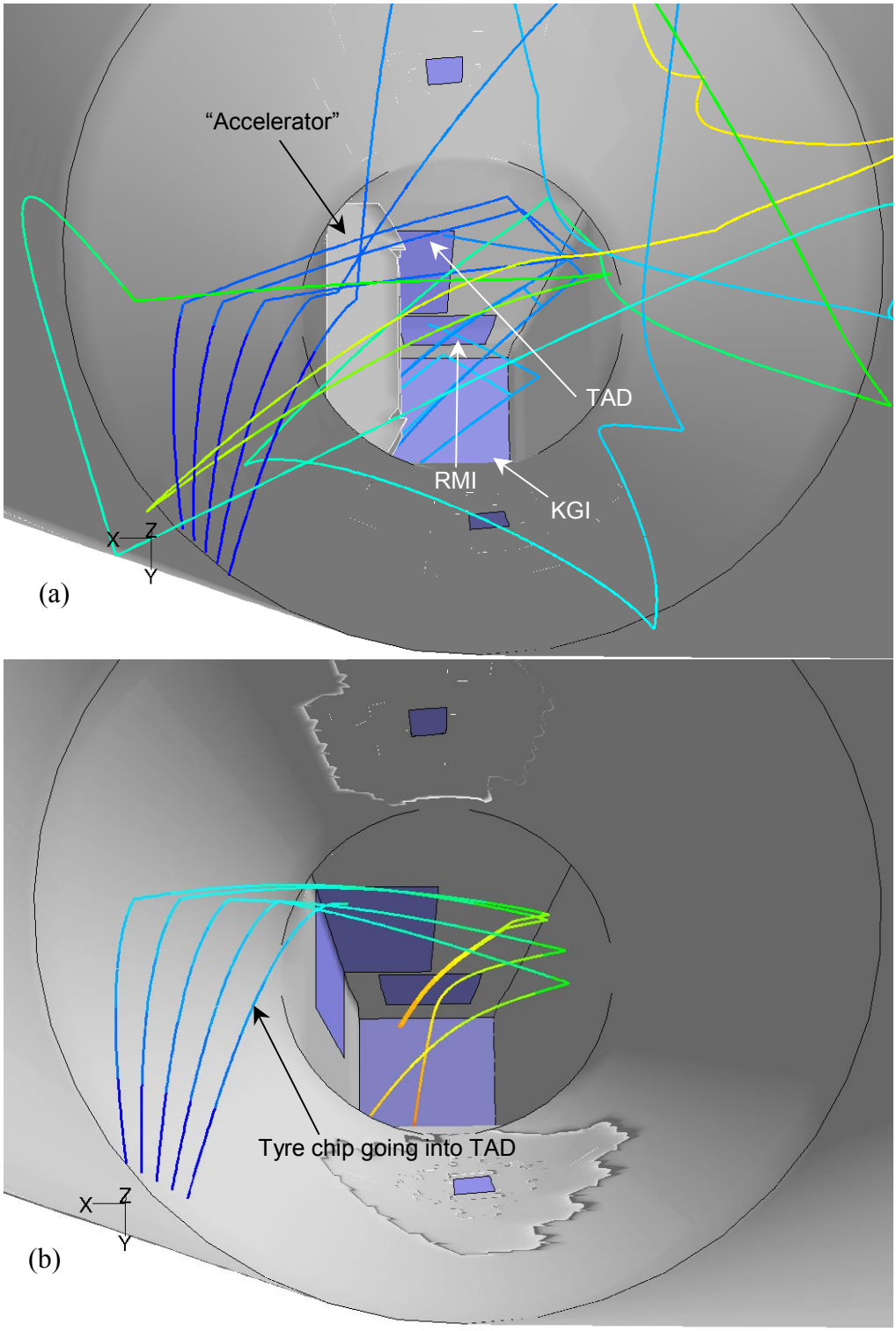

Fig. 7-17 Initial tyre chip trajectory in the model with the "accelerator" (a), and in the model without the "accelerator" (b). The "accelerator" tends to stop the right hand injection group from entering the TAD.

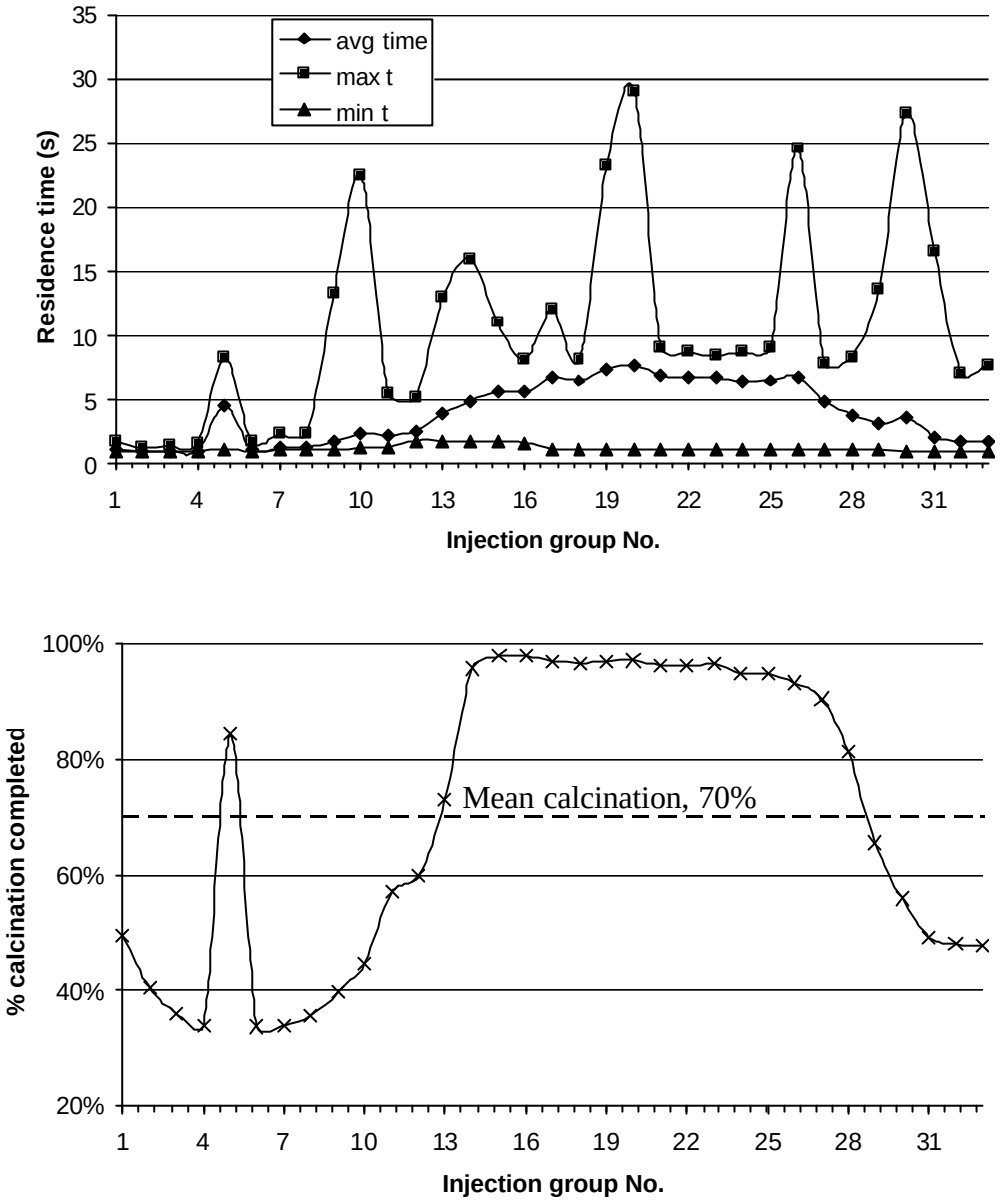

Fig. 7-18 Behaviour of the raw meal in the model with the "accelerator". (a) shows the mean, maximum and minimum residence time of particles to traverse from the RMI to the exit and (b) shows the degree of calcination achieved by exit.

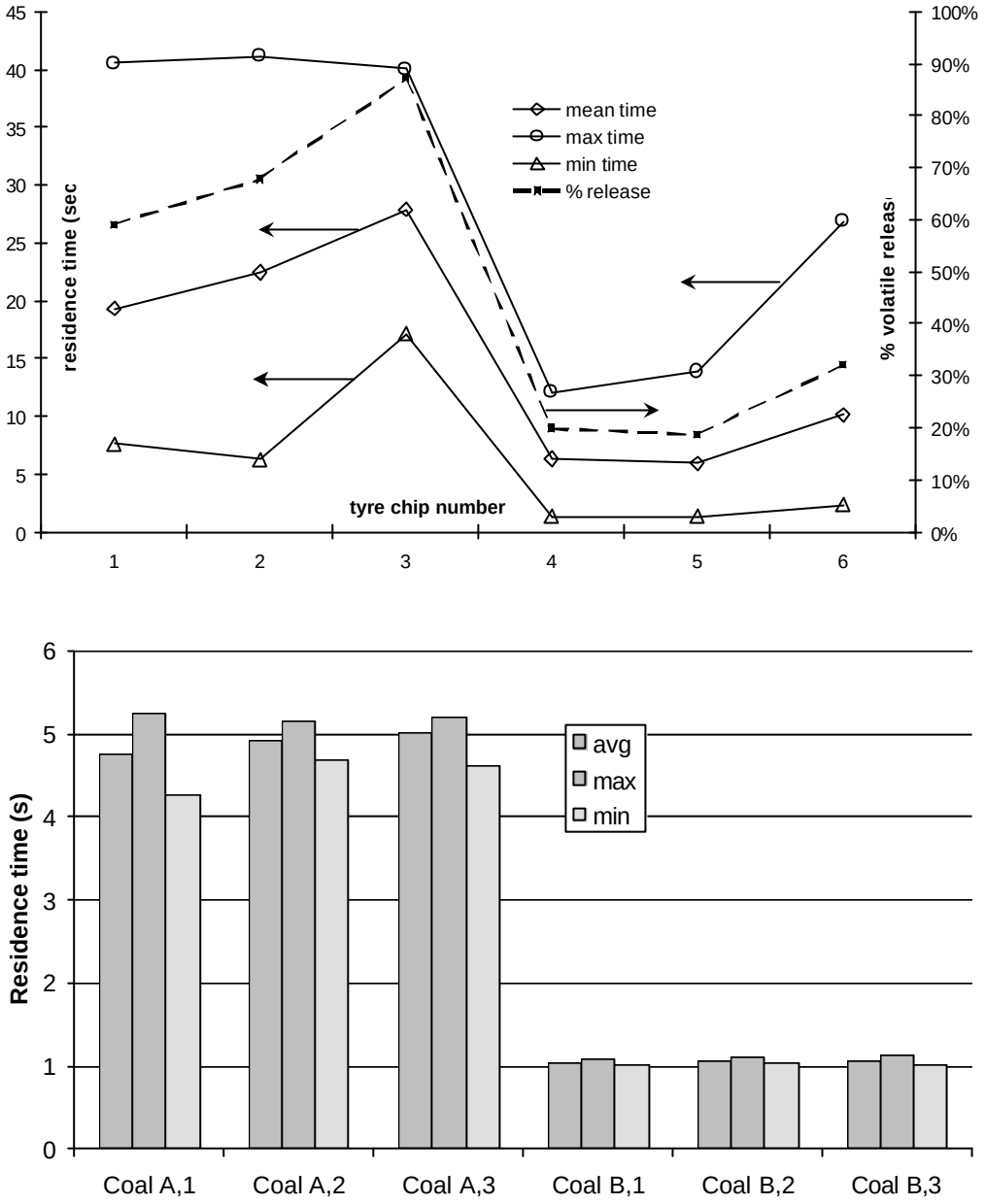

Fig. 7-19 Fuel behaviour in the precalciner model with "accelerator". (a) shows the mean, maximum and minimum residence times together with the amount of volatile released prior to exit for all tyre injection groups. (b) shows the mean, maximum and minimum coal residence times.

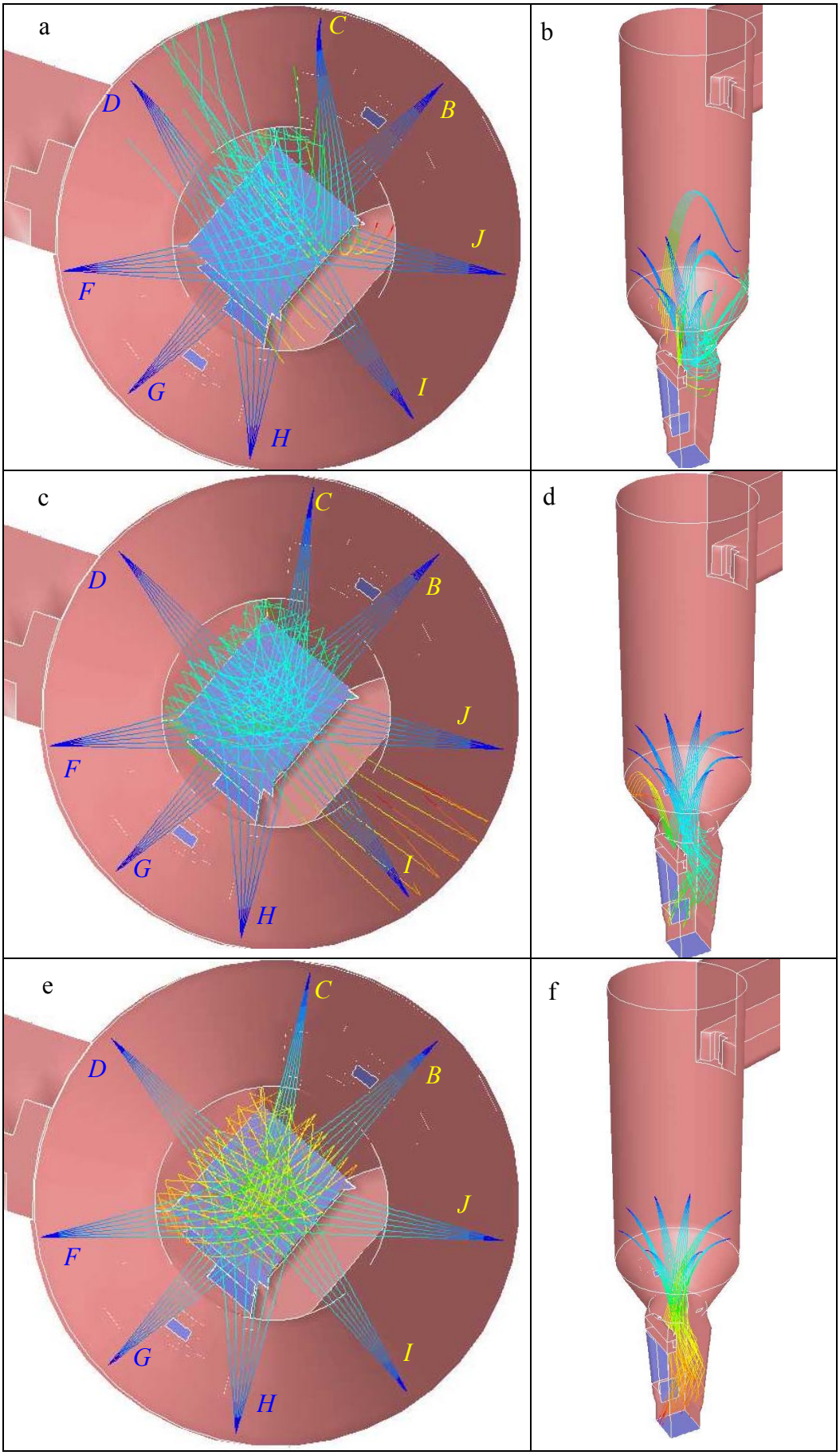

Fig. 7-20 Trajectory of injected tyre chips at current height.

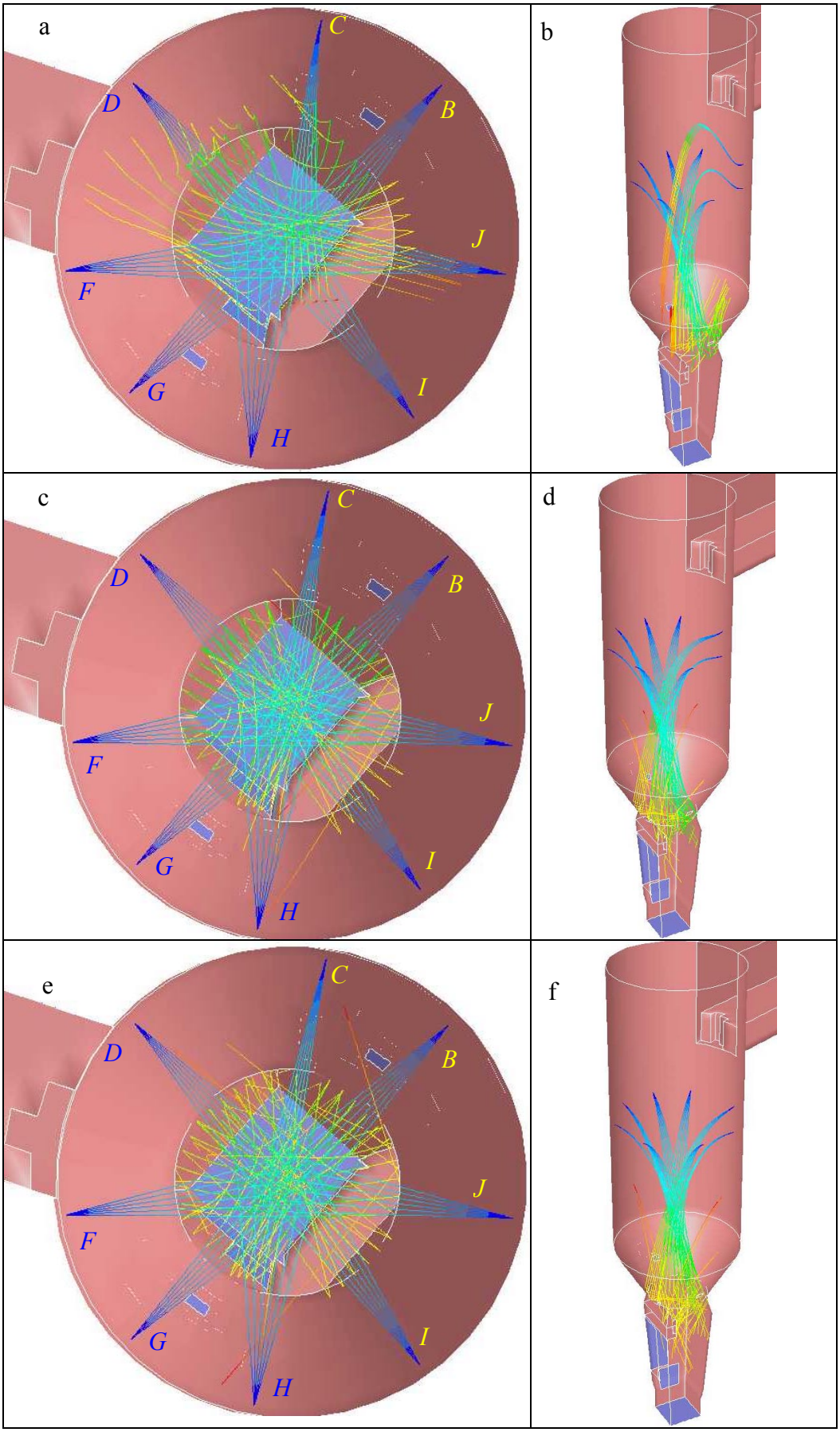

Fig. 7-21 Trajectory of injected tyre chips at current height plus 5m.

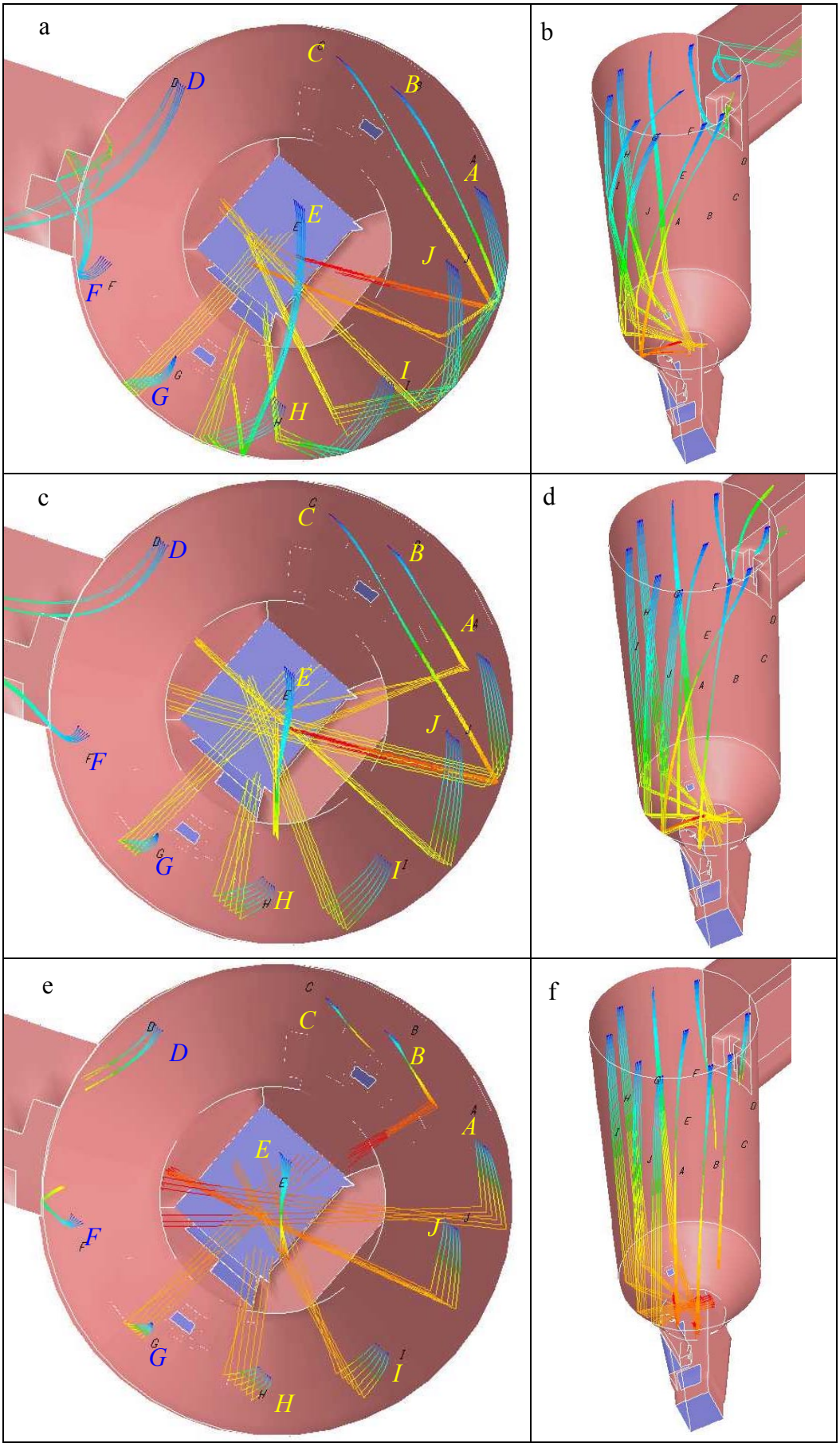

Fig. 7-22 Trajectory of roof injected tyre chips.

8 Conclusions

In closing the thesis, this chapter provides a statement of what has been achieved by the work described in it.

8.1 Statement of the aims and objectives of the work

Blue Circle proposed the project in order to understand better the combustion of tyre chips that is done in the precalciner at the Cauldon works. The original statement of objectives for the project was:

- gain understanding of the heat and mass balances of the process
- develop models of the precalciner vessel using computational fluid dynamics software
- perform experimental combustion of waste fuels to develop a methodology to assess alternatives
- validate the models on CFD against plant data
- perform experimental observation of tyre chip aerodynamic behaviour to develop a model within CFD to predict likely trajectories in the precalciner

The expected deliverables were:

- a CFD model of the precalciner fully representing operation with coal combustion and raw meal calcination
- a CFD model of the precalciner representing the full model with additional tyre chip aerodynamic and combustion representation

8.2 Level of attainment of objectives

A methodology was developed for successfully modelling a cement plant precalciner including:

- limestone (raw meal) reaction
- coal devolatilisation and char oxidation
- heat transfer to the walls of the precalciner
- gas flows representative of the gas flows in the plant

8.2.1 The first model and plant measurements

The first model developed was fully representative of the precalciner with calcination and coal combustion included. Representing the exact geometry of

the precalciner was difficult due to the limitations of the block structured grid generation. Ducts were rectangular instead of round. Connection to the vessel following the outlet from the precalciner was not modelled. Since the vessel following the precalciner is a cyclonic gas-particle separator, a great deal of effort was saved by assuming a much simpler exit condition. For the first model, an exit duct was attached to the outlet from the precalciner, which had a length of 10 times the hydraulic diameter. Two features of this arrangement relate well to the actual outlet configuration. Firstly, the condition at outlet was near fully developed giving a good relationship between the momentum and pressure fields in the model and secondly the length to the end of the duct was equivalent to the likely path length travelled by particles in the cyclone. Some grid refinement was performed in the region of the coal inlets to reduce the gradients of temperature and velocity. These changes effected a stable numerical solution.

A large-scale recirculation was demonstrated which dominated the flow patterns in the precalciner. The tertiary air inlet induced this feature.

According to the model, coal from the same side as the tertiary air duct was less well used than coal issuing from the other inlet. Raw meal introduced just below the tertiary air inlet was conveyed to the far wall of the precalciner and carried in a large-scale recirculation up that wall and down the opposite wall. Coal on that side of the precalciner was used well in supporting the high rate of calcination occurring there. Coal on the same side as the tertiary air inlet was carried up the centre of the precalciner and straight to the exit, raising the core temperature to the region of 1900°C. This temperature is sufficient to promote NO_x production by thermal NO_x. It was suggested that injecting all coal at the inlet on the side opposite the tertiary air inlet might cause a benefit to NO_x reduction. The cost of performing the investigation was prohibitive and it has not yet been attempted.

Measurements made on the precalciner at Cauldon showed reasonable correlation with the information presented by the CFD model. The harsh environment limited the measurements. Some indication of the vertical gas velocity was obtained by using an S-type Pitot tube periodically purged with air. The measurements showed the same gas velocity direction as the model

but the magnitudes were difficult to assess due to the fluctuations observed. Temperature measurements showed good agreement with the model within 50°C. An interesting phenomenon was observed, which suggested the possibility of roping of the raw meal particle stream near to the wall directly opposite the tertiary air inlet. The model supported the evidence by showing very high concentration of particles in that region.

The raw meal reaction level at exit from the model was compared to the level at the exit from the stage 4 cyclone (immediately prior to entry to the kiln). Production of raw meal CO_2 was 70% in the model on reaching the end of the outlet duct. Measurements showed production of 83%. The difference was attributed to the difference in gas-particle mixing between the duct and the cyclone. Subsequent analysis at the conclusion of the project showed that the short fall was most likely due to a 10% shortage of coal, such that calcination of the full raw meal feed was not possible in the model. The effect of this was not established by further modelling, since the project had reached its conclusion. It is proposed that the effect of increasing the coal supply will not significantly alter the qualitative observations made with the existing models.

8.2.2 Sensitivity analyses using CFD

Several additional cases were developed from the initial model to determine the effect of making changes, which represented realistic assumptions used in the model development. Observations from the sensitivity cases demonstrated that the initial model provided a good representation of the operation of the precalciner with coal and raw meal reactions. The features that were inspected were:

- mesh refinement in the cylindrical section to check for mesh independence
- inclusion of radiative heat transfer in the energy equation to investigate the effect of opacity caused by the dense particle cloud
- separating the CO_2 produced by the coal and raw meal to visualise the regions of greatest raw meal reaction
- injecting coal from the side opposite the tertiary air inlet only to predict the effect of operating the plant in this way
- injecting the raw meal uniformly across the kiln gas inlet to observe sensitivity to raw meal injection technique

- changing the coal inlet angle to more accurately represent the inlet angle of the plant coal
- adding an accelerator to represent plant modification
- mesh development using unstructured mesh with improved inlet connections to observe sensitivity to the shape of the inlet connections

The unstructured mesh model became unstable as the raw meal mass rate was increased beyond 60% of the full load. An error in the outlet duct height was found in the model. This was corrected in the model with the accelerator and no significant qualitative changes were apparently related to the correction.

8.2.3 Tyre chip experiments and representation in the model

Two sets of experiments were performed with tyre chips during the course of this work. Samples were placed in an ashing furnace at 900°C with the door open to promote combustion. Combustion tests showed that volatiles were released in still air within 2 minutes and that it is likely that this rate does not vary significantly for chips of different size since the thickness of tyre chips is limited by the tyre wall. It was assumed that the rate of release would be increased by a factor of four in the turbulent conditions encountered in the precalciner. Tyre material decomposed during devolatilisation to leave granules of char, which had a mean size of approximately 3mm diameter and a mean density of approximately 70 kg/m^3. In the furnace conditions, char oxidation was completed in approximately 20 minutes.

A rig was developed to investigate the aerodynamic behaviour of tyre chips when suspended in a stream of gas. Tyre chips were supported in a vertical column of air in an 8” diameter Perspex tube to observe the terminal velocity and any distinctive characteristics that might be observed. Sizes varied from 1” to 6” maximum dimension and the terminal velocity varied between 9 and 15 m/s with no apparent relation to size. Observed tyre chips moved randomly in the stream of air, but tended to present the maximum area perpendicular to the flow.

A suitably representative model of the tyre chips was included in the precalciner model to determine trajectories and heat release patterns. Tyre chips were modelled as spheres of a size and density that gave the same mass and drag coefficient as the face on tyre chip from previous wind tunnel tests.

Data for the drag coefficient of tyre chips of different sizes in orientations face on (maximum area presentations) and side on (minimum area presentation) were available from previous work at The University of Nottingham.

When these observed effects were included in a model of tyre chips in the precalciner, predicted trajectories showed that tyre chips tended to circulate on the conical section wall during devolatilisation. In the plant, this observation was confirmed by the presence of wire build-up on the conical walls apparent during plant maintenance shutdown periods. It was also apparent at the plant that a lot of tyre material accumulated in the tertiary air inlet by the precalciner in a three-month period of operation. The model showed that this was as a direct result of the configuration of the tyre chip inlet, which imparted a specific initial trajectory to some tyre chips that caused them to fall directly into the tertiary air inlet. Once tyre chips were supported in the gases in the precalciner model, they did not enter the tertiary air inlet.

Addition of the accelerator to the plant and reduction of the mean tyre chip size was performed at approximately the same time. Observations at the site indicated a change in the behaviour of the tyre chips. Previous NO_x measurements at the back end of the kiln had shown a beneficial reduction with the addition of tyre chips. Addition of the accelerator resulted in an increase of back end measured NO_x indicating that the tyre chips were having less effect there and in that case that less tyre chips were falling into the kiln from the precalciner. This observation was supported by the modelling work, which showed that smaller tyre chips were supported on the gas stream from the kiln and that larger tyre chips fell into the kiln. The accelerated flow at the neck section of the precalciner further prohibited tyre chips from entering the kiln that way. A further observation was the increase of tyre material residue in the collection of raw meal made routinely at the drop out from the stage 4 cyclone, indicating an increase in tyre material was being carried over into the cyclone. The model with the accelerator showed that tyre chips were carried to the exit rather than to the kiln.

A number of alternative injection positions were assessed using the model in order to suggest where additional tyre chips might be injected. The results showed that there were favourable and unfavourable positions to inject tyre chips depending on height and circumferential position. Favourable

injections had long residence times and mixed well in the main body of the precalciner.

8.3 Statement of original contribution of the thesis

The most important novel aspects of the work contributed by this thesis are the complete modelling of all aspects of the precalciner process with correct geometry and including a waste solid fuel.

All models generated for this thesis had body fitted meshes. Block-structured meshing was used to generate a model of the precalciner that was accurate in all respects except the coal inlets and the tertiary air duct. These features were square ducts in the model whereas they are round on the plant. Fully unstructured meshing was used to generate a model that accurately represented all geometric features of the precalciner. Such geometrically faithful models were not found in the literature. Some literature was found regarding modelling cement works precalciners. Grid generation had been performed with Cartesian meshes and were not body fitted so that inclined walls had steps.

The type of precalciner with the inlet and outlet configuration has not been modelled before according to the literature.

No modelling of tyre chip behaviour in combustion vessels has been attempted prior to this work according to the literature survey. Characteristics of tyre material combustion have been investigated, but the data produced was not appropriate to the size of tyre chips used in the precalciner regarding rate of devolatilisation of the volatile material.

- No similar information about combustion characteristics of tyre chips produced by the investigation in this thesis was found.
- No similar aerodynamic studies performed on the tyre chips in this thesis were found elsewhere.
- No implementation of the aerodynamic and combustion characteristics into a CFD model has been attempted previously.

The concept of determining the trajectories of tyre chips injected at different positions in the precalciner was entirely novel. The model can be adjusted to determine the likely behaviour of other waste fuels.

The code used from Fluent provided practical models to simulate the precalciner process. Useful visualisation of the complex interaction of particles and gases was obtained, which significantly improved confidence in understanding the characteristics of plant operation. Useful numerical data was available from the post-processing that was not practicably measurable. Some degree of confidence in the validity of these data was provided by the limited measurements that were performed. Despite the improvements in CFD, validation measurements are necessary to give such confidence. The latter work with different injection positions of tyre chips and the accelerator section showed that CFD can be used as an aid in the design process.

8.4 Future work

Directly useful work can be done with the models generated in this work to determine the characteristics of the Cauldon precalciner with minor modifications such as changes in geometry or fuel type. Modelling can be used to predict the likely behaviour in the precalciner of similar waste derived fuels such as sewage pellets and other briquette-formed wastes. Further investigation into the relationship between the precalciner and the stage 4 cyclone would be useful to determine the interdependence of the fluid flows and the combustion characteristics of fuels where the combustion continues in to the cyclone. Improvements in mesh generation software from Fluent make it possible generate models quickly. Incorporating the model characteristics of chemistry and heat transfer described in this work will enable relatively quick generation of new models. Alternative precalciner designs can thus be investigated using CFD with the boundary conditions based on this work. Model predictions must be validated by on site measurements. Development of cost effective measurement techniques for high temperature dust laden flows will provide more reliable verification of the model data than has hitherto been gained.

References

Anderson, J.D. 1990. Introduction to Computational Fluid Dynamics, Chapter 2. Von Karmen Institute for Fluid Dynamics. Belgium.

Badzioch, S. and **Hawksley, GW.** 1970. Kinetics of Thermal Decomposition of Pulverised Coal Particles. Ind. Eng. Chem. Process Des. Develop., Vol. 9, No. 4, 1970, pp 521-530

Baum, R.K. and **Street, J.H.** 1971. Predicting the combustion behaviour of coal particles. Combustion Sci and Tech, 3(5); 231--243.

Bech, C. and **Gundtoft, L.** 1998. Study of NOx, SOx, & CO mechanisms based on actual plant data. IEEE/PCA Cement Industry Technical Conference, May 17-21, 1998, pp 141-154

Belot, C. and **Goffe, D.** and **Grouset, D.** and **Bertrand, C.** and **Homassel, B.** and **Philippe, JL.** 1993. Optimization of a Cement Plant Preheating Tower, Equipped with a Precalciner, Burning Pulverized Coal. Combust. Sci. and Tech., Vol. 93, pp 9-25

Blumenthal, M. 1996. The use of tyre-derived fuel in the US cement industry. World Cement, April 1996, pp 24-27

Bogue, R.H. 1955. The Chemistry of Portland Cement. 2nd Ed. Reinhold Publishing Corporation, New York.

Borgwardt, RH. 1985. Calcination Kinetics and Surface Area of Dispersed Limestone Particles. AIChE Journal, Vol. 31, No. 1, January 1985, pp 103-111

Borman, G.L. and **Ragland, K.W.** 1998. Combustion Engineering. McGraw-Hill, USA.

Boynton, RS. 1980. Chemistry and Technology of Lime and Limestone. 2nd ed. Wiley, New York

Conesa, JA. and **Font, R.** and **Fullana, A.** and **Caballero, JA.** 1998. Kinetic Modelling for the Combustion of Tyre Wastes. Fuel, Vol. 77, No. 13, pp. 1469-1475.

Conroy, GH. 1997. Industrial Application and Results of Low NOx Precalciner Systems. 1997 IEEE/PCA 34th Cement Industry Technical Conference, pp 297-318

Crowe, C. and **Sommerfeld, M.** and **Tsuji, Y.** 1998. Multiphase Flows with Droplets and Particles. CRC Press LLC, USA

Crowe, C.T. and **Sharma, M.P.** and **Stock, D.E.** 1977. The Particle-Source-In-Cell (PSI-CELL) Model for Gas-Droplet Flows, ASME Journal of Fluids Engineering, June 1977, Vol. 99, pp.325-332.

Dennis, JS. and **Hayhurst, AN.** 1987. The effect of CO2 on the kinetics and extent of calcination of limestone and dolomite particles in fluidised beds. Chemical Engineering Science, Vol. 42, No. 10, pp 2361-2372, 1987

Dti Scrap Tyre Working Group. 1996. Industry/Government scrap tyre working group: first annual report to ministers. Department of Trade and Industry Environment Directorate.

Environment Agency. 1997. Best practicable environmental option assessments for integrated pollution control. Stationary Office.

Fluent Incorporated. 1996. User's Guide for FLUENT/UNS & RAMPANT, Release 4.0, April 1996, Vol. 1,2, & 4. Fluent Incorporated, Lebanon, NH 03766, USA.

Garret, HM. 1985. Precalciners Today - A Review. Rock Products. July 1985.

Govind, R. and **Shah, J.** 1984. Modeling and Simulation of An Entrained Flow Coal Gasifier. AIChE Journal, Vol. 30, No. 1, January 1984, pp 79-91

Guigliano, M. and **Cernuschi, S.** and **Ghezzi, U.** and **Grosso, M.** 1999. Experimental Evaluation of Waste Tires Utilization in Cement Kilns. J. Air & Waste Manage. Assoc. 49:1405-1414.

Haider, A. and **Levenspiel, O.** 1989. Drag Coefficient and Terminal Velocity of Spherical and Nonspherical Particles. Powder Technology, 58, pp 63-70

Hartman, M. and **Trnka, O.** and **Svoboda, K.** 1994. Free Settling of Nonspherical Particles. Ind. Eng. Chem. Res. 1994, 33, pp 1979-1983

Hottel, H.C. 1961. Radiative Transfer in Combustion Chambers. Journal of the Institute of Fuel, Vol 34, p220-234.

Holman, J.P. 1997. Heat Transfer. 8th edition. McGraw-Hill, USA.

International Combustion Ltd. 1993. Confidential report for Blue Circle Cement. November 1993.

Jepsen, OL. and **Miller, SW.** 1997. New Generation of Low NOx Calciners. 1997 IEEE/PCA 34th Cement Industry Technical Conference, pp 282-295

Kainer, H. 1982. Kopplung von Warme und Stoffaustausch mit chemisher Kinetik bei der Zersetzung von naturlichen Karbonaten. Dissertation and der TU Clausthal, 1982.

Klotz, B. 1997. New Developments in Precalciners and Preheaters. 1997 IEEE Cement Industry Conference, April 21-24 1997, Hershey, Pennsylvania.

Kobayashi, H. and **Howard, JB.** and **Sarofim, AF.** 1976. Coal Devolatilization at High Temperatures. 16th Symp. (Int'l.) on Combustion, The Combustion Inst., Cambridge, MA, Aug. 15-20.

Kolyfetis, E. and **Vayenas, CG.** 1988. Mathematical modelling of separate line precalciners (SLC). Zement-Kalk-Gips - Nr. 11/1988, pp 559-563

Launder, B.E. and **Spalding, D.B.** 1974. The Numerical Computation of Turbulent Flows. Comput. Methods Appl. Mech. Eng. Vol. 3, pp. 269-289.

Leung, DYC. and **Wang, CL.** 1999. Kinetic Modeling of Scrap Tire Pyrolysis. Energy and Fuels, 13, pp 421-427

Levendis, YA. and **Courtemanche, B.** 1997. NO-NO_2 emissions from the combustion of solid fuels. Proceedings of the International Technical Conference on Coal Utilization and Fuel Systems, 1997, pp 827-838

Levendis, YA. and **Atal, A.** and **Carlson, JB.** 1998. On the correlation of CO and PAH emissions from the combustion of pulverised coal and waste tires. Environ. Sci. Technol. 1998, 32, pp 3767-3777

Lockwood, FC. and **Ou, JJ.** 1993. Review: burning refuse-derived fuel in a rotary cement kiln. Proc Instn Mech Engrs Vol 207, Part A Journal of Power and Energy, 1993.

Magnussen, B.F. and **Hjerteger, B.H.** 1976. On Mathematical Modelling of Turbulent Combustion with Special Emphasis on Soot Formation and Combustion. 16th Symposium (Intl) on Combustion, The Combustion Institute, pp.719-729.

Makroum, HA. and **Mounir, AE.** 1995. Influence of variables on cement kiln performance. World Cement, April 1995, pp 63-66

Massey, BS. 1989. Mechanics of Fluids. 6th Ed. 1989, Chapman and Hall, London, UK

McQueen, AT. and **Bortz, SJ.** and **Hatch, MS.** and **Buening, HJ.** and **Shore, DE.** and **Leonard, RL.** and **Bouse, EF.** 1993. Cement Kiln NOx Control. 35th IEEE Cement Industry Technical Conference, pp 241-261, May 23-27, 1993, Ontario USA.

Morsi, SA. and **Alexander, AJ.** 1972. An investigation of particle trajectories in two-phase flow systems. J. Fluid Mech., V. 55 part 2, pp 193-208, September 26, 1972.

Mullinger, PJ. and **Jenkins, BG.** 1996. Optimising precalciner design and performance. World Cement, April 1996, pp 37-42

Patankar, S.V. 1980. Numerical Heat Transfer and Fluid Flow. Hemispher, Washington, D.C.

Perry, RH. and **Green, D.** 1984. Perry's Chemical Engineers' Handbook. 6th ed. 1984, McGraw-Hill, USA

Petrie, JG. and **Baldwin, S.** 1992. Devolatilisation and combustion of pelletised and briquetted wastes. Journal of the Institute of Energy, December 1992, 65, pp 185-191

Recycling Week. 1996. On the right track. Materials Recycling Week, October 11, 1996, p 8-11

Ritter, H. 1995. Combustion of Tyre Chips in a Cement Kiln. Undergraduate thesis, University of Nottingham Dept of Mechanical Engineering.

Rose, J.W. and **Cooper, J.R.** 1977. Technical Data on Fuels (Ed). 7th Edition. London, British National Committee, World Energy Conference.

Rosemann, R. 1986. Energy transfer in precalcining installations. Translation of Zement-Kalk-Gips No. 2/86, pp 84-86

Saito, I. and **Sakae, K.** and **Ogiri, T.** 1987. Effective use of waste tyres by gasification in cement plant. World Cement, September 1987, pp 264-268

Schrama, H. and **Blumenthal, M.** and **Weatherhead, E.C.** 1995. A survey of Tire Burning Technology for the Cement Industry. IEEE Cement Industry Technical Conference, June 4-9, 1995.

Siegel, R and **Howell, J.R.** 1992. Thermal Radiation Heat Transfer, Third Edition. Hemisphere Publishing Corporation, Washington.

Silcox, GD. and **Kramlich, JC.** and **Pershing, DW.** 1989. A Mathematical Model for the Flash Calcination of Dispersed CaCO3 and Ca(OH)2 Particles. Ind. Eng. Chem. Res. 1989, 28, pp 155-160

Smoot, L.D. 1993. ed. Fundamentals of Coal Combustion. ELSEVIER, Amsterdam, London.

Solomon, PR. and **Serio, MA.** and **Suuberg, EM.** 1992. Coal Pyrolysis: Experiments, Kinetic Rates and Mechanisms. Prog. Energy Combust. Sci. 1992, Vol. 18, pp 133-220

Tannehill, J.C. and **Anderson, D.A.** and **Pletcher, R.H.** 1997. Computational Fluid Mechanics and Heat Transfer. 2nd edition. Taylor and Francis, Washington D.C.

Taylor, H.F.W. 1997. Cement Chemistry, 2nd Ed. 1997. Thomas Telford Publishing, London.

Tokheim, LA. and **Bjerketvedt, D.** and **Husum, I.** and **Hoidalen, O.** 1998. NO_x reduction in a precalciner cement kiln using plastic as reburning fuel. Zement-Kalk-Gips, Nr. 1/1998 (51. Jahrgang)

Wadell, H. 1934. J. Franklin Inst. Apr 1934, p 459-

Williams, PT. and **Besler, S.** and **Taylor, DT.** 1990. The pyrolysis of scrap automotive tyres. Fuel, 1990, Vol. 69, December, pp 1474-1482

Published Papers

Giddings D. and **Eastwick C N**. and **Pickering S J**. and **Simmons K**. 2000. Computational fluid dynamics applied to a cement precalciner. Proc Instn Mech Engrs Vol 214 part A, 2000.

Giddings D. and **Pickering S J.** and **Simmons K.** and **Eastwick C N.** 1999. Using CFD to investigate combustion in a cement manufacturing process. Computational Fluid Dynamics: Technical Developments and Future Trends. 13-14 December 1999. IMechE.

Giddings D, and **Eastwick, C N**, and **Pickering, S J.** 1997. Mathematical modelling of the pre-calciner combustion chamber in a cement manufacturing plant. Waste Management and Waste Minimisation. 6th Annual East Midlands Environmental Conference, 2 July 1997. East Midlands Advisory Group on the Environment.

Appendix 1

CFD theory used by Fluent

Summary of the derivation of Navier Stokes equations.

This appendix is intended to refresh the reader about the meaning of the various terms in the Navier-Stokes equations. A full derivation is available in any Fluid Mechanics text book.

Mathematical definitions:

$\nabla = \vec{i}\frac{\partial}{\partial x} + \vec{j}\frac{\partial}{\partial y} + \vec{k}\frac{\partial}{\partial z}$, del or nabla operator

$div(\vec{F}) \equiv \frac{\partial u}{\partial x} + \frac{\partial v}{\partial y} + \frac{\partial w}{\partial z}$, divergence of a vector.

All terms are described according to unit volume in this brief summary.

Development of the continuity equation.

Summing the net convection of mass into the fluid cell and allowing for compressible flow:

$$\frac{\partial r}{\partial t} + div\vec{V} = 0$$

Development of the momentum equation in the x-direction.

Only the x-component is considered here; y and z-components are similar in form.

Rate of increase of momentum in fluid cell = sum of forces on the fluid cell

"Rate of increase of momentum in fluid cell" term is called *accumulation*.

"sum of forces on the fluid cell" are due to *body* forces (e.g. gravity) and *surface* forces in the form of direct stress and shear stress on the cell surface and the *net convection of x-momentum* into the cell

$$net\ convection\ of\ x\text{-}momentum = \frac{\partial(ruv)}{\partial y} + \frac{\partial(ru^2)}{\partial x} + \frac{\partial(ruw)}{\partial z}$$

body forces will be due to acceleration applied to the field in which the cell lies. This is called f_x in this context, a general acceleration term (ms^{-2}).

The direct stress term is derived from the pressure field, the rate of strain in the x-direction, and an additional contribution to allow for compressibility, which is zero in incompressible situations:

$$s_{xx} = -p + 2m\frac{\partial u}{\partial x} - \frac{2}{3}m(div\vec{V})$$

The shear stress terms are determined from the rate of angular deformation:

$$s_{xy} = m\left(\frac{\partial v}{\partial x} + \frac{\partial u}{\partial y}\right); s_{xz} = m\left(\frac{\partial w}{\partial x} + \frac{\partial u}{\partial z}\right); syz = m\left(\frac{\partial w}{\partial y} + \frac{\partial v}{\partial z}\right)$$

and it can be proven that $\sigma_{xy} = \sigma_{yx}$ etc.

So, the source term for the N-S equation is:

$$f_x - \frac{\partial}{\partial x}\left(p + 2m\frac{\partial u}{\partial x} - \frac{2}{3}m(div\vec{V})\right) + \frac{\partial}{\partial y}m\left(\frac{\partial v}{\partial x} + \frac{\partial u}{\partial y}\right) + \frac{\partial}{\partial z}m\left(\frac{\partial w}{\partial x} + \frac{\partial u}{\partial z}\right)$$

expanding and collecting terms results in the following expression:

$$f_x r - \frac{\partial p}{\partial x} + m\nabla^2 u + \frac{1}{3}mdiv\vec{V}$$

So the N-S equation for x-direction momentum is:

$$\frac{\partial(ru)}{\partial t} + \frac{\partial}{\partial x}\left(ru^2\right) + \frac{\partial}{\partial y}(ruv) + \frac{\partial}{\partial z}(ruw) = f_x r - \frac{\partial p}{\partial x} + m\nabla^2 u + \frac{1}{3}mdiv\vec{V}$$

This is the conservative form, in which the fluid may have variable density. If the density is assumed constant, then by subtracting the continuity equation from the L.H.S. of the equation the non-conservative form of the equation results.

$$r\frac{\partial u}{\partial t} + ru\frac{\partial u}{\partial x} + rv\frac{\partial u}{\partial y} + rw\frac{\partial u}{\partial z} = f_x r - \frac{\partial p}{\partial x} + m\nabla^2 u + \frac{1}{3}mdiv\vec{V}$$

The term $m\nabla^2 u$ is referred to as the diffusion term, since it represents terms from the derivation of shear and direct stresses on the surfaces of the cell.

Development of the Reynold's stresses.

In turbulent flow, all quantities are time dependent, but in steady flow, the mean values are constant. Turbulence results in mixing of the fluid between regions. Schlichting [1952] presents the nature of turbulence and boundary layers. The turbulent contributions that affect the momentum equation are found to be added in the convection terms where fluctuating quantities are multiplied together. This is due to the mathematical properties of time varying quantities when a mean value is taken. If a typical fluctuating quantity is represented by a mean and fluctuating component thus: $f = \overline{f} + f'$, then

considering all quantities in the N-S equation as fluctuating results in the following equation:

$$r\frac{\partial \overline{u}}{\partial t}+r\frac{\partial}{\partial x}\left(\overline{u}^2+\overline{u}'^2\right)+r\frac{\partial}{\partial y}\left(\overline{uv}+\overline{u'v'}\right)+r\frac{\partial}{\partial z}\left(\overline{uw}+\overline{u'w'}\right)=f_x r-\frac{\partial p}{\partial x}+m\nabla^2 u$$

another way of writing this equation collecting the fluctuating components of velocity is:

$$r\frac{\partial \overline{u}}{\partial t}+r\overline{u}\frac{\partial \overline{u}}{\partial x}+r\overline{v}\frac{\partial \overline{u}}{\partial y}+r\overline{w}\frac{\partial \overline{u}}{\partial z}=f_x r-\frac{\partial p}{\partial x}+m\nabla^2 u+\frac{1}{3}m div\vec{V}$$
$$-r\frac{\partial}{\partial x}\left(\overline{u'u'}\right)-r\frac{\partial}{\partial y}\left(\overline{u'v'}\right)-r\frac{\partial}{\partial z}\left(\overline{u'w'}\right)$$

The last three terms are equivalent to one normal and two shear stresses, and they are called Reynold's stresses.

Turbulence models.

In attempting to solve the N-S equations in 3 dimensions with turbulence, the solution cannot be "closed", i.e. there are more variables than distinct equations. The development of turbulence modelling occurred in the following sequence:

Boussinesq (1877) proposed an "effective viscosity" to relate the stress in a fluid element to its rate of strain.

Prandtl proposed a "mixing length" to describe the distance an element travels before it dissipates its excess momentum to surrounding fluid. This was a zero-equation model in that no transport effects were considered. Prandtl then developed the idea of kinetic energy replacing the velocity gradient, the kinetic energy being determined from a transport equation. This was a one-equation model.

Kolmogorov proposed the two-equation model using energy and frequency. The most popular two equation model is the k-ε model which has transport equations for the turbulence kinetic energy and the dissipation rate of the kinetic energy.

Reynold's stress modelling develops transport equations for the 6 independent Reynold's stresses. The advantage of the Reynold's stress model is that the fully 3 dimensional nature of the flow is represented. The other models are isotropic in that the turbulence is considered to be equally distributed in the three coordinate directions.

Development of the transport equations for turbulence in the standard k-e and the Realizable k-e models.

The standard k-ε model makes the assumption that the turbulence behaviour is isotropic (i.e. the same in all directions), and uses the turbulence kinetic energy (k) and the dissipation rate of the turbulence kinetic energy (ε) as transported quantities convected with the momentum of the flow. It uses the Boussinesq hypothesis to determine the turbulence viscosity:

$$-\rho\overline{u'_i u'_j} = \mu_t\left(\frac{\partial u_i}{\partial x_j}+\frac{\partial u_j}{\partial x_i}\right)-\frac{2}{3}\left(\rho k+\mu_t\frac{\partial u_i}{\partial x_i}\right)\delta_{ij}$$

$$\mu_t = \rho C_\mu \frac{k^2}{\varepsilon}$$

$$k = \frac{1}{2}(\overline{u'^2}+\overline{v'^2}+\overline{w'^2})$$

$$\varepsilon = 2\nu\overline{e'_{ij}.e'_{ij}}$$

$\delta_{ij} = 1$ if i = j, $\delta_{ij} = 0$ if $i \neq j$.

e' is the fluctuating component of the rate of deformation of a fluid element.

The transport equations for the two equation (k-ε) models are:

$$\rho\frac{Dk}{Dt} = \frac{\partial}{\partial x_i}\left[\left(\mu+\frac{\mu_t}{\sigma_k}\right)\frac{\partial k}{\partial x_i}\right]+G_k+G_b-\rho\varepsilon-Y_M$$

$$\rho\frac{D\varepsilon}{Dt} = \frac{\partial}{\partial x_i}\left[\left(\mu+\frac{\mu_t}{\sigma_\varepsilon}\right)\frac{\partial \varepsilon}{\partial x_i}\right]+C_{1\varepsilon}\frac{\varepsilon}{k}\left(G_k+C_{3\varepsilon}G_b\right)-C_{2\varepsilon}\rho\frac{\varepsilon^2}{k}$$

For the realizable k-ε model, the dissipation transport equation is:

$$\rho\frac{Dk}{Dt} = \frac{\partial}{\partial x_i}\left[\left(\mu+\frac{\mu_t}{\sigma_k}\right)\frac{\partial k}{\partial x_i}\right]+G_k+G_b-\rho\varepsilon-Y_M$$

$$\rho\frac{D\varepsilon}{Dt} = \frac{\partial}{\partial x_j}\left[\left(\mu+\frac{\mu_t}{\sigma_\varepsilon}\right)\frac{\partial \varepsilon}{\partial x_j}\right]+\rho C_1 S\varepsilon-\rho C_2\frac{\varepsilon^2}{k+\sqrt{u\varepsilon}}C_{1\varepsilon}\frac{\varepsilon}{k}C_{3\varepsilon}G_b$$

Where, $C_1 = \max\left[0.43,\frac{h}{h+5}\right], h = \frac{Sk}{\varepsilon}$, G_k is the production of k, G_b is the production due to buoyancy, which is included in the k equation and is optional for the ε equation. Ym is the dilation dissipation term for compressible flows.

In the realizable model the Cμ term is variable: $C_m = \frac{1}{A_0 + A_S \frac{Uk^*}{e}}$. The constants were used as defined in the Fluent User Guide [?].

The models consider a turbulent viscosity by analogy with kinetic theory, $\mu_t=\rho v_t l$, where vt is a characteristic velocity and l is a characteristic length. Prandtl developed this idea to give $m_t = rl^2\left|\frac{\partial u}{\partial y}\right|$.

The energy equation.

The Energy equation used in Fluent is stated in the following equation:

$$\frac{\partial}{\partial t}(re)+\frac{\partial}{\partial x_i}[u_i(rE+p)]=\frac{\partial}{\partial x_i}\left(k_{eff}\frac{\partial T}{\partial x_i}+u_j(t_{ij})_{eff}\right)+S_h$$

$$(t_{ij})_{eff}=m_{eff}\left(\frac{\partial u_j}{\partial x_i}+\frac{\partial u_i}{\partial x_j}\right)-\frac{2}{3}m_{eff}\frac{\partial u_i}{\partial x_i}d_{ij}$$

Where $k_{eff}=k+\frac{C_p m_t}{\mathrm{Pr}_t}, \mathrm{Pr}_t=0.85$.

τ_{ij} represents viscous heating and it is formed from the work done against the stresses on the fluid cell surface as indicated in the formulation of the x-momentum equation in the Navier Stokes equation in Appendix 3-1. It is not included by default in the segregated solver, which was used in this work. This was regarded as a reasonable assumption since the source term due to release of energy from reactions in the domain is several magnitudes greater than viscous and turbulent viscous work in the low-density gas mixture. This leaves the simplified energy equation:

$$\frac{\partial}{\partial t}(rE)+\frac{\partial}{\partial x_i}[u_i(rE+p)]=k_{eff}\frac{\partial^2 T}{\partial x_i^2}+S_h$$

Radiant heat transfer is included in the source term of the energy equation, S_h. The radiative heat transfer equation is:

$$\frac{dI(\vec{r},\vec{s})}{ds}+(a+s_s)I(\vec{r},\vec{s})=an^2\frac{sT^4}{p}+\frac{s_s}{4p}\int_0^{4p}I(\vec{r},\vec{s}')\Phi(\vec{s},\vec{s}')d\Omega'$$

The Rosseland model was used in the work of this thesis to give an approximate indication of a uniform absorptivity, α, across the entire

continuous fluid. It is based on the P-1 model, which is the simplest of the P-N type models as described by Siegel and Howell (1992). An effective radiative-conductivity is calculated and used in the energy equation. The effective conductivity is described by the following equation:

$$k_r = 16 s \Gamma T^3$$

Where Γ is a parameter from the P-1 model, which without the presence of scattering is 1/3a. The scattering coefficient (σ_s) was zero. The refractive index was assumed to be unity.

The Standard Wall Function for turbulence modelling near to walls.

The Standard Wall Function is described by the following equations:

$$U^* = \frac{1}{k} \ln(E y^*)$$

where the dimensionless groups U* and y* are defined as follows:

$$U^* = \frac{U_P C_m^{1/4} k_P^{1/2}}{t_w / r}$$

$$y^* \equiv \frac{r C_m^{1/4} k_P^{1/2} y_P}{m}$$

y_p = distance to wall, μ = dynamic viscosity. The equations are valid for y*>30~60 and are applied by Fluent for y*>11.225. For y*<11.225, U*=y*. The technique is similar for temperature.

Appendix 2

Calculation of boundary conditions of the precalciner

Calculation of the overall gas flow at the preheater exit

The calculation of the exit gas stream composition is not directly relevant to the precalciner boundary conditions, but it is necessary to determine the overall air requirement for the process. From this the quantity of tertiary air and the kiln gas stream composition can be determined in subsequent sections.

The combustion products of coal and the carbon dioxide yielded from calcination of the limestone can be determined from the mass injection rates. This combined with the oxygen content at the preheater exit can be used to determine the overall air requirement to support the process.

The raw meal CO_2 yield was calculated from the Loss On Ignition (LOI) and the injection rate,

$0.34 \times 47.71 = 16.22$ kg/s

The coal injection rate (Dry Ash Free, DAF) was determined from the hourly coal consumption converted to kg per second and from the moisture and ash content,

$$\frac{14{,}000}{3{,}600} \times \left(\frac{100 - 7.9 - 10.6}{100} \right) = 3.169 \text{ kg/s.}$$

The stoichiometric combustion calculation was done (Table 4-2) and combined with the excess air requirement to produce firstly the combustion product gas data and then the preheater exit-gas-stream composition data. In this table, the nitrogen associated with consumed oxygen was calculated as the "total O_2 consumed" multiplied by the mass ratio of nitrogen to oxygen in atmospheric air:

$8.648 \times 3.292 = 28.472$ kg/s

Coal product calculation (based on DAFelemental compostion of coal)						Exit gas stream composition		
	%	kg/s	product	product kg/s	O_2 consumed kg/s		kg/s	kmol/s
C	88.1	2.792	CO_2	10.237	7.445	CO_2	26.457	0.601
H	5.0	0.158	H_2O	1.422	1.264	H_2O	1.422	0.790
O	3.8	0.120	O_2	0.120	-0.120	O_2	2.772	0.087
S	1.9	0.060	SO_2	0.120	0.060	SO_2	0.120	0.002
N	1.2	0.038	N_2	0.038	0.000	N_2	37.599	1.343
			total O2 consumed		8.648	total	68.370	2.823

Table Appendix 2-1 Stoichiometry and exit gas stream for the whole process.

The preheater exit O_2 content was calculated by using the sum of gases produced by combustion and calcination and using the calculation:

$$\%O_2 = \frac{(\text{volume of } O_2 \text{ leaving the preheater})}{(\text{total volume of gases leaving preheater})} \qquad \textbf{Equation Appendix 2-1}$$

Calculation of gas content of kiln delivery to precalciner

The gases entering at the bottom of the precalciner are determined by combustion in the kiln. Two-fifths of the coal combustion for the overall process occurs in the kiln. Unreacted limestone entering the kiln from the precalciner is negligible so no carbon dioxide is attributable to that reaction in the kiln. Table Appendix 2-2 shows the calculated gas-stream composition passing from the kiln to the precalciner. The calculation involved data from Table Appendix 2-1, from the previous section, for coal combustion and the same method of excess air calculation with 3.2% at the exit from the kiln.

Kiln combustion (based on DAFelemental compostion of coal)						Kiln exit gas stream composition			
	%	kg/s	product	product kg/s	O_2 consumed kg/s		kg/s	kmol/s	%
C	88.1	1.117	CO_2	4.095	2.978	CO_2	4.095	0.093	22%
H	5.0	0.063	H_2O	0.569	0.505	H_2O	0.569	0.032	3%
O	3.8	0.048	O_2	0.048	-0.048	O_2	0.644	0.020	3%
S	1.9	0.024	SO_2	0.048	0.024	SO_2	0.048	0.001	0%
N	1.2	0.015	N_2	0.015	0.000	N_2	13.523	0.483	72%
			total O2 consumed		3.459	total	18.878	0.629	

Table Appendix 2-2 Stoichiometry and gas stream for kiln gas exit.

Since this calculation is for the air requirement to the kiln, the CO contribution to the exit gas stream has been neglected.

Calculation of the air injected at the coal inlets

The volume flow rate of air to the two coal inlets is 18.8 m^3/min at 47°C at the point of measurement. The supply pipes have internal diameter 3.5". By using the gas law, the mass flow rate is given by the following calculations:

$$r = \frac{p}{RT} = \frac{100{,}000}{287 \times 320} = 1.089 \text{ kg/m}^3,$$

where R is the specific gas constant of atmospheric air mixture;

$\dot{m} = 1.089 \times 18.8 = 0.341$ kg/s of air.

The proportion of nitrogen to oxygen is 3.929 by mass, which means the following gas injection at the coal inlets (Table 4-4):

	kg/s	kmol/s
O_2	0.080	0.002
N_2	0.262	0.009
total	0.341	0.012

Table Appendix 2-3 Coal inlet air composition.

Calculation of gases entering at the tertiary air duct

The tertiary air is drawn through a duct running parallel to the kiln from the same source as the kiln air supply. The quantity must be calculated since the division of air supply to kiln and tertiary air duct is not measured in practise. The method of calculation is by deduction from the preheater exit gas stream composition (calculated above) and the kiln gas calculation (above).

From coal combustion, the amount of O_2 consumed in the precalciner is:

8.648-3.459=5.189 kg/s

This was calculated from the difference between the overall combustion O_2 in Table Appendix 2-1 and kiln combustion O_2 in Table Appendix 2-2.

The excess air from the kiln exit was found to be 0.644 kg/s O_2 in Table Appendix 2-2 and the excess air at the preheater tower exit was 2.772 kg/s in Table Appendix 2-1.

Therefore the amount of O_2 delivered by the tertiary air duct is:

$$5.189 + 2.772 - 0.644 = 7.317 \text{ kg/s}$$

and the associated N_2 is therefore:

$$3.292 \times 7.317 = 24.087 \text{ kg/s}$$

Calculation of gases entering at the raw meal inlet

The stage III material drop chute (see Fig. 2-2) has a damper flap, which is opened by the raw meal falling on to it as it passes from stage III to the precalciner. The gases passing through this route are neither calculable (since no indicative measurements are done in this section of the precalciner) nor measurable (due to the heavy particle loading). The gas velocity at the raw meal inlet to the precalciner in the model was 8 and 10 m/s. The assumption was that there would be a venturi effect caused by the rapidly rising kiln gas stream passing the inlet, which might well cause a velocity of this magnitude. The model composition of the raw-meal inlet gas stream was the same as the kiln gas inlet based on the assumption of similar combustion reactions upstream of both inlets.

Calculation of the wall heat transfer to the surroundings

Heat transfer from the outside surface of the precalciner takes place by radiative and convective heat transfer from the steel shell. Heat transfer through the wall by conduction due to the resulting temperature difference between the inside and outside walls is easily calculable since the wall temperatures can be estimated. The inside wall temperature is approximately 900°C and the temperature of the shell is known from measurement using an infra-red thermometer, approximately 100°C. The conductivity of the refractory lining of the precalciner was estimated from standard data (Rose and Cooper, 1977).

The refractory lining of the precalciner is constructed in two layers. The inner layer is made of a refractory brick, 114 mm thick, with thermal conductivity approximately 1.67 $Wm^{-1}K^{-1}$. The layer in contact with the steel

shell is made of an insulating refractory, 115 mm thick, with thermal conductivity approximately 0.209 $Wm^{-1}K^{-1}$. The steel shell is 12 mm thick with thermal conductivity approximately 43 $Wm^{-1}K^{-1}$. The rate of heat conduction was calculated thus:

$$\dot{q} = -kA\left(\frac{dT}{dx}\right) = -\frac{\Delta T}{\sum \frac{\Delta x}{k}}$$ **Equation Appendix 2-2**

where the calculation has been made per m^2. Putting in the values from above:

$$\dot{q} = \frac{800}{\left(\frac{0.114}{1.67} + \frac{0.115}{0.209} + \frac{0.012}{43}\right)} = 1293 Wm^{-2}$$

Appendix 3

Derivation of the limestone calcination rate from Fluent

This appendix presents the calculation of the limestone calcination rate data used in the CFD models. The discrepancy in the use of Borgwardt's data (1985) is also explained and the validity of the of the values used in the CFD models is justified.

Starting with the equation used for mass loss rate in a devolatilizing particle:

$$-\frac{dm_p}{dt} = k(m_p - (1-f_{v0})m_{p0}) \qquad \textbf{Equation Appendix 3-1}$$

the equation can be solved in the following way:

$$\int_{m_{p0}}^{(1-f_v)m_{p0}} \frac{dm_p}{m_p - (1-f_{v0})m_{p0}} = -\int_0^t k dt$$

$$\left[\ln(m_p - (1-f_{v0})m_{p0})\right]_{m_{p0}}^{(1-f_v)m_{p0}} = -kt$$

$$\ln\left[(1-f_v)m_{p0} - (1-f_{v0})m_{p0}\right] - \left[\ln(m_{p0} - (1-f_{v0})m_{p0})\right] = -kt$$

$$\ln(f_{v0} - f_v)m_{p0} - \ln(f_{v0}m_{p0}) = -kt$$

$$\ln\frac{f_{v0} - f_v}{f_{v0}} = -kt$$

$$\ln(1-x) = -kt$$

Equating the two expressions for the rate:

$$k = k_s S_g$$

k_s is found to be 2.5×10^{-8} mol cm^{-2} s^{-1} at 670°C by Borgwardt and 1.6×10^{-6} mol cm^{-2} s^{-1} at 850°C by other research results quoted by Borgwardt. Borgwardt extrapolated the data to temperatures outside the range of experiments and derived a linear relationship between the log of the calcination rate constant and the temperature. The data is reproduced in Fig. A3-1. The significance of

this figure was not realised until after the conclusion of the project. It is important to consider the implications.

Considering first the values at 670°C used in the work described in this thesis, using the B.E.T. surface area of limestone from Borgwardt of 0.12 m^2/g of limestone and the molar mass of calcium oxide of 56g/mol, then for Borgwardt's value of k_s at 670°C:

$$k_s S_g = 2.5\times10^{-8} mol.cm^{-2}.s^{-1} \times 0.12 m^2 g^{-1} \times 56 g.mol^{-1} \times 10{,}000 cm^2 m^{-2} = k$$

$$\therefore k = 0.00168 s^{-1}$$

Applying these values of k in the Arrhenius expression:

$$0.00168 = A\exp\left(-2.05\times10^8 \big/ 8314.5\times943\right)$$

$$\therefore A = 3.81\times10^8 s^{-1}$$

for the Borgwardt result. The time to decompose 95% of the volatile component according to this rate is:

$$\ln(1-x) = -kt$$

$$\ln(0.05) = -0.00168t$$

$$t = 1783 s$$

or 30 minutes. This result is reasonable considering the relatively low temperature. Using the A and E values at 900°C:

$$k = 3.81\times10^8 \exp\left(-2.05\times10^8 / 8314.5\times1173\right)$$

$$k = 0.28$$

which results in a time to decompose 95% of the volatile component of 10.7 s, showing the accelerating effect of the higher temperature.

At the temperatures encountered in the precalciner, nominally 900°C (1173K), the corresponding calcination rate from Fig. A3-1 is $k_s = 3\times10^{-6}$ mol cm^{-2} s^{-1}, which is equivalent to k of 0.2016. This results in $A = 2.7\times10^8$ and a time to decompose 95% of the volatile component of 14.9 s, which is of the same order of magnitude as the values used in this thesis and thus the suitability of the data used in the model is justified.

Appendix 4

Raw meal sample collection and quenching pot

Design of the collection pot.

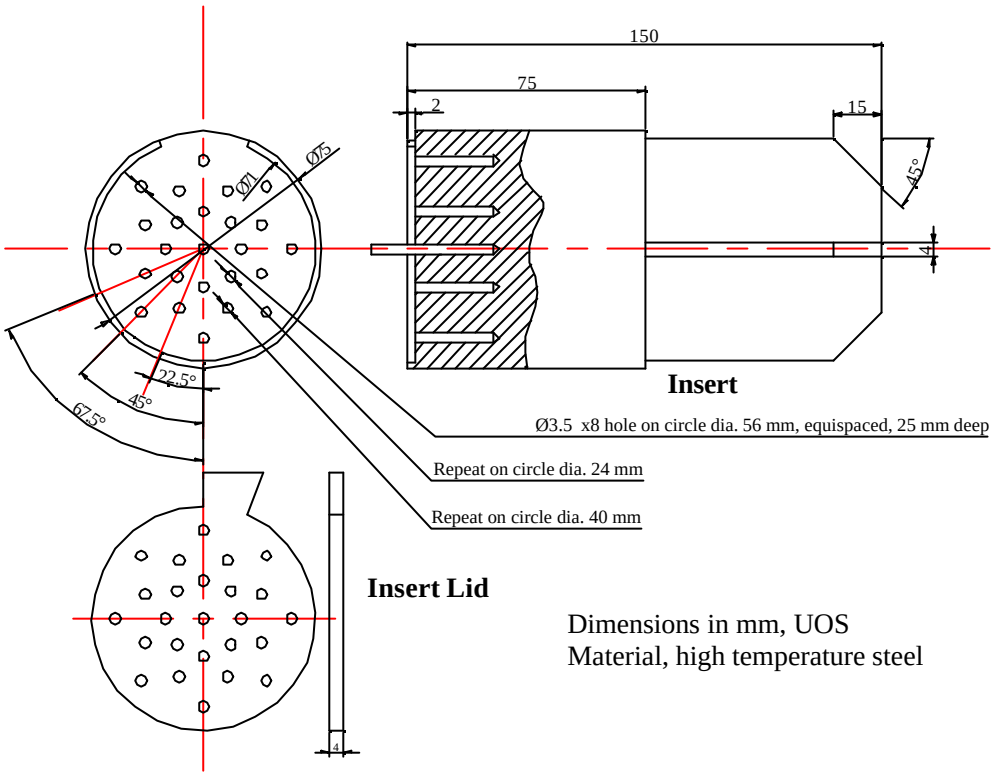

Fig. A4-1 Detail drawing of the sample pot and lid.

Heat transfer calculation.

The rate of heating of the "rods" of raw meal in the holes of the pot was estimated using the lumped capacity approach described in Holman (1997). Properties of calcium carbonate were obtained at 700°C (a temperature between 900°C and 500°C) from Perry and Green (1984) as follows:

- thermal conductivity, k_{tc} = 2.252 W m^{-1} K^{-1}
- heat capacity, C_p = 1,250 J kg^{-1} K^{-1}
- density, r = 2,450 kg m^{-3}
- thermal diffusivity, $a = k/r\ C_p$ m^2 s^{-1}

The Biot number, $Bi = h\,s\,/\,k_{tc}$, provides a measure of the ratio of convective heat transfer to internal conductive heat transfer. It was considered to be "large" in this case since the effective convection of heat away from the surface is very rapid compared to the internal transfer of heat in the insulating material surrounded by a conductor. Holman presents a chart of temperature difference ratio, $\frac{q_0}{q_i} = \frac{t_0 - t_1}{t_i - t_1}$, vs. Fourier number ($Fo = \alpha\, t \,/\, r_0^2$) corresponding to the Biot number reciprocal. The estimated time to drop from 880°C to 500°C, by which stage the calcination reaction should effectively have ceased, was 2.2 s. This was considered to be sufficiently fast for the purpose of the experiment since the calcination rate decreases rapidly as the temperature decreases from 900°C.

Appendix 5

Data obtained from the tyre injection position experiments

Injection position experiments.

The data in this appendix refers to the alternative injection point analysis described in section 7.6. Three tables of data are provided to summarize the alternative injection point modelling work. Six tyre chips of each size injected from each position indicated A-J. Exit through ports other than the exit duct is indicated in the chart by the rows titled "Alt. Exit". In that row the number of 6 injected chips, which do not leave through the stage IV exit, is indicated.

The letters indicate the alternative exit port with the following designations:

C – coal inlets

K – kiln gas inlet

T - tertiary air duct

R - raw meal inlet

In each chart, the first row describes chips <2", the second row describes chips <3", and the third row describes chips <4".

The range of residence times (in seconds) for each set of injections is indicated in the rows titled "Res time s".

Figure 7-18a-f: CURRENT HEIGHT INJECTION

Position	A	B	C	D	E	F	G	H	I	J
Res time s		7-28	10-69	9-26		11-50	9-46	7-51	17-33	6-21
Alt Exit		1C								
Res time s		7-22	11-34	16-71		16	34-36	14	19-48	29
Alt Exit		2K	4K			5K,C	4K	5K,R	2K	5K,T
Res time s										
Alt Exit		6K	5K,1R	6K		6K	5K,1R	6K	6K	5K,1R

Figure 7-19a-f: CURRENT HEIGHT +5M

Position	A	B	C	D	E	F	G	H	I	J
Res time s Alt Exit		10-31	9-50	7-35		10-48	7-32	6-50	10-24	14-20
Res time s Alt Exit		23-57 2K	21 5K,1R,1T	7-56		19-62 2K,1C	16-24 2K,1R	12-57 1K	9-48 1C	17-66
Res time s Alt Exit		5K,1R	4K,1R,1C	8-39		18-43 2K,1R	1R,5K	1R,5K	6K	6K

Figure 7-20a-f: ROOF INJECTION

Position	A	B	C	D	E	F	G	H	I	J
Res time s Alt. Exit	10-36	11-49	8-43	3-4	10-28	4-5	8-27	12-29	10-30	8-38
Res time s Alt Exit	18-49	22-64 (1C)	12-52 (1C)	5-6	28-47 (1K)	4-5	22-60	9-59 (2R)	15-83	15-32 (1T)
Res time s Alt Exit	22 (5T,K)	12-37 (1T)	13-38	9-72	25-35 (3K)	17-40	13-33	10 (5K)	11-32 (2T)	8-44 (2T)

Check on the validity of using a small tyre chip sample.

The table in this section represents the results of a check done to ensure that the 6 chip sample for each alternative injection was representative of the random effects of turbulence on tyre chip trajectories.

20 stochastic attempts were made resulting in 120 chips injected for each group.

This table, compared with the results from the previous section for Figure 7-19a-f: CURRENT HEIGHT +5M, shows that the 6 chips give a good representation of the average behaviour of the whole sample.

Group	Out	Kiln	Meal	Tertiary	Coal
B1	119				1
B3	68	32	3	15	1
B5		100	20		
C1	118				2
C3	48	44	7	16	4
C5					
D1	120				
D3	116	1			2
D5	113	2		4	1
F1	117				3
F3	99	12	5	1	1
F5	85	18	13	4	
G1	118				2
G3	76	31	11		1
G5	9	70	33	8	
H1	119				1
H3	93	24	1		2
H5					
I1	119				1
I3	105	5			7
I5		117		3	
J1	119				1
J3	112	6	2		
J5	4	108	1	7	

Table Appendix 5-1 Analysis of stochastic attempts for tyre chips at different injection points.

Table Appendix 5-2 shows the group designation and the number of chips of the 120 sample exiting each port described by Out (outlet duct), Kiln (kiln gas inlet), Meal (raw meal inlet), Tertiary (tertiary air inlet) and Coal (both coal inlets).